UNIVERSITY OF NICE - SOPHIA ANTIPOLIS

GRADUATE SCHOOL STIC
INFORMATION AND COMMUNICATION TECHNOLOGIES AND SCIENCES

T H E S I S

to fulfill the requirements for the degree of

Ph.D. in Computer Science

from the University of Nice - Sophia Antipolis

Specialized in : CONTROL, SIGNAL AND IMAGE PROCESSING

presented by

Ender KONUKOĞLU

Modeling Glioma Growth and Personalizing Growth Models in Medical Images

Thesis supervised by Nicholas AYACHE

prepared at the INRIA Sophia Antipolis, ASCLEPIOS Project

defended the February 17, 2009.

Jury :

M. Nicholas AYACHE,	Ph.D.	-	Director
M. Pierre-Yves BONDIAU,	M.D./Ph.D.	-	Invited member
M. Olivier CLATZ,	Ph.D.	-	Examiner
M. Hervé DELINGETTE,	Ph.D.	-	Examiner
M. Guido GERIG,	Professor	-	Reviewer
M. Emmanuel MANDONNET,	M.D./Ph.D.	-	Invited member
M. Gábor J. SZÉKELY,	Professor	-	Reviewer
M. William WELLS,	Ph.D.	-	Examiner

UNIVERSITÉ DE NICE - SOPHIA ANTIPOLIS

ECOLE DOCTORALE STIC
SCIENCES ET TECHNOLOGIES DE L'INFORMATION ET DE LA COMMUNICATION

T H È S E

pour obtenir le titre de

Docteur en Sciences

de l'Université de Nice - Sophia Antipolis

Mention : INFORMATIQUE

présentée par

Ender KONUKOĞLU

Modélisation de la Croissance des Gliomes et Personnalisation des Modéles de Croissance à l'aide d'Images Médicales

Thèse dirigée par Nicholas AYACHE

préparée à l'INRIA Sophia Antipolis, Projet ASCLEPIOS

soutenue le 17 Février 2009.

Jury :

M. Nicholas AYACHE,	Ph.D.	-	Directeur
M. Pierre-Yves BONDIAU,	M.D./Ph.D.	-	Invité
M. Olivier CLATZ,	Ph.D.	-	Examinateur
M. Hervé DELINGETTE,	Ph.D.	-	Examinateur
M. Guido GERIG,	Professor	-	Rapporteur
M. Emmanuel MANDONNET,	M.D./Ph.D.	-	Invité
M. Gábor J. SZÉKELY,	Professor	-	Rapparteur
M. William WELLS,	Ph.D.	-	Examinateur

To the long lost peace in the Middle East...

Acknowledgements

First of all I would like to thank Nicholas Ayache, for supervising my research and for giving me the opportunity to work in his group for the last 3 and a half years. He has been always there supporting my work even at times I doubted myself.

I thank Olivier Clatz for being there all the way during this thesis. He has been a colleague, a co-advisor and most of all a friend giving me advice, direction and courage. This thesis is mostly a result of our day-long discussions.

I would like to thank Hervé Delingette and Maxime Sermesant for all their support and help from which I benefited a lot during my research. They have beared my bursts into their offices which ended in dirty and unintillegible white boards most of the time.

I take this opportunity to express my gratitude to the members of the committee:

1. Guido Gerig and Gábor Székely for accepting to be the reviewers of this thesis. Thank you for the time and attention you have devoted to this thesis and also for the comments and the very encouraging compliments.

2. William Wells for accepting to preside the jury and also for showing interest in this work both during and at the end of the thesis. Thank you for your compliments, valuable advices and most of all for your help.

3. Pierre-Yves Bondiau and Emmanuel Mandonnet for being a part of the jury and more importantly for demonstrating interest in this work. They have been very constructive throughout this research. Thank you for your support both in terms of knowledge and images, which made this thesis possible, and also in terms of encouragement.

I should not forget to thank Bjoern Menze whose help added immense value to this thesis. Thank you for supporting the ideas proposed in this thesis, for sharing an important database, for sharing knowledge and for devoting your time. I also thank Marc-André Weber and Bram Stieltjes from the German Cancer Research Center (DKFZ) for sharing their databases and their clinical knowledge.

I would also like to take this opportunity to thank Kilian M. Pohl who has helped me in all aspects of the PhD. Thank you for devoting your time and teaching me both about science and about life.

The ones who have the biggest role in all what I have done are undoubtedly my family. I thank my parents for providing me all the possibilities. I thank my brother Ali Emre Konukoğlu for all his support and friendship. I thank my uncle Orhan Konç for showing me the light side of life when I needed the most.

Abstract

Mathematical models and more specifically reaction-diffusion based models have been widely used in the literature for modeling the growth of brain gliomas and tumors in general. Besides the vast amount of research focused on microscopic and biological experiments, recently models have started integrating medical images in their formulations. By including the geometry of the brain and the tumor, the different tissue structures and the diffusion images, models are able to simulate the macroscopic growth observable in the images. Although generic models have been proposed, methods for adapting these models to individual patient images remain an unexplored area.

In this thesis we address the problem of "personalizing mathematical tumor growth models". We focus on reaction-diffusion models and their applications on modeling the growth of brain gliomas. As a first step, we propose a method for automatic identification of patient-specific model parameters from series of medical images. Observing the discrepancies between the visualization of gliomas in MR images and the reaction-diffusion models, we derive a novel formulation for explaining the evolution of the tumor delineation. This "modified anisotropic Eikonal" model is later used for estimating the model parameters from images. Thorough analysis on synthetic dataset validates the proposed method theoretically and also gives us insights on the nature of the underlying problem. Preliminary results on real cases show promising potentials of the parameter estimation method and the reaction-diffusion models both for quantifying tumor growth and also for predicting future evolution of the pathology.

Following the personalization, we focus on the clinical application of such patient-specific models. Specifically, we tackle the problem of limited visualization of glioma infiltration in MR images. The images only show a part of the tumor and mask the low density invasion. This missing information is crucial for radiotherapy and other types of treatment. We propose a formulation for this problem based on the patient-specific models. In the analysis we also show the potential benefits of such the proposed method for radiotherapy planning.

The last part of this thesis deals with numerical methods for anisotropic Eikonal equations. This type of equation arises in both of the previous parts of this thesis. Moreover, such equations are also used in different modeling problems, computer vision, geometrical optics and other different fields. We propose a numerical method for solving anisotropic Eikonal equations in a fast and accurate manner. By comparing it with a state-of-the-art method we demonstrate the advantages of our technique.

Résumé

Les modèles mathématiques et plus spécifiquement les modèles basés sur l'équation de réaction-diffusion ont été utilisés largement dans la littérature pour modéliser la croissance des gliomes cérébraux et des tumeurs en général. De plus la grande littérature de recherche qui concentre sur les expériences biologiques et microscopiques, récemment les modèles ont commencé intégrer l'imagerie médicale dans ses formulations. Incluant la géométrie du cerveau et celle de la tumeur, les structures des différentes tissues et la direction de diffusion, ils ont montré qu'il est possible de simuler la croissance de la tumeur comme c'est observé dans les images médicales. Bien que des modèles génériques ont été proposés, les méthodes pour adapter ces modèles aux images d'un patient reste un domaine inexploré.

Dans cette thèse nous nous adressons au problème de "personnalisation de modèle mathématique de la croissance de tumeurs." Nous nous focalisons sur les modèles de réaction-diffusion et leurs applications sur la croissance des gliomes cérébrales. Dans la première étape, nous proposons une méthode pour l'identification automatique des paramètres "patient-spécifiques" du modèle à partir d'une série d'images. En observant la divergence entre la visualisation des gliomes dans les IRMs et les modèles réaction-diffusion, nous déduisons une nouvelle formulation pour expliquer l'évolution de la délinéation de la tumeur. Ce modèle "Eikonal anistropique modifié" est utilisé plus tard pour l'estimation des paramètres à partir des images. Nous avons théoriquement analysé la méthode proposée à l'aide d'un base donne synthétique et nous avons montré la capacité de la méthode et aussi sa limitation. En plus, les résultats préliminaires, sur les cas réels montrent des potentiels prometteurs de la méthode d'estimation des paramètres et du modèle de réaction-diffusion pour la quantification de la croissance de tumeur et aussi pour la prédiction de l'évolution futur de la tumeur.

En suivant la personnalisation, nous nous concentrons sur les applications cliniques des modèles "patient-spécifiques". Spécifiquement, nous nous attaquons au problème de la visualisation limitée d'infiltration de gliome dans l'IRM. En effet, les images ne montrent qu'une partie de la tumeur et masquent l'infiltration basse-densité. Cette information absente est cruciale pour la radiothérapie et aussi pour d'autre type de traitements. Dans ce travail, nous proposons pour ce problème une formulation basée sur les modèles "patient-spécifiques". Dans l'analyse de cette méthode nous montrons également les bénéfices potentiels pour la planification de la radiothérapie.

La dernière étape de cette thèse se concentre sur les méthodes numériques de l'équation "Eikonal anisotropique". Ce type d'équation est utilisé dans beaucoup de problèmes différents tel que la modélisation, le traitement d'image, la vision par ordinateur et l'optique géométrique. Ici nous proposons une méthode numérique rapide et efficace pour résoudre l'équation Eikonal anisotropique. En la comparant avec une autre méthode état-de-l'art nous démontrons les avantages de la technique proposée.

Contents

Introduction

Contents

1.1 Context

How can we describe the progression of tumors through mathematical models and computer simulations? This question has been keeping scientists busy for the last 30 years. Mathematicians, clinicians, biologists, physicists and computer scientists are collaborating to tackle this problem. Considering the complexity of the dynamics of tumor growth and the fact that most of the underlying phenomena have not been discovered yet, these attempts will continue for a while. This thesis is a humble contribution towards these goals.

Cancer is one of the leading causes of death and it is not necessary to describe its graveness. The important point to note is that it is becoming more common and we have not yet totally understood the reasons for its occurrence and the way to cure it. Vast amount of experimental research in biology and medicine enlightens many different aspects of the dynamics of cancer progression. They provide information in many different scales from genetics to tissue. Mathematical modeling is important in this respect as it provides a melting pot for all these experimental results. Models provide a systematic structure that brings these results together and shows us the overall picture. This gives us the opportunity to better understand the tumor growth and interaction between different factors and also to help clinicians in diagnosing and treating tumors.

Mathematical modeling of tumor growth has received considerable attention during the last 30 years. Different modeling attempts have been proposed spanning a large range of scales and techniques describing different dynamics and phenomenon in the growth process. Although lots of efforts have been given to formulate more realistic and detailed models, little attention has been given to the applicability of these models to clinical data and their personalization. As the models become more sophisticated the gap between the information clinically available and needed by the models widen. As a result adapting mathematical models to patient data become harder.

The motivation of this thesis is therefore to study the link between mathematical tumor growth models and medical images in attempt to create tools useful in

clinical settings. Instead of going one step further in detailing existing models and making them more realistic, we take a step backward and search for ways to apply these models to specific patient data using images. In this manner we take a more pragmatic approach to tumor growth modeling.

Although tumors in different parts of the body have certain common characteristics they also differ in many ways. Therefore, each tumor should be studied separately. In this thesis we focus on the modeling of a specific type of brain tumor, gliomas. In attempt to link medical images and the growth models, we start from an existing model explaining the growth of gliomas, which is based on the well known Reaction-Diffusion (RD) equations, and study its link with the available information in Magnetic Resonance Images (MRI).

1.2   Problems Investigated

In the previous section we have set the general motivation of this thesis as studying the link between tumor growth models and medical images. This is a very complex problem with different components such as theoretical analysis of the models, physics of the image acquisition and biological analysis of the tissue response to tumor growth. Of course, this thesis does not aim to provide solutions to all these problems. It is rather intended to be a part of a collaborative work tackling all these mentioned components. In this thesis we focus on the theoretical analysis of a type of tumor growth model, which is based on reaction-diffusion equations. In this respect we focus on three different problems:

- **Image Guided Personalization of Reaction-Diffusion Type Tumor Growth Models:** The first problem we tackle is adapting the reaction-diffusion tumor growth model to specific patient images, personalizing the model. This adaptation can also be formulated as estimating the parameters of the reaction-diffusion tumor growth model using time series of medical images taken from the same patient. So the exact question we try to solve is: *How to estimate these patient-specific parameters that would best explain the progression of the tumor observed in the images? How to create the patient-specific model?*

- **Extrapolating Extents of Glioma Invasion in MRI:** Medical images are one of the main source of information in diagnosing and treating brain tumors. Especially in radiotherapy, images are crucial in planning the therapy and outlining the area which will be irradiated. The images however, cannot show the whole extent of gliomas due to the invasive nature of this type of tumor. The extent of the whole tumor goes beyond the visible part in the image and the possible direction of this "undetectable" extension is important in outlining the irradiation area. The second question we tackle in this thesis is: *How can we extrapolate this undetectable extension from the visible part of the tumor in the image using patient-specific models?*

- **Anisotropic Eikonal Equations:** The third point of focus in this thesis arose from the first two questions detailed above. The mathematical formula-

tions we derived to solve the first two questions ended up to have the form of modified anisotropic Eikonal equations. Moreover, after reviewing other type of models for different organs and pathologies we realized the importance of this type of equations. Therefore, the third question we ask is a more methodological question: *How to solve anisotropic Eikonal equations in a fast and accurate manner?*

1.3 Organization of the Thesis

This thesis is organized around the three questions explained in the previous section. We first start by providing general information about gliomas and medical images followed by background information on tumor growth modeling. After the background we present our work on the three main questions making up the contributions of this thesis. The detailed description of the material covered in each chapter is given below.

Chapter 2 gives some general knowledge on brain tumors and more specifically on gliomas. Different types of gliomas, the grading conventions and different behavior of these tumors are explained briefly. We also give some information about the appearance of gliomas in MRI as this is crucial for the understanding of the remainder of the thesis.

Chapter 3 provides an overview of the literature on tumor growth modeling. In this chapter we do not distinguish between brain tumors and tumors in the other parts of the body as the modeling attempts are linked together. The main approaches of modeling, different scales of models, different techniques and different phenomena modeled are covered in this chapter. We discuss briefly about models focusing on microscopic dynamics and models working with information coming from medical images. In this chapter we also give a review of different image analysis techniques which use tumor growth modeling to tackle different problems such as segmentation and registration.

Chapter 4 explains our approach to the problem of personalizing the reaction-diffusion type tumor growth models. In this chapter we focus on the discrepancy between the information required by the reaction-diffusion models and the information available in medical images. Reaction-diffusion models describe the evolution of tumor cell density distributions however, in medical images we only observe boundaries between the enhanced/unenhanced tumoral region and the healthy tissue. In order to solve this discrepancy, through asymptotic approximations we derive a formulation which describes the evolution of tumor delineations in the images based on the dynamics of reaction-diffusion growth models. Using this more consistent mathematical description, we formulate the parameter estimation problem for reaction-diffusion type tumor growth models using time series of patient images.

Chapter 5 analyzes the parameter estimation methodology presented in Chapter 4. We present experimental results on synthetic and real images. Through synthetically created data sets we perform theoretical analysis of the method and show the feasibility of the parameter estimation problem under the constraint of medical images, specifically we show the non-uniqueness of the solution of the most general case. We also show that under certain assumptions the parameter estimation problem can be solved and certain values unique to each tumor can be extracted from medical images, such as the speed of progression. Following this analysis, on real data we present promising results showing the ability of the method in finding the set of parameters which well describes the evolution of the tumor observed in MR images. Moreover, we demonstrate the power of the estimated parameters and the reaction-diffusion models (or rather the formulation derived from the RD models) in predicting the future evolution of the tumor in images.

Chapter 6 explains the problem of limited visualization of gliomas in medical images. In this chapter we propose a solution to this problem based on dynamics described by the reaction-diffusion models. Again through asymptotic approximations we derive an extrapolation formulation which starting from the visible part of the glioma in the MR image extrapolates the possible extents of the glioma undetectable in the image. In other words the proposed method constructs the tumor cell density distribution beyond the visible mass in the image.

Chapter 7 presents the synthetic experiments we have performed to test the extrapolation method described in Chapter 6. We first analyze the method to see if the extrapolated invasion extent matches the actual tumor cell density distribution of a synthetically grown tumor. After verifying this we turn our attention to the planning of radiotherapy. We focus on the phase of outlining the irradiation margins starting from the tumor delineation in the image. In conventional radiotherapy a constant margin of 1.5-2 cm is outlined around the tumor delineation to account for the undetectable extent of the glioma. In this chapter we show that a variable margin constructed according to the possible extent of the glioma, theoretically, may better target the tumor and harm less healthy brain tissue.

Chapter 8 focuses on the numerical solutions of a type of partial differential equation, the anisotropic Eikonal equations. This type of equations arise in the first two problems we presented in Chapters 4 and 6. Moreover, anisotropic Eikonal equations also arise in the modeling of different organs and pathologies, especially in cardiovascular and wound healing models. On the other hand, these equations are not inherent to biological/physiological modeling, they also arise in different fields such as geophysics and computer vision. Therefore, fast and accurate solvers for such equations are important for different domains. In this chapter we propose a numerical method for anisotropic Eikonal equations which extends the well known Fast Marching method to work in anisotropic domains. We detail our method and provide several experiments including comparison with one of the state-of-the-art solvers to demonstrate the performance of the proposed algorithm.

Chapter 9 concludes this thesis by going over the contributions we have proposed in each chapter and providing the perspectives for the future work.

Appendix A gives a brief overview on Hamilton-Jacobi equations which are extensively used in this thesis. This overview is by no means complete and it just aims to introduce this topic coarsely to readers who are not familiar with it. Hamilton-Jacobi equations is a wide class of partial differential equations and the emphasis in this appendix is given to the type of equations mentioned in this thesis.

Appendix B gives the algorithmic details on the minimization algorithm used in Chapter 4. This algorithm is proposed by Powell in [Powell 2002] and the review in this Appendix goes over the basic steps of the method for completeness of the thesis.

Brain Tumors and Medical Images

Contents

Context

The techniques and methods presented in this work deal with the mathematical modeling of brain tumors and the use of magnetic resonance images for this purpose. Therefore, some knowledge about brain tumors, magnetic resonance images and appearance of tumors in these images is necessary. In this chapter we provide brief information about brain tumors in Section 2.1 and specifically brain gliomas in Section 2.2 since they are the main focus of this thesis. In Section 2.3 we describe shortly the magnetic resonance imaging and the appearance of brain gliomas on these images. Detailed information about any of these three topics is outside the scope of this work. Please refer to [Wilson 1999] for information on gliomas and brain tumors and refer to [Westbrook 1998, Liang 2000] for detailed information on magnetic resonance imaging.

2.1 Brain Tumors

The term "tumor" originally means abnormal swelling of the flesh and is derived from the Latin word *tumor* which means swelling. In the current use tumor means a lesion which is formed by abnormal growth and uncontrolled rapid cellular proliferation that possesses no function, a neoplasm. A tumor that is located in the brain is called a brain tumor. Brain tumors are not very common pathologies, current statistics indicates around 100 incidences per year in 100,000 people in the developed world. In the case of children the rate of incidence is even lower, 4.5 incidences in 100,000. Even though these values are not very high, brain tumors are among the leading cause of cancer-related death for all ages [DeAngelis 2001, ABTA 2008a].

Brain tumors can be coarsely divided into groups using two different classifications, according to the degree of their aggressiveness and according to their origin. In terms of aggressiveness the brain tumors are classified as benign and malignant.

Benign brain tumors proliferates slowly and they rarely spread to the surrounding tissue. They would have a normal appearance under the microscope and globally they would show distinct borders between the tumor and the brain tissue. Most of the time, if it can be done, the tumor can be totally removed by surgery. Although most of these tumors are not life threatening, they may be so depending on their size and their location in the brain. Malignant brain tumors on the other hand, proliferate rapidly and invade the healthy areas of the brain. Their borders are not clear due to their infiltrative nature making surgical removal difficult. Moreover, they show neoangiogenesis and necrosis. Their cells can travel and colonize other parts of the brain and the spinal cord through cerebrospinal fluid. These tumors are life-threatening with a low survival rate [Tovi 1993, Wilson 1999, DeAngelis 2001].

The distinction between benign and malignant brain tumors is not obvious and requires the definition of a set of criteria and grading systems. In order to facilitate the diagnosis and the therapy planning, tumors are graded based on their aggressiveness. The most commonly used grading system is the one proposed by the World Health Organization (WHO). Grading of a tumor takes into account different factors such as mitotic index, vascularity, presence of a necrotic core, invasive potential and similarity to normal cells. In the WHO system 4 grades are used to classify tumor which are summarized in the Table 2.1

Table 2.1: WHO Tumor Grades and Characteristics

Grade	Characteristics
Grade I	- slow proliferation - cells look like normal - long survival rate - e.g.. pilocytic astrocytomas
Grade II	- relatively slow proliferation - cells look like almost normal - may invade - may recur as grade II or a higher grade
Grade III	- rapidly reproducing - cells look abnormal - vascular proliferation - invade surrounding tissue - tends to recur - e.g.. Anaplastic astrocytomas
Grade IV	- very rapid proliferation - very abnormal appearance of cells - invasion of large areas - recurs - necrotic core - forms new vascularization to support growth - e.g. Glioblastoma Multiforme

The classification of brain tumors in terms of their origin also has two groups: primary and metastatic. Primary tumors are the ones that originate from the brain cells and stay in the brain. They can occur at any age however, statistically they are more common in children and in older adults. These tumors can be benign or malignant. Different tumors in this group are named based on the type of cells they originate from. Examples of these tumors are gliomas, meningiomas, medulloblastomas, ependymomas and pituitary tumors. Among these the most important ones are meningiomas as they form the biggest part of all primary brain tumors and gliomas because they represent the majority of the malignant brain tumors [DeAngelis 2001]. Metastatic brain tumors are formed by cancer cells which began growing in another part of the body and then traveled to the brain. These tumors are by nature malig-

nant and they are the most common type of brain tumors. Majority of the cancers which metastasize to the brain are lung and breast.

2.2 Gliomas (Astrocytomas)

In this thesis we mainly focus on a specific type of brain tumor, the gliomas. Gliomas are the neoplasms of glial cells which support and nourish the brain. These tumors appear most commonly in the cerebral hemisphere but they can also be found anywhere else in the brain like the cerebellum. They can arise either alone or as a recurrence of a pre-existing tumor. The factors that cause glial tumors is mostly unknown but the only identified risk for these tumors is the ionizing radiation [DeAngelis 2001].

Gliomas have varying histopathological features and biological behavior. They cover a large range aggressiveness and grades from benign grade I, pilocytic astrocytomas, to malignant grade IV, glioblastoma multiforme (GBM). The different factors analyzed for grading these tumors include mitosis rates, microvascular proliferation, nuclear atypia and necrosis [Wilson 1999]. The lowest grade gliomas, namely the pilocytic astrocytomas, stand a little different than the other ones. These tumors do not infiltrate and they grow very slowly by means of mitosis. Although they can become large, they are not life-threatening and most of them are curable. Grade I gliomas are most commonly seen in pediatric cases. The higher grade gliomas from II to IV are called *diffuse gliomas* and they share certain characteristics. These tumors infiltrate into the surrounding tissue and invade the healthy brain. The grade II ones, diffusive astrocytomas, grow slowly however they show malignant progression despite therapy. The higher grade ones, anaplastic astrocytomas and glioblastoma multiforme, grow very rapidly and invade the brain in tentacles penetrating into the brain parenchyma. They are usually surrounded by edema and the grade IV ones create extensive network of blood vessels and contain necrotic core. Due to their rapid growth and the edema they exert pressure on the brain tissue and cause local mass effect [Wilson 1999, DeAngelis 2001].

The most important dynamic in the growth of diffuse gliomas is the invasion of the healthy brain. The infiltration into the surrounding tissue is seen in different grades of diffuse gliomas and it is a very complex molecular process [Demuth 2004]. The tumor cells infiltrate mostly through the white matter tracts but also use cerebrospinal fluid and the vascular conduits [Wilson 1999]. The myelinated fiber tracts act as a route of invasion on which the migration capabilities of cells enhance [Giese 1996]. Diffuse gliomas also show cortical infiltration demonstrating that they can invade the gray matter as well. However, the gray matter infiltration is slower than the white matter one.

The other two high grade specific characteristics seen in the growth of gliomas are the formation of the necrotic core and the vascularization [Wilson 1999]. When the tumor grows very rapidly, the cells compete for the limited nutrition and oxygen. In the case of gliomas the tumor starts growing as a spheroid getting the necessary nutrition from the periphery. Due to the rapid growth and the competition less and less nutrition becomes available for the tumor cells in the center. As a result cells in

the center undergoes necrosis and a necrotic core forms. The existence of necrotic core is used in distinguishing between grade III and grade IV gliomas. Therefore by definition it only exists in the case of glioblastoma multiforme. The other dynamic that takes place as a result of the extensive need of nutrition of the rapidly growing tumor is the vascularization. As the tumor needs more blood flow it forms its own blood vessel systems within the tumor. These systems are either formed through *angiogenesis* or remodeling of the existing vasculature. The vascular systems in the low grade gliomas are similar to the one of the brain while it is much more prominent in the case of higher grade gliomas.

The treatment course of brain gliomas includes surgery, radiation therapy and chemotherapy. The exact planning of the treatment and the type of therapy to be applied depend on the grade and the location of the tumor. The treatment strategies of grade I gliomas and the others differ due to the infiltration present in the higher grade tumors. The grade I gliomas have distinct boundaries therefore surgical removal when total resection is possible might suffice. When total resection is not possible, due to the location or the size of the tumor, then additional radiotherapy and/or chemotherapy is applied to the remaining part [ABTA 2008b]. In general the average survival rates for patients of grade I gliomas is pretty high. The treatment of grade II to grade IV gliomas on the other hand is much more difficult. The first step is again surgical removal when it is possible. However, the total resection is not possible due to the infiltrative nature of diffuse gliomas. Even when the visible tumor is totally resected, removal of microscopic infiltration into the brain parenchyma is not possible [Wilson 1999, DeAngelis 2001]. Therefore, patient follow-up with additional treatment in the form of radiotherapy and/or chemotherapy is applied. The infiltration also poses problems for the additional treatments and as a result the tumor recurs. In the case of grade II gliomas the tumor may recur as a higher grade glioma showing malignant progression. The average survival rates for patients of these tumors is 5-10 years however, the variability is large. For grade III and IV gliomas the applied treatment is much more aggressive however the progression of the disease is much faster as well. The prognosis for these cases is really low, the average survival rates remain around 3 years and 1 year for the grade III and grade IV gliomas respectively. In the view of this scenario extensive research is being conducted on different chemotherapeutic agents and radiation therapy schemes [Ricard 2007, Batchelor 2007, Fiveash 2003, Mahajan 2005, Nandi 2008].

2.3 Imaging Gliomas with Magnetic Resonance

2.3.1 Magnetic Resonance Imaging (MRI)

Magnetic Resonance (MR) is an imaging technique which uses the the nuclear magnetic resonance (NMR) signals emitted from the objects themselves. In this respect it differs from the other imaging techniques like X-ray Computed Tomography (CT) or Positron Emission Tomography (PET), where either a beam is irradiated or a radioactive agent is given to the body. The principle of MRI is based on the natural spinning of nuclei present in every object. In addition to this spinning, the nuclei of certain atoms present in the human body (such as hydrogen, carbon, oxygen,...)

creates a natural magnetic field when combined with the spin. Clinical MR focuses
on the hydrogen which is the most abundant atom in the human body. The mag-
netic moments of hydrogen nuclei in the body are randomly oriented under normal
conditions. In the presence of an external magnetic field these nuclei align them-
selves along the external field and continue their precessing around the direction of
field. This relationship forms the basis of MRI.

During MR imaging a constant base magnetic field B_0 is applied to the body
aligning the nuclei, which keep precessing at a frequency called as *precession fre-
quency*. When a Radio Frequency (RF) pulse with the same frequency as the pre-
cession is applied, the nuclei resonate, gain energy, change their alignment and go
in phase with each other. As every element has a different precession frequency a
specific RF pulse only resonates with the nuclei of specific elements. As the RF is
stopped the nuclei relax and lose their energy. This process is called relaxation and
the energy emitted in relaxation is the MR signal we detect. There are two impor-
tant properties of the applied RF pulse, the repetition time (TR) and the echo time
(TE). The repetition time is the time difference between each RF pulse and the echo
time is the time elapsed between application of an RF pulse and the peak signal
obtained. The relationship between TR and TE creates the contrast visible in the
MR images and gives the context in MR. By changing this relationship one obtains
different images such as T1-weighted and T2-weighted. Based on similar ideas an
MR image can be made to be a spatial map of density of the spins, of the relaxation
times or of the water diffusion. As a result different images such as diffusion tensor
(DT) MRI, MR spectroscopy (MRS) or functional MRI (fMRI) can be obtained.

MR is very good in soft tissue discrimination compared to other imaging tech-
niques. The two extreme cases in terms of contrast difference in MR are the fat
and the water. In T1-weighted images the fat tissue is enhanced while the water is
not, showing the fluid around the cortical areas and within the ventricles as dark
regions. On the other hand, in T2-weighted images free water and water embedded
in the tissue is strongly enhanced and appears bright, see Figures 2.1(a) and (b).
Although this high intrinsic contrast differences are very useful in discriminating
brain tissues, they may not always be enough to detect pathologies accurately. In
order to increase the contrast between pathologies and the brain tissue, enhance-
ment agents may be given to the patient and additional images might be acquired.
One important agent that is widely used for imaging brain tumors is *Gadolinium*
(Gd). Gadolinium injection is followed by a T1-weighted image acquisition and it
helps increasing the enhancement of water molecules neighboring tissue. In the MR
images this is especially visible in highly vascular regions (vessels themselves or re-
gion with abnormal angiogenesis). Tumors and other lesions are therefore strongly
enhanced due to the injection [Westbrook 1998]. Another modality which is very
useful in the case of pathologies is the *FLAIR*. The important property of the flair
is that the cerebrospinal fluid (CSF) is not enhanced as in the T2-weighted images.
Therefore, the pathologies adjacent to the CSF are seen much more clearly.

In the methods presented in this thesis, besides the anatomical MR images, we
also focus on the diffusion tensor MR images (DT-MRI). The DT-MRI is not an
acquired modality but it is rather constructed from the diffusion weighted images
(DWI). DWIs give local directional information on the diffusivity of water inside

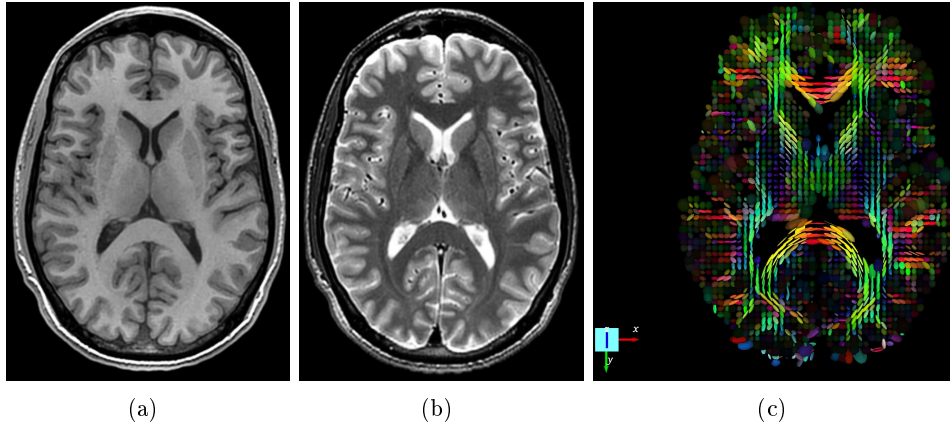(a)   (b)   (c)

Figure 2.1: (a) An axial slice of a T1-weighted image of a healthy brain. (b) The same axial slice of the T2-weighted image of the same brain. We see that in T1-weighted images the fat tissue is enhanced while the water is not. On the other hand, in T2-weighted images the appearence of fat and water are inverse. This flexibility in MR imaging gives us the opportunity to have a very different appearance of the same brain in two different modalities. (c) An axial slice of a DT-MRI image of the same brain as shown in Figures (a) and (b). Each tensor is visualized as an ellipsoid and the image is subsampled for a clearer visualization. The colors of the ellipsoids represent the direction of their major axis.

the brain tissue. Using these images we can understand how much a water molecule can migrate along each direction in a given location. Through acquiring DWIs along different directions we can construct local estimates of covariance matrices representing the local directional diffusion information of water. These covariance matrices are called *diffusion tensors* and the image consisting of these matrices in different locations is called DT-MRI. In Figure 2.1(c) we show a single slice of an example DT-MRI image where each point consists of a tensor describing the local diffusivity of the water molecule.

2.3.2   Appearance of Gliomas in MRI

The MR images are one of the most important radiological information in the diagnosis and grading of brain gliomas and tumors in general [DeAngelis 2001, Tovi 1994, Price 2007]. The appearance of gliomas in MR images differ depending on the grade of the tumor and the modality of the image. The most important property of the tumors that is visualized in the anatomical MR is the excessive content of free water. Due to this gliomas appear as hyper-intense regions in the T2-weighted images and hypo-intense in the T1-weighted, as shown in Figures 2.2 and Figures 2.3. When gadolinium is injected the highly vascularity in the tumor gets enhanced in the T1-weighted image and we get hyper-intensity regions inside the tumor for the T1-weighted images, Figure 2.3(c).

Appearance of low grade gliomas (grade I and II) are pretty homogeneous un-

(a) (b) (c) (d)

Figure 2.2: In the images above we show axial slices of (a) T1-weighted, (b) T2-weighted, (c) T1-weighted post gadolinium injection and (d) FLAIR images of a pediatric patient with a diffusive astrocytoma of grade II. We see that the tumor is enhanced in the T2-weighted and the FLAIR images.

der MR images. In Figure 2.2 we show axial slices of MR images of a diffusive astrocytoma (grade II) detected in a pediatric patient. We observe that the tumor is enhanced in the T2-weighted and the FLAIR images with clear boundaries separating the tumor from the healthy tissue. On the other hand we only observe hypo-intense regions in the T1-weighted and the T1-weighted after gadolinium injection images. The clear boundaries seen in the T2-weighted images in the case of grade-II-astrocytoma might be misleading due to the infiltrative nature of the tumor [DeAngelis 2001]. Although we see such clear separation, the tumor might have penetrated the brain parenchyma beyond the enhancement of the MR signal [Wilson 1999, Johnson 1989, Tovi 1994].
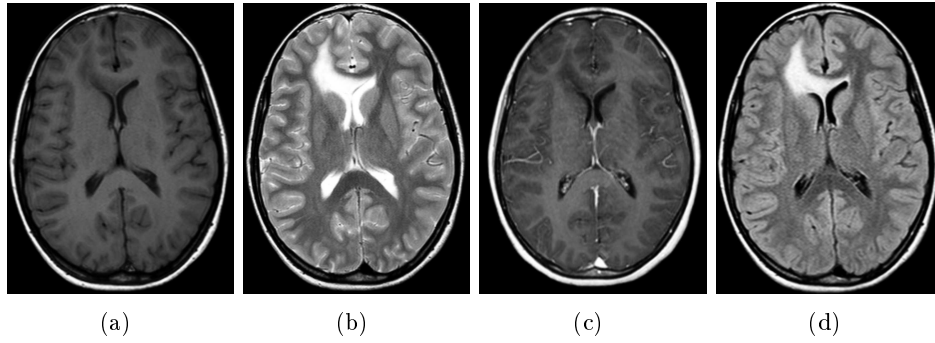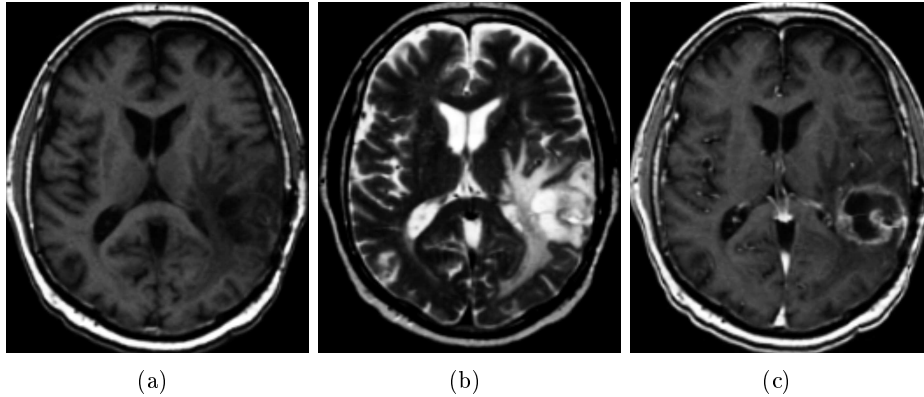

(a) (b) (c)

Figure 2.3: In the images above we show axial slices of (a) T1-weighted, (b) T2-weighted and (c) T1-weighted post gadolinium injection images of a patient suffering from a grade IV glioma, glioblastoma multiforme. The appearance of GBM is very irregular in the MR images.

In the case of high grade gliomas, especially the grade IV gliomas, the MR

appearance of the tumor is very irregular. In the T1-weighted image again we do not see any enhancement in the tumor region. In T2-weighted images on the other hand we see several compartments of the tumor which are well enhanced. Looking at Figure 2.3(b), we observe the very highly enhanced middle part of the pathology which includes the highly active part of the tumor and the necrotic core. However, the necrotic core cannot be distinguished. Around this part we observe another highly enhanced part, which corresponds to the edema. The edema region is also infiltrated with tumor cells however, the number of tumor cells per volume is much lower than the active part [Johnson 1989, Tovi 1994]. In the T1-weighted image after gadolinium injection we clearly see the most active part of the tumor and the necrotic core. The dark area inside the pathology is the necrotic core where there are no live cells. The bright rim around this area is the actively proliferating region of the tumor where the vascularization is very dense and the tumor cell density is high. In the case of grade III gliomas these images look different as there is no necrotic core and the there might not be any edema region.

One of the most crucial points of MR appearance of gliomas is the infiltration of the tumor which beyond a certain core region is not enhanced in the images. Different experiments comparing histopathological analysis with MR images have shown that tumor cells exists beyond the enhanced region in the T1-weighted image and the T2-weighted image [Tovi 1994, Johnson 1989]. In the images the difference between the tumorous region and the brain tissue seems abrupt. However, the hypothetical distribution of tumor cell density is smoother. In Figure 2.4 we show the hypothetical cross section of a GBM where the tumor cell density is represented by the height of the blue curve. The T1 and T2 image intensities are shown in the figure as different thresholds on the tumor cell density [Swanson 2008b]. We see that hypothetically the transition between the enhanced region in the post gadolinium T1-weighted image and the enhanced region in the T2-weighted image is smooth. Moreover, the tumor cell density continue to drop after the T2 threshold suggesting infiltration beyond the enhanced region in the image. This detection problem poses difficulties for the treatment of the tumor especially in the case of radiotherapy where images guide the irradiation. In order to deal with this problem in radiotherapy a normal looking band around the tumor is also irradiated [Kantor 2001]. However, these efforts seem to be not enough because diffuse gliomas tend to recur due to the infiltration [Wilson 1999, DeAngelis 2001].

Recent research on other MR modalities such as DT-MRI and MRS have shown that these images can also be used to gather information about the tumor characteristics and its spatial distribution. As the tumor invades the brain through white matter it damages the underlying fiber structures. DT-MRI images have shown to be useful in detecting this damage by using different measures [Lu 2003, Lu 2004, Roberts 2005, Sinha 2002, Price 2003].. The first change that occurs is that the mean diffusivity (MD) increases in the regions invaded by the tumor or by edema, see Figure 2.5(b). Moreover, as the fiber structures are damaged the directional organization of the fibers is lost and this can be quantified by the fractional anisotropy (FA) 2.5(c). MR spectroscopy on the other hand, gives information about the metabolic activity inside and around the tumor. Activities regarding certain molecules are specific to brain tumors therefore, use of MRS can
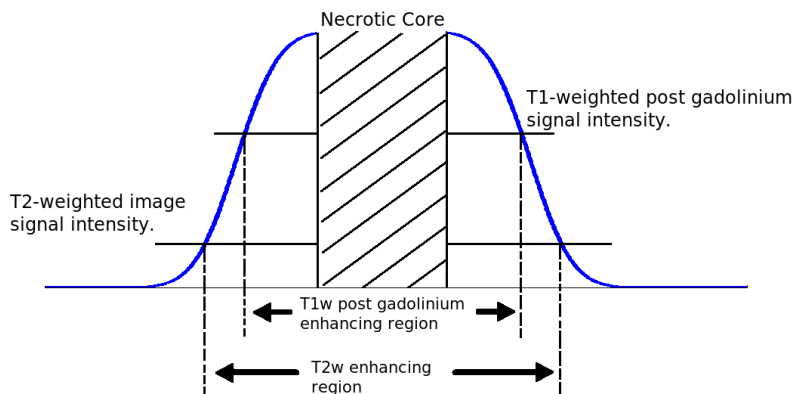
Figure 2.4: The MR images of grade II to grade IV gliomas are not able to show the whole infiltration of the tumor inside the brain parenchyma. In the plot we show hypothetical distribution of the tumor cell density and the relation of it to the enhanced region in the MR images. We see that tumor cell density drops smoothly suggesting infiltration beyond the enhanced region in the T2-weighted image.

(a)   (b)   (c)
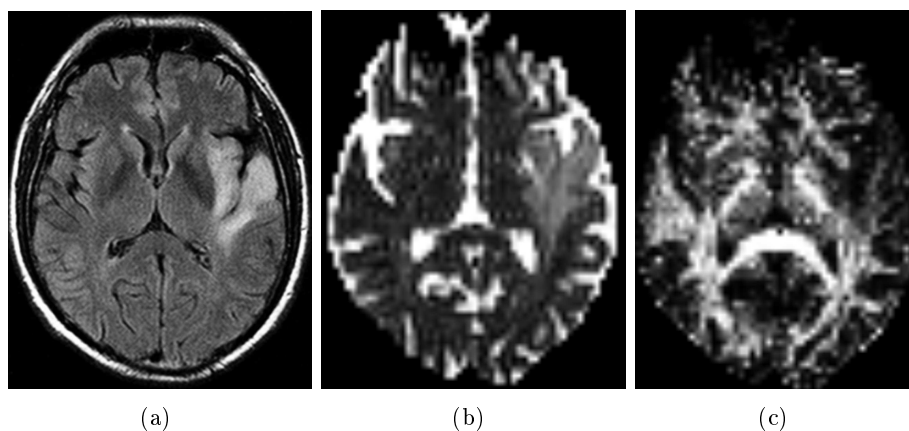
Figure 2.5: The DT-MRI images can show different effects of the tumor to the fiber structures providing us another mean to visualize the pathology. (a) FLAIR image of a grade II astrocytoma, (b) Mean Diffusivity (MD) image of the same patient derived from the DT-MRI, (c) Fractional anisotropy (FA) image of the same patient again derived from the DT-MRI. We observe that in the tumor region the MD image shows extra enhancement while the FA image shows degradation in the same region.

help us gather some information about the tumor and its extent [Devos 2005]. The problems with these two modalities, DT-MRI and MRS, is the resolution of the images which are inferior to the anatomical images. Accurate local information is

not very possible to obtain however, as the MR technology improve these problems
will be solved as well.

There are also other imaging techniques which provide different information
about gliomas than MRI. Positive emission tomography for instance gives local
metabolical information about the tumor. In PET a radioactive agent is injected
and the uptake of this material is correlated with the existence of tumor cells.
Different studies have analyzed and shown discrepancies and similarities between
the appearance of gliomas in PET and MRI [Ogawa 1993, Kracht 2004, Kato 2008,
Miwa 2004]. They have demonstrated that the appearance in both imaging tech-
niques might be different. Therefore, using these images together might be the
optimum choice.

Tumor Growth Models: Literature Review

Contents

Context

In this chapter we present an overview of mathematical tumor growth modeling. We explain the main approaches by going through different models proposed. We talk about microscopic models, different stages of tumor growth and their modeling, macroscopic models and some image analysis tools using these models.

3.1 Introduction

The domain of mathematical tumor growth modeling in the research community is vast. There is extensive existing research both on brain tumors and on tumors in other parts of the body. In order to situate the methods presented in this work a good understanding of the literature is necessary. In this chapter we provide an overview of the literature published on tumor growth models. A complete review of all the works on this topic would be too long therefore, we provide the main steps and the research orientations. For further reviews on the topic refer to [Araujo 2004, Mantzaris 2004, Sanga 2007].

The main aim of tumor growth modeling is to develop mathematical models explaining interactions of tumor cells with each other and with the surrounding tissue,

which lead to the growth of the tumor, via mathematical abstractions. In order to explain the underlying mechanisms as accurately as possible, such abstractions take into account many different biological factors, which were observed through experimentation. Such factors include internal dynamics of cancerous cells, their interactions with each other and with healthy tissue, nutrition and oxygen transport from the extracellular matrix (ECM) and from the vascular network, chemicals secreted by tumor cells, type of the underlying tissue, and many more. Models aim to combine all these factors in a unified mathematical framework, which would agree with the observed results. While most of the work in the literature has been concentrated in modeling the growth process in a general framework, there has been some recent attempts to develop patient specific models. These developments are directed more on describing the growth of the tumor using the observations obtained from the patient.

Benefits of describing the tumor growth mathematically are numerous. First of all, such descriptions would help us to combine experimental findings made in many diverse fields of cancer research in a common mathematical ground. These models allow us to interpret experimental results and understand the underlying mechanisms of tumor growth and behavior of cancerous cells. Virtual experiments and simulations give us the opportunity to observe effects of different treatments on cancerous cells, and would lead us to improve these treatments or suggest new ones. On the other hand, patient-specific models could be used in treating patients. Such models could be used for therapy planning, suggesting radiotherapy margins adapted to the growth dynamics or helping the oncologist make a choice between different types of drugs that would best suit the patient. Virtual realizations of the tumor and the brain structures could help neurosurgeons during operations, providing precise locations of vital structures. Another benefit of tumor growth models is that they could allow us to make predictions. The shape and invasion margins of an existing tumor in a future time could be predicted using such models and computer simulations. The predictions would give the medical doctor the opportunity to foresee the problems the patient might undergo and also would help him decide on the best time of operation if necessary. Including the genetic information in such models, one could even produce the probability of occurrence of a brain tumor in the future.

As we said the mathematical work on tumor growth modeling is trying to develop mathematical abstractions that would best explain the observed phenomenon; hence, it is very closely associated with the experimental and clinical work being done in cancer research. Most growth models use observations coming from different sources like *in-vitro* experiments, *in-vivo* experiments done on animal subjects, biopsy results, autopsy results and medical images of patients like Computed Tomography (CT) scans or Magnetic Resonance Images (MRIs). These experiments and images are keys to developing models describing the tumor growth process accurately. Observations used can be classified in two groups based on the scale: macroscopic and microscopic scales. Experiments concentrated on the cellular activities can be placed under the microscopic class, like *in-vitro* and *in-vivo* experiment, while larger scale views like medical images can be placed under macroscopic class. Although the macroscopic and microscopic classification can be done in other man-

ners, in this thesis we make distinction based on the use of medical images.

There has been great advances in tumor growth modeling, there are several problems on the way of developing more accurate models. The most crucial problem is the lack of knowledge on the behavior of tumor cells in the living tissue. Observations coming from *in-vitro* and *in-vivo* experiments gives us insight on the behavior of tumor cells on laboratory set-ups like petri dish or on animal subjects. However, *in-vivo* observations on human beings, which is the case the tumor models aim to describe, are scarce. The best one can do is to propose assumptions on the behavior of tumor cells in the human brain, using observations available at hand. Another problem related to observations is limitations in macroscopic imaging techniques, [Tovi 1994]. Medical imaging techniques are able to enhance and detect regions containing tumor cells, only if the number of tumor cells are above some threshold. There are several estimates given in the literature on the lowest detection threshold of CT images (1-40 % of the maximum number of tumor cells brain parenchyma can handle), [Tracqui 1995, Swanson 2008b]. Although there is no work being done on the detection threshold of MRIs for tumor cells, the extent of the tumor (invasion margin) in these images are very similar to the one in CT images thus, it is a common practice to accept the same threshold.

In the rest of this chapter we will give general information about tumor growth models, summarize some of the milestones in tumor growth modeling and also review recently proposed tumor growth models trying to give an overview on the state of the art. In Section 3.2 we will introduce a classification of tumor growth models which we will use throughout this chapter to analyze different models proposed. Based on this classification we review the corresponding literature of microscopic models in Section 3.3 and macroscopic models in Section 3.4. In Sections 3.5 and 3.6 we focus on the applications on medical images and explain some of the models proposed for therapy planning and other works which use models for segmentation and registration.

3.2   Classification

Research being done on tumor growth modeling can be coarsely classified into two large groups. This classification is based on the scale of the model and there are two classes: microscopic models and macroscopic models. The main difference between these classes is the scale of observations they are trying to explain and formulate. Microscopic models concentrate on observations in the microscopic scale, like *in-vitro* and *in-vivo* experiments. They try to explain the growth phenomena at the microscopic level by describing the interactions between different cells, different chemicals secreted by cells, nutrition sources, oxygen and nearby vessels. Macroscopic models on the other hand, are concentrated on observations at the macroscopic scale like the ones provided by medical images. They formulate the average behavior of tumor cells and their interactions with underlying tissue structures, which are visible at this scale of observation (gray matter, white matter, bones, ...). These models try to describe the behavior of the tumor as a whole, consisting of clusters of cells.

Further classification within these groups can be made based on the stage of the

tumor growth being analyzed or the effect of the growth on the brain. Classification based on the stage criteria is more suitable for the microscopic models and will be used for those models only. On the other hand the effect criteria will be used for the macroscopic models.

The classification based on stages of the tumor growth consists of three classes, which are basically three different phases of the growth: the **avascular growth**, the **angiogenesis** and the **vascular** growth. At this point, we would like to give very simplified explanations for these stages for completeness. The avascular growth corresponds to the stage where the process is mostly governed by the proliferation of tumor cells. In this stage the tumor is considered to be a solid mass, which is growing by means of mitosis. Although not completely known, it is thought that there is no invasion of the healthy tissue. The interactions between tumor cells and the healthy tissue is also thought to be limited, [Araujo 2004]. The tumor cannot grow indefinitely in the avascular stage because as the tumor mass grows, less and less nutrition is available for the cells deep inside the avascular mass. As a result necrosis begins, tumor cells that are not getting enough nutrition die, and only cells on the outer perimeter of the tumor continue to proliferate. At one point necrosis and the proliferation balances each other and the avascular tumor reaches a limiting size, which is assumed to be around 1-3 mm in diameter, [Orme 1996b]. Angiogenesis (vascularization) is the stage where tumor cells in the avascular mass modify the existing vascular structure, to create new vessels that would feed them. Through this process the tumor can overcome its limit size, grow much faster and invade the surrounding tissue. Due to the crucial role of angiogenesis on the tumor growth, its underlying mechanism has captured attention and many models have been proposed trying to explain it. The third stage of the tumor growth, vascular growth, has been paid less attention than two previous stages. The complexity of the tumor growth in this stage is higher because there are several processes going on simultaneously. In addition to cellular and chemical interactions going on in the first two stages, tumor cells start to invade the surrounding tissue via mechanisms not clearly known yet. At this stage, the tumor becomes diffusive and is not considered to be solid anymore. While the difference between cancerous and healthy regions are clear in the avascular stage, this difference vanishes during the vascular growth because tumor cells move towards healthy regions.

Classification based on the effect of tumor growth on the brain is more appropriate for macroscopic models. We can distinguish two major groups: mechanical models, which concentrate on the mass-effect of the tumor and diffusive models, which concentrate on the infiltration of the brain tissue. In following sections we will go over some of important and recent models that have been proposed. While mentioning different models we will try to make use of classification types explained above, which is summarized in figure 3.2.

3.3   Microscopic Models

Tumor growth models, which can be named as microscopic, aim to describe the tumor growth process at the cellular level using experimental observations at this
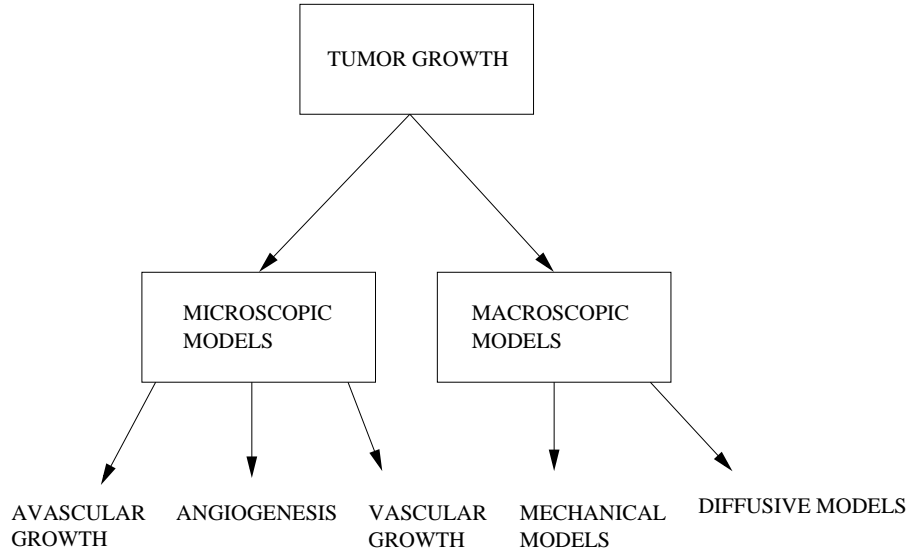
Figure 3.1: Classification of tumor growth models

level. They take into account physical and chemical interactions between cells and the ECM, and build a cause-result relationship between the tumor growth and these interactions using mathematical formulation. Mechanical phenomenon like cohesion forces, adhesion forces and pressures are often included to describe physical interactions between cancerous and healthy cells. As for chemical interactions, they include processes like diffusion of nutrition and oxygen, secretion of different factors by tumor cells and their effects on the ECM, blood vessels and other cells. Mathematical systems obtained are usually very detailed as they try to take into account all the factors observed to affect the tumor growth. Formulations used in creating microscopic models enjoy a large variety of mathematical methods. Most commonly used methods are partial differential equation (PDE) systems, cellular automata and statistical models.

3.3.1 Avascular Growth/Solid Tumor

Most of the modeling work at the microscopic scale has been concentrated on the avascular stage of the growth. In the beginning it was thought that the whole process of tumor growth was only governed by the proliferation of cells. Models using only population growth dynamics like exponential growth or Gompertzian growth were proposed. In table 3.1 we give some of the population growth equations commonly used. u in these equations is the normalized density of tumor cells (normalized by the maximum tumor cell density the underlying tissue can handle), $\partial u/\partial t$ denotes the change of u in time and ρ is the proliferation rate of tumor cells which is taken to be $\rho = 1$ in the figures. One of the first papers employing this idea was published by Mayneord in 1932, [Mayneord 1932]. This work explained the effect of different distributions of actively dividing cells on the growth, based on histological experiments telling that viable cells are only found on the outer periphery of the

Table 3.1: Commonly used population growth terms

Exponential (green)	Gompertz (red)	Logistic (blue)
$\partial u/\partial t = \rho u$	$\partial u/\partial t = \rho u \ln(1/u)$	$\partial u/\partial t = \rho u(1-u)$
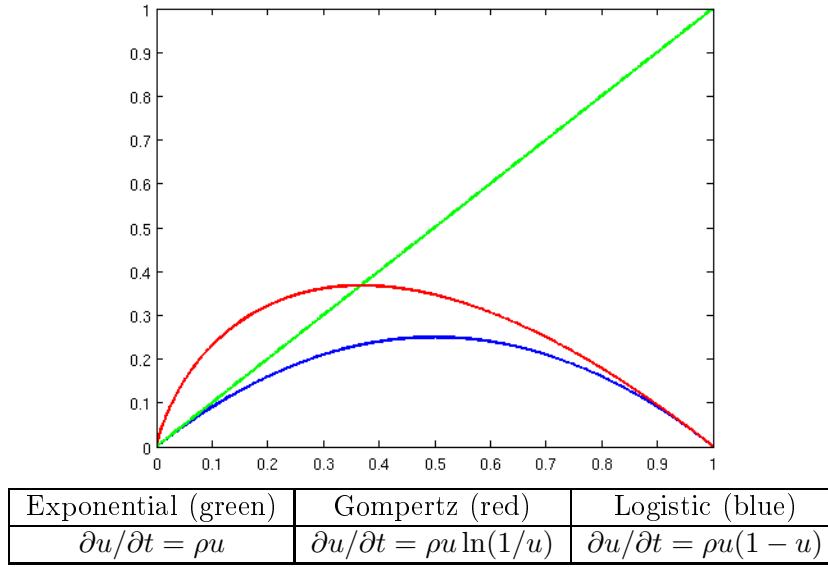
solid tumor.

In light of further experiments, diffusion and consumption of oxygen was included in the model as a factor in the mitosis rate and necrosis. Models proposed by Thomlinson *et al.* and Burton [Thomlinson 1955, Burton 1966] examined this effect and showed that when the blood supply (as a supply of oxygen) was limited to the perimeter of the tumor, formation of the necrotic part could be explained as a result of lack of oxygen. These developments showed that the Gompertzian model better fits the tumor growth. Although these models were able to match the growth rate of the tumor, they were not able to explain its compactness. Greenspan in [Greenspan 1972], included surface tension among living cells on the periphery, in order to obtain a compact tumor. In this paper, he assumed that necrotic cells were dissolving and due to the surface tension, cells on the periphery were pushed towards the necrotic region. He also tried to explain the inhomogeneity in the mitosis rate throughout the tumor via the secretion of growth inhibiting factors (GIF) by tumor cells in a spatially uniform manner. The tumor radius evolution followed an integro-differential equation, which was coupled to reaction-diffusion equations explaining the distribution of nutrition and GIFs. Although including the oxygen consumption in the model was a big step, it was unable to explain the slow thinning of the viable rim following the formation of a necrotic core. Deakin in [Deakin 1975] included inhomogeneous consumption of oxygen in the tumor explaining this phenomenon. Besides the cell loss in the tumor due to necrosis, McElwain *et al.* [McElwain 1978] included another cell loss mechanism, apoptosis, following the experiments showing that tumor cells may die even though they do not lack nutrition nor oxygen. The constant cell loss rate coming from apoptosis, was also causing the tumor to stay at a limit size.

Besides the deterministic models of growth that has been proposed there has also been some stochastic ones emphasizing the probabilistic nature of the growth. One of the first works in this context is of Wette *et al.* in [Wette 1974a, Wette 1974b]. The main argument of such models is that fluctuations around the average behavior may be more important than the average behavior itself, when the population assumes small values. These models simply add the possibility that average values like mitosis rate or diffusion of factors may deviate a lot.

Later on, the effect of GIFs on the growth process was analyzed by Adam *et al.* in [Maggelakis 1990]. They showed that GIFs indeed play a crucial role on the dormancy of the tumor in the avascular stage. In their model they included inhomogeneity of nutrition consumption and GIF production using spatially dependent functions, assuming GIFs were produced more in the necrotic core and decrease linearly towards the perimeter. Even though they did not include the volume loss in the necrotic core, they were able to obtain limiting sizes, showing GIFs alone can also cause dormancy in solid tumors. By including both inhomogeneous formation of GIFs and consumption of oxygen they combined all previous ideas in one formulation.

Following experiments suggesting that cells in solid tumors tend to grow towards blood vessels, McElwain *et al.*, [McElwain 1993] introduced an active migration towards nutrition gradient in their model. Describing the motion of cells with two parts: passive motion towards the necrotic core caused by pressures and the chemotaxis towards nutrition sources. However, experiments showed that not all cells followed the active migration. Pettet *et al.* [Pettet 2001] proposed to use the cell cycle to explain this. In this model, cells that were going through mitosis were not chemotactically active. Only quiescent cells were affected by the chemotaxis towards the nutrition gradient.

As models describing the motion of a single element, tumor cells, are getting more and more elaborate, some attention has started to be given to multiphase models to be applied to tumor growth. Please *et al.* in [Please 1999] used the theory of multiphase to model the tumor growth using two phases: tumor cells and extracellular matrix. They modeled physical interactions between these two phases and analyzed the effect of mechanical stresses in the tissue on the formation of the necrotic region. Both phases in this model were assumed to be inviscid. Later on, Landman *et al.* added the interphase drag forces in this formulation and using the model, showed the effect of surface tension on the formation of the necrotic core and also on the stable limiting size of the tumor, [Landman 2001]. Breward *et al.* in [Breward 2002], also used two phases, however, they took into account the interactions between tumor cells by modeling cellular cohesion between them. Hence, the pressure in the tumor differentiated from the pressure of the extracellular matrix, due to these interactions. Byrne *et al.* in [Byrne 2003] took a different approach to two phase models. They used theory of mixtures to model the tumor as an organic balloon creating a solid-cellular phase and the surrounding media as a liquid containing nutrition and different growth factors. The dynamics of the growth were described by mass and momentum balances in addition to the constitutive laws. The mechanical interaction combined with the mass exchange between two phases enabled them to compute local stress induced within in the tumor. In their work,

they study the effect of this stress on the rate of proliferation and the equilibrium configuration of the avascular tumor. Consistent with *in-vitro* experiments they show that external loads and stress exerted on tumor cells affect the size of the avascular tumor. As a result they demonstrated that avascular tumors can reach their limiting size either through nutritious equilibrium or stress equilibrium.

Most of the previously mentioned models use exponential, Gompertz or logistic growth for the proliferation of tumor cells. There has also been some recent work on type of growth equation that would best fit tumor mitosis. Tabatai *et al.* proposed to use a different set of growth models called hyperbolastic models, [Tabatai 2005]. They say that the increase in the number of tumor cells can be better explained using such a model with more flexibility.

Tumor-Induced Angiogenesis

Tumor-induced angiogenesis is a very complex process including lots of chemical and mechanical phenomena, which has not been totally understood. Mantzaris *et al.* in [Mantzaris 2004] reviewed some of the known biological processes taking place in angiogenesis. The basic observable consequence is that tumor cells affect nearby blood vessels to sprout new vessels towards themselves creating new vascular structure as a source of nutrients and oxygen, see figure 3.2. As a result of angiogenesis the tumor receives extra nutrition and the growth speeds up. Mathematical formulations modeling angiogenesis, usually takes into account motion of endothelial cells (ECs), tumor angiogenesis factor (TAF), fibronectin structures of extracellular matrix (ECM), vascular endothelial growth factor (VEGF) and angiogenesis inhibitor factors.

There have been some attempts to model the initial phase of angiogenesis. The process starts by production of VEGF by tumor cells and their binding to nearby vessels. This factor initiates the detaching of ECs from the vessel, moving of ECs towards the tissue by means of haptotaxis (cells move up a gradient of adhesion) and beginning the formation of buds. Orme *et al.* [Orme 1996a] tried to model this process in 1D, using reaction-diffusion equations for the motion of ECs, based on haptotaxis. The bud formation was formulated as a combination of reaction, diffusion and taxis, surprisingly having no relation to the density of VEGF. In [Levine 2000] using this model as a basis, Levin *et al.* formulated a very complex system containing 31 parameters to model the angiogenesis initialization. They formulated complex interactions between TAFs, ECs, protease and fibronectin. Although the model was created to be very realistic, some included interactions are not observed yet.

Later stages of the angiogenesis have received more attention from the mathematical community. One of the first models, which included factors like TAF, was proposed by Byrne *et al.* in [Byrne 1996]. The 1D model included two different populations of ECs: cells at the tip and cells forming the sprout. The reason for this is that, EC proliferation and the branching of the vessel only occurs at the tip. The model included the effect of TAF in EC proliferation and branching of the tip. Chaplain *et al.* extended this model in 2D, including EC density, concentration of TAF and fibronectin in their model in [Chaplain 1998]. Motion of ECs were modeled as haptotaxis using fibronectin structures of ECM. The common feature of most of
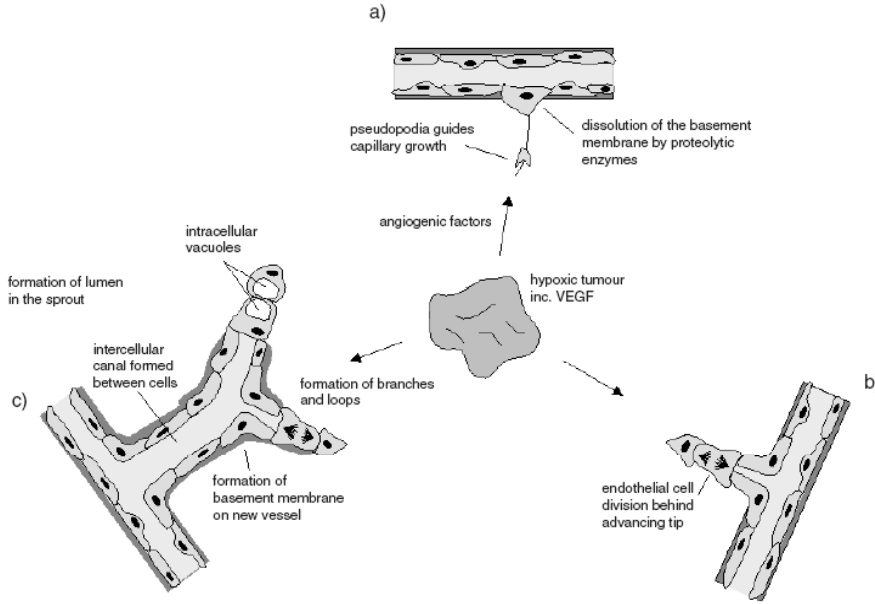
Figure 3.2: Sketch of the angiogenesis process showing different stages of the process starting from (a) to (c), image taken from [Mantzaris 2004].

the later models is that TAF concentration was assumed to be at steady state, since this factor diffuses much faster than ECs. This model showed the importance of haptotaxis for a successful angiogenesis.

Anderson *et al.* tried to model the angiogenesis process in the absence of EC proliferation, [Anderson 2000]. The aim was to show that angiogenesis would be incomplete without the proliferation. In their 1D model they included diffusion of TAF and ECs, with the effect of haptotaxis with fibronectin and chemotaxis towards TAF gradient. Chaplain *et al.* in [Chaplain 2000] extended this model in 2D, showing that ECs do not reach the tumor in the absence of proliferation. Effect of angiogenesis inhibitor factors was included in another model of Anderson *et al.* in [Anderson 2000]. They have formulated the secretion of angiogenesis inhibitor factors from an existing tumor to prevent the vascularization of a second tumor. In the model, they showed that under the effect of inhibitor factors, vascularization was ceased for the second tumor.

While most of the models proposed for angiogenesis used only reaction-diffusion systems, taking into account the chemical interactions, some models formulated the physical interactions between EC and ECM. The chemical interactions between EC and ECM were described by haptotaxis through fibronectin. On the other hand, EC cells exert traction forces on the ECM fibers creating displacement of the matter. Holmes *et al.* included this mechanical interaction besides the chemical interactions of previous works in their model in [Holmes 2000]. They observed that below a critical traction value, the structure of vascular network was homogeneous, while above this value the structure was highly heterogeneous. This is a critical step,

since, heterogeneity of vascular structures, would affect the growth process greatly.

Besides the models explained above, some discrete models were also proposed to predict the vascular structure itself. One of the most important work in this was proposed by Stokes and Lauffenburger in [Stokes 1991]. In their model they treat each sprout individually and track the motion of growing tips in 2D. Their formulation included position and velocity for every tip, where evolution of the velocity of a tip was given by a stochastic differential equation adding a white noise to take into account the randomness. The position and the velocity of the a tip was affected by the TAF concentration through the phenomena of chemotaxis. They have taken the TAF concentration at steady state in their model, which was later relaxed by Tong and Yuan in [Tong 2000].

Anderson and Chaplain also proposed a model to predict the vascular structure, [Anderson 1998]. Their model start by calculating values of EC density, TAF and fibronectin concentration using the formulation they proposed in [Chaplain 1998]. Using these values, they assign probabilities to cells moving to different grid points. Based on these probabilities they have visualized the vascular structures in 2D. Since probabilities included the information coming from diffusion, chemotaxis and haptotaxis, so did vascular structures.

Recently, Habbal formulated a Nash game for the angiogenesis process, [Habbal 2005]. The vascularization is been modeled as a competition between the tumor, which tries to provide itself an optimal drainage, and the host tissue, which wants to keep its structural integrity, not letting any blood vessels to form. The agents of the game are TAFs secreted by the tumor and antiangiogenic factors. Using finite elements Habbal solved for the Nash equilibria and visualized the formation of the vascularate structure in 2D. This model is unique in the sense that the ECM is modeled explicitly as a resistance to tumor-induced angiogenesis.

Vascular Growth/Invasive Tumor

Most of the recent work on microscopic tumor growth modeling concentrates on the vascular growth. Moreover, they combine all three phases of the growth. We include such unified works in this part. The difference between vascular and avascular growth is the existence of blood vessels within the tumor. These vessels might have been formed by angiogenesis or the tumor might have initialized around a vessel, as in the case of tumor cords. Since the nutrition source of tumor cells is not just limited to diffusion from the perimeter, as opposed to avascular tumors, formation of necrotic regions is much more complex, if they exist at all. Moreover, due to the same reason, vascular tumors are not compact masses of cancerous cells, they don't have a limiting size and can grow indefinitely. They are invasive and tend to diffuse towards the surrounding tissue. The tumor region and the healthy tissue region are not separated with a boundary as in the case of avascular tumors, due to this invasive nature.

Works on modeling the tumor invasion began by trying to explain the dynamics of the metastatic process, which causes the tumor to spread to other tissues by means of traveling through the vascular system. Saidel *et al.* [Saidel 1976] began by considering the metastasis from a solid tumor, creating a model taking into

account different populations like tumor cells inside the vessel, around the vessel and in the metastatic foci. In their work they focused on describing the interactions between vessel surfaces and tumor cells. Although metastases is not a critical issue for brain tumors, modeling work on this process initialized other works trying to model diffusion of tumor cells. One of the first models describing the diffusion was proposed by Liotta *et al.* in [Liotta 1974]. Using coupled diffusion-reaction equations, they tried to explain the change in tumor cells density and the change in vessel surface area (in the form of density) inside the tumor, which was not a very accurate model for migration of vessels in the tumor. In this model, tumor cell diffusion and proliferation were dependent on the vessel surface area. Necrotic core formation was also analyzed in this work, as a result of low levels of nutrition cause by not enough vascularization.

In [Orme 1996b], Orme *et al.* continued to use diffusion systems to model vascular tumor growth, where they included an active diffusion of tumor cells towards blood vessels (up gradient of vessels) and also explained the formation of necrotic core by too much proliferation of tumor cells resulting in collapse of vessels. Using a similar idea Byrne *et al.* proposed a non-necrotic tumor growth model, also based on diffusion-reaction systems, [Byrne 1995]. Besides including diffusion of nutrients from vessels towards tumor cells, they have also included diffusion and secretion of growth inhibitor factors and analyzed effects of them. Unlike most other works, they have also considered apoptosis as a tumor cell death, and included it in their model. One alternative to the diffusion-reaction formalism was proposed in [Perumpanani 1999] by Perumpanani *et al.*. They modeled the tumor invasion and growth, based on the idea that the invasion is governed by proteolysis and haptotaxis. In their formalism the random motion of cells did not exist, cells moved towards extracellular gradient. This was different than all the previous models in two ways. The first difference was that the cell motion was based on haptotaxis instead of being dominated by diffusion towards blood vessels. The other difference was in the type of resulting mathematical system; the directed cell motion resulted in a reaction-advection system rather than a reaction-diffusion system.

Besides different factors that have been proposed to affect tumor growth like nutrition and oxygen concentration, growth inhibiting factors, physical forces and cell cycle, acidity of the extracellular matrix was also used in some models to affect the tumor invasion. One of the first models that examined the acid-mediated invasion was proposed by Gatenby *et al.* in [Gatenby 1996]. They formulated the observation that tumor cells produce H^+ ions during their metabolismic reactions and by releasing them to the extracellular matrix, they increase the acidity of the environment. This in turn help their invasion in three ways: killing healthy cells, stimulating the production of acidic enzymes for proteolysis and reducing the cohesion between tumor cells, setting them free to move. They modeled these effects by creating a reaction-diffusion system describing densities of each chemical component like H^+ ions and glucose. Patel *et al.* [Patel 2001] used a similar formulation for the acidity in simulating early tumor growth and examining the effect of existing vascular network and tumor cell metabolism in the growth process. They created a hybrid cellular automaton (CA) model, where motion, secretion and consumption of glucose and H^+ ions were modeled by reaction-diffusion systems and the dynamics

of cells were set by CA rules. Using this model they were able to simulate tumors starting from several cells and growing up to huge sizes, giving the opportunity to examine the early growth, see Figure 3.3.
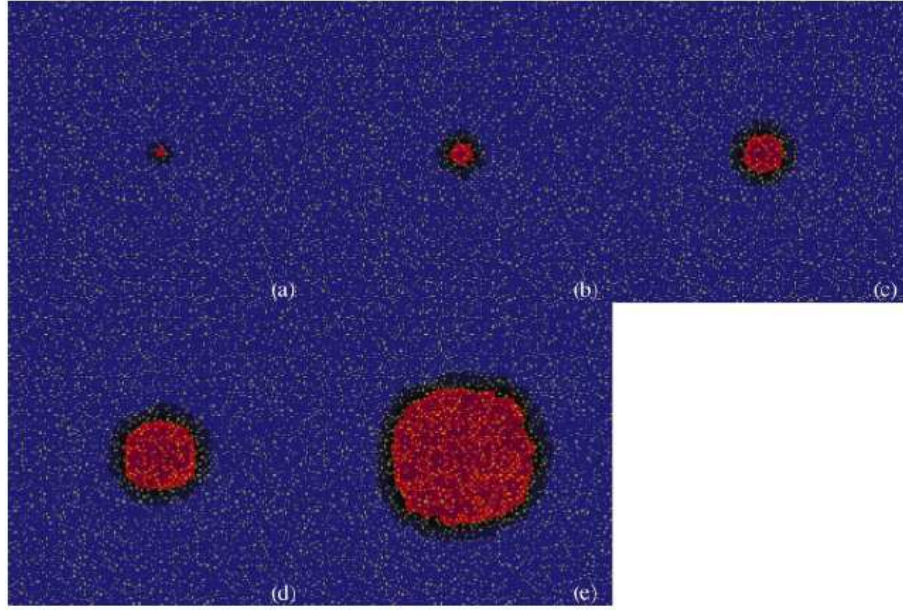
Figure 3.3: Example of an early growth process where vascularity of the tumor is coming from existing vessels. Tumor's size increase several scales of magnitude, image taken from [Patel 2001].

In [Athale 2005], Athale *et al.* proposed a 2D discrete model which focused on the experimental observations of Giese *et al.* stating that glioma cells either migrate or proliferate but they do not show both phenotypes at the same time [Giese 1996]. They have included this in their model as a decision process for each cell. They modeled the gene-protein interactions using different ligands and epidermal growth factor receptors (EGFR). They showed that using a EGFR related decision network one can simulate the *dichotomy* between migrating and proliferating cells observed in reality. In their following article [Athale 2006] they examined the effect of the EGFR density on the growth patterns of the tumor. Zhang *et al.* have built on this model and carried the computation in 3D [Zhang 2007].

Bertuzzi *et al.* examined the dynamics of cancerous cells in tumor cords, where cells simply grow surrounding a vessel, forming a vascular tumor, [Bertuzzi 2003]. In their model, they took into account that viable cells in a tumor can consist of quiescent and proliferating populations. To get a more realistic model, they also considered the cell-cycle of a proliferating cell and integrated it in the model. While the vessel acting as the nutrition source, death of tumor cells were modeled either due to insufficient nutrient supply or apoptosis. This model was one of the first ones, integrating cell cycles in the growth process. Later on, Alarcón *et al.* created a model using cellular automata, to examine the effect of oxygen and nutrition

inhomogeneity on the growth process induced by the blood flow through vascular network, [Alarcón 2004]. Besides modeling the blood flow, vascular adaptation and diffusion of oxygen and nutrition towards cells, they have also taken into account effect of cell cycles in the invasion and proliferation processes. Effects of extracellular oxygen levels on cell cycles were modeled explicitly for the first time, using the information that tumor cells can adapt their cycle better than healthy cells in case of low oxygen. Recently Byrne *et al.* have used this model to analyze the effect of chemotherapy on vascular growth of tumors [Byrne 2006].

In [Cristini 2003], Cristini *et al.* reformulated the model in [Greenspan 1972] to model non-necrotic tumors. While the model of Greenspan only span avascular tumors, the model presented by Cristini *et al.* is able to simulate vascular and avascular growth, through adding capillary density within the tumor in their model. They have used reaction-diffusion system to formulate dynamics of nutrients and GIFs, where blood is the main source of all chemicals. One of the most important contributions of the paper is the observation that the invasive growth can occur without any *fingerings* of the tumor. They have concluded that in order to obtain fingerings in the growth process, some kind of anisotropy coming from the tissue should be included. Later on, Zheng *et al.* in [Zheng 2005], extended this by adding

(a)   (b)
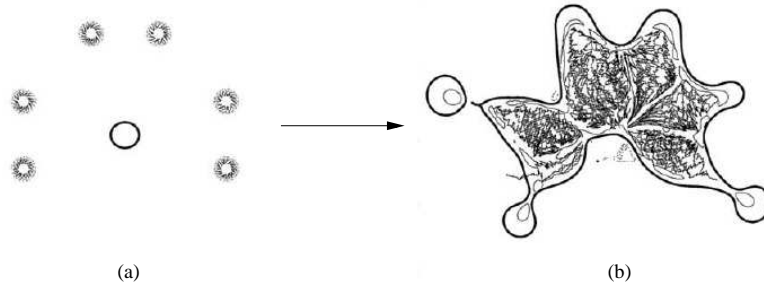
Figure 3.4: Zheng *et al.* were able to simulate the growth starting from an initial avascular tumor with a surrounding vascular structure, (a), going to an invasive and vascular tumor, (b). Black boundary shows the extent of the tumor and thin line bundles represent blood vessels, which are away from the tumor in (a) and inside the tumor after angiogenesis (b). (Image taken from [Zheng 2005])

a formulation to model the transition through avascular to vascular tumor, angiogenesis. Moreover, they also added the onset of necrosis to the previous model. Reaction-diffusion formalism was used to formulate growth processes while a combined discrete-continuum model was used to describe angiogenesis. Distinct parts of the model used to explain different stages of the growth are not as sophisticated as some of the models explained above. However, the significance of this work lies in the completeness of the model proposed, which combines all three stages of the tumor growth. This way, one can observe how ongoing vascularization would affect the tumor invasion and also simulate the growth starting from a multi-cell spheroid going to an invasive tumor, see figure 3.4.

In the aim of combining all stages of the tumor growth Frieboes *et al.* continued on the model proposed by Cristini *et al.* [Frieboes 2007]. In this work the authors explain the tumor morphology and the invasion pattern in the tissue scale by linking the dynamics to phenotype of cells, molecular factors and phenomena in the micro-environment. In this sense their model is one of the first multi-scale models. The link consists of complex nonlinear relationships and functionals which are said to be based on experimental results. In their invasion dynamics they have included chemotaxis, haptotaxis and the mechanical pressure due to proliferation. They also coupled their growth model with a model of angiogenesis given in [Plank 2004]. In order to set the values of some parameters, such as the proliferation rate and the apoptosis rate, they used *in-vitro* cell lines and *ex-vivo* patient data. For the other parameters, like the rate of diffusion of vital parameters, they solve the model numerically and determine the values that result in growth and invasion.

Following a similar path Lloyd et al. in [Lloyd 2007] also proposed a growth model which aims at combining all three stages of the tumor growth. Especially they concentrate on coupling the angiogenesis process with the vascular growth. Besides taking into account the different factors affecting the tumor growth such as oxygen diffusion and different enzymes secreted, they also model the vasculature explicitly. This explicit scheme includes a 3D finite element model where the angiogenesis process is modeled in detail. Biomechanical effects of the tumor growth on the vasculature is taken into account explicitly. Later on, in [Lloyd 2008] they enlarge their modeling framework by including cellular-level simulation of the oxygen diffusion into the tissue and different mechanisms of vessel remodelling due to shear stress.

There have also been some multiphase models proposed for vascular tumor growth, with the most recent one being from Breward *et al.*, [Breward 2004]. They have extended their previous work for avascular tumors, by introducing blood vessels as a third phase. Physical interactions between different phases are modeled explicitly in terms of pressures. In their model they have also included the collapse of blood vessels due to pressure exerted on them, creating a better realization of the tumor dynamics.

We have seen that most models explained above either use discrete or continuum formulation, and in some cases both. The link between the discrete and continuum formulation has also been studied however, much less than the models themselves. In [Stevens 2000], Stevens *et al.* have started from a discrete set of tumor cells migrating under the effect of chemical agent, performing chemotaxis. They have shown that in the limiting case when the number of tumor cells increase one can describe the chemotaxis using advection-reaction-diffusion equations, notably a continuum formulation. Later on Hillen *et al.* have achieved the same result for another invasion dynamics, mesenchymal motion [Hillen 2006]. In this type of motion the tumor cells moves in a fiber network following the fiber directions. These works stand different than the models explained however, they have a big importance for the models as they can be the link between different scales of tumor modeling.

3.4 Macroscopic Models

Observations at the macroscopic scale consists of medical images like Computed Tomography scans (CT), Magnetic Resonance Images (MRI) and MR diffusion tensor images (MR-DTI). Since the resolution of these observations is limited, typically around $1mm \times 1mm \times 1mm$ in the best case, observable factors are limited. Due to this reason, compared to the models explained in Section 3.3 macroscopic models include fewer factors and their formulations are usually simpler. On the other hand, while microscopic models simulate the tumor growth in theoretical settings (infinite boundaries, known location of different structures,...), macroscopic models use real settings, e.g. real boundaries of the brain, gray-white matter segmentation, geometry of the tumor.

To review the recent macroscopic models we are going to use a different classification than the one used in Section 3.3. Based on the targeted effect of the tumor on the brain, macroscopic models can be classified into two different classes: mechanical models, which concentrate on the mass-effect of the tumor on the brain tissue, and diffusive models, which concentrates on the invasion of surrounding tissue by tumor cells. In terms of mathematical formulations, unlike microscopic models, almost all macroscopic models use continuum formulations, where tumor cells are assumed to be a continuum. As a result, formulations contain several ordinary and/or partial differential equations to describe the growth process.

3.4.1 Diffusive Models

Almost all macroscopic models, formulating the growth process concentrating on the diffusive nature of the tumor, use the reaction-diffusion formalism [Murray 2002, Mandonnet 2008]. This formalism models the invasive tumor by adding a diffusion term to the simple solid tumor growth models, which formulate proliferation of cells, see table 3.1. The 'building block' equation of this formalism is the partial differential equation (PDE) given as:

$$\frac{\partial u}{\partial t} = \nabla \cdot (D\nabla u) + R(u,t) \tag{3.1}$$

$$(\eta \cdot \nabla)u = 0 \tag{3.2}$$

where in equation 3.1 u is the tumor cell density, $\partial/\partial t$ is the differentiation operator with respect to time, D is the diffusion tensor for tumor cells and $R(u,t)$ is the so-called reaction term. This equation isolates two different characteristics of the tumor growth in two terms: diffusion and proliferation. The first term on the right hand side, $\nabla \cdot (D\nabla u)$ describes the invasion of tumor cells by means of a Brownian motion, which is characterized by the diffusion tensor D. The second term in the equation, $R(u,t)$, describes the proliferation of tumor cells. For this term population growth equations are commonly as summarized in Table 3.1. In macroscopic models, Equation 3.1 is usually solved using real geometries therefore, boundaries should be included in the model. Equation 3.2 is the no-flux boundary condition which is applied at the brain boundary and at the ventricles with the normal directions η, formulating the fact that tumor cells do not diffuse in these structures.

One of the first models using the reaction-diffusion formalism for the tumor
growth was proposed by Cruywagen *et al.* in [Cruywagen 1995]. They argue that, a
growth model that uses equation 3.1 and which consists only a single cell population
was not able to capture the growth dynamics seen in CT images. Hence, they
proposed to use a model with two populations of tumor cells, which is formulated by
coupling two equations of the form 3.1, each one describing a different population.
Through the coupling terms they were able to describe the competition between
populations for nutrients and growth factors. The second population of tumor cells,
were assumed to be a mutation of the first type. The occurrence of these cells was
attributed to the use of chemotherapy and/or radiotherapy, causing cells to mutate
into a more resistant type. They also included the effect of treatment in their model
as a constant cell loss mechanism, which is basically another reaction term. Their
final formulation had the form:

$$\frac{\partial u_1}{\partial t} = D_{u_1} \nabla^2 u_1 + f(u_1, u_2) - C_1(u_1, t)$$
$$\frac{\partial u_2}{\partial t} = D_{u_2} \nabla^2 u_2 + g(u_1, u_2) - C_2(u_2, t)$$

where reaction terms f and g describe the coupling between tumor populations
given by u_1 and u_2, while C_1 and C_2 formulate effects of therapy. In their model,
Cruywagen *et al.* formulated the invasion of tumor cells as an isotropic-homogeneous
diffusion where speed of diffusion was given by coefficients D_{u_1} and D_{u_2}.

In [Swanson 2000, Swanson 2002b], Swanson *et al.* revised the hypothesis that
tumor cells diffuse homogeneously in the brain made in the previous works. In the
light of the experimental results of Giese *et al.* regarding the differential motility of
tumor cells on gray and white matters [Giese 1996], they formulated the invasion of
tumor cells by isotropic-nonhomogeneous diffusion. In this formulation the diffusion
tensor D in Equation 3.1 was assumed to be isotropic and nonhomogeneous (spa-
tially varying). Its form was given as: $D = d(\mathbf{x})\mathbf{I}$, where $\mathbf{I}$ is an identity matrix and
$d(\mathbf{x})$ is the diffusion rate. $d(\mathbf{x})$ took two different values in the white matter,d_w, and
in the gray matter, d_g, where $d_w >> d_g$ corresponding to the observation that tu-
mor cells move faster on myelin sheath. In this work, only one population was used
and the no-flux boundary conditions were applied. For the reaction term, authors
used exponential growth, taking into account only the proliferation of tumor cells
(see Table 3.1). Later on, Swanson *et al.* in [Swanson 2002a] included the effect of
chemotherapy through a negative reaction term. Instead of modelling the effect of
therapy via a constant cell loss, they took into account the temporal effectiveness
of drugs used and also the possible spatial heterogeneity of drug efficacy. In both
works CT and MR images were used and the attention for validating the model was
given to predicting survival times after diagnosis.

Extending the idea of Swanson *et al.* regarding the differential motility of tumor
cells on different tissues, Clatz *et al.* and later Jbabdi *et al.* included anisotropy to
the invasion mechanism of tumor cells, [Clatz 2005] and [Jbabdi 2005]. They mod-
elled the diffusivity of tumor cells through an anisotropic-nonhomogeneous diffusion.
The assumption they have made is that tumor cells not only move faster on myelin,
but also follow the white matter fiber tracts in the brain. They have constructed

Table 3.2: Differential motility between white and gray matter. The fiber tract is along the y-axis in the second image. (Images taken from [Clatz 2005]) In the construction of D, α is the multiplicative constant between gray and white matter motility and f is the relation between water diffusion and tumor diffusion.

$D_g = d\mathbf{I}$	$D_w = \alpha d\mathbf{f}(D_{water})$
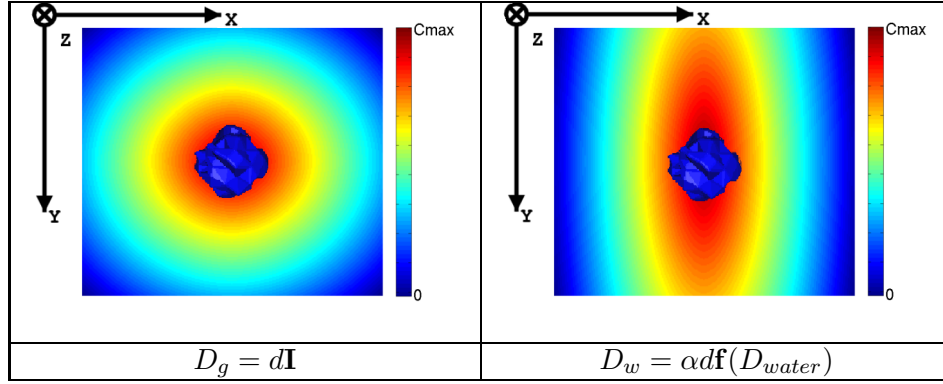
the tumor diffusion tensor (TDT) from the water diffusion tensor using magnetic resonance diffusion tensor images (MR-DTI). Although methods of construction of the TDT were different in these works, the main idea was to assign isotropic diffusion in the gray matter and anisotropic diffusion in the white matter having greater diffusion along the fiber direction as given in table 3.2. By including the anisotropy of tumor diffusion in the formulation, these models were able to capture the "spiky" and fingering patterns of tumors observed in the images, see Figure 3.5. Both of the works proposed an evaluation of their models by comparing visible tumors in the MR images with the ones simulated with the model. Recently Hogea *et al.* built on the anisotropic reaction-diffusion model and included the observation that one of the mechanisms tumor cells migrate is that they push each other [Hogea 2007]. They included this rather mechanical dynamics of invasion in their model by adding an advection term in the Equation 3.1.

The reaction-diffusion models as proposed in [Swanson 2000, Clatz 2005, Jbabdi 2005, Hogea 2007] are appropriate for explaining the invasive parts of the tumor which are far away from the core of the tumor. The growth of the central part of the tumor, where tumor cells are very dense, is not well captured by the diffusion process. This region grows rather like a compact ball, exponentially rapid at the beginning and then linearly. Stein *et al.* deals with this problem for the case of *in-vitro* experiments, [Stein 2007]. Instead of applying the reaction-diffusion model to the whole tumor they use two reaction-diffusion models describing the core and the invasive regions as two different populations. The two populations are coupled by a velocity bias applied on the invasive region such that the tumor cells try to move away from the core of the tumor. They show that a two population model such as the one they propose, is able to capture the different dynamics of the invasive region and the core of the tumor in the case of petri dish experiments.

Besides the continuum formulations explained above, recently Stamatakos *et al.*
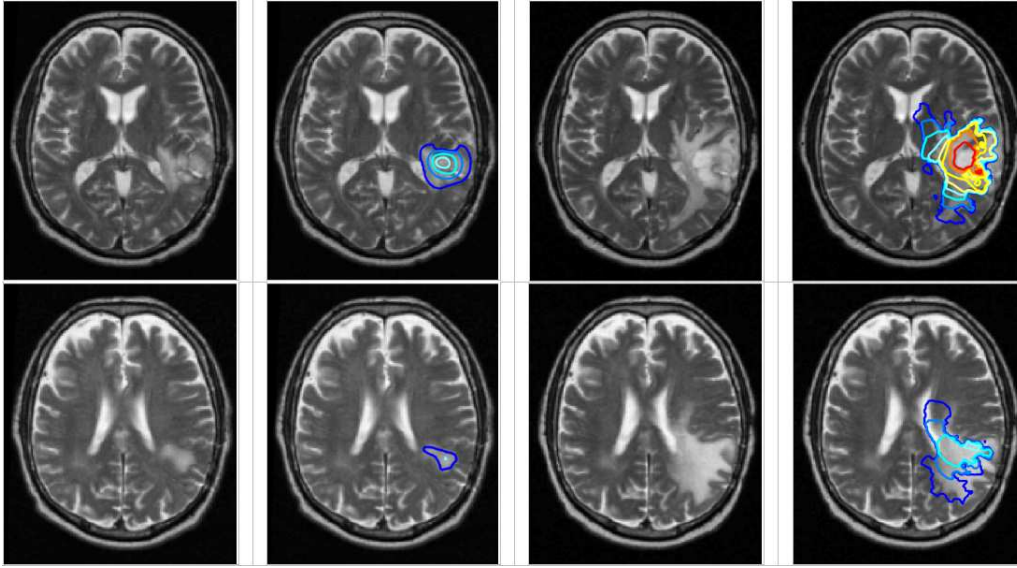
Figure 3.5: Diffusive models including anisotropy in the tumor diffusion are able to capture spiky nature of tumor growth. Figures show evolution of the tumor in two different axial slices. First two columns show the initial image and initial state of the model respectively, while the third column shows the tumor after 6 months and the fourth column shows the evolved tumor using the model given in [Clatz 2005].

proposed to use a cellular automata based algorithm to model tumor growth in medical images [Stamatakos 2006a] and [Stamatakos 2006b]. Their model discretizes the visible tumor volume in the post gadolinium T1-weighted MR image into mesh cells containing groups of tumor cells. They explain growth by assigning certain probabilistic set of rules to every mesh cell, which define cell cycle dynamics for the group of cells inside that mesh cell. These rules take into account nutrition distribution throughout the tumor, effect of abnormal p53 gene expression and type of metabolic activity of the cell in assigning transition probabilities between different phases of the cell cycle, mitosis, apoptosis (controlled death of cells) and necrosis (infected death of cells). As a result, the growth phenomena is explained by the cell cycle, governed by probabilistic transition rules. Although some of these features are not well observable in medical images they model them based on assumptions coming from biological experiments. As an example, the nutrition distribution is taken to be decreasing homogeneously from the periphery of the tumor to the center. Their model does not take into account the infiltration of tumor cells, but rather only the growth through mitosis. Through the probabilistic nature of their model they were able to obtain realistic looking differentiated tumor growth.

3.4.2   Mechanical Models

Mechanical models, which concentrate on the mass-effect of the tumor, contain two distinct formulations, one for the tumor growth and one for the mechanical characteristics of the brain tissue. These models combine these formulations through

coupling, to describe the mechanical interactions between the brain tissue and the tumor growth leading to deformations. There have been many works on characterizing the mechanical properties of the brain tissue, which is deformable but not elastic. In [Wasserman 1996] it is said that the brain tissue is a sponge like material, possessing instantaneous properties of elastic materials and time-dependent properties of the viscoelastic ones. Moreover, there is a great variation between elastic parameters of brain tissue within similar tissues as well as between differing tissues. Instead of formulating these complex mechanical characteristics, almost all models use assumptions to simplify brain tissue's characteristics.

Wasserman *et al.* proposed one of the first mechanical models in [Wasserman 1996]. In this 2D model they assume the brain tissue is a linear elastic material for which stress-strain relations can be given by generalized Hooke's law. Moreover the amount of strain caused on a given volume, by a specific amount of stress, was proportional to the density of brain tissue in that volume. For the tumor growth part, they assumed a very simple formulation including only the proliferation of cells, in which the rate of mitosis was set to be constant. The coupling between the growth and constitutive equation of the tissue was established by assigning a homogeneous pressure proportional to the number of tumor cells per volume. Through this coupling they were able to model the growth of the tumor under mechanical constraints and interactions in CT images. In [Kyriacou 1999], Kyriacou *et al.* assumed that brain tissue can be better characterized by a nonlinear elastic material than a linear one. They modelled white, gray and tumor tissue as nonlinear elastic solids obeying equations of an incompressible nonlinearly elastic neo-Hookean model. With the introduction of nonlinear elasticity into the model and the use of nonlinear geometry, they were able to describe large deformations through their formulation. Tumor growth was kept as a pure proliferation process with uniform growth causing uniform outward strain. They have applied this model in registering images of patients with tumor induced deformations to brain atlases. Their 2D model was applied on individual cross-sectional images obtain by CT or MR.

Mohamed and Davatzikos extended this model by modelling the brain tissue as an isotropic and homogeneous hyperelastic material, [Mohamed 2005]. With this they relaxed the incompressibility assumption made in [Kyriacou 1999] and ignored the viscous effect, keeping in mind that times related to deformations was very large compared to viscosity time constants. In addition to modeling the mass effect due to bulk tumor growth they have also taken into account the expansion caused by the edema and the fact that part of the mass effect should be attributed to edema. They have also assumed a proliferation model for the tumor growth, which had a constant mitosis rate. Coupling of tumor growth and mechanical interactions was done the same way as in Wasserman's model. As in the work of Kyriacou *et al.*, this model was also able to describe large deformations. In [Hogea 2006], Hogea et al. reformulated the model within a general Eulerian framework, with a level-set based approach for the evolving tumor aiming at a more efficient method, see Figure 3.6. They have also mentioned that for patient specific models, parameters should be found via solving an inverse problem. However this work was aiming to generate large number of brain anatomies deformed by simulated tumors, hence they did not concentrate on the patient specific modelling. In order to validate their model they

have compared deformations seen in MR images with the ones simulated with their models.

Tumor growth process has been kept very simple and has been associated with only proliferation of tumor cells in all previous macroscopic models, which concentrate on the mass-effect of the tumor. Clatz *et. al* combined two approaches of the macroscopic modelling in [Clatz 2005] in creating a formulation for glioblastoma multiforme (GBM). They have formulated the invasive nature of the tumor growth, besides proliferation, and the deformation this causes on the brain tissue. They assumed that brain tissue is a linear viscoelastic material, which can be modeled using a static equilibrium equation, since the time scale of tumor growth is very large. The coupling of the growth with the mechanical deformation on brain tissue was established using two different mass-effects: one for the bulk tumor and the other for the tumor infiltrated edema. The effect of bulk tumor was set as a homogeneous pressure caused by the volume increase as a result of cell proliferation. The
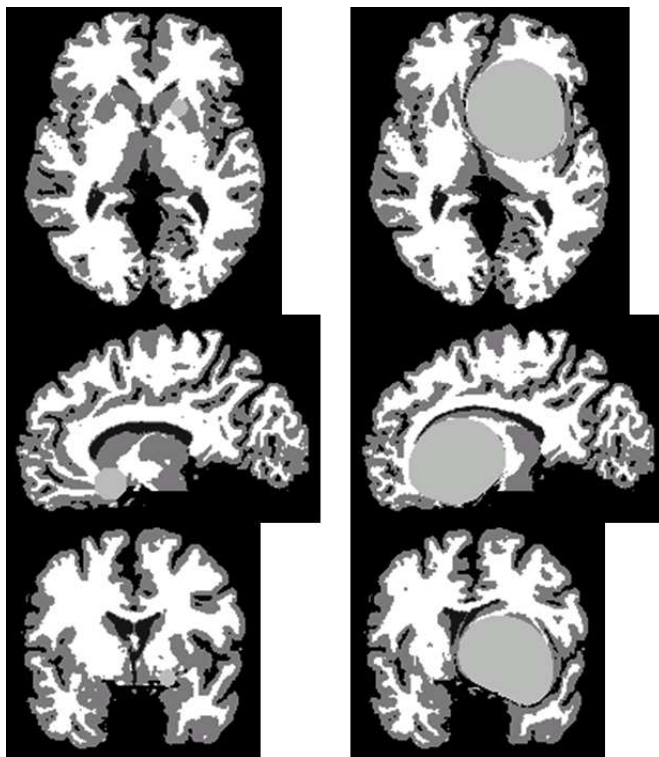
Figure 3.6: Models can model large deformations due to tumor growth and edema. Simulated tumor growth in a normal brain template, starting from a small initial seed, orbital-frontal left, using the modeling framework in [Mohamed 2005] and [Hogea 2006]. Left: original healthy segmented brain template (axial, sagittal, coronal) with a small tumor seed; Right: corresponding deformed template with the grown tumor at the end of the simulation. Large deformations can be clearly observed.

mass-effect of the tumor infiltrated edema included the effect of invasion through a stress term which contained tumor cell density as given in Equation 3.3.

$$\nabla \cdot (\sigma - \lambda \mathbf{I}_3 c) + f_{ext} = 0 \tag{3.3}$$

where $\nabla \cdot$ is the divergence operator, σ is the strain tensor, c is the tumor cell density at a location, f_{ext} is the external force and λ is the coupling factor. With this model they were able to simulate both the invasion and the mass effect simultaneously.

Previous works on macroscopic modeling have concentrated on creating realistic models and focused on the modeling framework. Garg and Miga in [Garg 2008] preferred to build on these existing models and focused on the inhibitory effects of the mechanical stress on the tumor growth. In their work they have added the inhibitory effect of the mass effect for the reaction-diffusion tumor growth models. They have shown that this effect has a big impact on such modeling frameworks and it should not be left aside.

3.5 Image Guided Tools for Therapy Planning

The tumor growth models explained in the previous section can be very useful for diagnosis and therapy planning in the clinical practice [Mandonnet 2008]. Using the dynamics of the tumor growth, they can provide realistic simulations of the therapy or predict the extent of the tumor. Such tools aim at helping the doctor in planning the therapy course by quantifying and predicting the efficacy of a given scheme. The effect of therapy on the tumor and on the brain tissue is extremely complex and not known totally. In order to include all the known information in the model one needs to combine microscopic and macroscopic approaches because inter and intra cell dynamics play important role [Gardner 2003]. Several authors have included the effect of therapy in their macroscopic models, specifically chemotherapy. Cruywagen *et al.* for example modeled the effect of drugs through a constant cell loss mechanism using a negative reaction term.

One of the first elaborate macroscopic models focusing on therapy was proposed by Swanson *et al.* [Swanson 2002a, Swanson 2004]. They improved the idea of integrating the therapy as cell loss mechanism and formulated temporal effectiveness of the drugs and spatial heterogeneity of their efficacy. Including these two effects they were able to get more realistic simulations of the growth of the tumor under the effect of chemotherapy.

Recently in [Stamatakos 2006a] Stamatakos *et al.* have modeled the effect of chemotherapy based on their cellular automata growth model, which was explained in the previous section. The effect of the drug is included as a damage to each cell, which if large enough drives the cell to apoptosis. The relation between drug dose administered orally (D) and the plasma concentration (C_p) the tumor encounters is given by the relation

$$C_p = \frac{FDk_a}{V_d(k_a - k_{el})}(e^{-k_{el}t} - e^{-k_a t}) \tag{3.4}$$

where F is the fraction of drug reaching the circulation, V_d total volume the drug will distribute in, t time elapsed since drug administration, k_a and $k_e l$ are the

absorption and elimination rate respectively. For those parameters that are not observable through clinical situations and medical images, like k_a, population mean values proposed in the literature are used. The damage given to a cell is computed through survival fraction

$$SF = e^{-K_{SF}T_{SF}C_p},\qquad\qquad(3.5)$$

which depends on K_{SF} survival fraction constant and T_{SF} exposure of tumor cells to the drug. Equation 3.5 depends on the type of drug used and the given form is for the drug called Temozolomide (TMZ), which the authors used in their simulations. Using this model they simulated two different oral administration schemes with 3 different doses and compared the outcomes in terms of the number of proliferating tumor cells. Using probabilities for cell cycle and drug damage they captured the stochastic nature of the therapy and tumor growth. In their simulations they use the drug TMZ and a patient data with a high grade glioma. They start using the real tumor delineation and demonstrate a virtual realistic evolution, see Figure 3.7.

In another work of the same group [Stamatakos 2006b], Stamatakos *et al.* have used their cellular automata based model in modeling the effect of radiotherapy and simulating therapy. They have included in the model the damage caused in a tumor cells (group of cells in their case) due to irradiation. This is explained by survival probabilities given by the linear-quadratic model

$$S(D) = exp[-(\alpha D + \beta D^2)].\qquad\qquad(3.6)$$

$S(D)$ is the survival probability of a cell given that it takes D dose of irradiation (in Gy). The α and β parameters define the radiosensitivity of the cell and they are varying according to the phase of the cell-cycle, p53 gene expression and the metabolic activity type of the cell (oxic or hypoxic). Parameters not observed from medical images are set by assumptions and mean values coming from experiments in biology. Their model was able to demonstrate conformal shrinkage of the tumor due to irradiation, which is observed in real cases. Using their model, they simulated standard and hyper fractionation of irradiation and compared these two strategies through simulation. Although they obtained realistic results several phenomena are not taken into account in their model such as infiltration of tumor cells and the effect of irradiation on the surrounding healthy tissue. As in the case of the chemotherapy modeling, simulations start from the real tumor delineation and demonstrates a virtual evolution.

3.6   Applications to Registration and Segmentation

Tumor growth models, besides being used to create therapy planning tools, have been used to aid registration and segmentation tools as well. Problems of brain tissue segmentation and atlas to patient registration in the presence of a pathology have received attention from the medical imaging community for a long time. Lately there have been several works proposed for these purposes using the tumor growth dynamics. These works can be classified into two related groups: atlas to patient registration and synthetic brain image creation consisting of a tumor.
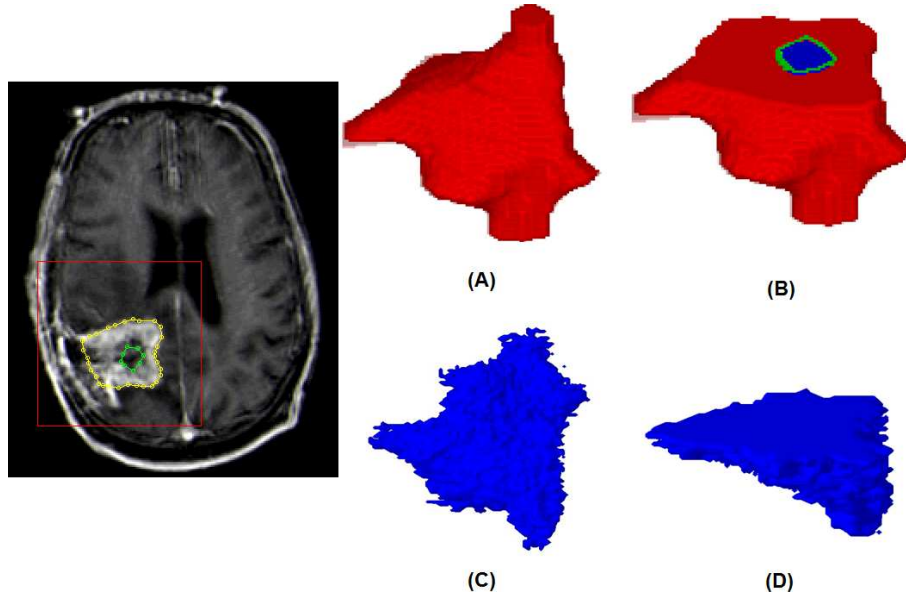
Figure 3.7: Left: An MRI axial slice depicting a glioblastoma multiforme tumour. Both the gross volume of the tumour and its central necrotic area have been delineated. The same procedure has been applied to all MRI slices. Right: 3D visualization of the simulated response of a clinical glioblastoma multiforme tumor to one cycle of chemotherapeutic scheme (150 mg/m orally once daily for 5 consecutive days/28-day treatment cycle, [fractionation scheme A)]. (A) External surface of the tumor before the start of chemotherapy, (B) internal structure of the tumor before the start of chemotherapy, (C) external surface of the tumor 20 days after the start of chemotherapy, and (D) internal structure of the tumor 20 days after the start of chemotherapy. Pseudocolor Code: red: proliferating cell layer, green: dormant cell layer (G0), blue: dead cell layer. The following "99.8 %" criterion has been applied: "If the percentage of dead cells within a geometrical cell of the discritizing mesh is lower than 99.8 % then [if percentage of proliferating cells > percentage of G0 cells, then paint the geometrical cell red (proliferating cell layer), else paint the geometrical cell green (G0 cell layer)] else paint the geometrical cell blue (dead cell layer)" [Stamatakos 2006a].

3.6.1 Registration

The registration of an anatomical atlas to a patient with a brain tumor is a difficult task due to the deformation caused by the tumor. Registration algorithms proposed for normal to normal registration fail due to this reason. Recently, several authors proposed to include the tumor growth models in their registration algorithms to tackle this difficult task. The important ingredient the growth models can add is the quantification of the tumor-induced deformation on the brain structures through model parameters. Proposed algorithms use these model parameters in separating the deformation field between the atlas and the patient image into the tumor-induced

deformation and the normal inter-subject variation.

Kyriacou *et al.* proposed one of the first atlas to patient registration algorithms based on the tumor growth dynamics [Kyriacou 1999]. Starting from the patient image, their algorithm first simulates the biomechanical contraction in the case of the removal of the tumor to estimate patient anatomy prior to the tumor. A normal to normal registration between the atlas and the tumor-free patient brain follows the contraction. At this point instead of deforming the registered atlas with the inverse of the deformation field obtained during the contraction, they perform a nonlinear regression in order to estimate the tumor growth parameters that would best fit the observed tumor-induced deformation. These parameters consist the center and the amount of expansion of the tumor. Once the parameters are estimated they perform the biomechanical tumor growth inside the registered atlas to obtain the final atlas to patient registration, which was performed in 2D.

In contrast to separating the deformation caused by the tumor and the deformation explaining inter-subject variability, in [Cuadra 2004], Cuadra *et al.* proposed to combine these two in a nonlinear *demons* based registration algorithm [Thirion 1998] for the atlas to patient registration. The algorithm starts by placing the two brains on the same frame and scale using a global affine registration. An expert manually places the tumor *seed* on the affinely registered atlas, which corresponds to the place of it in the patient image. The seeding is followed by a nonlinear registration algorithm with adaptive regularization. The tumor growth is modeled as an outward pressure causing radial displacement of the surrounding structures. Authors included this displacement field in their registration algorithm to take into account the tumor-induced deformation.

Mohamed *et al.* took a statistical approach for the atlas to patient registration problem in [Mohamed 2006]. They propose a statistical model on the deformation map created by applying a nonlinear elastic registration to match an atlas with the patient image. This model is based on the fact that although normal registration techniques would fail in the vicinity of the tumor, they will provide the right deformation field for the other parts. Their statistical model uses the space of displacement fields and decomposes any deformation field on two orthogonal hyperplanes, one describing the tumor-induced deformations and other inter-subject variability. The formulation of the hyperplanes is done by principal component analysis (PCA) assuming linearity of the governing space and that displacement fields are realizations of two independent Gaussian random vectors. The training of the PCA for the inter-subject variability is done by samples coming from registering the atlas to a dataset of healthy subjects. On the same dataset they grow artificial tumors using their growth model explained in Section 3.4 for different sets of growth parameters, including center of the tumor, expansion of the tumor and the edema extent. These instances serve as the training samples of the PCA for the tumor-induced deformation. When a new patient image is encountered, they decompose the deformation field and find the tumor growth parameters specific for the patient as

$$U_f \approx \mu_c + \mathbf{V}_c \mathbf{a} + \mu_d + \mathbf{V}_d \mathbf{b} \qquad (3.7)$$

where U_f is the total displacement field, μ_c and $\mathbf{V}_c$ are the mean and covariance matrix displacement fields for inter-subject registration, and μ_d and $\mathbf{V}_d$ are the

(a)

(b)
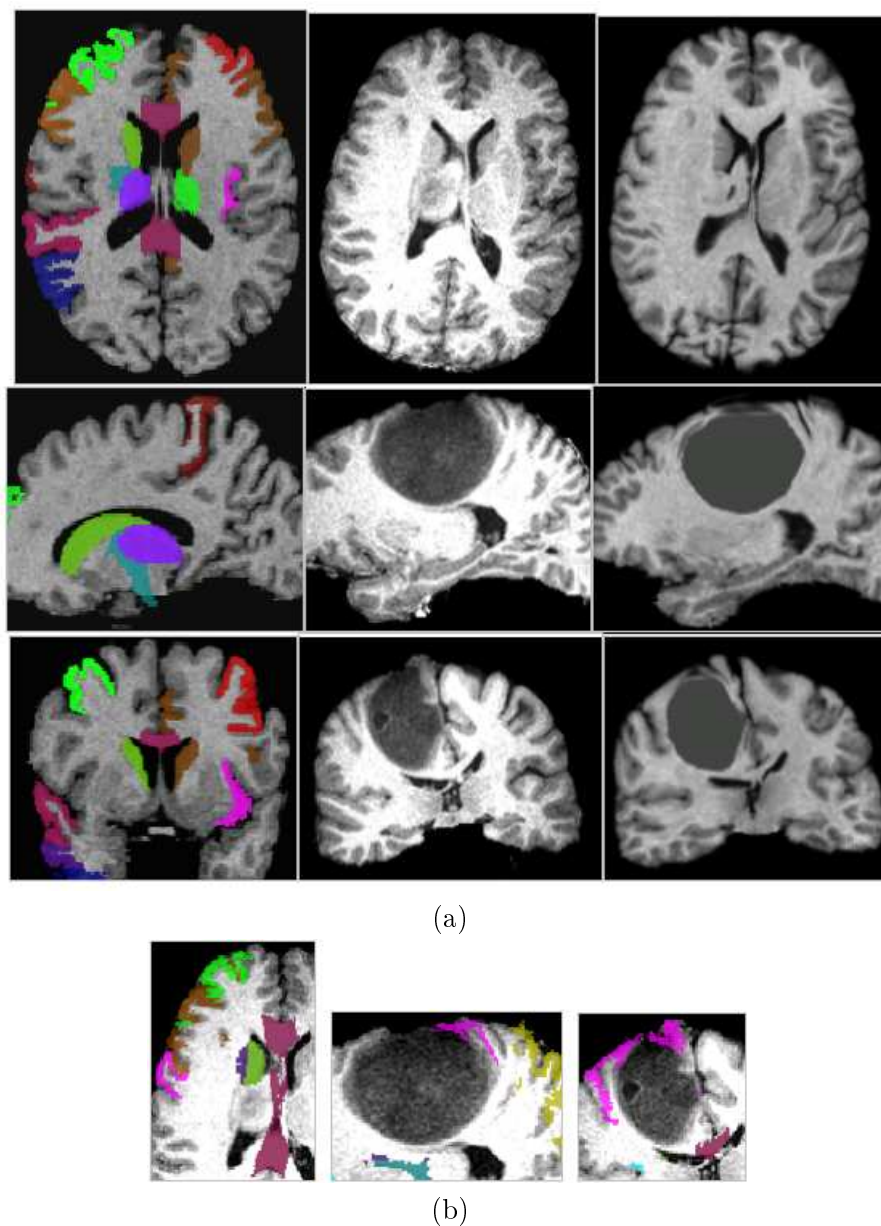
Figure 3.8: Left to right: the atlas image with manually labeled regions, the patient image, the atlas to patient registration result using the algorithm explained in [Mohamed 2006], which includes tumor growth modeling. (b) The selected labels in the atlas are warped and correspondingly superimposed on the patient's image

same identities corresponding to tumor-induced deformation. Once the deformation field linking atlas to subject and tumor growth parameters are found, the atlas is registered and the tumor is grown in it. Zacharaki *et al.* in [Zacharaki 2006] proposed to improve the registration algorithm used in this work by a more flexible one, based on HAMMER algorithm [Shen 2002], taking into account the fact that

around the tumor region the deformation field is distorted when the tumor model parameters are not optimal. To tackle this, they introduced a patient-specific optimization framework based on similarity matching and smoothness properties of the deformation around the tumor, see Figure 3.6.1.

3.6.2   Segmentation

Another application of tumor growth modeling is the synthetic dataset creation for validating segmentation algorithms. Presence of a tumor is a big challenge for the segmentation algorithms. Algorithms are compared with expert manual segmentations for validation and performance analysis. Manual segmentations however, show high inter-expert variability and contains human error due to fatigue and other reasons. In order to tackle this problem, several works proposed to generate synthetic realistic MR images containing tumors, for which ground truths are known and can be used for validation and analysis. There are two different subproblems for the generation. One of them is to simulate the tumor growth realistically. The other one is to mathematically describe the effect of tumor growth on MR signal intensities. In other words, how the image intensities change in different parts of the image (e.g. edema, actively proliferating tumor region, tumor free part,...).
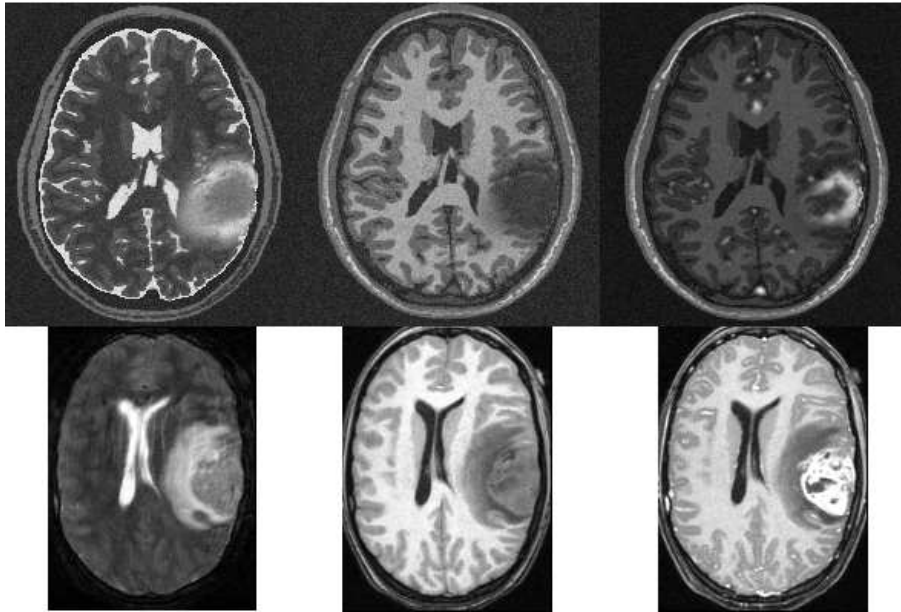
Figure 3.9: Upper row shows the synthetic images generated of a patient with glioma using the algorithm proposed in [Prastawa 2005]. T2w, contrast enhanced T1w and T1w images from left to right. Bottom row shows the same images coming from a real patient.

Rexilius *et al.* proposed one of the first models for this problem in [Rexilius 2004]. They have modeled the tumor with three compartments: the active tumor tissue, the necrotic (dead) tumor core and the edema. The active tissue and the necrotic

part are drawn in the desired location with the desired size. Later on reasonable gray values are assigned to these regions including Gaussian noise to make the intensities realistic. As an example, in the case of contrast enhanced T1w image the realistic values included contrast accumulation in the active tumor part. The mass effect of the drawn tumor is applied to the underlying healthy subject MR image assuming linear elastic material properties for tissues. The growth is simulated by a radial displacement applied to surrounding tissues using finite element methods. Lastly for the edema, they use the distance transform of the tumor on the white matter mask of the underlying image and deform it with the same mass effect applied to the brain. Based on the resulting distance transform values they assign intensity values corresponding to edema infiltration.

In order to create more realistic MR images, Prastawa *et al.* [Prastawa 2005, Prastawa 2008] have tackled the same problem using a more sophisticated tumor growth model and adding contrast accumulation properties of different tissues. They have adopted the growth model proposed by Clatz *et al.* [Clatz 2005]. In addition to this model, in their formulation they took into account the displacement and destruction of white matter fibers using image warping and nonlinear interpolation, based on the observations of Lu *et al.* [Lu 2003]. For the image generation part, they have modeled the contrast agent diffusion inside the brain using the reaction-diffusion formalism. Using such a formulation they were able to simulate the high contrast accumulation in CSF and in active tumor regions. As a result they obtained realistic looking synthetic data with contrast irregularities as in Figure 3.6.2.

3.7 Discussions

In this chapter, we have reviewed some works on mathematical tumor growth modeling and its applications proposed by the medical image analysis community. Away being from a complete review on this subject, this chapter is an attempt to highlight the main approaches and applications.

In terms of realistically modeling the growth phenomena, some solid attempts have been taken. However, there are very exciting challenges awaiting to be solved. Tumor growth is a very complex phenomena, including different scales of ingredients from genetic to macroscopic. The biggest lacking point at the moment is the link between these scales. Observations that can be obtained from medical images are limited and obtaining microscopic observations for a large view-area is not possible at the moment. One approach that can be taken to tackle this problem would be to included information coming from different modalities of images in growth models. Including techniques like positron emission tomography (PET), magnetic resonance spectroscopy (MRS) and functional-MRI (fMRI) would yield information about nutrient, oxygen and metabolite levels in the tumor giving an opportunity to integrate microscopic phenomena in macroscopic models and for patient specific models.

Personalization of the tumor growth models and therapy models summarized in this chapter is an important missing link between mathematical methods and clinical applications. Inter-patient variation of parameters can be large, hence obtaining the

necessary parameters automatically through inverse problems is a required step in adapting general growth models to individual patients. Such inverse problems also serve as quantification tools that can assess the efficacy of a therapy or understanding the amount of deformation caused as we have seen in Section 3.6.1. Moreover, intra-patient variation of these parameters has also not been studied yet. Variation within the same tumor might result in different growth patterns than the one expected by the growth models formulating the average behavior of the tumor. The heterogeneity in a single tumor might be high strengthening the need for stochastic approaches for tumor growth models.

One other big challenge for creating more accurate models, is the lack of a proper quantitative validation technique. For macroscopic models the comparison is done with observed medical images, which are not able to visualize the whole tumor. Although some quantitative validation methods were proposed by some authors, [Clatz 2005, Mohamed 2005, Prastawa 2008], the field still lacks a golden standard in validation methodology.

Improving imaging techniques and more accurate models will yield valuable tools for clinical oncology in the future. Patient-specific models combining information from different scales will enable us to perform patient-specific simulations. Such simulations, either for therapy or simple growth will aid in patient treatment and hopefully improve prognosis.

Traveling Time Formulation for Tumor Delineation and Parameter Estimation for Reaction-Diffusion Models Using Time Series of Images: Method

Contents

Context

Reaction-diffusion based tumor growth models have been widely used in the literature for modeling the growth of brain gliomas. Lately, recent models have started integrating medical images, specifically anatomical and diffusion atlases, in their formulation. Including different tissue types, geometry of the brain and the directions of white matter fiber tracts improved the spatial accuracy of reaction-diffusion models. The adaptation of the general model to the specific patient cases on the other hand have not been studied thoroughly yet. In this chapter we address this adaptation. We propose a parameter estimation method for reaction-diffusion tumor growth models using time series of medical (Magnetic Resonance) images. This method estimates the patient specific parameters of the model using the images of the patient taken at different successive time instances. The proposed method formulates the evolution of the tumor delineation visible in the images based on the reaction-diffusion dynamics therefore it remains consistent with the information available.

4.1   Introduction

The reaction-diffusion models provide a general framework where the integration of information coming from medical images is possible. We have seen in Chapter 3 some of these models and how they integrated information coming from images into their formulation. The general formulation for the reaction-diffusion models are based on the equations

$$\frac{\partial u}{\partial t} = \nabla \cdot (D(\mathbf{x})\nabla u) + \rho u(1-u) \tag{4.1}$$

$$D\nabla u \cdot \mathbf{n}_{\partial\Omega} = 0, \tag{4.2}$$

where u is the tumor cell density, D is a local diffusion tensor (i.e. symmetric positive definite 3x3 matrix), ρ is the proliferation rate, Ω is the brain domain, $\partial\Omega$ represents the boundaries of the brain and $\mathbf{n}_{\partial\Omega}$ is the normal direction to the boundary. Equation 4.1 describes the temporal evolution of tumor cell density while Equation 4.2 represents the no-flux boundary conditions. Once the integration of medical images in this model is achieved the next step is to adapt the model to specific patients data, in other words to *personalize* the model. This can be done via estimating the parameters of the general model, D and ρ, which best simulates the evolution of the tumor observed in the time series of images (images of the same patient taken at successive time instances). The difficulty in this estimation is due to the sparsity of the available information. The reaction-diffusion models describe the temporal evolution of tumor cell densities while in the images we only observe the evolution of the tumor delineation which is assumed to correspond to an iso-density contour [Burger 1988], as shown in Figure 4.1. In this chapter and in other parts of the thesis the terms tumor delineation, tumor front and tumor boundary are used interchangeably to describe the boundary of the visible part of the tumor in the medical images.

The problem of estimating parameters from time series of images in the context of tumor growth models is a rather unexplored problem. A first attempt was made by Tracqui *et al.* in [Tracqui 1995] where they optimized the parameters of their model by comparing the area of the tumor observed in CT images at different times and the area of the simulated tumor. The drawback of this approach was to use tumor cell densities requiring an initialization of the density distribution throughout the brain while these densities are not observable in the images. More recently, in [Hogea 2007], Hogea *et al.* have optimized their parameters by comparing locations of some manually placed landmarks with the model generated ones. In addition to the parameters of the reaction-diffusion model they optimize the parameters of their mechanical model as well. However, they also use tumor cell density distribution in their optimization process which is not available in the images. Moreover, a detailed analysis of the estimated parameters and their minimization framework is not provided. Recently Swanson *et al.* in [Swanson 2008a] proposed a parameter estimation method for the diffusion process in petri-dish experiments, which is consistent with the observables in the images as it uses the tumor boundaries rather than tumor cell densities. They have derived analytical approximations for the evolution of the tumor delineation for 2 dimensional circular growth. Using the
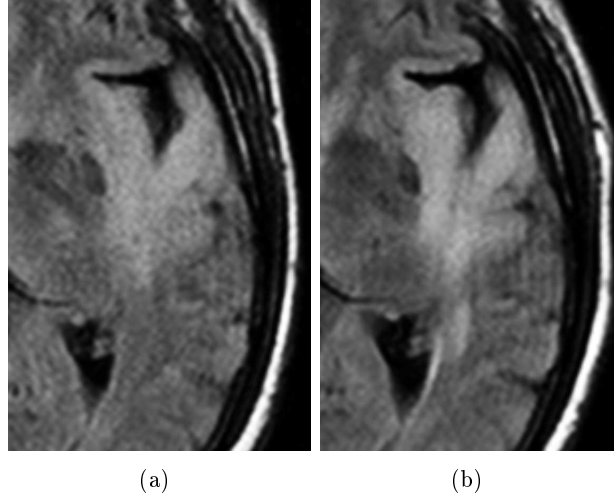
(a)   (b)

Figure 4.1: MR Flair images of a grade II astrocytoma: (a) image at the first examination (b) image at the second examination. In the anatomical MR images we observe the boundary of the visible part of the tumor rather than the tumor cell densities.

formulation for the tumor delineation they have estimated the diffusion coefficient for the petri-dish experiments. The difficulty one would encounter if one wants to apply this method to medical images is that the method assumes radial symmetric growth which is not the case in the brain (*in-vivo*). Moreover, the existence of a reaction term results in a different evolution than pure diffusion.

In this chapter, we propose and analyze a parameter estimation method for reaction-diffusion based tumor growth models using time series of medical images. The method is based on the evolution of the tumor delineation rather than tumor cell densities and in this respect it is consistent with the observations in the images. In Section 4.2, we explain our method, detail the anisotropic Eikonal approximation we use for describing the temporal evolution of the tumor delineation and formulate the parameter estimation problem.

4.2   Method

The parameter estimation methodology and the choice of the estimated parameters depend naturally on the exact formulation of the underlying reaction-diffusion model.   In this work we focus on the specific formulation proposed in [Clatz 2005, Jbabdi 2005]. However, due to the similarities of reaction-diffusion models the ideas we present here can be adjusted for other formulations. The model for tumor growth proposed in [Clatz 2005] is formulated by the system given in Equations 4.1 and 4.2. The diffusion tensor D is an anisotropic tensor taking into account two different phenomena: differential motility of tumor cells in different tissues and directional preference of tumor cell diffusion. The construction of D,

which is obtained from the DT-MRI, is as follows:

$$D(\mathbf{x}) = \begin{cases} d_g I & , \mathbf{x} \in \text{gray matter} \\ d_w D_{water} & , \mathbf{x} \in \text{white matter} \end{cases} \tag{4.3}$$

where tumor cells are assumed to diffuse isotropically in the gray matter with a rate d_g and diffuse along the white matter tracts proportional to the diffusion tensor for the water molecules D_{water} through a coefficient d_w. D_{water} in this construction is obtained from DT-MRI and normalized such that the highest diffusion rate in the brain would be 1.

We note that in [Clatz 2005] the authors also couple the evolution of the tumor with its mass effect on the brain but for this work, as a first step, we focus only on the reaction-diffusion part ignoring the mechanical effect. Once the problem for the growing tumor is solved and understood then the parameter estimation can also take into account the mechanical model.

The reaction-diffusion model given by Equations 4.1, 4.2 and 4.3 describes the temporal evolution of local tumor cell densities. As we have noted before, this creates an inconsistency with the observables in the images, see Figure 4.1. In order to solve the parameter estimation problem we need a formulation consistent with the images in which the evolution of the tumor delineation instead of the evolution of the tumor cell densities will be mathematically described. In section 4.2.1 we detail the construction of such a formulation, which is a projection of the reaction-diffusion equation. Once such a formulation is available then one can optimize the parameters using different error measures and optimization schemes. In section 4.2.2 we detail our choice for the error measure and the optimization scheme.

4.2.1   Eikonal Approximation for Reaction-Diffusion Models

The asymptotic properties of the reaction-diffusion equations under certain conditions allow us to construct a traveling time formulation for the tumor delineation. Reaction-diffusion equations and their asymptotic properties have been well studied in the literature [Aronson 1978, U. Ebert 2000] and these properties have been used for different applications [Maini 2004, Murray 2002, Keener 1998, Sermesant 2007]. Here we wish to summarize some of the relevant results in these works.

At large times, the constant coefficient case of Equation 4.1 admits a traveling wave solution in the infinite cylinder. In other words, when the change of u is non-zero in only one direction, $\mathbf{n}$, for very large times the solution of Equation 4.1 can be given in the form:

$$u(\mathbf{x}, t) = u(\mathbf{n} \cdot \mathbf{x} - vt) = u(\xi) \ \text{ as } \ t \to \infty. \tag{4.4}$$

where v is the asymptotic speed of the front and $\xi = (\mathbf{x} \cdot \mathbf{n} - vt)$ is the moving frame of the traveling wave. The center of the moving frame ξ is at $u = 0.5$. Plugging this asymptotic form of the solution into the reaction-diffusion equation given in Equation 4.1 we obtain an ordinary differential equation (ODE)

$$\mathbf{n}' D\mathbf{n} \frac{d^2 u}{d\xi^2} + v\frac{du}{d\xi} + \rho u(1-u) = 0 \tag{4.5}$$

This is a constant coefficient nonlinear equation and in order to have admissible solutions the asymptotic speed v should depend on the diffusion tensor D and ρ, and also on the shape of the initial condition $u(\mathbf{x}, 0)$. When the initial condition has a compact support the asymptotic speed of the traveling wave can be given as, [Aronson 1978, Murray 2002]:

$$v = 2\sqrt{\rho \mathbf{n}' D \mathbf{n}} \tag{4.6}$$

The planar initial condition with compact support converges to a travelling plane
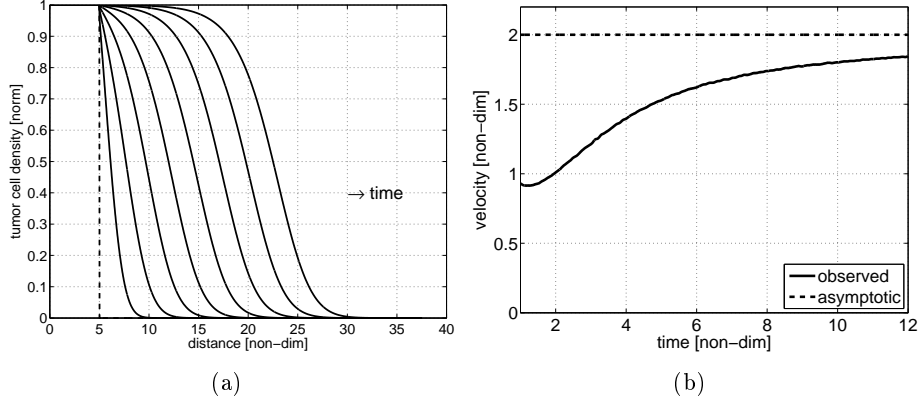

(a)   (b)

Figure 4.2: (a) The tumor distribution evolving with the constant coefficient reaction-diffusion equation (cross-section of the tumor cell density distribution in the infinite cylinder) is plotted at different times (non-dimensional). We see that the shape of the tumor cell density distribution approaches a constant shape in time and becomes a traveling wave. (b) The speed of a single iso-density contour ($u = 0.5$) is plotted in time along with the asymptotic speed v. In the non-dimensional form of the Equation 4.1 the coefficients are unit therefore $v = 2$. We observe that the speed the iso-density contour convergence to the asymptotic one but the rate of convergence is not very high, in $O(1/t)$. The convergence characteristics of the speed also depends on the iso-density value. For each u value the curve given in (b) will be different. However, this dependence is on the order of $O(1/t^2)$ therefore, the difference between the curves will die out faster and will not be significant [U. Ebert 2000].

with speed v in time. As the speed of the travelling plane converges to v its shape also converges to a constant shape, which depends on the reaction term and does not have an analytical form for the term we use (logistic growth term). Figure 4.2 illustrates the convergence of the front shape and the speed of the traveling wave in time.

The fact that reaction-diffusion equations admit traveling wave solutions in certain cases (constant coefficients and in the infinite cylinder) states that any iso-density contour of u at large times under certain conditions will move with a speed of v. Therefore, we can formulate the speed of the tumor delineation observed in the images using v. Although this gives the general idea, it is not complete because the convergence of the observed speed of an iso-contour to v is slow, in $O(1/t)$.

Ebert *et al.* have studied this convergence behavior and derived the rate analytically [U. Ebert 2000]. In their study they noticed that the convergence rate can be approximated with a time varying function which does not depend on the value of u on the iso-density contour. This approximation assumes that all the iso-density contours of u behaves like the $u = 0.5$ one, which is the origin of the moving frame. Following these studies we include the effect of convergence in v and have a time varying estimate of the speed of the $u = 0.5$ iso-density contour as

$$v(t) = \sqrt{\mathbf{n}'D\mathbf{n}}\frac{4t\rho - 3}{2t\sqrt{\rho}}. \tag{4.7}$$

The speed variation of the $u = 0.5$ iso-density contour with time is different from the other ones. However, the effect of the value of the iso-density contour is shown to be $O(1/t^2)$ and therefore we ignore it [U. Ebert 2000]. The differences between the observed speed of the moving frame, the asymptotic speed and time varying estimate is shown in Figure 4.3(a). In Figure 4.3(b) we show the integrals of these speeds starting from the same initial condition to demonstrate the effect of the convergence on the location of the moving frame (which corresponds to the tumor delineation in the context of this work). At this point we can readily formulate the
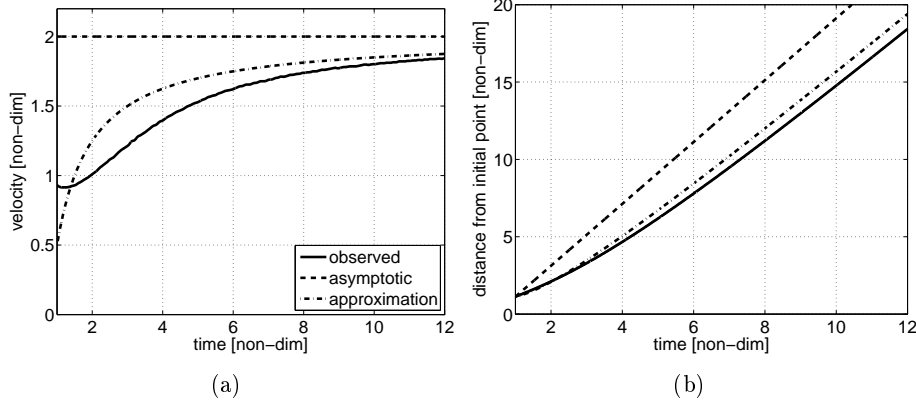
Figure 4.3: (a) The traveling wave has an asymptotic speed shown with a dashed curve. However, when we observe the speed of an iso-density contour in time we notice the low rate of convergence to this speed (see the solid curve). An approximation of the speed of the iso-density contour including the convergence effect yields a closer curve to the the observed on (see point-dashed curve). (b) Starting from the same point the integrals of the speed curves, namely the distances to the initial point as a function of time, are shown. Notice that we get a much better approximation when we add the convergence effect. All axis are in non-dimensional coordinates.

traveling time formulation for the tumor delineation. Based on the ideas presented in using [Sethian 1999], $v(t)$ can seen as

$$|\nabla T| = 1/v(t) = \left[2\sqrt{\rho\mathbf{n}'D\mathbf{n}} - \frac{3}{2T}\sqrt{\frac{\mathbf{n}'D\mathbf{n}}{\rho}}\right]^{-1} \tag{4.8}$$

where T is an implicit time function such that it embeds the locations of the tumor delineation as iso-time surfaces ($T(x)$ is the function representing the time when the tumor delineation passes over the point x). As a result of this $\mathbf{n}$ can be written as $\nabla T / |\nabla T|$ and we can write the traveling time formulation as

$$\sqrt{\nabla T' D \nabla T} = \frac{2\sqrt{\rho} T}{4\rho T - 3}, \tag{4.9}$$

where the equation has the Eikonal form (: $F \sqrt{\nabla T' D \nabla T} = 1$ with F being a general speed function.) This equation alone only gives the relation of successive iso-time surfaces of T. In order to build the solution throughout the domain we need a Dirichlet type boundary condition, namely an initial surface for which we know the T value. In the context of the tumor growth modeling this surface is given as the tumor delineation in the first image. Using this we can write the necessary Dirichlet condition as

$$T(x) = T_0 \ \forall x \in \Gamma \tag{4.10}$$

where T_0 is the initial time and Γ is the tumor delineation found in the first image. As a result the final traveling time formulation is given by the equations

$$\sqrt{\nabla T' D \nabla T} = \frac{2\sqrt{\rho} T}{4\rho T - 3} \tag{4.11}$$

$$T(x) = T_0 \ \forall x \in \Gamma \tag{4.12}$$

where in the context of tumor growth T_0 is the time elapsed since the tumor has started diffusing until the acquisition of the first image. The value of T_0 is not available in the images but as we are going to explain in Section 4.2.2 it can be regarded as another parameter of the model. Here we would like to note a limiting case of this formulation when $T_0 = \infty$. In this case we do not take into account the time convergence of the speed of the tumor delineation and model the evolution of the tumor delineation only using the asymptotic behavior of reaction-diffusion models. The limiting case formulation has the form

$$2\sqrt{\nabla T' \rho D \nabla T} = 1, \tag{4.13}$$

where the T dependence of the equation is gone. We see that if we do not consider the convergence effect and use the asymptotic speed v then T_0 is not necessary in the problem. We also observe that in the equation, ρ and D appear in the product form and cannot be separated. In this formulation the pairs ρ, D with the same product will give us exactly the same evolution of the tumor delineation.

The formulation given in Equations 4.11 and 4.12 is valid in the infinite cylinder where the evolution is in one direction (in this case the traveling wave is a plane). In the case of the growth of a tumor, the delineation is curved therefore its evolution is not similar to an evolution in the infinite cylinder. We can still apply the formulation found in the infinite cylinder to more general cases (non-planar cases) in 3D by assuming that within a voxel the tumor delineation is planar and the model coefficients are constant. Then by starting from the initial tumor delineation and sweeping the domain outwards we can construct the solution. However, such

a generalization does not take into account the effect of curvature in the more general evolutions. Several works in the literature have extended the Eikonal equations and included the effect of curvature [Keener 1998, Franzone 1990] (where they have not taken into account the effect of convergence). In this work we focus on the method proposed by Keener *et al.* in [Keener 1998]. The authors demonstrate a way to take into account the effect of curvature for slightly curved surfaces in the case of isotropic diffusion. Following the same principles we can derive the general formulation for anisotropic diffusion.

Derivation of the Effect of the Curvature for Anisotropic Tensors

Here we follow the derivation given in [Keener 1998] and modify it for the anisotropic tensor case. The reaction-diffusion model has the general form:

$$\frac{\partial u}{\partial t} = u_t = \nabla \cdot (D\nabla u) + \rho u(1 - u). \tag{4.14}$$

We apply a coordinate change by parameterizing the moving frame of the u function as

$$\mathbf{x} = X(\xi, \tau), \ t = \tau. \tag{4.15}$$

We assume that this parameterization is a diffeomorphism. By chain rule the partial derivatives using the new coordinates can be written as

$$\frac{\partial}{\partial \xi_i} \ = \ \frac{\partial X_j}{\partial \xi_i} \frac{\partial}{\partial x_j} \tag{4.16}$$

$$\frac{\partial}{\partial \tau} \ = \ \frac{\partial}{\partial t} + \frac{\partial X_j}{\partial \tau} \frac{\partial}{\partial x_j} \tag{4.17}$$

where the indices are summed (this is the case throughout this section). Likewise the partial derivatives with respect to the Euclidean coordinates can be written in terms of the new coordinate system.

$$\frac{\partial}{\partial x_i} \ = \ \alpha_{ij} \frac{\partial}{\partial \xi_j} \tag{4.18}$$

$$\frac{\partial}{\partial t} \ = \ \frac{\partial}{\partial \tau} - \alpha_{jk} \frac{\partial X_j}{\partial t} \frac{\partial}{\partial \xi_k} \tag{4.19}$$

are the partial derivatives in terms of the new coordinate system. α_{ij} is the ij^{th} component of the inverse of the Jacobian matrix with respect to the parameterization X. We identify ξ_1 as the normal direction to the isosurfaces of u at every point. We also define the tangent and the normal vectors of the parameterization as

$$\mathbf{r}_i \ = \ \frac{\partial X_j}{\partial \xi_i} \tag{4.20}$$

$$\mathbf{n}_i \ = \ \mathbf{r}_j \times \mathbf{r}_k, \ j, k \neq i. \tag{4.21}$$

Using this we can define the $[\alpha]$ matrix using these vectors:

$$\alpha_{ij} = \frac{(\mathbf{n}_j)_i}{\mathbf{r}_j \mathbf{n}_j}. \tag{4.22}$$

For the ease of derivation, through the choice of the parameterization we let $\mathbf{r}_1 \cdot \mathbf{r}_2 = 0$ and $\mathbf{r}_1 \cdot \mathbf{r}_3 = 0$ ($\mathbf{r}_1 \parallel \mathbf{n}_1$) and set it as the normal vector to the iso-surface of the u function. The derivative terms in the reaction-diffusion equation become

$$u_t = \frac{\partial u}{\partial \tau} - \alpha_{jk} \frac{\partial X_j}{\partial \tau} \frac{\partial u}{\partial \xi_k} \tag{4.23}$$

$$\nabla \cdot (D\nabla u) = \alpha_{kp} \alpha_{ij} d_{ki} \frac{\partial^2 u}{\partial \xi_p \partial \xi_j} + \frac{\partial}{\partial x_k} (d_{ki} \alpha_{ij}) \frac{\partial u}{\partial \xi_j}. \tag{4.24}$$

Then the whole equation can be written as

$$\alpha_{kp} \alpha_{ij} d_{ki} \frac{\partial^2 u}{\partial \xi_p \partial \xi_j} + \frac{\partial}{\partial x_k} (d_{ki} \alpha_{ij}) \frac{\partial u}{\partial \xi_j} \tag{4.25}$$
$$- \left(\frac{\partial u}{\partial \tau} - \alpha_{jk} \frac{\partial X_j}{\partial \tau} \frac{\partial u}{\partial \xi_k} \right) + \rho u(1 - u) = 0.$$

Here we use the two strong assumptions made in [Keener 1998]. The first assumption says that the spatial variation of ξ_1 is much smaller than for ξ_2 and ξ_3. This means that the normal to the tumor delineation changes faster than the tangent space of the parameterization. Therefore the effect of curvature is in a lower order than the speed of the moving frame. Remembering that the $[\alpha]$ is the inverse Jacobian matrix of the parameterization X this assumptions lets us say that $\alpha_{j1} = O(1)$ while $\alpha_{jk} = O(\epsilon)$.

The second strong assumption is that to the leading order in ϵ, u is independent of τ. In the planar evolution this assumption readily holds since the solution of the reaction-diffusion equation is a traveling wave and therefore does not depend on time. However, for the curved evolution this does not hold. This assumption on the dependence on τ lets us treat the curved evolution as if it admits a traveling wave. Using the singular perturbation method we can gather the first order terms and Equation 4.25 reduces to

$$\alpha_{k1} d_{k1} \alpha_{i1} \frac{\partial^2 u}{\partial \xi_1^2} + \frac{\partial}{\partial x_k} (d_{ki} \alpha_{i1}) \frac{\partial u}{\partial \xi_1} \tag{4.26}$$
$$\alpha_{j1} \frac{\partial X_j}{\partial \tau} \frac{\partial u}{\partial \xi_1} + \rho u(1 - u) = O(\epsilon).$$

Gathering the terms and recognizing the matrix multiplications this equation can be rewritten in the compact form

$$\alpha' D\alpha \frac{\partial^2 u}{\partial \xi_1^2} + \left(\nabla \cdot (D\alpha) + \alpha \cdot \frac{\partial X}{\partial \tau} \right) \frac{\partial u}{\partial \xi_1} + \rho u(1 - u) = O(\epsilon), \tag{4.27}$$

where α vector is defined as $[\alpha]_i = \alpha_{1i}$ Now in order to have a traveling wave solution this ODE should have the same form as the one in Equation 4.5. This means that we need the coefficients of this equation to be constants and satisfy the relation given as the one given in Equation 4.6. However, this will not be possible for every iso-contour of the function u. The curvature will have different effects for different

iso-surfaces. Hence, we require it only for the origin of the moving frame ($u = 0.5$ iso-contour in the case of logistic growth). Using this we obtain

$$\alpha' D\alpha = \rho \tag{4.28}$$

$$\nabla \cdot (D\alpha) + \alpha \cdot \frac{\partial X}{\partial t} = 2\rho. \tag{4.29}$$

At this point we remember that $\alpha \parallel \mathbf{n}_1$ which is normal to the iso-surface of u. We define a level set function S such that the zero-level set of S will correspond to the origin of our moving frame therefore, $\nabla S / |\nabla S| = \mathbf{n}$. We can then write α as $\alpha = -K\nabla S$ where K is just a coefficient to be determined. From Equation 4.28 we find K as

$$K = \sqrt{\frac{\rho}{\nabla S' D \nabla S}}. \tag{4.30}$$

On the other hand, the Equation 4.29 gives us

$$-\nabla \cdot (DK\nabla S) - K\nabla S \cdot X_t = 2\rho. \tag{4.31}$$

In order to replace X_t we need one more relation which comes from the fact that the value of function S at the origin of the moving frame doesn't change by construction. Therefore,

$$\frac{\partial}{\partial t} S(\mathbf{x}, t)|_{\text{on the moving frame origin}} = 0 \tag{4.32}$$

$$\nabla S \cdot X_t + S_t = 0. \tag{4.33}$$

Placing this in Equation 4.31 we obtain

$$\nabla \cdot (DK\nabla S) + KS_t = 2\rho \tag{4.34}$$

$$\nabla \cdot \left(D\nabla S \sqrt{\frac{\rho}{\nabla S' D \nabla S}} \right) + \sqrt{\frac{\rho}{\nabla S' D \nabla S}} S_t = 2\rho. \tag{4.35}$$

We transform the dynamic equation given above into a static one by inverting the embedding method explained in [Osher 1993]. We apply the following embedding and the transformation derived from it:

$$S(\mathbf{x}, t) = 0 \quad \leftrightarrow \quad T(\mathbf{x}) = t,$$
$$\nabla T \quad = \quad \frac{\nabla S}{S_t}.$$

As a result of this transformation and the embedding we obtain the anisotropic Eikonal equation with the curvature term

$$\nabla \cdot \left(D\nabla T \sqrt{\frac{\rho}{\nabla T' D \nabla T}} \right) + \sqrt{\frac{\rho}{\nabla T' D \nabla T}} = 2\rho. \tag{4.36}$$

Relocating terms we get our formulation:

$$\left\{ 2\sqrt{\rho} - \nabla \cdot \frac{D\nabla T}{\sqrt{\nabla T' D \nabla T}} \right\} \sqrt{\nabla T' D \nabla T} = 1. \tag{4.37}$$

The Equation 4.37 is derived using the asymptotic speed v, but we can also replace v by $v(t)$ and include the effect of convergence in this formulation. Adding it all together we obtain the following equation to describe the evolution of the tumor delineation in 3D based on the reaction-diffusion dynamics.

$$\left\{ \frac{4\rho T - 3}{2\sqrt{\rho T}} - \nabla \cdot \frac{D\nabla T}{\sqrt{\nabla T' D \nabla T}} \right\} \sqrt{\nabla T' D \nabla T} = 1 \qquad (4.38)$$

where the term $\nabla \cdot (D\nabla T / \sqrt{\nabla T' D \nabla T})$ is the effect of the curvature. In the derivation of this term it is assumed that the surface is slightly curved which requires the effect of curvature to be of a lower order than the term $2\sqrt{\rho}$ (the first assumption). However, the value of the curvature might be high in the general case especially in the presence of the anisotropy in the diffusion process. Therefore one would need to saturate the effect of the curvature to satisfy the assumption. In [Franzone 1990] Franzone *et al.* have overcome this problem by using a slightly different term then the curvature term derived above. Their formulation included the divergence of ∇T as follows

$$\left\{ \frac{4\rho T - 3}{2\sqrt{\rho T}} - \frac{\nabla \cdot D\nabla T}{\sqrt{\nabla T' D \nabla T}} \right\} \sqrt{\nabla T' D \nabla T} = 1 \qquad (4.39)$$

Notice that the difference between the terms is the location of the divergence operator $\nabla\cdot$. The divergence operator creates a more diffusive scheme than the curvature and therefore, we call this term as the diffusive scheme. In order to better understand the need of saturation and compare Equations 4.38 and 4.39 we analyze a specific case of growth where the analytical solution of the reaction-diffusion equation is available.

Analysis in Spherical Growth

In most cases the solution for the reaction-diffusion equation given in Equation 4.1 cannot be written analytically especially in the presence of nonlinear reaction term [Rodrigo 2003, Petrovskii 2001]. But for certain geometries and boundary conditions, analytical solutions for the *linearized* reaction-diffusion equation can be found. In this part we focus on the growth of a spherically symmetric tumor initialized as a point source in a medium with homogeneous diffusion and reaction coefficients. We examine how a single iso-density contour of this tumor evolves and compare it with the evolution described with traveling time formulation (Equation 4.38).

The exact problem we focus on is the linear reaction-diffusion equation with homogeneous parameters.

$$u_t = d\Delta u + \rho u, \qquad (4.40)$$

where d is the scalar diffusion coefficient, ρ is the proliferation rate and Δ is the Laplacian operator. For a simpler analysis we can non-dimensionalize this equation by using the transformations

$$\overline{x} = \sqrt{\frac{\rho}{d}}x, \ \overline{t} = \rho t, \qquad (4.41)$$

where the $\overline{x}$ and the $\overline{t}$ are the non-dimensional space and time variables.   Using these variables in the reaction-diffusion equation we get rid of the parameters [Murray 2002]. For simplicity we drop the line over the $\overline{t}$ and the $\overline{x}$. As a result of the transformations we obtain the non-dimensional form

$$u_t = \Delta u + u \tag{4.42}$$

$$u(x,0) = \delta(x), \tag{4.43}$$

where $\delta(x)$ is the Dirac delta function. Equation 4.43 is the initial condition which is set to be a point source. Notice the reaction term is linear which is different from $u(1 - u)$. As long as we limit our analysis in this part for low u values these two reaction terms are very similar. We also note here that the point source initialization is not realistic in the case of *in-vivo* growth. The more realistic situation would be to set a boundary condition such as

$$u(0,t) = 1, \tag{4.44}$$

which would corrrespond to the existence of a spheroid [Araujo 2004]. The diffusion then starts from the spheroid and during the diffusion the density of the spheroid would remain 1. However, the solution of this problem is harder to analyze therefore we stick to the point initialization [Rodrigo 2003, Petrovskii 2001]. Equations 4.42 and 4.43 describe a symmetric evolution therefore we can change the coordinate system into the spherical one. Using Green functions [Kevorkian 2000] the solution for this problem can be written analytically as

$$u(r,t) = \frac{1}{8\pi^{3/2}t^{3/2}}e^{\frac{-r^2}{4t}}e^t, \tag{4.45}$$

where r is the radial distance from the center. All the iso-density surfaces of this evolution are spheres moving away from the center. We can describe the motion of a single iso-density surface in terms of the radius as a function of time

$$r^*(t) = 2t\sqrt{1 - \frac{1}{t}\ln(8\pi^{3/2}t^{3/2}u^*)}, \tag{4.46}$$

where r^* is the radius of the iso-density surface with the value u^*. We observe that the evolution of the iso-density surface depends on the density value u^*. In Figure 4.4(a) we plot the $r^*(t)$ function for different values of u^*. We notice that some of these iso-density surfaces reduce in size first and then start growing. This is due to the point source initialization in the formulation given in Equation 4.43 and it is not realistic. The more realistic case for any iso-density surface would be that first it remains dormant and then starts growing. Keeping this in mind we focus on the u^* value which produces an evolution like this even in the case of point source initialization. Therefore, searching for the u^* which satisfies

$$\min\left(\frac{dr^*}{dt}\right) = 0, \tag{4.47}$$

we find $u^* = 0.0346$ and we focus our analysis on the evolution of this iso-density surface (shown in red in Figure 4.4).
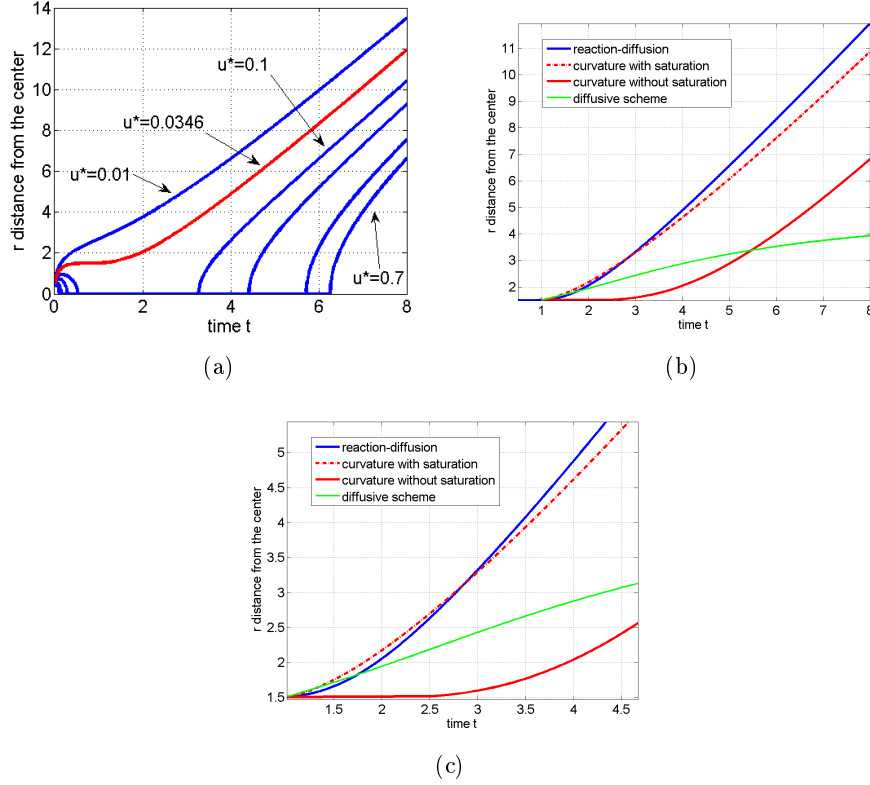
(a)

(b)

(c)

Figure 4.4: (a) $r^*(t)$ is plotted for different values of u^*. The red curve is the biologically reasonable evolution of an iso-density surface and is given by $u^* = 0.0346$. (b) In blue, the evolution of the $u^* = 0.0346$ iso-density surface is drawn. The solid red and the solid green curves are the evolutions described by the traveling time formulations given in Equations 4.38 and 4.39 respectively. The dashed red curve is the evolution obtained by saturating the effect of the curvature as in Equation 4.53. (c) We zoom in the plot (b) around the region where the tumor is smaller. In this region the diffusive scheme is close to the real evolution however, it diverges as the tumor gets larger.

The two traveling time formulations given in Equations 4.38 and 4.39 in the spherically symmetric and homogeneous parameter case take the forms

$$\left[\frac{4T - 3}{2T} - \frac{2}{r}\right] T_r = 1 \tag{4.48}$$

$$\left[\frac{4T - 3}{2T} - \frac{2}{r}\right] T_r = 1 + T_{rr} \tag{4.49}$$

respectively. In these equations T is again the traveling time function, T_r represents the derivative with respect to r and $2/r$ is the mean curvature given in terms of radius. Note that these equations are also in non-dimensional form. Equations 4.48 and 4.49 formulate the evolution of the delineation of a spherically symmetric tumor

whose real evolution is given by Equation 4.46 for $u^* = 0.0346$. In Figure 4.4(b) we plot the evolutions described by these three formulations where the traveling time formulations start from the delineation of the tumor at $t = 1$ and T_r is not allowed to fall below 0. In the figure we plot the distance of the delineation from the center of the tumor as a function of time (radius as a function of time). The blue curve is the real evolution, the red curve is the evolution under the effect of curvature as given in Equation 4.48 and the green curve is the evolution with the divergence term as given in Equation 4.49. We observe that neither of these evolutions is close to the real one. The evolution including divergence of ∇T is close to the real evolution when the tumor is small, see Figure 4.4(c), however later it diverges greatly, see Figure 4.4(b). On the other hand the evolution including the curvature is very bad when the tumor is small and it gets better in terms of slope of the evolution (speed) as the tumor gets bigger. This observation is consistent with the assumption we had done during the derivation of the curvature term in Section 4.2.1. When the tumor is small in size its curvature is high therefore our assumption of low curvature fails. In order to overcome this problem we propose to saturate the curvature effect using a saturation function

$$f(\kappa_{eff}) \quad = \quad sign(\kappa_{eff})\kappa_{sat}\left(1 - e^{-|\kappa_{eff}|/\kappa_{sat}}\right) \tag{4.50}$$

$$\kappa_{eff} \quad = \quad \frac{2}{r} \tag{4.51}$$

where κ_{sat} is the saturation value for the curvature term κ_{eff} and $sign()$ is the sign function. The exact form of the function is not very important but what is important is that at $\kappa_{eff} = 0$ the derivative of the function is 1. When we put this in Equation 4.48 and apply curvature saturation in the spherical case we obtain the final traveling time formulation in the spherically symmetric case

$$\left[\frac{4T - 3}{2T} - \kappa_{sat}\left(1 - e^{-2/(r\kappa_{sat})}\right)\right]T_r = 1 \tag{4.52}$$

Remembering that the order of $2\sqrt{\rho}$ should be higher than the curvature effect and by fitting the evolution defined by Equation 4.52 to the one defined by Equation 4.46 we find $\kappa_{sat} = 0.15(2\sqrt{\rho})$. We note that small changes on this value do not affect the evolution much. In Figure 4.4(b) we plot the evolution of the tumor delineation obtained using Equation 4.52 in red dashed curve. Again we solve this Equation starting from the tumor delineation at $t = 1$ and T_r is not allowed to fall below 0. Notice that this evolution is much closer to the real one plotted in blue than the others.

The Traveling Time Formulation for the Tumor Delineation

Adding the saturation of the curvature effect to the Equation 4.38 we obtain the final formulation which describes the evolution of the tumor delineation based on the reaction-diffusion formalism:

$$\left\{\frac{4\rho T - 3}{2\sqrt{\rho}T} - 0.3\sqrt{\rho}\left(1 - e^{-|\kappa_{eff}|/(0.3\sqrt{\rho})}\right)\right\}\sqrt{\nabla T' D \nabla T} = 1 \tag{4.53}$$

$$\kappa_{eff} = \nabla \cdot \frac{D\nabla T}{\sqrt{\nabla T' D\nabla T}} \tag{4.54}$$

$$T(x) = T_0 \ \forall x \in \Gamma \tag{4.55}$$

where we have chosen to use the exponential form for the saturation function but any other choice would work as well. In this formulation we notice that the left hand side of the Equation 4.53 can become negative especially for low values of T. This is due to the fact that the approximations for the time convergence and curvature effects get worse for lower T values [U. Ebert 2000]. In order to overcome this approximation error, in our scheme we do not let the left hand side drop lower than

$$\left\{ \frac{4\rho T - 3}{2\sqrt{\rho T}} - 0.3\sqrt{\rho} \left(1 - e^{-|\kappa_{eff}|/(0.3\sqrt{\rho})} \right) \right\} \geq \{0.1\sqrt{\rho}\}, \tag{4.56}$$

which serves as the minimum threshold for the speed of the tumor. In terms of the speed of progression of the tumor delineation, this limit can be written as

$$v_{min} = 0.1\sqrt{\rho \mathbf{n}' D\mathbf{n}}, \tag{4.57}$$

where $\mathbf{n}$ is the direction of the vector ∇T. As a result of this constraint we have a growing tumor delineation at all times, consistent with the reaction-diffusion model.

Numerical Method

Equations 4.53, 4.54 and 4.55 constitute the formulation describing the evolution of the tumor delineation in 3D. This formulation is based on the hypothesis that the tumor delineation corresponds to an iso-density surface of the tumor cell density u (the value is not specified) whose evolution is defined by the reaction-diffusion model given in Equations 4.1 and 4.2. Equation 4.53 is a static partial differential equation having a similar form as the Hamilton-Jacobi equations (see Appendix A). Several methods have been proposed to solve such equations numerically in the literature [Osher 1993, Bryson 2003, Qian 2006, Sethian 2003, Kao 2005]. In this thesis, to solve this equation numerically, we adopt an algorithm we propose in Chapter 8.

The static Hamilton-Jacobi equation given in Equation 4.11 is a first order equation and has the form of an anisotropic Eikonal equation. Just as a reminder, the anisotropic Eikonal equations have the general form

$$F(x)\sqrt{\nabla T' D\nabla T} = 1, \tag{4.58}$$

where the additional $F(x)$ is a spatially varying speed function. The numerical method proposed in Chapter 8 is dedicated to solve such equations. It is based on the Fast Marching method [Sethian 1999] and modifies it in order to take into account the anisotropy in the equation. It starts from a given initial contour and sweeps the domain outwards following the characteristic directions of the partial differential equation. The differential equation has 2 different solutions at each voxel and in this scheme we choose the value such that as we move away from the delineation the T value increases (since the tumor delineation will pass from those

points at a later time in the case where the tumor grows). The advantages of this method are that it is a sweeping method and it only uses the immediate neighbors of a point rather than using points far away [Sethian 2003] to compute the values. Therefore, it is a fast and accurate method for solving anisotropic Eikonal equations. For the details of the algorithm please refer to Chapter 8. Here, regardless of the details of the algorithm, we continue our discussion based on the fact that we have a sweeping algorithm which solves anisotropic Eikonal equations in a fast manner.

The Equation 4.38 (and the Equation 4.53) is a second order equation due to the divergence term. Hence, it is not obvious to solve it with sweeping methods. These equations can be solved with other iterative methods [Osher 1993, Qian 2006] however, these methods are not very fast. In order to benefit from the advantages of the sweeping methods we separate the curvature part from the equation and construct an iterative method that solves anisotropic Eikonal equations at each iteration with different updated speed terms. The form we use for Equation 4.38 (it is the same construction for Equation 4.53) becomes

$$\{\frac{4\rho T - 3}{2\sqrt{\rho T}} - \nabla \cdot \frac{D\nabla T}{\sqrt{\nabla T' D \nabla T}}\}\sqrt{\nabla T' D \nabla T} = 1 \tag{4.59}$$

$$\{\frac{4\rho T - 3}{2\sqrt{\rho T}} + F_{curv}\}\sqrt{\nabla T' D \nabla T} = 1. \tag{4.60}$$

Viewing the convergence term as a speed term independent of T as F_{curv} enables us to use the sweeping method and construct the simple iterative scheme

$$F_{curv}^0 = 0 \tag{4.61}$$

$$\{\frac{4\rho T^{n-1} - 3}{2\sqrt{\rho T^{n-1}}} + F_{curv}^{n-1}\}\sqrt{\nabla T'^{n-1} D \nabla T^{n-1}} = 1 \tag{4.62}$$

$$\text{Compute } T^{n-1} \tag{4.63}$$

$$C^{n-1} = -\nabla \cdot \frac{D\nabla T^{n-1}}{\sqrt{\nabla T'^{n-1} D \nabla T^{n-1}}} \tag{4.64}$$

$$F_{curv}^n = F_{curv}^{n-1} + \alpha(C^{n-1} - F_{curv}^{n-1}). \tag{4.65}$$

where $\alpha < 1$ is the parameter determining the rate of convergence which in our case is taken as $\alpha = 0.8$. In Equation 4.65 we see that the F_{curv}^n is updated with a proportional gain using the error made in the previous iteration. In this respect this scheme is similar to the feedback control loops. We iterate this algorithm until

$$\sum_{x\in\Omega} |C^n - F_{curv}^n| < \epsilon \tag{4.66}$$

where the sum represents the summation over all points in the domain of computation and ϵ is a small value. Once this criteria is satisfied we know that F_{curv} is indeed the effect of the curvature. The rate of convergence depends on α however, in our experiments we have observed that for a large range of $\alpha \in (0.2, 0.8)$ the rate is very rapid (see Figure 4.5). For lower α values the scheme takes longer time to converge and for higher values we observed oscillations therefore, the time of convergence also increased.
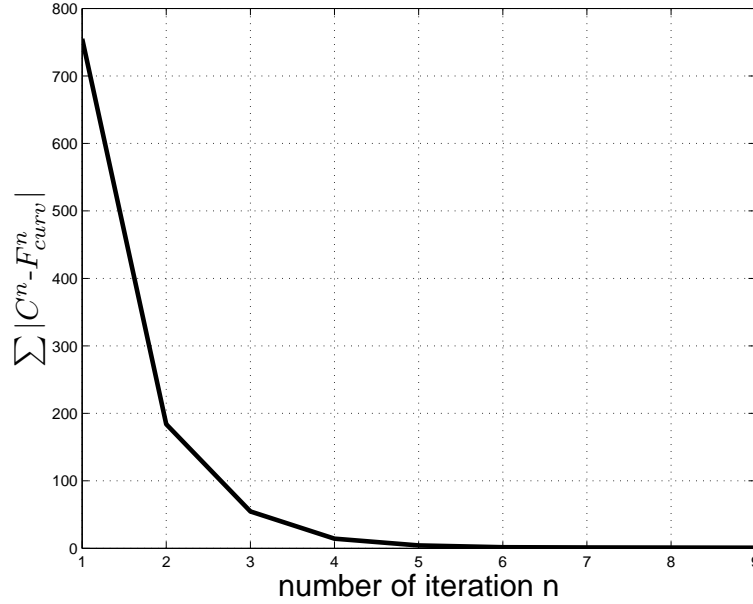
Figure 4.5: The curve showing the rate of convergence for the iterative scheme given by Equations 4.61-4.65. We visualize the difference $\sum_{x \in \Omega} |C^n - F^n_{curv}|$ as a function the iteration number n. The curve is obtained for the example shown in Figure 4.6.

The Evolution of the Tumor Delineation

The traveling time formulation given by Equations 4.53, 4.54 and 4.55 combines different approximations and due to this it does not produce exactly the same propagation as the reaction-diffusion model. In order to understand how close an evolution we obtain with two formulations we compare the evolution of the tumor delineations. First we virtually grow a synthetic tumor using the reaction-diffusion growth model. This provides us the evolution of the tumor cell densities $u(x,t)$ at every point. From the tumor cell density distribution, we extract the iso-density surface $u = 0.4$ (value consistent with the one proposed in [Tracqui 1995]) at each time instance and obtain the evolution of the tumor delineation that would be visible in medical images. In Figure 4.6 we show this evolution for one example. The white contours are the tumor delineations observed at the days 400, 600, 800, 1000 and 1200 from inwards to outwards. Following this, we set the inner white tumor delineation (delineation in the image at day 400) as the starting point for the traveling time formulation and evolve it using the same growth parameters as the reaction-diffusion model with T_0 set as 400. We obtained the black contours as the evolved tumor delineations at the same dates. The similarity shows us that in the case of images where we cannot directly apply the reaction-diffusion models, the traveling time formulation given by Equations 4.53, 4.54 and 4.55 can provide us a very good approximation of the evolution described by the model. In Figure 4.7 we also show the same evolution however, this time the curvature effect is modeled using the diffusive scheme as proposed by Franzone *et al.* in [Franzone 1990]. As explained above this scheme

includes the divergence of ∇T as given in Equation 4.39. In Section 4.2.1 we show that this scheme actually lags behind the actual evolution of the tumor delineation described by the reaction-diffusion equation. In Figure 4.7 we observe this lagging and we also note that the lag is less dramatic than the theoretical analysis due to the large size of the tumor we are modeling. In Section 5.1.1 we provide quantitative analysis of the quality of this approximation.
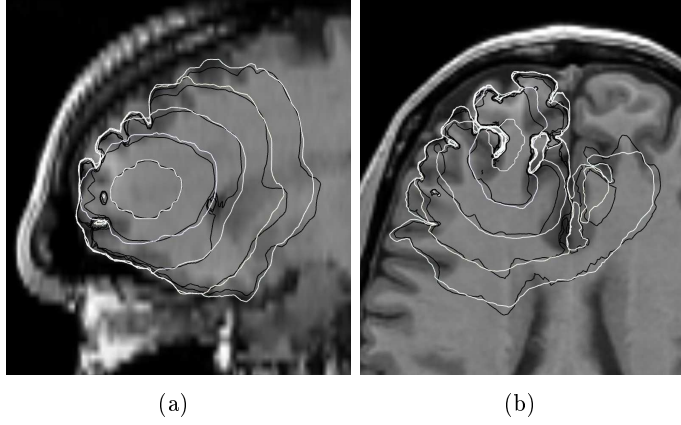

(a) (b)

Figure 4.6: The temporal evolution of the iso-density contour is demonstrated for a synthetic tumor. Contours are shown for days 400, 600, 800, 1000 and 1200 from the innermost to outermost respectively. The synthetic tumor is virtually grown using the reaction-diffusion model. White contours are obtained by thresholding the tumor cell densities at $u = 0.4$ for the respective day values (400-600-800-1000-1200). Then in order to simulate the evolution of the iso-density contour (assumed to correspond to tumor delineation in real images) starting from day=400, without the knowledge of the tumor cell density distribution we use the traveling time formulation. Black curves are the contours we obtain at days 600 (2nd innermost) to 1200 (outermost). We notice that the traveling time formulation is quite accurate in describing the evolution of the tumor delineation in the case of synthetic tumors. The tumors were grown in the images of a healthy subject for whom we also have the DT-MRIs. Parameters: ($d_w = 0.25\ mm^2/day$, $d_g = 0.01\ mm^2/day$, $\rho = 0.012\ day^{-1}$ $T_0 = 400\ days$) The number of iterations for including the curvature effect in this example was 4.

4.2.2 The Parameter Estimation Problem

The parameter estimation for the reaction-diffusion model from time series of images becomes possible once we link the evolution we observe in the images to the model. The traveling time formulation $T(x)$ serves as such a link. In the reaction-diffusion model given by Equations 4.1, 4.2 and 4.3 we have three different parameters, d_w, d_g and ρ. Moreover, in the previous section by integrating the convergence characteristics of traveling wave solutions into the traveling time formulation we added another parameter T_0. This gives us 4 parameters to estimate for: (d_w,d_g,ρ,T_0). In
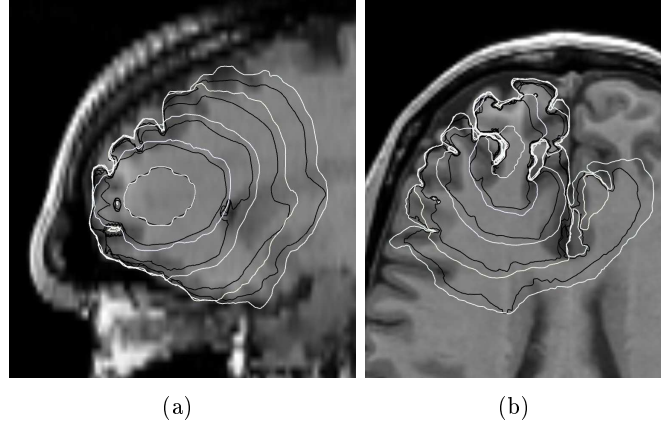
(a)   (b)

Figure 4.7: The temporal evolution of the iso-density contour is demonstrated as the one given in Figure 4.6. However, this time the effect of curvature in the traveling time formulation is taken as suggested by Franzone *et al.* in [Franzone 1990], the diffusive scheme given in Equation 4.39. We see that, as expected, the evolution of the tumor delineation described by this scheme lags behind the actual evolution given by the reaction-diffusion model. This problem is resolved by the formulation proposed in this chapter.

this work we try to optimize these parameters such that the evolution we simulate using the traveling time formulation best fits the real evolution we observe in the images, which are taken at different times for the same patient.

In order to formulate the parameter estimation problem we need to define an error measure. In a series of N images taken from the same patient at different times $t_0, t_1 ..., t_{N-1}$, we have N snapshots of the tumor delineation at different times. t_0 in this frame is the acquisition time of the first image. For a given parameter set, starting from the first time image we can simulate the evolution of the tumor delineation and compare it with the real delineations. We note that the value of t_0 is not known and regarding the time instances we only know the differences between acquisitions $\Delta t_0 = 0, \Delta t_1, ..., \Delta t_N$. Using this idea we can define

$$C_1(d_w, d_g, \rho, T_0) = \sum_{1}^{N-1} \text{dist}(\Gamma_i, \widehat{\Gamma}_i)^2 \qquad (4.67)$$

$$\widehat{\Gamma}_i = \{x | T_{(d_w, d_g, \rho, T_0)}(x) = T_0 + \Delta t_i\} \qquad (4.68)$$
$$\text{with } T(x) = T_0 \ \forall x \in \Gamma_0$$

where dist() is the symmetric distance between two surfaces normalized by the surface area of the surfaces, Γ_i is the surface enclosing the tumor in the image taken at t_i and $\widehat{\Gamma}_i$ is the tumor delineation simulated by the traveling time formulation at t_i. In this formulation we notice that T_0 is the estimate of t_0. The estimation of t_0, maps the time instances, for which we only know the successive differences, on the respective convergence curve (like the example given in Figure 4.3).

One information we have not used completely in C_1 is the size of the visible tumor in the first image Γ_0. In our experiments we observed that in order to correctly map the time instances on the convergence curve we need to include this size. The inquiry we make is whether it would have been possible to obtain Γ_0 at T_0 using the traveling time formulation if we had started from the time the tumor had started diffusing, namely $T = 0$. The assumption we make here is that the tumor started diffusing from a set of isolated small regions. These small regions actually correspond to the avascular masses that start diffusing and speed up after vascularization. In order to include this in our error measure we run the traveling time formulation backwards in time starting from Γ_0 within the delineation. We do this by solving the Equation 4.53 within the visible tumor in the first image. As explained in Section 4.2.1 we start from the delineation Γ_0 and sweep the region enclosed by Γ_0. The only difference this time is that in Section 4.2.1 the T values were increasing as we move further from the first delineation while in this case T values decrease as we go backwards in time. This backward evolution in time provides us a minimum T value, T_{min} and the corresponding point from which the tumor is assumed to start from (or a set of points) x_{min}. We notice that if the parameter set d_w, d_g, ρ, T_0 is consistent with the size of Γ_0 then $T_{min} = T_0$. Therefore the error we need is a function of $|T_{min} - T_0|$. In order to have a measure consistent with C_1 we need to convert the time difference into a spatial distance. For this we use the minimum allowable speed value (see Section 4.2.1)

$$v_{min} = 0.1\sqrt{\rho \mathbf{n}'_{max} D(x_{min}) \mathbf{n}_{max}} \tag{4.69}$$

at the point x_{min}, where $\mathbf{n}_{max}$ is the principal eigenvector of $D(x_{min})$ providing the highest diffusion rate and the factor 0.1 comes from the minimum threshold for the speed of the tumor explained in Section 4.2.1. Using v_{min} we obtain

$$C_2(d_w, d_g, \rho, T_0) = (v_{min}|T_{min} - T_0|)^2 \tag{4.70}$$

$$C = C_1 + C_2 \tag{4.71}$$

Combining C_1 and C_2 we obtain the error criteria C we wish to minimize with respect to the model parameters.

The minimization of C is a multidimensional optimization problem and it can be handled using different methods. One important criteria affecting the choice of the minimization algorithm is that explicit derivatives of C with respect to different parameters are not easily available. Another point is that although the parameters have biologically relevant bounds (such as $d_w, d_g, \rho, T_0 > 0$) this constraint is not restrictive. Based on these observations we have chosen to use the unconstrained minimization algorithm proposed by Powell in [Powell 2002], see Appendix B for details. The attractive feature of this algorithm is that it does not require derivatives of the objective function. Instead, its local quadratic approximations are used in the minimization. The algorithm requires different instances of the objective function-which are computed using the traveling time formulation-to construct the quadratic approximation and updates it as the minimization proceeds. For each instance C_1 and C_2 are computed and fed to the optimization algorithm.

4.3 The overall algorithm

Finally in this section we provide the overall parameter estimation algorithm explained in this chapter. The algorithm is composed mainly of three different parts: the traveling time formulation, the error measure and the minimization algorithm. In Sections 4.2.1 and 4.2.2 we have explained the first two parts which are our contributions. In Appendix B we briefly explain the minimization algorithm we used in this work which was proposed by Powell [Powell 2002]. The pseudocode for the parameter estimation method explained in this chapter is given in Algorithm 1 and the flowchart given in Figure 4.8.

Algorithm 1 Pseudocode for the parameter estimation methodology.

Inputs: Tumor delineations in the time series of anatomical images, DT-MRI of the patient, White-gray matter segmentation, Initial estimate of the parameters

repeat

- Construct the tumor diffusion tensors using the parameters d_w, d_g, the DT-MRI image and the white-gray matter segmentation.
- Simulate the evolution of the tumor delineation starting from the 1st image in the time sequence as explained in Section 4.2.1.
- Compare the simulated evolution of the tumor delineation with the actual delineations at the given dates (The days images where acquired). Compute $C_1 + C_2 = C$ as explained in Section 4.2.2.
- Minimization algorithm chooses a new set of parameters with which the evolution of the tumor delineation will be simulated and the error C will be computed (see Appendix B).

until Optimization algorithm converges (see Appendix B)

INPUTS:
– Tumor delineations in the times series of anatomical MRIs
– DT–MRI of the patient
– White–grey matter segmentation
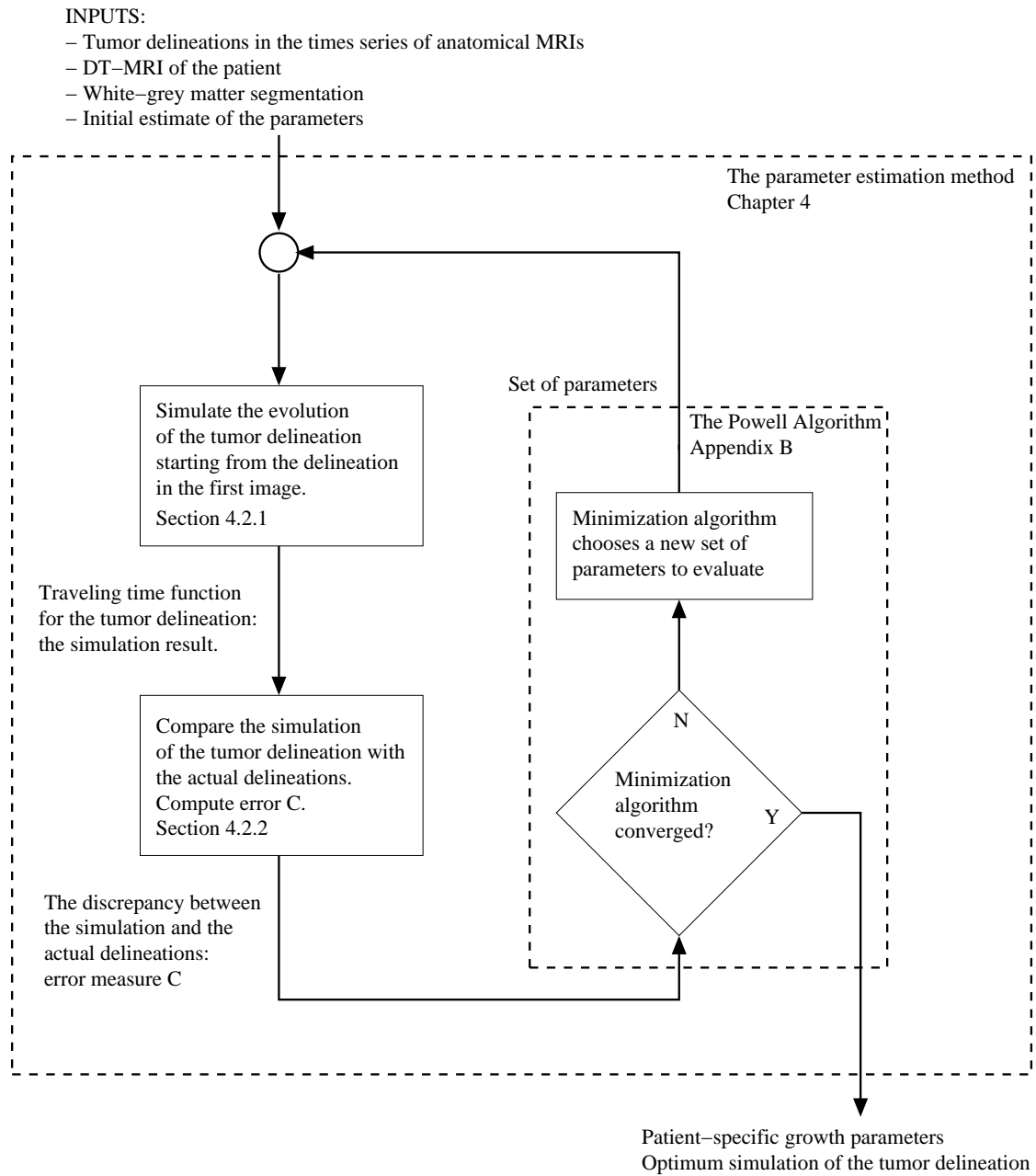– Initial estimate of the parameters

Figure 4.8: The overall algorithm of the parameter estimation method for reaction-diffusion tumor growth models.

Parameter Estimation for Reaction-Diffusion Models Using Time Series of Images: Results

Contents

Context

We devote this chapter for the experiments and analysis of the parameter estimation methodology explained in Chapter 4. In the first section we analyze the proposed methodology "theoretically" using synthetic tumors virtually grown by reaction-diffusion models. We provide a thorough analysis in order to understand the performance of the proposed method and also to understand the dynamics of the parameter estimation problem itself. In the second section we show some case studies using patient images. We show some promising preliminary results in the few cases we focus on.

5.1 Results for Synthetic Tumors

In the evaluation phase of the parameter estimation method, we test the capabilities of the method for retrieving the real parameters of the tumor growth. We first perform tests with synthetic tumors for which the parameters are known. We construct

a dataset of 180 tumors using the reaction-diffusion model composed of 60 different parameter sets at 3 different locations in the brain. The different parameter sets of the model were constructed using different combinations of d_w, d_g and ρ values given in the table below.

$d_w \; [mm^2/day]$	0.025	0.05	0.1	0.25	0.5
$d_g \; [mm^2/day]$	0.005	0.01	0.025		
$\rho \; [1/day]$	0.009	0.012	0.018	0.024	

As can be seen from the values for each parameter the final parameter sets cover a large range of growth speed and anisotropy. Each tumor was initialized in a single voxel and grown in the MR image of a healthy subject with a resolution of $1x1x2.6mm^3$. The diffusion tensor D was constructed using the DT-MRI of the same subject. In order to create the synthetic images of these tumors, we assumed a simple imaging process where a voxel is visualized as tumoral if the number of tumor cells exceeds 40% of the maximum tumor cell capacity the brain parenchyma can handle ($u > 0.4$) [Tracqui 1995]. For each tumor, the detection and the first image acquisition is made when the visible tumor size reaches a diameter of 1.5 cm. The time the tumor reaches this size depends on the parameters of the model therefore the T_0 value is different for each parameter set.

5.1.1   Comparing Traveling Time with Reaction-Diffusion

The first thing we do before starting the experiments for parameter estimation is to evaluate the resemblance between the evolution of the tumor delineation described by the reaction-diffusion equation and the traveling time formulation. In other words quantify the similarity seen in Figure 4.6. For each of the 180 synthetic tumors explained we simulate the evolution of the tumor delineation by the traveling time formulation using the exact same parameters as the reaction-diffusion equation used to grow the tumor. We initialize the traveling time formulation with the first image of each tumor and predict the tumor delineation at 200, 300 and 400 days after the detection. Then we compare the predicted delineations with the synthetic images constructed for the corresponding days. We compute the error measure C_1, which measures the symmetric distances between the real and the predicted delineations, for each of the synthetic tumors. In Table 5.1 we summarize the results of the comparison. The columns named after the parameters of the model denote all the tumors having that value for the specific parameter. For example, the cell $\rho = 0.009/day$ represents all the synthetic tumors having the ρ value as $0.009/day$. There are 15 different tumors for this specific value with different diffusion coefficients, set as combinations of different d_w and d_g values. The cell on the right hand side of the $\rho = 0.009/day$ cell shows the mean and the standard deviation of C_1 values computed for the 15 different tumors represented in that cell. The rest of the table is interpreted likewise. We notice that all the error values are around 1mm which is approximately 1 voxel. Observing the error values in this table we can conclude that the traveling time formulation describes the evolution of the delineations of synthetic tumors grown by the reaction-diffusion model very well. We did not include C_2 in this analysis because the aim of this part

ρ	C_1 [mm]	d_w	C_1	d_g	C_1
0.009	0.92 ± 0.17	0.025	0.94 ± 0.12	0.005	0.97 ± 0.16
0.012	0.94 ± 0.12	0.05	0.89 ± 0.10	0.01	0.94 ± 0.13
0.018	0.94 ± 0.10	0.1	0.85 ± 0.03	0.025	0.92 ± 0.09
0.024	0.99 ± 0.10	0.25	0.94 ± 0.07		
		0.5	1.11 ± 0.11		

Table 5.1: Resemblance between the travelling time formulation and the reaction-diffusion equation. We observe that the evolution of the tumor delineation simulated by the traveling time formulation is on the average at most $1.11mm$ away from the real delineation observed in synthetic images. Keeping in mind the resolution of the images used ($1x1x2.6mm^3$) we can say that the traveling time formulation is successful in describing the evolution of the delineations of the synthetic tumors.

is to understand how close we can simulate the evolution of tumor delineation with the right parameters of the model, which is defined by the error measure C_1.

5.1.2   Problem of Non-Uniqueness

In the first set of experiments we tried to estimate all the parameters of the reaction-diffusion model (d_w, d_g, ρ) and the first acquisition time T_0 (the time elapsed between the emergence of the tumor and its detection) using the traveling time formulation. In these experiments we observed the non-uniqueness of the solution to this problem caused by the coupling between proliferation and diffusion rates and the sparsity of the information contained in the images. The reaction-diffusion model combined with the imaging process can result in very similar evolutions of the tumor delineation with very different parameters. In Figure 5.1 we show the evolutions of two different tumors (green and red) for which the diffusion and proliferation parameters are given in the accompanying table. The contours with the same color are the delineations of the same tumor in different images taken at successive time instances. The inner contour is the delineation in the first image and the other contours as we go outwards are from the images taken at 200, 300 and 400 days after the first image acquisition respectively. We observe that although the parameters are different the evolutions are almost the same. Quantitatively, the difference between these two evolutions measured by the error criteria C (see Equation 4.71) is 0.644 mm^2. On the other hand, the closest tumor delineation evolutions we can get to these ones using the traveling time formulation with the optimum parameters have errors of $C = 1.28$ mm^2 for the red and $C = 1.29$ mm^2 for the green tumor. This shows us that with the current resolution of medical images we cannot distinguish between these two parameter sets if we observe either of the evolutions. Therefore, we leave aside the question of estimating the diffusion and the proliferation rates separately.

One observation about the values of the parameters is that between the two cases in Figure 5.1 the functions $2\sqrt{\rho d_w}$ and $2\sqrt{\rho d_g}$ remain almost the same, around 0.1 mm/day and 0.03 mm/day respectively. This is consistent with the fact that the asymptotic speed of reaction-diffusion equations are given by $2\sqrt{\rho \mathbf{n}'D\mathbf{n}}$, see

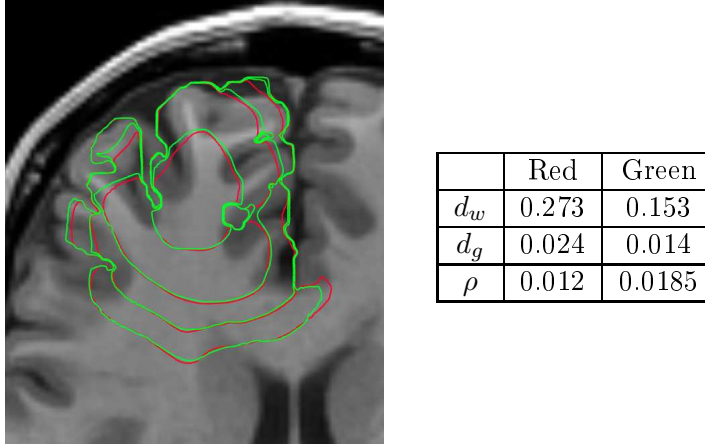|	Red	Green
d_w	0.273	0.153
d_g	0.024	0.014
ρ	0.012	0.0185

Figure 5.1: In the image we show the evolution of two different synthetic tumors virtually grown using the reaction-diffusion model with different parameters. The contours of the same color are the tumor delineations for the same tumor in 4 different images taken at 4 successive time instances (T_0, $T_0 + 200$, $T_0 + 300$ and $T_0 + 400$ days after the first image). The reaction-diffusion model parameters for these tumors are given in the table. We observe that although the diffusion and proliferation rates of these tumors are different the evolutions are almost the same. The difference between these evolutions measured using C is 0.644 mm^2 which is lower than the minimum error we find by estimating the parameters using the traveling time formulation ($C = 1.28$ for red and $C = 1.29$ for green). This shows that we cannot distinguish between these two parameter sets if we observe either of the evolutions. We also observe that the products $d_w\rho$ and $d_g\rho$ are very close for the two tumors. This tells us that although distinguishing between d_w, d_g and ρ is not obvious estimating the product of $d_{w,g}\rho$ is possible.

Section 4.2.1. Therefore, even though we cannot estimate the proliferation and the diffusion rate separately we can estimate the speed of evolution in the white and in the gray matter by fixing the value of ρ.

5.1.3   Fixing ρ and the 3 Parameter Case

Since estimating all the parameters of the reaction-diffusion equation proved itself to have a non-unique solution (under the given hypotheses) we turn our attention to the case when we can fix a parameter. The proliferation rate ρ is a microscopic parameter and its coupling with the diffusion rate creates the non-uniqueness of the solution. Here we assume that the value of ρ can be estimated using biopsy results and microscopic analysis or an average value of ρ can be provided as a result of the staging and grading of the tumor. Therefore, we can have a good estimate of ρ and fix it in the parameter estimation problem. In our analysis we assume we know the real value of ρ and fix it, once it is fixed the problem becomes solvable. In this case we are left with three parameters to estimate (d_w, d_g) and T_0.

For each of the synthetic tumors previously described we create a dataset of 3

images, the first image taken at the time of detection and two other images taken at 200 and 400 days after the detection 5.2. Using these images and the time difference between acquisitions we estimate the diffusion parameters and T_0. We show and discuss the obtained estimates based on two different analyses. The first one is the proximity of the estimated parameters to the real ones and the sensitivity which tells us if we are able to distinguish between two different tumors with close parameters. The second analysis is about the shape of the minimization surface around the estimated point. The parameter estimation method, as explained in the previous section, minimizes the objective function C. The shape of this function around its minimum shows us the feasibility of the minimization process.
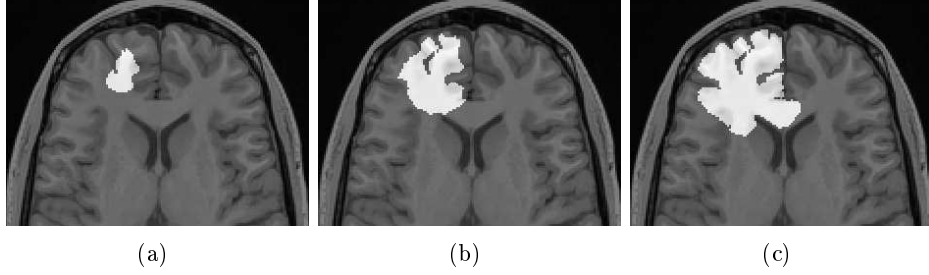

(a) (b) (c)

Figure 5.2: An example of the synthetic dataset created for each virtual tumor for the theoretical analysis of the proposed parameter estimation method. (a) Shows the 1st image acquired at the time of detection. The white region is the visible part of the virtual tumor. (b) Shows the 2nd image of this dataset taken 200 days after the first one. (c) 3rd image of this dataset taken 400 days after the first one. For illustrative purposes we show a fast growing tumor.

Analysis of the Estimated Parameters

In Figures 5.3(a) we show the estimated diffusion parameters along with the real ones. In order to demonstrate the results, we project the high dimensional parameter space onto the 2D (d_w, d_g). The larger markers in the plot represent the real parameters used to grow the synthetic tumors and the smaller ones represent the estimated parameters retrieved from the images. Each small marker with a specific shape and color is the estimate for the larger marker with the same shape and color. Although there is only one estimate for each parameter set d_w, d_g, ρ there are multiple small markers for each large marker due to projecting onto lower dimensional space. In other words, different small markers of the same shape and color are the estimated parameters of the tumors with different ρ but same d_w and d_g.

Analyzing the Figure 5.3 we observe that the parameter estimation method is able to retrieve the value of d_w with good accuracy. Moreover, the method is able to distinguish between different tumors with close diffusion coefficients. The estimation of d_g on the other hand seems to be less accurate. We notice the consistent positive bias in the estimate of d_g which increases with increasing d_w. We believe there are two reasons for this. The first one is the difference between numerical schemes we
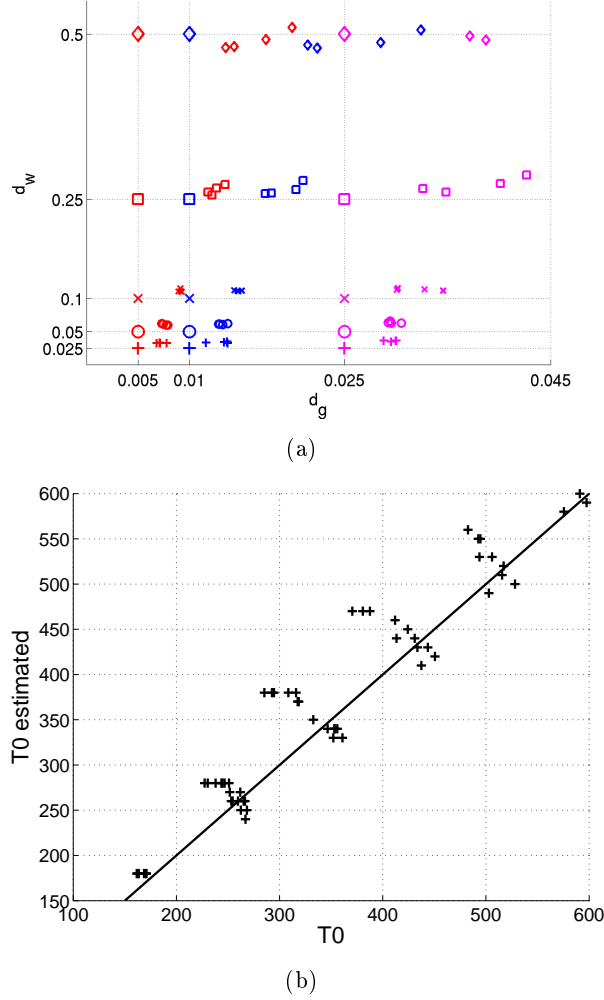
(a)

(b)

Figure 5.3: The results of the parameter estimation from time series of images for the synthetic tumor experiments. The synthetic tumors are grown with the reaction-diffusion model with known parameters and synthetic images were created from these tumors at 3 different time points (at the detection time T_0, $T_0 + 200$ days and $T_0 + 400$ days after the detection). The parameter estimation method was applied to these images to retrieve the parameters of the model. The plot (a) shows the real diffusion rates d_w and d_g (the large markers) and the estimated diffusion rates (the small markers). Small markers of a specific shape and color are the estimates of the larger marker with the same shape and the same color. Figure(b) plots the estimated initial time estimate T_0 (the time elapsed between the emergence of the tumor and the detection) vs. its real value. $y = x$ line is also drawn for better comparison.

use to solve the reaction-diffusion PDE and the traveling time formulation. The numerical scheme for the PDE [McCorquodale 2001] uses linear interpolation of the

diffusion tensors between voxels creating higher diffusion within the gray matter neighboring white matter. The traveling time formulation, which uses the diffusion tensors on the voxels, accounts for this by increasing d_g therefore estimating a higher d_g. As a result as the value of d_w increases the bias on d_g increases. The second reason is computing the curvature effect term in Equation 4.54 using the images, where the contour enclosing the tumor delineation has sharp corners (due to discretization) which causes high curvature. Since the high curvature slows down the evolution, the traveling time formulation accounts for this by increasing the diffusion coefficient. This second reason is especially observed for the tumors where d_w is low. Even in the presence of this bias we notice that for slowly diffusing tumors the d_g estimates are very close to the real values and the method is able to distinguish between different tumors with close diffusion coefficients. For highly diffusing tumors the d_g estimates are rather unreliable however the order of the ratio between d_w and d_g is well captured. Regarding the estimation of T_0, in Figure 5.3(b) we plot the estimated value of T_0 in the y-axis versus its real value in the x-axis where the $y = x$ line is also drawn. Observing this plot we notice that the estimates for T_0 remains within the 10-15% margin of the real value, which shows that the proposed method is able to retrieve T_0.

Analysis of the Minimization Surface

Regarding the shape of the minimization (error) surface on the global scale, in our experiments we observed that this surface, which is defined by 3 dimensions (d_w, d_g, T_0) namely the parameters we are minimizing for, remains convex for all the tumors. However, the exact shape of the surface and the slope of the surface in different directions around the minimum point varied. We know that the estimated parameters provide us the best fit to the evolution of the tumor delineation we observe in a set of images, let us say with an error of C^*. The question we want to answer is how much this evolution varies from the optimum when we slightly move away from the "best" parameter set. In order to answer this question, for an estimated parameter set (d_w^*, d_g^*, T_0^*) which gives a minimum error of C^* we find the other parameter sets which give an error smaller than $C^* + \epsilon$. In other words parameter sets which provides an evolution of the tumor delineation which is ϵ away from the best fit in the average. In our high dimensional parameter space these parameter sets are enclosed in an ellipsoid around the estimated point which we name ϵ-ellipsoid.

Construction of ϵ-Ellipsoids

The parameter estimation problem in this work is formulized as the optimization problem with the objective function C. For a given set of images, the method tries to find the parameters of the tumor growth model which would minimize the value of the function C. ϵ-ellipsoids is a simple way to understand the shape and the steepness of the minimization surface around the minimum point. The construction of the ϵ-ellipsoids is as follows. For a given parameter estimation problem let us say the estimated parameters p^* corresponds to an error value of C^*. As a consequence

C^* is the minimum of the objective function C for this problem. We first construct the quadratic approximation of C around p^*

$$\overline{C} = C^* + g'(p - p^*) + \frac{1}{2}(p - p^*)'G(p - p^*), \qquad (5.1)$$

where g is the gradient vector and G is the Hessian at p^*. Since p^* is the minimum we know that $g = 0$. Moreover since the point p^* is the minimum of C the G is a positive definite matrix. The construction of the quadratic approximation is done by sampling the function C and fitting a quadratic function by least square minimization.

Once the quadratic approximation of C is obtained we define the ϵ-ellipsoid as follows

$$P = \{p|\overline{C}(p) = C^* + \epsilon\}, \qquad (5.2)$$

where the set P is the ϵ-ellipsoid and p is an arbitrary parameter set. Since G is a positive definite matrix we are sure that P is a closed surface and for all the points remaining inside P, $\overline{C}(p) < C^* + \epsilon$.

Using the ϵ-ellipsoid we enclose a set of parameters (parameter sets p's) for which each parameter set produces an evolution of the tumor delineation that is ϵ close to the optimum evolution created by p^*. This means if the ϵ-ellipsoid is big for a problem then the minimization surface is flatter therefore, it is harder to find the minimum point. Moreover, the directions of the semi-major and semi-minor axis of the ellipsoid provides us the coupling between different parameters.

In Figures 5.4(a,b) we show the projections of some of these ϵ-ellipsoids (for $\epsilon = 0.1mm^2$) on the respective parameter spaces where the round dots are the actual parameters, the crosses are the estimated parameters and ellipses around each cross are the projections of the ϵ-ellipsoids.

Observing Figure 5.4(a) we notice that the major axis of the ellipses remain parallel to d_g axis however, this is due to the difference of scale between d_w axis and the d_g axis. When placed on the same scale these ellipses are rather circular. The second thing we notice is that the ellipses grow with increasing d_w. This is a consequence of using normalized distances between surfaces in our error measure, see Equation 4.67. As d_w increases the tumor diffuses faster in the white matter and its size increases. As a result the boundaries of the visible tumor reaches the extent of the white matter and most of the surface enclosing the tumor delineation in the image remains in the gray matter (as gray matter diffusion is much lower the tumor stops in the white-gray matter boundary) or reaches the boundaries of the brain. Therefore changing d_w does not affect these portions of the surface and its contribution to the error measure decreases resulting in the larger ellipses we observe. This shows us that for more diffusive tumors a larger set of parameters yields similar errors therefore minimization surface is flatter. In Figure 5.4(b) we observe the coupling between d_w and T_0. One can obtain a similar evolution by increasing d_w and decreasing T_0 (and vice-versa). The reason for this can be explained by the effect of convergence given in Equation 4.11, see Figure 4.3. We see that when T_0 is lower the speed of the tumor delineation is slower but if we increase the value of the diffusion we would obtain a similar evolution. The shape of the convergence curve
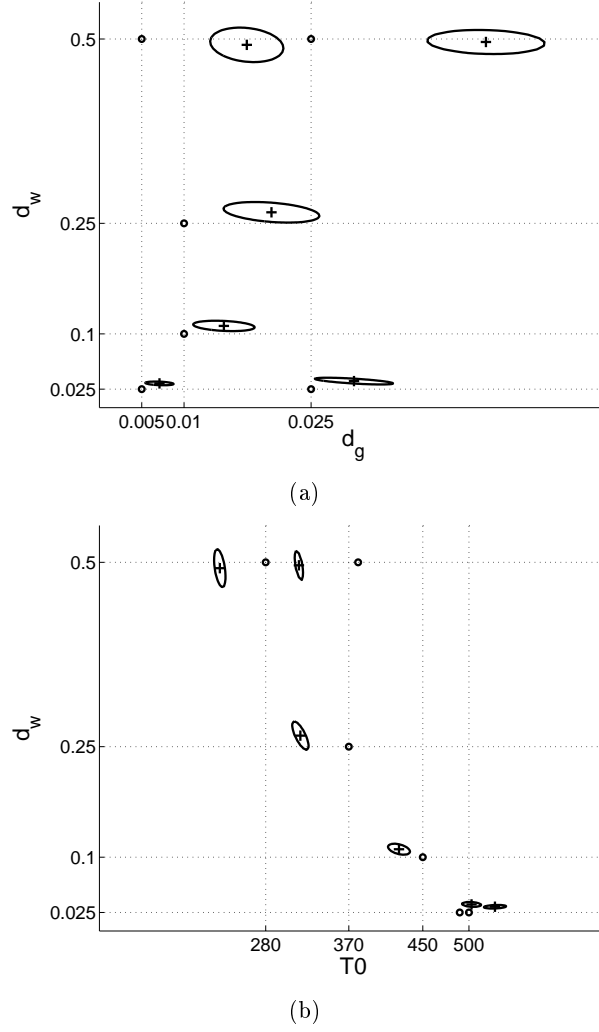
(a)

(b)

Figure 5.4: Figures plot the projections of some of the ϵ-ellipsoids on the respective parameter spaces. The round dots are the real parameters of the reaction-diffusion model, the crosses are the estimated parameters and ellipses are the projections of the ϵ-ellipsoids for each cross. For a given cross, the cross represents the minimum of the respective minimization surface with an error of C^* and all the points inside the ellipse surrounding that cross are the parameters who has error less than $C^* + 0.1$. In other words ellipses enclose all the parameters producing very similar evolutions of the tumor delineation as the cross in the center.

in Figure 4.3 allows us to distinguish between these different cases and therefore find a minimum. In Equation 4.11 we also notice that if T_0 is very high then a small change in T_0 does not affect the speed of the tumor delineation and this is the reason why we observe ellipsoids with major-axis parallel to the T_0 axis at high T_0 values. One can think of the extreme case where T_0 is very large and the effect of convergence becomes negligible. In this case we would expect its value not to

change anything however, including the size of the tumor in the first image using the error term C_2 (Equation 4.70) helps us distinguish between very high T_0 values.

5.1.4   Changing the fixed ρ and Speed of Growth

In all the above experiments we have fixed the value of ρ to its real value. Naturally the diffusion rate estimates depend on the value of ρ. Therefore, by fixing ρ we actually determine the location of the d_w and d_g estimates. In order to understand the effect of the value of ρ on the estimation of diffusion rates and the coupling between ρ and D we have performed a slightly different experiment. Instead of fixing ρ to its real value we have set it to a different value and then estimated the other parameters d_w, d_g and T_0. For the ease of demonstration we only show the estimation results for the synthetic tumors with $\rho = 0.012/day$. The experiment

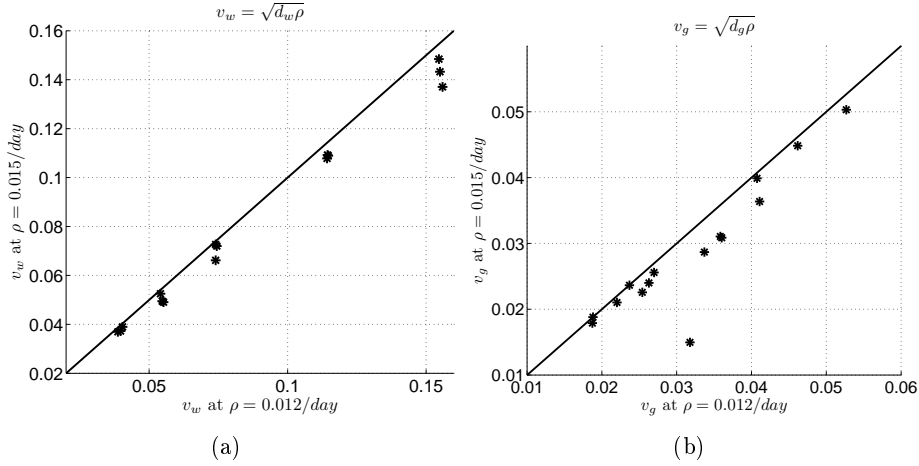(a)   (b)

Figure 5.5: In the figures we plot $v_{(w,g)} = 2\sqrt{d_{(w,g)}\rho}$ values estimated by fixing $\rho = 0.015$ versus $\rho = 0.012$. We also plot the $y = x$ line for a better comparison. We know that the estimated d_w and d_g values depend on where we fix the ρ. However, observing these figures we note that no matter what value we fix ρ to, the product of ρ and the estimated diffusion coefficient $d_{(w,g)}$ remains constant. Therefore the asymptotic speed of growth of the tumor in the white matter and in the gray matter can be estimated uniquely.

we performed is the same as the one explained in the previous section however, this time in the estimation method we set $\rho = 0.015/day$. As expected the estimated diffusion rates are lower than the values estimated by setting $\rho = 0.012/day$. The interesting point however, was not the change in the values but the coupling between D and ρ. In Figure 5.5(a) we plot $v_w = 2\sqrt{d_w\rho}$ computed with $\rho = 0.015$ and the d_w value estimated by fixing ρ to this value versus v computed using $\rho = 0.012$ and the d_w estimated with this ρ. Figure 5.5(b) is the same plot for d_g values. We observe from these graphs that the estimated diffusion rates change when we change the fixed ρ however, the product of the proliferation and the diffusion rates remain constant. The value $v = 2\sqrt{d_{(w,g)}\rho}$ is the asymptotic speed of tumor growth and

even though we cannot estimate the proliferation and the diffusion rates separately we are able to estimate v for each tumor regardless of which value we fix ρ to.

5.1.5   Reducing the Number of Images Used

In the experiments shown above we have always used 3 successive images of the same patient taken at the time of detection, 200 days after and the last one 400 days after the time of detection. In normal clinical routine the number of images does not have to be the same for each patient. The follow-up can be very irregular for some patients and the intermediate images in time might not be available. In this part we analyze the effect of the number of images used for parameter estimation on the proposed methodology. In these experiments we estimated the growth parameters (d_w, d_g, T_0) using only 2 images, one taken at the time of detection and the other one taken at the end of the study, 400 days after the time of detection. As we have done in Section 5.1.3, we analyze the estimated parameters and the shape of the minimization surface C around the estimated parameters. In Figures 5.6(a)

(a)   (b)
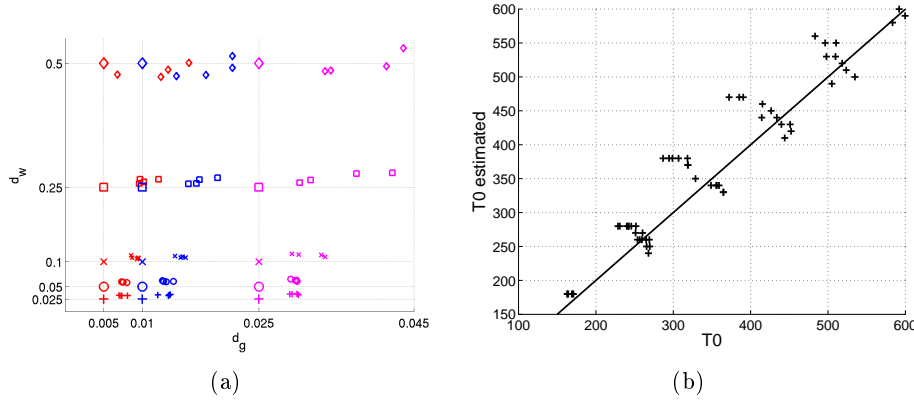
Figure 5.6: The results of the parameter estimation experiments for the synthetic tumors using only 2 successive images in time. In figures we show the same pattern as Figures 5.3(a) and (b) but the parameters are estimated using 2 images. Comparing the estimates obtained using 3 successive images in time given in Figures 5.3 and these Figures we notice that the locations of the estimated parameters are not affected by the decrease in the number of images.

and (b) we show the estimated diffusion coefficients (d_w, d_g) and the estimated initial time T_0. We observe that the locations of the estimated parameters and their relations with the real ones are very similar to the case where we have used 3 images. Between Figures 5.3(a) and 5.6(a), we observe the same positive bias in the diffusion coefficients and the same unreliability of d_g estimated when the d_w value is high. The estimation of T_0 also shows very similar behavior in Figures 5.3(b) and 5.6(b). Based on these observations we conclude that the estimated parameters are not affected by reducing the number of images used in estimation to 2.

On the other hand, the objective function C changes when the number of images changes. Therefore, the local shape of the minimization surface around the estimated

parameters change as well. In Figures 5.7(a) and (b) we plot the projections of the ϵ-ellipsoids onto the respective parameter spaces for some of the estimated parameter sets. Comparing Figure 5.7(a) with Figure 5.4(a) we observe that the size of the
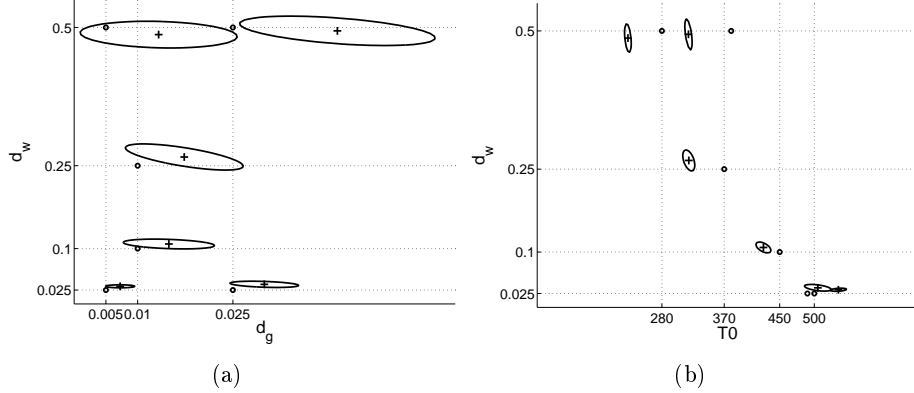

(a)   (b)

Figure 5.7: Figures plot the projections of some of the ϵ-ellipsoids on the respective parameter spaces for the experiments using only 2 successive images in time. Figures are drawn the same way as Figures 5.4 (a) and (b). Comparing these Figures with the ones given in 5.4 we observe that using more images in the estimation gives us a better confidence on the estimated parameters especially for the diffusion rates.

ellipses in the (d_g, d_w) space are much bigger in the case where we use 2 images to estimate the parameters. The uncertainty on the diffusion coefficients increased and the reliability of the parameters decreased. This observation is coherent with the general expectation that the more images we use the more reliable estimates we obtain. When we observe the Figures 5.4(b) and 5.7(b) we notice that changing the number of images also increased the size of the ellipses in the T_0, d_w space but the change is not big. The reliability of the T_0 estimate remained almost the same. From this we understand the most important factor determining the value of T_0 is the size of the tumor in the initial image. This factor was included in the parameter estimation scheme by using C_2 in the Equation 4.70 in Section 4.2.2.

5.1.6   Forgetting the Convergence Effect and T_0

The last issue we tackle in our analysis for synthetic tumors is the effect of including the time convergence and the initial time estimate T_0 on the estimated parameters. Specifically on the estimated diffusion rates. In this part we set the $T_0 = \infty$ and concentrate on the asymptotic behavior of the reaction-diffusion model. More precisely we would like to estimate the diffusion coefficients d_w and d_g using only the asymptotic speed of the tumor delineation with the formulation given in the Equation 4.13 in Section 4.2.1. In Figures 5.8 (a) and (b) we show the estimated (d_w, d_g) pairs and the ϵ-ellipsoids for these pairs. These pairs are estimated without using the time convergence of the speed of the tumor delineation. We observe that the estimated diffusion rates are much lower than the real values especially for the tumor with high diffusion rates. When the time convergence is not included we over approximate the
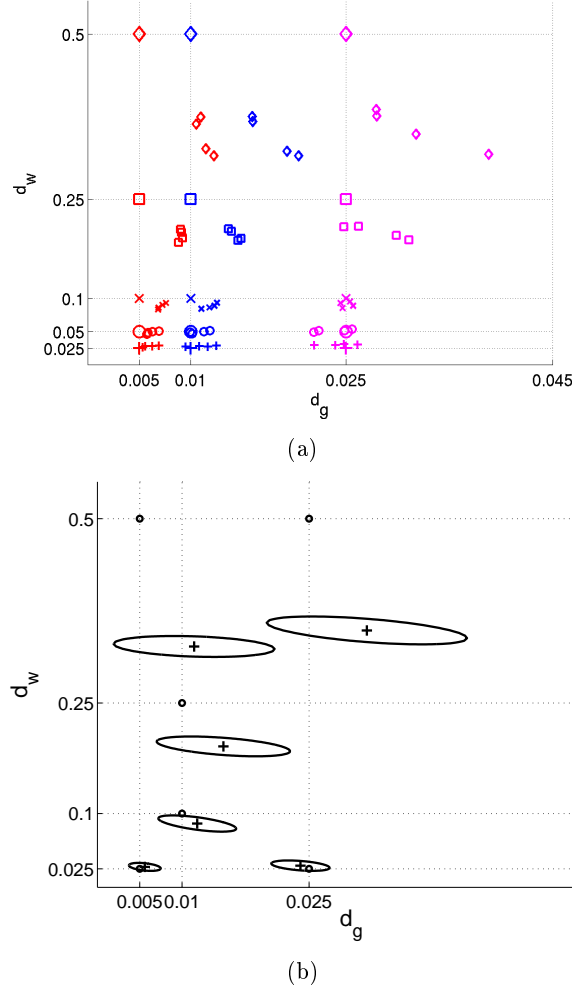
(a)

(b)

Figure 5.8: The results of the parameter estimation experiments for the synthetic tumors without including the time convergence of the tumor delineation speed and T_0. Figure (a) is plotted the same way as Figure 5.3(a). Comparing the estimates shown in Figure 5.3(a) and these ones we notice that the estimated diffusion rates are much lower when T_0 is not taken into account. This effect is especially stronger for fast growing tumors. For slowly growing tumors the change in the estimated parameters is smaller. Comparing the ϵ-ellipsoids given in Figure 5.4(a) and the ones given in Figure (b) here we see that the shape of the minimization surface is not affected by including the time convergence of the speed of growth.

speed of the tumor delineation (see Figure 4.3) and therefore in the end we obtain lower estimates for the diffusion rates. For the tumors with lower diffusion rates we observe that the effect of including the convergence is more subtle. This is due to the fact that slow tumors take longer time to grow and their initial T_0 values are already very high therefore replacing it with $T_0 = \infty$ does not affect the estimates

that much. The local shape of the minimization surface remains unchanged as observed from the shapes of the ϵ-ellipsoids. Viewing these results we conclude that for all tumors including the convergence of speed in time and the initial time estimate T_0 improves the quality of the estimated diffusion rates. On the other hand, this effect is much smaller for the slowly growing tumors whose diffusion rates are lower.

5.1.7   Different Tensor Construction

All the results above are based on the model proposed in [Clatz 2005] where the tumor diffusion tensor D is constructed as given in Equation 4.3. In this part we would like to test the parameter estimation algorithm for a different tensor construction. In the construction used above the diffusion tensor D in the white matter is obtained by scaling the water diffusion tensor with the coefficient d_w. In [Clatz 2005], using this type of construction the authors have shown high resemblance between the simulated tumor growth and the evolution of grade IV gliomas, glioblastome multiforme. In a very similar model Jbabdi *et al.* [Jbabdi 2005] have proposed to use another tensor construction to describe the evolution of low grade gliomas. In their construction they create a more anisotropic diffusion tensor D as follows

$$D(\mathbf{x}) = \left\{ \begin{array}{ll} d_g I & , \mathbf{x} \in \text{gray matter} \\ V(\mathbf{x}) \left[diag(\alpha e_1(\mathbf{x})d_w, d_g, d_g) \right] V(\mathbf{x})^T & , \mathbf{x} \in \text{white matter} \end{array} \right. , \qquad (5.3)$$

where $V(\mathbf{x})$ is the eigenvector matrix obtained by decomposing the water diffusion tensor D_{water}, $e_1(\mathbf{x})$ is the principal eigenvalue of the same tensor and α here is a normalization factor such that highest e_1 value in the brain becomes 1. The difference between this construction and the one given in Equation 4.3 is that in this one tumor cells are assumed to diffuse much faster along the fiber and they diffuse very slowly in the transverse direction. In the construction the diffusion rate in the gray matter is used also for this transverse diffusion rate. As a result of such a construction the evolution obtained is much more anisotropic and creates more "spiky" tumors, see Figure 5.9.

In order to understand the effect of using a different tensor construction on the parameter estimation methodology we have run the same set of experiments as explained above. This time however, the synthetic tumors were grown using the reaction-diffusion model that uses the tensor construction given in Equation 5.3 as proposed in [Jbabdi 2005]. All the other details of the experiments are exactly the same as the ones described in Section 5.1.3. The results of these experiments are summarized in Figure 5.10. We observe that the results are similar to the ones obtained for the previous tensor construction, see Section 5.1.3. The estimated parameters and the shape of the minimization surfaces at the estimated parameters are pretty similar with some differences. Comparing Figures 5.10 with 5.3 and 5.4 we notice that the parameter estimation method works better for the d_g in the case presented in this section. This is natural since, in the tensor construction given in Equation 5.3 the parameter d_g plays a more dominant role and affects the white matter diffusion as well as the gray matter diffusion. As a result it becomes significant and easier to estimate. The other difference we observe is at the extreme case where the white matter diffusion is very high and gray matter diffusion is

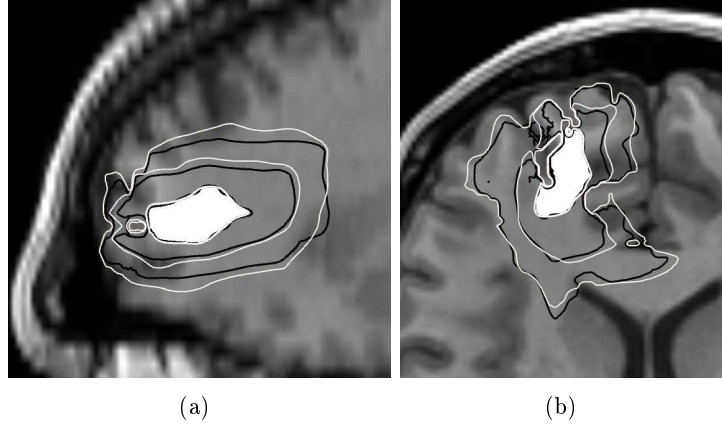(a)   (b)

Figure 5.9: The evolution of the iso-density contour in time is demonstrated for
a synthetic tumor created by the tensor construction given in Equation 5.3. The
details of the images are exactly the same as Figure 4.6. In summary the white con-
tours show the evolution of the tumor delineation in time and black contours show
the evolution simulated by the traveling time formulation. Comparing this figure
with the one given in Figure 4.6 we see that the anisotropic tensor construction yields
more "spiky" and anisotropic growth of the tumor. We also see that the traveling
time formulation is quite accurate in describing the evolution of the tumor delin-
eation in this type of synthetic tumors as well. Parameters: ($d_w = 0.25\ mm^2/day$,
$d_g = 0.01\ mm^2/day$, $\rho = 0.012\ day^{-1}$)

low. This case is observed on the upper left hand corner of Figure 5.10(a). We
see that the diffusion coefficients, especially the d_w is over estimated. The reason
for this is the effect of curvature. When the anisotropy is very high the tumor
delineation has a very spiky form and contains lots of very high curvature regions.
This behavior can be seen up to some extent in Figure 5.9. As we have explained
in the previous sections the traveling time formulation cannot capture the evolution
of very curved tumor delineations with very good accuracy. When the curvature is
too high the simulated evolution of the tumor delineation is slower than it should
be and to account for this gap the parameter estimation method overestimates the
d_w and d_g. We also observe this effect in the shape of the minimization surface in
the Figure 5.10(c). We see that at the extreme anisotropic case the minimization
surface has a very narrow and long valley in the direction of d_w. This is caused
by the saturation of the curvature effect we integrate in our method. When the
curvature is too high we saturate its effect, in other words we saturate the speed of
the front, therefore, the effect of change in d_w is reduced in the final shape causing
this long and narrow valley.

(a)   (b)
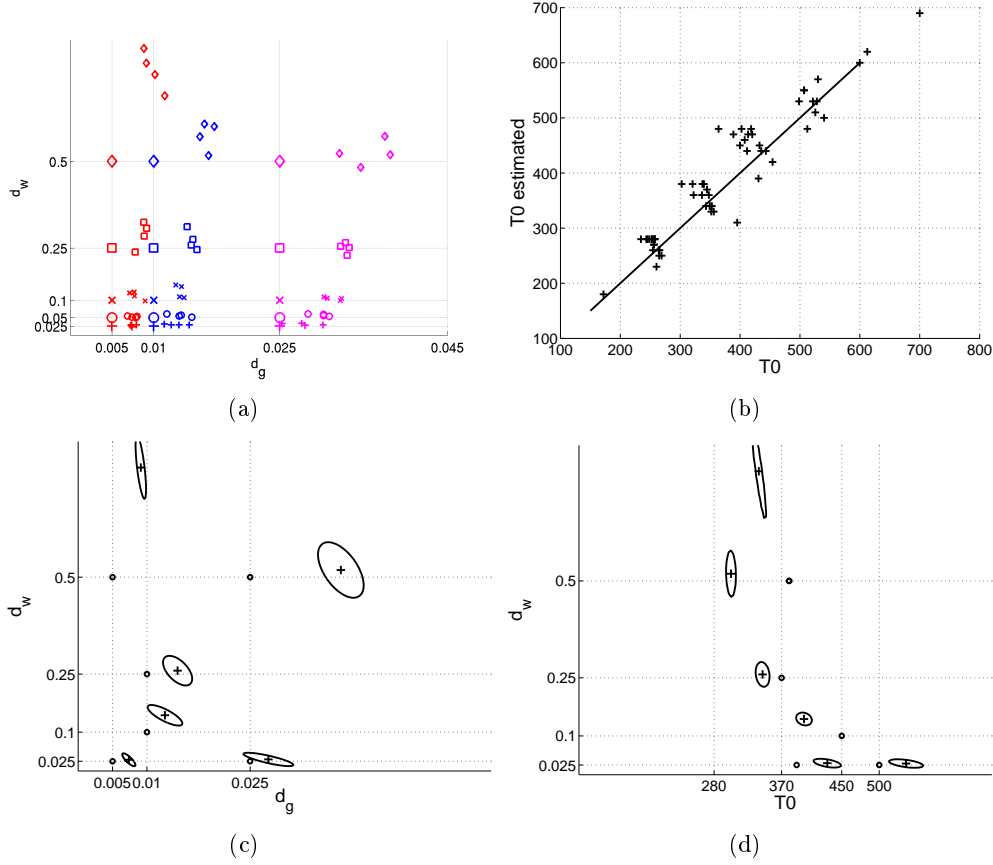
(c)   (d)

Figure 5.10: The results of the parameter estimation from time series of images for the synthetic tumor experiments using the anisotropic tensor construction given in Equation 5.3. The figures are plotted the same way as Figures 5.3 and 5.4. Comparing the Figures 5.3 and 5.4 with this one we observe overall the results are very similar. The differences are that in this case the estimation of d_g is more successful. However, in the extreme case of very anisotropic tumor (upper left corner in Figures(a) and (c)) the parameter estimation method encounters problems. This is due to the high curvature regions obtained in a very anisotropic tumor. Very high curvatures pose difficulties for the traveling time formulation of the tumor delineation as explained in Section 4.2.1.

5.2   Preliminary Results with Real Cases

The evaluation of parameter estimation for tumor growth models using real patient images is not easy because we do not have access to the real values of the parameters. The real values could be found using microscopic *in-vivo* analysis however, up to the best of our knowledge such a study has not been done yet. In this work we perform indirect evaluation for the proposed parameter estimation method using patient images. The first type of study we explain here is to use the images of a patient to find the patient specific parameters using the proposed methodology. We

compare the actual evolution of the tumor observed in the images with the evolution obtained using the optimum parameters and the traveling time formulation. The resemblance shows us how well the estimated parameters explain what is observed, Section 5.2.1. In the second type of study, for a given patient dataset, we estimate the parameters using all but the image taken at the last time point. Then using the estimated parameters, we simulate the evolution of the tumor delineation starting from the image taken just before the last one for the same number of days as the time difference between the last image and the one before it. We then compare the evolution predicted using the estimated parameters and the traveling time formulation with the one observed in the last image. The correlation between the prediction and the observed delineation provides us with a qualitative evaluation of the estimated parameters, Section 5.2.2.

Here we impose two strong assumptions. The first one is we assume that the values of the model parameters remain constant between the images. Considering therapy and other effects on the tumor this assumption is not very realistic. However, we consider the estimated parameters as the average parameters over time including all the effects and carry on with the analysis. The second point we assume is that the fiber structure of the patient will not change in time in the regions not enhanced as tumor. In other words, the local fiber structure will keep intact until the visible tumor covers them. We do not have to pay attention to the regions already covered by the tumor since these regions do not affect the further evolution of the tumor in the traveling time formulation. This assumption on the stability of the fiber structure in time is also not realistic since due to mass effect of the tumor and the undetectable infiltration the fiber structure changes. For the sake of simplicity and coherence with the available data, here we neglect this change.

As a preliminary step, in this work we use two patient datasets which include anatomical and diffusion tensor MR images. The dataset for the first patient, who suffers from a high grade glioma (Glioblastoma Multiforme), includes three T1-post gadolinium MR images (with the resolution of 0.5x0.5x6.5 mm^3) taken at successive time points. The time interval between the first two images is 21 days while the difference between the second and the third is 46 days. There also exists the diffusion tensor MR image (with the resolution of 2.5x2.5x2.5 mm^3) taken at the second time point. The second patient suffers from a low grade glioma (grade II astrocytoma) and the dataset for this patient includes T2 flair MR images (with the resolution of 0.5x0.5x6.5 mm^3) taken at 5 successive time points and a DT-MRI image (with the resolution of 2.5x2.5x2.5 mm^3) taken at the first time point. The time intervals between successive images for this patient are as follows: 38 days between the first two, 82 days between second and third, 90 days between third and fourth and 180 days between the fourth and the fifth. The DT-MRI images of the patients are used to construct the diffusion tensor D of the tumor growth model. Since we perform all our computations on the anatomical image space we register the DT-MRI rigidly to the anatomical image of the same patient. The tensor transformations are taken into account during this registration to keep the directions of the tensors physically coherent [Alexander 2001]. In constructing the diffusion tensor D for tumor cells we adapt the models proposed in [Clatz 2005] and [Jbabdi 2005]. Clatz *et al.* have proposed the tensor construction as given in Equation 4.3 for the high grade gliomas,

following this we use this type of construction for the high grade case. On the other hand, Jbabdi *et al.* proposed to use the construction given in Equation 5.3 for the low grade gliomas therefore, we use this type of construction for the low grade case.

5.2.1   Fitting the Observed Evolution

In this part, for both patient cases, we first estimate the parameters of the reaction-diffusion model using all of the patient images. Once the parameters are estimated we simulate the evolution of the tumor delineation between successive images. In other words, we initialize the traveling time formulation using the image taken at the time t_{n-1} and simulate its evolution until t_n using the estimated parameters. We then compare the evolution observed in the images and the evolution simulated using the estimated parameters and the traveling time formulation. In Figures 5.11 and 5.12 we show the patient images used in estimation and the results in terms of the estimated parameters and also the evolution described by these parameters. In both Figures each row shows the evolution of the tumor in a difference axial slices and in each column we show the images taken at different time instances. In the images we also show the manual delineation of the tumor in white and the evolution of the tumor delineation simulated using the estimated parameters in black. The estimated parameters are given in the accompanying tables. Also in Appendix C, in Figures C.1- C.3 and Figures C.4- C.8 we provide additional slices (axial) of the images given in Figures 5.11 and 5.12 respectively.

In the images of the first patient, in Figure 5.11, the tumor showed evolution in two different regions. In the first region seen on the upper left corner of the images the tumor has a much larger volume, contains a necrotic core and exerts visible mass effect. The second region, the region we apply our analysis on, on the other hand is newly emerging in the images and it does not exert observable mass effect. This part is believed to be a diffused branch of the larger region however, no connection was visible in the images most probably due to slice spacing. We apply our analysis to the newly emerging part because it does not exert a mass effect and it is ideal for our analysis. Following the discussions given in Section 5.1.2 we fix the value of ρ to be able to estimate the diffusion parameters. The proliferation rate was set at $\rho = 0.05/day$, based on the discussions with a neurosurgeon as a value around the suggested average value in the literature [Swanson 2002a]. Using the three successive images and the ρ value we estimate for the diffusion rates, which are given in the table in Figure 5.11. Observing the correlation between the dark contours and the manual delineations (white) we note that the traveling time formulation (or the reaction-diffusion model) together with the estimated parameters is in good agreement with the real evolution of the tumor. The overall shape of the tumor and the direction of its progression is well captured.

For the low grade tumor, based on our discussions with a neurosurgeon, we picked a lower proliferation rate than the one in the previous case since it is a lower grade tumor (our discussions showed that there should be an order of 10 difference). This rate was set to $\rho = 0.008/day$. This choice is rather heuristic however as we have shown in Section 5.1.4 the product of the diffusion and the proliferation rates are rather independent of the specific values. Observing Figure 5.12, we see that

| (a) Initial Image | (b) 21 days after | (c) 67 days after |

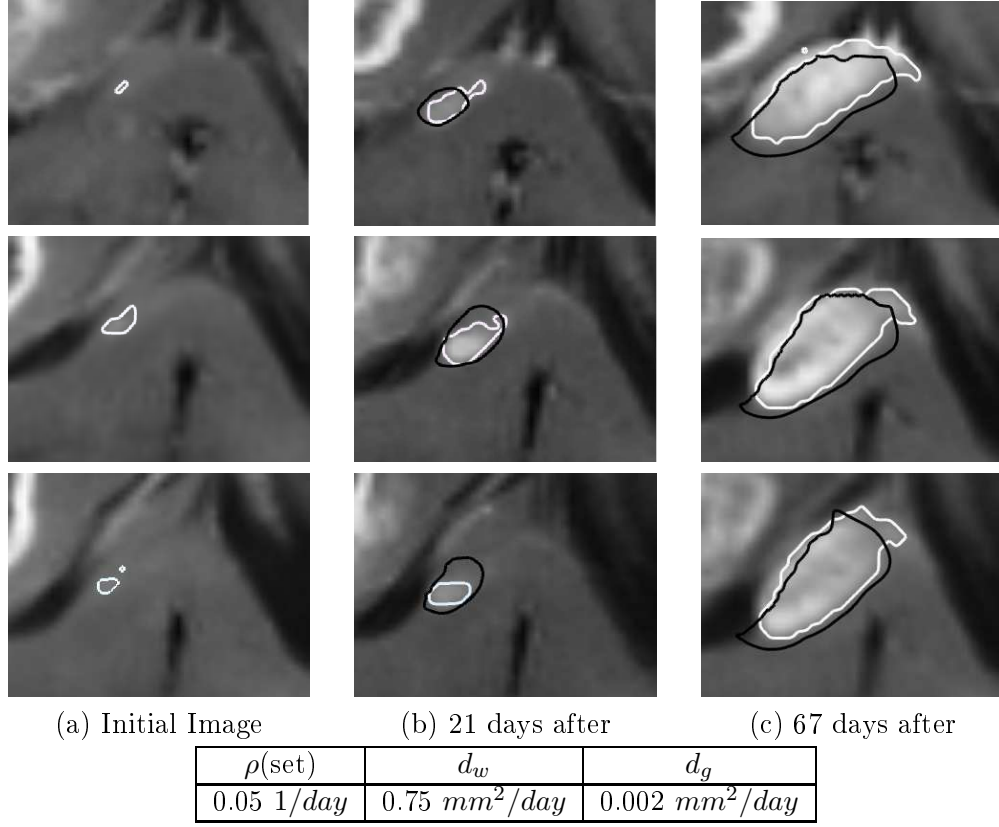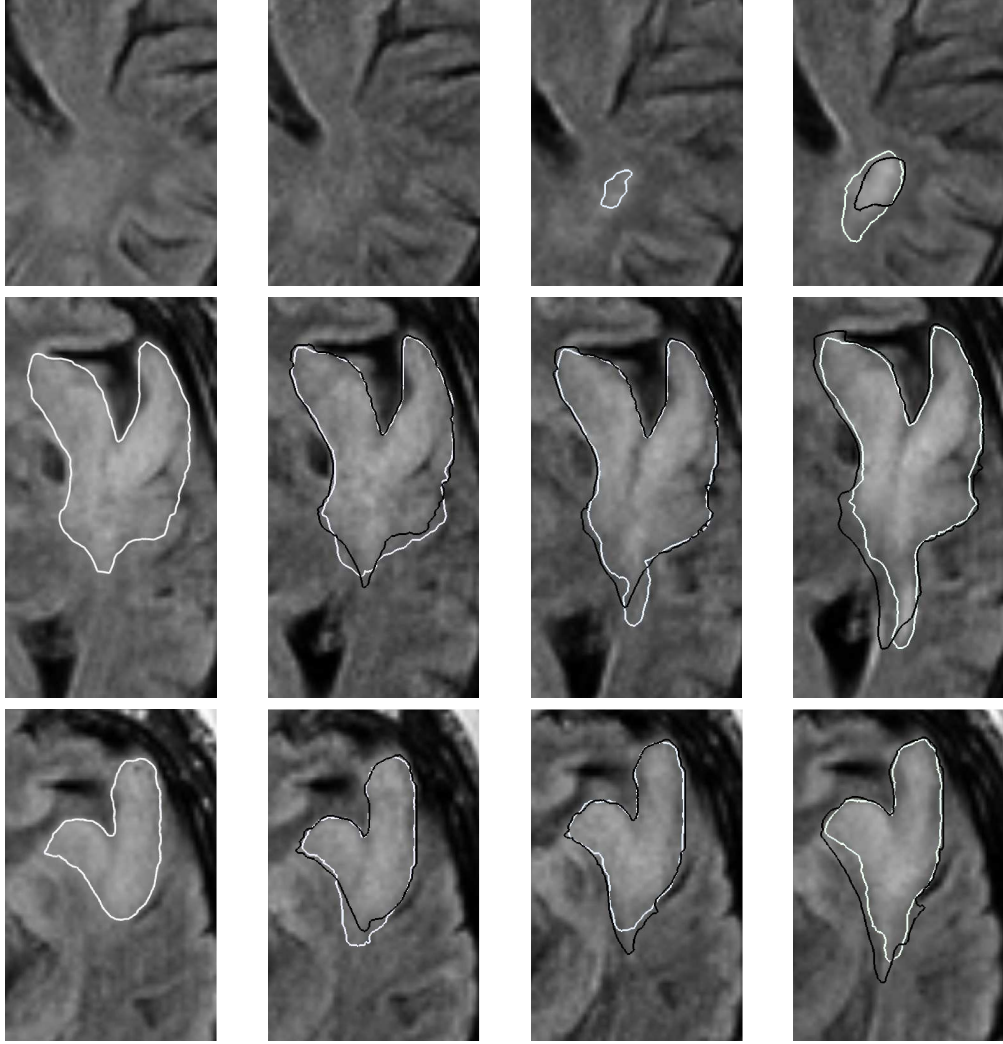| ρ(set)	d_w	d_g
0.05 $1/day$	0.75 mm^2/day	0.002 mm^2/day

Figure 5.11: The parameter estimation method is applied to the images of a patient suffering from a high grade glioma. In columns we show the images taken at different times and in rows we illustrate different axial slices of the same image. We observe the evolution of the tumor, where the manual delineations are also contoured in white. Using these images we estimate the parameters of the reaction-diffusion model as given in the table. We also show the evolution of the tumor delineation simulated using the traveling time formulation and the estimated parameters in black. We observe that the simulated evolution well captures the real evolution of the tumor visible in the images.

the correlation between the evolution of the tumor delineation simulated with the estimated parameters (in black) and the observed evolution (in white) confirms our previous arguments. The direction of the progression and the overall shape is well captured using the optimum parameters and the traveling time formulation. We also notice the differences between the diffusion rates for the high grade tumor and the low grade one (although different tensor constructions were used for the two tumors). The estimated speed of evolution in the white matter for the high grade glioma is $v_w = 0.39 \ mm/day$ while for the low grade one it is $v_w = 0.07 \ mm/day$. We also see a similar difference for the speeds in the gray matter.

(a) Initial Image   (b) 120 days after   (c) 210 days after   (d) 390 days after

ρ(set)	d_w	d_g
0.008 $1/day$	0.165 mm^2/day	0.0005 mm^2/day

Figure 5.12: As a second case we applied our methodology to the images of a patient suffering from a low grade tumor. The images and the contours are plotted the same way as the Figure 5.11. Here we also observe that the real evolution of the tumor visible in the images is well captured by the estimated parameters and the traveling time formulations.

5.2.2   Predicting Future Evolution Beyond Observed Image Data

In the second type of experiments with the patient images, we tested if the estimated parameters combined with the model are able to predict the further progression of the tumor. As explained, for this purpose we estimate the parameters of the tumor growth model using all but the image taken at the last time point. Then we simulate

the evolution of the tumor delineation in the image taken one before the last using the estimated parameters. We run the simulation until the acquisition time of the last image and compare this evolution with the visible tumor. In Figures 5.13 and 5.14 we show the results of this prediction along with the estimated parameters (in the accompanying table). The top rows show the axial slices of the image taken just before the last one where the manual delineations are also overlaid in white. On the bottom rows we show the slices of the image taken at the last time point along with the predicted (in dark) and the actual tumor delineation (in white). As in the previous section, in Appendix C we show additional slices (axial) of the images given in Figures 5.13 and 5.14 in Figures C.9- C.10 and in Figures C.11- C.12 respectively.

(a) The image taken at the time just before the last acquisition

(b) The last image: Taken 46 days after the one above.

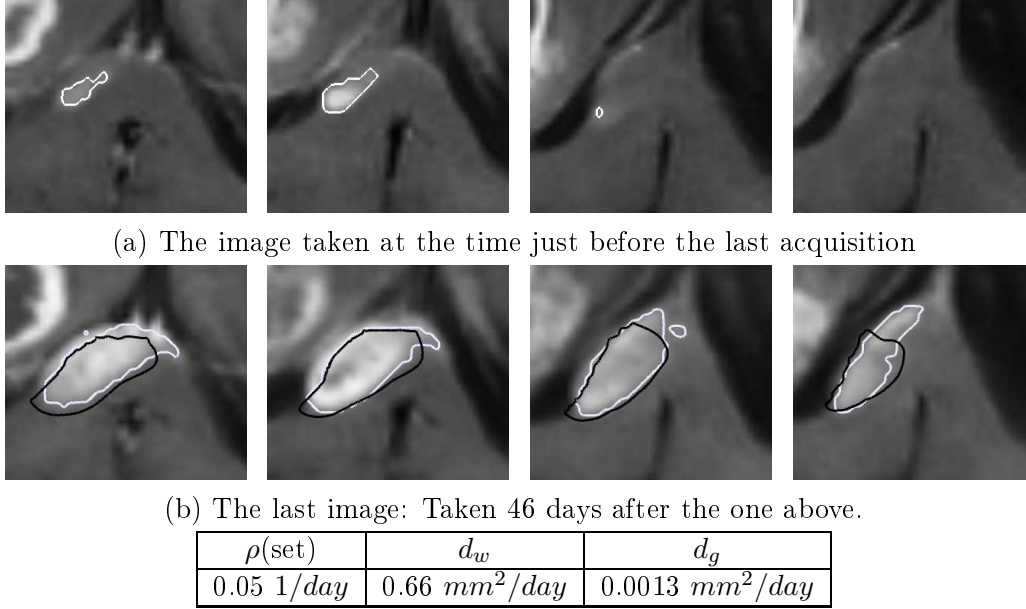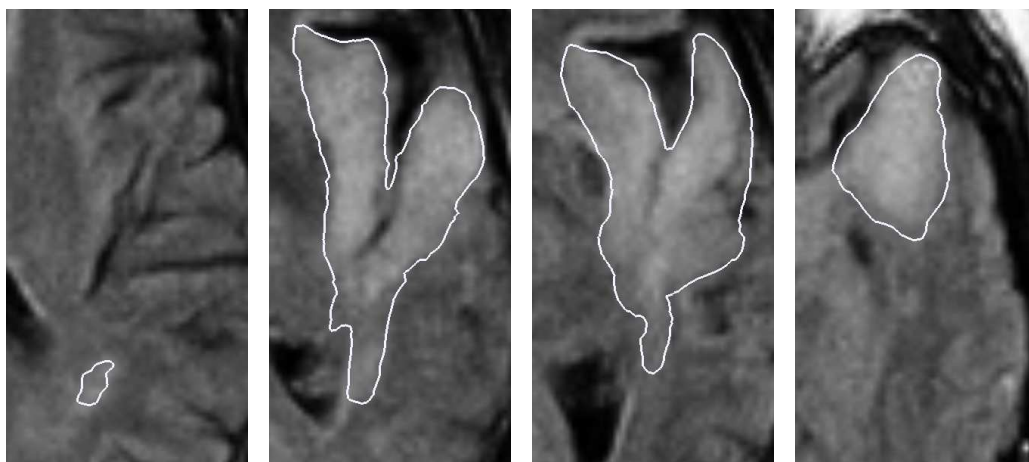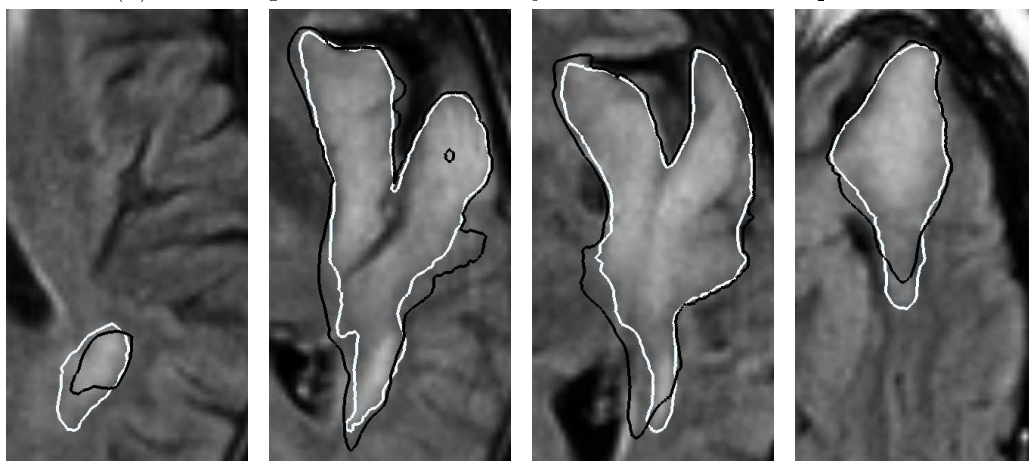| ρ(set)	d_w	d_g
0.05 $1/day$	0.66 mm^2/day	0.0013 mm^2/day

Figure 5.13: Predicting the further evolution of the tumor for the high grade case: In the top row we show the image taken one time step before the last image with the tumor manually delineated in white. The bottom row shows the images taken at the last acquisition time showing the state of the tumor also delineated in white. In black we show the state of the tumor delineation predicted starting from the image at the top row using the estimated parameters and the traveling time formulation. As explained in the text, the parameters used for this prediction were estimated using only the first two images in time and not the last one. The overlays of the real and predicted tumor boundaries illustrate the degree of agreement of our modeling scheme.

In the case of the high grade glioma, Figure 5.13, the predicted delineation of the tumor is in good agreement with the actual delineation. We observe that although we start simulating the growth from a small tumor, the parameters and the traveling time formulation captures the rapid progression of the glioma. This tells us that overall average dynamics of the evolution are well captured with the

estimated parameters. We see a very similar result for the low grade glioma as well, see Figure 5.14. In this case the tumor already has a large volume at the time we start the simulation. The progression of the tumor is very spiky and it is along the direction of the fiber tracts. We observe that the predicted tumor delineation also shows this behavior illustrating good agreement with the actual progression.

(a) The image taken at the time just before the last acquisition

(b) The last image: Taken 180 days after the one above.

ρ(set)	d_w	d_g
0.008 $1/day$	0.20 mm^2/day	0.0007 mm^2/day

Figure 5.14: Predicting the further evolution of the tumor for the low grade case: The images are shown in the same manner as the Figure 5.13. We see that amount of growth and the spiky nature of the evolution of the tumor is well predicted.

5.3 Conclusions

In the previous we proposed and analyzed a parameter estimation methodology for the reaction-diffusion tumor growth models in the context of brain gliomas. The proposed methodology formulates the evolution of tumor delineations in the medical images based on the dynamics of the reaction-diffusion model. As a consequence, it does not use the information of tumor cell density distribution throughout the brain. In this respect the method is consistent with the information available in the images.

We analyzed the proposed algorithm using synthetic tumors for which the growth model parameters are known. The reaction-diffusion model used here includes 3 different parameters: the diffusion rate in the gray matter d_g, the diffusion rate in the white matter d_w and the proliferation rate of tumor cells ρ. In our analysis we have shown that these parameters are coupled and therefore there is not a unique solution constrained by the observations made on medical images. However, we have shown that once the proliferation rate ρ is fixed, we can uniquely estimate the diffusion rates in gray matter d_g and in white matter d_w. Moreover, in this case we can also estimate the time elapsed between the emergence of the tumor and its detection, T_0. In fixing ρ we assumed that its value can be found through microscopic analysis of biopsy results. We have also shown that the value of ρ determines the estimates of the other parameters. In that sense fixing ρ means determining the values of the other parameters especially the diffusion rates. Investigating the coupling between diffusion and the proliferation rate we have shown that no matter what ρ value we fix the product of the estimated diffusion rates with ρ remains constant for the same tumor. Therefore, using the proposed method the speed of growth of the tumor, which is given by the mentioned product, can be estimated uniquely for each tumor.

In our experiments we analyzed the effect of the number of images used in estimating the parameters. We have seen that the diffusion coefficients and the initial time estimate T_0 can be estimated (by fixing ρ) using 2 images of the same patient taken successively in time. Using more images does not change the location of the estimates however it increases the reliability of the estimates and our confidence on them.

We also applied our method to two real cases, one high grade glioma and one low grade. We have estimated parameters for these tumors and performed indirect evaluations by prediction of growth showing promising preliminary results. The strongest assumption we made during this analysis was that the parameters of the growth model do not change in time and they do not vary in space. This is not very realistic for the exact values of the parameters considering the existence of different types of therapies and the random nature of the tumor progression. On the other hand, independent parameter estimation and analysis could be done between each set of two successive images as well. Such an analysis combined with the time course of the therapy could give us hints on the effect of the therapy on different parameters and on the growth speed of the tumor.

In the methods proposed in this thesis, as a first step, we ignored the mass effect of the tumor. In most glioma cases the mass effect is apparent, smaller in the low grade gliomas and larger for the higher grades. For a complete modeling in the

parameter estimation methodology the mass effect should be taken into account.

Eventually a more thorough analysis of the estimated parameters and the estimation methodology should be performed using a large dataset of patient images. In the follow-up of this work we plan to focus on this direction. There are several problems that should be overcome for this purpose. The first problem is the lack of diffusion tensor imaging for the patients. As we have seen the DTI is very important in the modeling and in the estimation of the parameters therefore, it is crucial to have this information. The advances in the registration methods can be helpful to solve this problem as they would give us the opportunity to register DT-MRI atlas on the patient images. The second problem is regarding the surgery applied in glioma cases. The surgery changes the structure of the brain as well as the properties of the tumor. In order to overcome this problem, we need to adjust the traveling time formulation such that it can describe the evolution of the tumor delineation between pre-op and post-op images.

In terms of clinical use, estimated parameters, especially the speed of growth which can be estimated uniquely, can serve as a quantification measure for tumor growth and help the diagnosis process. Moreover, the proposed methodology gives us the opportunity to construct *patient-specific* tumor growth models. Through personalizing the generic growth models, we can describe the specific evolution of a patients tumor. Such patient-specific models can be used to better plan the therapy process and predict possible outcomes of the therapy administered to the patient.

Extrapolating Glioma Invasion in MR images: Method

Contents

Context

In the treatment of brain gliomas, especially in the planning of radiotherapy, medical images such as magnetic resonance (MR) and computed tomography (CT) images play a crucial role. They provide information on the spatial extent of the tumor. However, images can only visualize parts of the tumor where cancerous cells are dense enough, masking the low density infiltration. In radiotherapy, the approach taken to handle this problem is to irradiate the visible tumor plus a 2cm constant margin around it. This approach does not take into account the growth dynamics of gliomas, particularly the differential motility of tumor cells in white and in gray matter. In this chapter, we propose a novel method for estimating the full extent of the tumor infiltration starting from its visible mass in the patients' MR images. We derive a formulation starting from the reaction-diffusion based tumor growth models, explained in the previous chapter. By using asymptotic properties of these models, we obtain an extrapolation method that constructs the tumor cell density distribution beyond the visible part of the tumor in the images.

6.1 Introduction

For the diagnosis and the therapy of gliomas, clinicians rely on medical images, such as Magnetic Resonance (MR) and Computed Tomography (CT) images, which show the mass part of the tumor. As explained in Chapter 2, current imaging techniques are not able to expose the low density infiltration [Tovi 1994, Johnson 1989, Tracqui 1995, Swanson 2004] posing a problem for the experts in outlining the whole tumor and in understanding its extent. Figure 6.1(a) is an example of a T2 weighted MR image of a patient with grade IV glioma. The image shows the two clinical target volumes (CTV) used in radiotherapy, the bulk tumor (CTV1)

and the tumor infiltrated edema (CTV2) enclosed in black and white delineations respectively [Seither 1995]. Figure 6.1(b) on the other hand, shows the hypothetical tumor profile along the white line drawn on the MR image. In radiotherapy, this problem of visualizing low density infiltration is addressed by outlining the CTV2 and assuming the whole tumor infiltration is contained within a constant margin of 2cm around that volume [Seither 1995, Kantor 2001]. Therefore, the irradiation region is constructed accordingly. This approach however, does not take into account the infiltration dynamics of gliomas, particularly the higher motility of tumor cells in white matter compared to gray matter [Giese 1996]. As a result, the irradiation region ignoring these dynamics might not reach the full extent of the tumor infiltration in white matter and irradiate healthy gray matter. Mathematical tumor growth models can offer solutions to this problem by integrating clinical information and theoretical knowledge about tumor cell dynamics [Swanson 2002b, Stamatakos 2006a, Stamatakos 2006b]. Here we describe a new formulation which aims to solve the problem of estimating tumor cell density distribution beyond the visible part in an image (low density infiltration) for gliomas. It uses the anatomical MR images and diffusion tensor imaging (DTI) to suggest irradiation margins taking into account the growth dynamics.

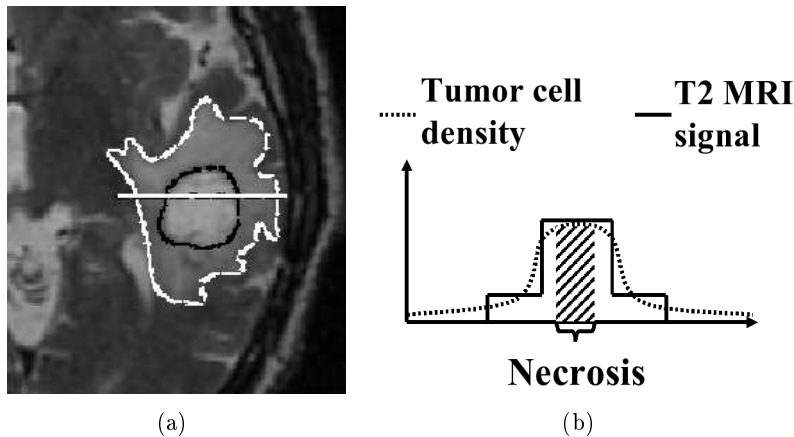(a)   (b)

Figure 6.1: (a) T2-weighted MR image showing a high grade glioma. Two clinically important volumes, the bulk tumor (CTV1) and the infiltrated edema (CTV2) are enclosed in black and white contours, respectively. (b) Distribution of tumor cell density is given by the dashed curve. T2 weighted MRI signal intensity on the other hand is given by the solid curve. The MR signal does not reveal the presence of tumoral cells when their density is below a certain threshold.

The literature on predicting irradiation margins on medical images using automatic methods is rather limited. In [Kaspari 1997], Kaspari *et al.* used artificial neural networks to model statistically the way the radiotherapist constructs the irradiation margin. In their work they focused on predicting margins as constructed by the radiotherapist not including the growth dynamics of gliomas. Zizzari *et al.* started from the same framework and included mathematical growth models in their

prediction of the irradiation volume [Zizzari 2004]. They use their model to predict further growth of the tumor and then use this prediction to construct the irradiation margins through artificial neural networks. However, these works do not focus on the spatial distribution of tumor cells at a given time and they do not include the differential motility of glioma cells in different tissues.

In this chapter, we propose a formulation to extrapolate the tumor cell density distribution of diffusive gliomas beyond their visible mass in MR images taking into account the growth tendencies of the tumor. In the previous chapter we have seen that we can personalize reaction-diffusion type growth models by estimating their patient specific parameters. Based on this, to derive our formulation we started from these type of growth models as given in [Clatz 2005, Jbabdi 2005]. Applying reaction-diffusion models to solve the previously mentioned problem poses several difficulties. As we encountered in Chapter 4, in order to perform simulations, reaction-diffusion models require the knowledge of tumor cell densities at every point in the brain while in reality only CTV1 and/or CTV2 contours are observable in the images. We have seen that this problem can be solved using the traveling time formulation explained in the previous chapter. The other problem is that the reaction-diffusion models describe the time evolution of tumor cells, however, the problem we are tackling is static, dealing with the distribution of tumor cells at a single time instance. As in the previous chapter, we use asymptotic approximations to overcome these difficulties and derive a static formulation to solve the problem of estimating low density infiltration of gliomas in an image. The proposed method starts from the delineation of the tumor in the image (manual delineation or automatic segmentation) and constructs an approximation for the tumor cell density distribution beyond the visible part taking into account the underlying tissue characteristics by using anatomical and diffusion tensor images. With such a formulation, we aim to construct irradiation margins that would be more efficient in targeting tumor cells and reducing the irradiation of healthy brain tissues.

In Section 6.2, we explain the reaction-diffusion type models in detail and derive our formulation. Subsequently, in chapter 7 we assess the quality of the approximation constructed by the proposed formulation using virtual tumors. In addition to that, we use our formulation to construct a variable irradiation margin and compare it to the conventionally used constant irradiation margin in terms of number of tumor cells and volume of healthy tissue targeted in the case of synthetic tumors. In Section 7.4 we conclude by summarizing the work with our results and provide future directions.

6.2 Method

In this section we use asymptotic approximations to derive a formulation based on reaction-diffusion models which offers a solution to the problem of visualizing low density infiltration. In Chapter 4 we have studied some of the asymptotic properties of reaction-diffusion models. We have focused our attention on the speed of the tumor delineation. Here we are going study other aspects of the asymptotic properties and focus on the shape of the tumor distribution below a certain density

value. As in Chapter 4 we assume that the iso-density surface at this density value corresponds to the tumor delineations observed in the images. Therefore, our focus in this section will be on the tumor cell distribution beyond the tumor delineation in the images.

Before we delve into details let us mathematically formulate the problem we solve. Reaction-diffusion growth models describe the temporal change of tumor cell densities denoted by $u(\mathbf{x}, t)$ at every point in the brain (u can also be inferred as the probability of finding tumor cells). In terms of u, the imaging process of gliomas can be modeled with a simple Heaviside function as done in the previous works [Swanson 2002b, Tracqui 1995] and the previous chapter:

$$Im(u(\mathbf{x}, t)) = \begin{cases} 1 & \text{if } u \geq u_0 \\ 0 & \text{if } u < u_0 \end{cases} \tag{6.1}$$

where Im is the imaging function and u_0 is the detection threshold. A detection threshold u_0 is given for CT images in [Tracqui 1995], and based on the coherence of observations obtained from MR images, radiologists assume a similar threshold. As we have done in the previous chapter, here we use the same threshold as proposed in [Tracqui 1995], $u_0 = 0.4$. In this setting, the problem of extrapolating low density infiltration of a tumor, starting from the visible part in the image taken at a time instant $t = t_0$ can be described as constructing an approximation

$$u(\mathbf{x}, t_0) \approx \tilde{u}(\mathbf{x}) \; \forall \; \mathbf{x} \in \{\mathbf{x} | Im(\mathbf{x}) = 0\}. \tag{6.2}$$

This equation basically states that $\tilde{u}$ approximates the actual tumor distribution u at the time instant t_0 in the regions where the image is not visualizing the tumor. Unlike the reaction-diffusion models, which are **dynamic** and describe time evolution of gliomas, the construction of this approximation is a **static** problem. Moreover, in the clinical situations the value t_0, which indicates the time elapsed between the emergence of the tumor and the imaging, is not available. Therefore, the approximation $\tilde{u}$ should not depend on t_0.

In the following sections we derive a formulation for constructing the approximation $\tilde{u}$ which is the proposed solution to the problem of extrapolating low density infiltration for gliomas. As in the previous chapter we focus on the reaction-diffusion model proposed in [Clatz 2005]. However, we note that the same formulations and analysis can be carried over to other types of reaction-diffusion models such as [Swanson 2002a, Jbabdi 2005].

$$\frac{\partial u}{\partial t} = \nabla \cdot (D(\mathbf{x}) \nabla u) + \rho u (1 - u) \tag{6.3}$$

$$D \nabla u \cdot \overrightarrow{n}_{\partial \Omega} = 0, \tag{6.4}$$

$$D(\mathbf{x}) = \begin{cases} d_g I & , \mathbf{x} \in \text{gray matter} \\ d_w D_{water} & , \mathbf{x} \in \text{white matter.} \end{cases} \tag{6.5}$$

We have seen in the previous chapter that the parameters of the model d_w, d_g and ρ can be identified up to some extent for each patient using time series of images. In this chapter we assume that these parameters are found and we continue our study

from there on. However, even if the parameters are not known (the case where there is only one image of the patient) the proposed method aims to provide the radiotherapist a tool with which he/she can visualize different possible distributions by playing with the parameters. We also remind that ρ and D of the model cannot be identified separately using time series of images 5.1.2. We take into account this ambiguity in our analysis and study its effect.

6.2.1 Tumor Cell Density Extrapolation

The asymptotic properties of reaction-diffusion equations explained in the previous chapter help us construct the approximation we seek for, $\tilde{u}(\mathbf{x})$. We use the existence of an asymptotic traveling wave to extrapolate the low density infiltration regions of diffusive gliomas. We know that the reaction-diffusion equations admit traveling wave solutions under homogeneous parameters and in the infinite cylinder. This means that the solution of the equations can be given as

$$u(\mathbf{x},t) = u(\mathbf{n} \cdot \mathbf{x} - vt) = u(\overline{\xi}) \text{ as } t \to \infty. \tag{6.6}$$

where v is the asymptotic speed, $\overline{\xi} = (\mathbf{x} \cdot \mathbf{n} - vt)$ is the moving frame of the traveling wave and $\mathbf{n}$ is the direction of motion of the traveling wave. In the previous chapter we have used that the speed of the traveling wave $v = 2\sqrt{\mathbf{n}'D\mathbf{n}}$ to solve for the parameter estimation problem. In this chapter we use the shape of the traveling wave, namely its slope. In order to have an analytical description of the asymptotic shape we focus on the infinite cylinder case with homogeneous parameters. As the tumor cell density distribution converges to the traveling wave the shape of the distribution also converges. In Figure 6.2 we show this behavior both for the overall distribution and the shape of the distribution below $u = u_0$.

The analytical description of the shape of the asymptotic traveling wave can be obtained by placing the solution $u(\overline{\xi})$ in Equation 6.3. By noticing that $\mathbf{n}$ is in the direction of $\overline{\xi}$ and in the infinite cylinder the change of u is only nonzero in the $\mathbf{n}$ direction we can transform the partial differential equation into an ordinary one

$$D_{\mathbf{n}}\frac{d^2u}{d\overline{\xi}^2} + 2\sqrt{\rho D_{\mathbf{n}}}\frac{du}{d\overline{\xi}} + \rho u(1-u) = 0 \tag{6.7}$$

$$D_{\mathbf{n}} = \mathbf{n}'D\mathbf{n}, \tag{6.8}$$

where the partial differentials become derivatives with respect to $\overline{\xi}$, also shown in Equation 4.5. The solution for this nonlinear equation does not have an analytical form due to the nonlinear reaction term $\rho u(1-u)$. In this section our aim is to find an approximation to the solution of Equation 6.7 without using global linearization of the nonlinear term. Instead of global linearization, we can locally linearize this term and obtain analytical solutions for local patches. Here, we propose to construct these local solutions and then combine them to obtain the form of the traveling wave. Assume that at a point $\overline{\xi}^*$ we know the value of the tumor cell density $u = u^*$ (in the images this corresponds to having the delineation of the tumor and assuming that it corresponds to an iso-density surface). When we linearize the Equation 6.7
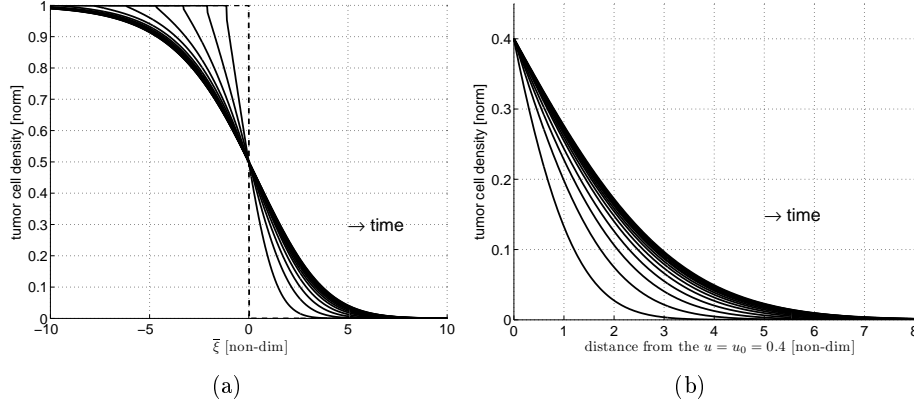
(a)   (b)

Figure 6.2: (a) The tumor distribution evolving with the constant coefficient reaction-diffusion equation (cross-section of the tumor cell density distribution in the infinite cylinder) is plotted at different times (non-dimensional). We plot the distribution at different times on the moving frame $\overline{\xi}$. Observe that as time passes the shape of the distribution converges to an asymptotic shape. (b) When we plot the distribution below $u = u_0$ at different times again we observe the convergence behavior of the shape of the traveling wave.

around the point $\overline{\xi}^*, u^*$ we get

$$D_{\mathbf{n}}\frac{d^2u}{d\overline{\xi}^2} + 2\sqrt{\rho D_{\mathbf{n}}}\frac{du}{d\overline{\xi}} + \rho u(1 - u^*) = 0. \tag{6.9}$$

Equation 6.9 can be solved analytically and the solution has the form

$$u_{\overline{\xi}^*}(\overline{\xi}) = Be^{-\lambda(1+\sqrt{u^*})\overline{\xi}} + Ae^{-\lambda(1-\sqrt{u^*})\overline{\xi}} \tag{6.10}$$

$$\lambda = \sqrt{\frac{\rho}{D_{\mathbf{n}}}}, \tag{6.11}$$

where A and B are integration constants and $u_{\overline{\xi}^*}$ is the local solution around $\overline{\xi}^*$. Due to the smooth properties of the reaction-diffusion equations this solution can be used as an approximation for the solution of Equation 6.7 in a small neighborhood around $\overline{\xi}^*$ [Taylor 1996]. Then using the u values found on the boundary of this neighborhood one can construct the approximations for the adjacent neighborhoods and cover the whole domain like this. By constructing and combining these local approximations in a successive manner, we reconstruct the shape of the traveling wave $u(\overline{\xi})$ starting from the known point $u(\overline{\xi}^*) = u^*$. This idea is demonstrated in Figure 6.3.

In order to obtain the relationship between the two constants A and B we use the fact that $u = 0.5$, the origin of the moving frame $\overline{\xi}$, is an inflection point of the traveling wave. Therefore, the second derivative of u at $u = 0.5$ should be zero. When we impose this to the local solution around u^* which is close to $u = 0.5$ we
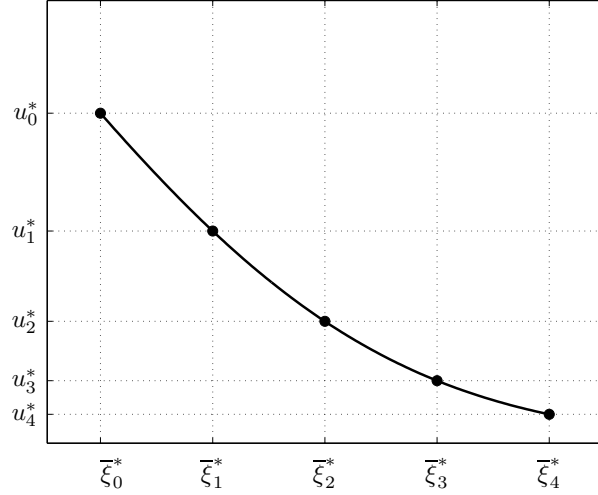
Figure 6.3: The shape of the traveling wave can be reconstructed starting from one known point and building local linear approximations to the reaction-diffusion equation with nonlinear reaction term. If the known point is $u(\overline{\xi}_0^*) = u_0^*)$ then we can use the local linear approximation at this point to find the value $u(\overline{\xi}_1^*) = u_1^*$. Then using the linear approximation at $\overline{\xi}_1^*$ we can find the value u_2^* and the reconstruction process goes on like this.

get

$$\frac{A}{B} = \frac{(1 + \sqrt{u^*})^2}{(1 - \sqrt{u^*})^2}. \tag{6.12}$$

For values of u^* close to 0.5 this ratio remains well over 20. The contribution of $Be^{-\lambda(1+\sqrt{u^*})\overline{\xi}}$ is much smaller than the other part. Therefore, we ignore this part of the solution given in Equation 6.10. As a result the local approximation $\tilde{u}_{\overline{\xi}^*}$ of the tumor profile around u^* can be given as

$$u_{\overline{\xi}^*}(\mathbf{x}, t) \approx \tilde{u}_{\overline{\xi}^*}(\mathbf{x}) = \tilde{u}_{\overline{\xi}^*}(\overline{\xi}) = Ae^{-\lambda\overline{\xi}(1-\sqrt{u^*})} \ \text{ for } \ \lambda = \sqrt{\rho/D_{\mathbf{n}}}. \tag{6.13}$$

We notice that the value of the integration constant A depends on the value of $\overline{\xi}$. The value of $\overline{\xi}$ at a point corresponds to its distance from the inflection point of the traveling wave, which is at $u = 0.5$ (see Figure 6.2(a)). From the images however, we can observe the regions where tumor cell density is greater than u_0. Therefore, we do not have access to the value of $\overline{\xi}$ at a point. For each local approximation this problem can be solved easily. For a point $\overline{\xi} = \overline{\xi}^* + \Delta\overline{\xi}$ we can write

$$\tilde{u}_{\overline{\xi}^*}(\overline{\xi}^* + \Delta\overline{\xi}) = Ae^{-\lambda(1-\sqrt{u^*})(\overline{\xi}^* + \Delta\overline{\xi})} \tag{6.14}$$

$$= Ae^{-\lambda(1-\sqrt{u^*})\overline{\xi}^*}e^{-\lambda(1-\sqrt{u^*})\Delta\overline{\xi}} \tag{6.15}$$

$$= u^*e^{-\lambda(1-\sqrt{u^*})\Delta\overline{\xi}}, \tag{6.16}$$

where $\Delta\overline{\xi}$ is a small distance as we remain close to the point u^*. As a result we replace the unknowns A and $\overline{\xi}^*$ with the knowns u^* and $\Delta\overline{\xi}$. Using ξ variable instead

of the $\Delta\overline{\xi}$ we obtain our final local approximation for the form of the tumor profile (traveling wave)

$$\tilde{u}_{\overline{\xi}^*} = u^* e^{-\lambda(1-\sqrt{u^*})\xi} \quad \text{for} \quad \lambda = \sqrt{\rho/\mathbf{n}'D\mathbf{n}}. \tag{6.17}$$

We note that in the local neighborhood of $(\overline{\xi}^*, u^*)$ this solution can be written as the integral

$$\tilde{u}_{\overline{\xi}^*} = \int_0^{\xi} -\lambda(1 - \sqrt{u^*})\tilde{u}_{\overline{\xi}^*} d\varphi \quad \text{with} \quad \tilde{u}_{\overline{\xi}^*}(0) = u^*. \tag{6.18}$$

When we take small enough neighborhoods around each u^*, in the limit, we replace u^* in the integrand with $\tilde{u}_{\overline{\xi}^*}$. Here we assume that in such a small neighborhood $\tilde{u}_{\overline{\xi}^*}$ values will be close to u^*. Considering the smoothness of the reaction-diffusion equations this approximation becomes valid [Taylor 1996]. With this approximation the local solution given by the integral becomes

$$\tilde{u}_{\overline{\xi}^*} = \int_0^{\xi} -\lambda(1 - \sqrt{\tilde{u}_{\overline{\xi}^*}})\tilde{u}_{\overline{\xi}^*} d\varphi \quad \text{with} \quad \tilde{u}_{\overline{\xi}^*}(0) = u^*. \tag{6.19}$$

Combining these local solutions in different neighborhoods using this integral form we obtain the global approximation for the form of the traveling wave

$$\begin{aligned} \tilde{u}(\mathbf{x}) &= \int_0^x -\lambda(1 - \sqrt{\tilde{u}})\tilde{u}d\xi \quad \text{with} \quad \tilde{u}(0) = u_0, \\ \lambda &= \frac{\sqrt{\rho}}{\sqrt{\mathbf{n}'D\mathbf{n}}}, \end{aligned} \tag{6.20}$$

where x is the distance of the point $\mathbf{x}$ from the known point $u = u_0$. In our context $\mathbf{x}$ is the distance from the tumor delineation. We will use this global approximation for our extrapolation formulation. However, just to understand its link to the nonlinear PDE given in Equation 6.7, we look for the nonlinear PDE the solution given in Equation 6.20 solves. For this placing this solution in Equation 6.7 we see that the global approximation $\tilde{u}$ solves the equation

$$D_{\mathbf{n}}\frac{d^2u}{d\overline{\xi}^2} + 2\sqrt{\rho D_{\mathbf{n}}}\frac{du}{d\overline{\xi}} + \rho u(1 - u) + \rho\frac{u\sqrt{u}(1 - \sqrt{u})}{2} = 0, \tag{6.21}$$

where the additional nonlinearity $\rho u\sqrt{u}(1 - \sqrt{u})/2$ is the error we make as a result of the assumptions we have done in the derivation. We notice that this additional nonlinearity remains well below $\rho u(1-u)$ for $u \in [0,1]$ Once we write Equation 6.20 we notice that the slope of the form of the tumor cell density distribution depends on $\lambda = \sqrt{\rho/\mathbf{n}'D\mathbf{n}}$, which is a ratio between the proliferation and the diffusion rate. Remembering from Chapter 4 that the speed of the tumor front $v = 2\sqrt{\rho\mathbf{n}'D\mathbf{n}}$ is related to the product of these parameters we have a better insight on the effect of the parameters of the model on the evolution of the tumor cell distribution. These effects are summarized on the theoretical tumor profile in Figure 6.4.

In Figure 6.5 we plot the asymptotic form of the traveling wave and the approximation that reconstructs this traveling wave using Equation 6.20. The approximation uses the location of a single point shown in dark dot in both figures in
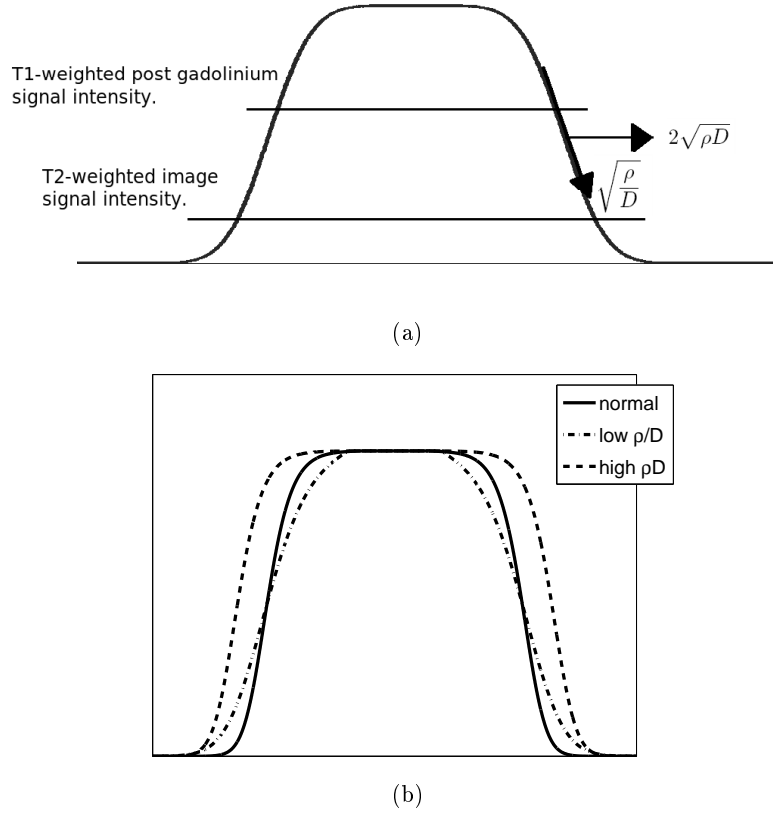
(a)

(b)

Figure 6.4: The shape and the speed of the hypothetical tumor profile depends on the parameters of the reaction-diffusion model, D and ρ. The speed of the tumor and how fast it grows depends mainly on the product of the parameters $D\rho$. On the other hand the shape of the profile and how far it has infiltrated into the brain parenchyma depends on the ratio of these parameters ρ/D. In the figures we show these relationships. For simplification we denote D as a scalar. (b) In solid line we show the hypothetical density profile of a glioma. In dash-dot line we show another profile with the same ρD product but a lower ρ/D ratio. We see that its infiltration is further away. Lastly in the dashed lines we show a tumor profile with the same ρ/D ratio as the solid profile but with a higher ρD product. We see that this tumor has the same profile shape but it moves faster.

reconstructing the tumor cell density distributions. The fit is very accurate especially around the point where we start the reconstruction. Since we are interested in the tumor cell density distribution below some threshold $u_0 = 0.4$ we focus on that region. In Figure 6.6 we zoom on this region and the performance of the approximation as a function of time. We plot the shape of the traveling wave (low density regions of the tumor profile) reconstructed by Equation 6.20 as a function of the distance from the known point (tumor delineation) along with the real form
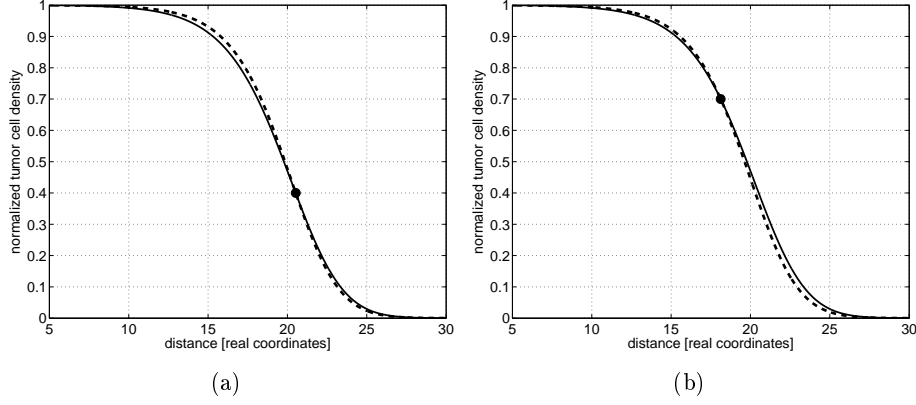
Figure 6.5: Figures show the shape of the traveling wave in solid lines and the reconstructed approximations using Equation 6.20 in dashed curves. (a) We start from the point $u_0 = 0.4$ and reconstruct the whole profile using only the location of this point. This point is shown in the plot. (b) We do the same thing but this time we start from $u_0 = 0.7$. We see that the approximation to the shape of the traveling wave given in Equation 6.20 can accurately reconstruct the whole shape of the traveling wave and therefore the hypothetical tumor cell density distribution in this case.

of the traveling wave taken at different time instants for the infinite cylinder case. We observe that this approximation is reasonable for the tails of the profile and it gets better as time elapses.

The approximation explained above is constructed for the case where the coefficients of the reaction-diffusion equation are constant over the whole domain and the motion is only in one direction. This is not the case for general media and for the brain. Moreover, when the tumor front is curved its motion would not be in one direction and the solution of the reaction-diffusion equation cannot be given in terms of a traveling wave. In order to reconstruct the hidden part of the tumor cell density distribution in MR images we make the following assumptions: within a voxel, the coefficients are constant and the motion of the front is only in one direction. Based on these assumptions we can construct the local approximations given in Equation 6.20 in each voxel separately. The computation in each voxel uses the values at its neighbors as it is the case for the reconstruction in the infinite cylinder. Using this principle, we sweep the domain starting from the visible part of the tumor and going outwards computing the tumor cell density estimate at each voxel. In this construction the direction of motion and the initial value for each voxel are defined by its adjacent voxels.

Following our assumptions, the integrand in Equation 6.20 can be written as the gradient relation in 3D,

$$\frac{\partial \tilde{u}}{\partial \mathbf{n}} = \lambda(1 - \sqrt{\tilde{u}})\tilde{u}. \tag{6.22}$$

Placing λ in this equation and replacing $\mathbf{n}$ with $\nabla \tilde{u} / \mid \nabla \tilde{u} \mid$, we obtain the following static Hamilton-Jacobi equation that constructs the approximation $\tilde{u}$ given in
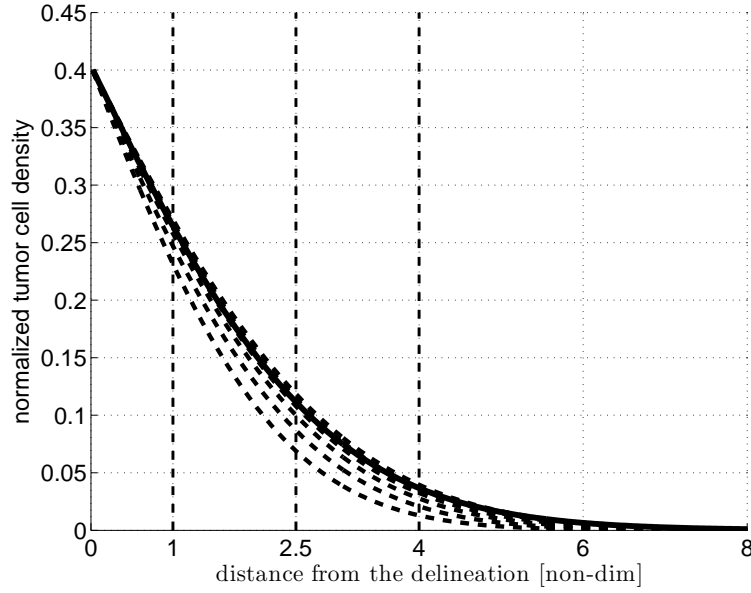
days after detection	density difference at 1.0	at 2.5	at 4
0	0.037	0.044	0.024
1	0.021	0.026	0.016
2	0.010	0.013	0.010
3	0.005	0.005	0.005
4	1×10^{-4}	-0.001	0.001
5	-0.003	-0.005	0.002

Figure 6.6: Approximation constructed for the low density regions of the tumor profile in the infinite cylinder case. All the time and distance values are dimensionless. To give an idea, for a high grade glioma each time unit would correspond to 60 days and each distance unit would correspond to 0.5 cm. The tail approximation constructed using Equation 6.20 (solid curve) is plotted with the actual tails of the tumor front. The detection for the tumor in the infinite cylinder is assumed to take place when the tumor has grown for 1.5 cm of diameter (the corresponding non-dimensional unit). We show the low density regions of the at the time of detection, 1, 2, 3, 4 and 5 time units after the detection, the dashed curves from left to right respectively. As time increases the solid curve approximates the actual tail better. The associated table shows the difference in tumor cell density between the tail approximation and the actual tail at a given day for different locations in the moving frame denoted by the vertical dashed lines in the figure.

Equation 6.2 at each voxel with the principle shown in Figure 6.3.

$$\frac{\sqrt{\nabla \tilde{u} \cdot (D\nabla \tilde{u})}}{\sqrt{\rho}\tilde{u}(1 - \sqrt{\tilde{u}})} = 1, \ \tilde{u}(\Gamma) = u_0 \tag{6.23}$$

where Γ is the contour around the visible part of the tumor in the image ($u \geq u_0$).

As a reminder in this chapter u_0 is taken as 0.4 following the assumptions made in [Tracqui 1995].

Equation 6.23 has two solutions at each point, one with increasing and the other one with decreasing $\tilde{u}$. Since the reaction-diffusion equation tells us that as we move away from the visible contour, the values of $\tilde{u}$ will decrease, for all points we choose the decreasing solution. Using Equation 6.23 we start from Γ and sweep the domain moving outwards as we find $\tilde{u}$ values for each voxel.

The Equation 6.23 is a static Hamilton-Jacobi equation. Several different numerical methods have been proposed to solve this kind of equations [Qian 2006, Sethian 2003]. In this thesis, we adopt a fast marching (FM) based approach to solve it which is coherent with the sweeping idea we propose to construct the low density infiltration estimate $\tilde{u}$. The details of the proposed numerical method used is explained in Chapter 8. The original FM method as proposed by Sethian and Osher solves the Eikonal equation but does not take into account the anisotropy [Sethian 1999]. The method we use modifies the original FM algorithm to include the effect of the anisotropy, Chapter 8. In this way it enjoys the efficiency of the FM method and provides an accurate solution in the case of high anisotropy. As a result of sweeping the domain outwards starting from the tumor delineation, the continuity of the constructed $\tilde{u}$ is ensured. On the other hand, implicit interpolation between different voxels, in other words the patching between planar solutions in different voxels, depends on the order of the numerical scheme, which is linear in our case. One can imagine a second order patching by including the effect of the curvature in the extrapolation given by Equation 6.23.

Algorithm 2 The algorithm for extrapolating tumor cell density distribution ignoring the boundary conditions.

Inputs: Tumor delineation in the anatomical image, DT-MRI of the patient, White-gray matter segmentation, personalized tumor growth parameters for the reaction-diffusion model (or a parameter set the radiotherapist/radiologist would like to try for visualizing different possible tumor density distributions).

- Construct the tumor diffusion tensors using the parameters d_w, d_g, the DT-MRI image and the white-gray matter segmentation.
- Initialize the extrapolation by setting $\tilde{u}$ to u_0 on the tumor delineation.
- Compute $\tilde{u}$ value at each voxel which has a neighbor whose $\tilde{u}$ value is set using the numerical method in Chapter 8.
- Among the two computed $\tilde{u}$ values choose the one that is decreasing and set it for that voxel.
- Sweep the domain in this respect outwards starting from the delineation.

Equation 6.23 constructs the low density infiltration estimate $\tilde{u}(\mathbf{x})$ based on the reaction-diffusion model (Equation 6.3) in the infinite domain. However, the total model consists of a no-flux (Neumann) boundary condition (Equation 6.4) as well, which affects the distribution of the tumor cell density in the brain. In Section 6.2.2 we include the effect of the boundary in our extrapolation formulation. Before going into details of the boundary conditions in Algorithm 2 we summarize the method explained in this section through an algorithm.

6.2.2 Including Effects of the Boundary Condition

The estimate for low density infiltration of gliomas as constructed by Equation 6.23 does not take into account the effects of the Neumann boundary condition given in Equation 6.4. This condition states that tumor cells trying to pass across the boundary (skull and ventricles) bounce back from it and continue their motion within the tissue. Thus, the effects of the Neumann boundary condition are not only confined to the points neighboring the boundary. The condition affects the tumor cell density distribution throughout the brain.

Construction in 1D

In order to understand and approximate this effect on the tumor profile, we examine the 1-D linear reaction-diffusion equation including a boundary residing at $x = 0$ given as:

$$u_t = du_{xx} + \rho u \text{ for } x \leq 0 \tag{6.24}$$

$$u_x|_{x=0} = 0. \tag{6.25}$$

where d is the scalar diffusion coefficient in 1-D. For such systems, we can use the *method of reflection* to construct the approximation for the low density parts of the tumor in the presence of the boundary condition [Strauss 1992]. The method of reflection is used to construct solutions of linear partial differential equations such as the diffusion equation in finite domains, [Strauss 1992]. It uses the solution under no boundary condition, reflects it with respect to the boundary and superpose these two, relying on the linearity of the equation. By adding the reflected solution, the boundary condition (Equation 6.25) is satisfied and since the problem given by Equations 6.24 and 6.25 has a unique solution, the one created by this method is the solution. In Figure 6.7(a), we illustrate the method of reflection by solving the 1-D linear reaction-diffusion equation numerically following the steps of the method.

In the case of the nonlinear reaction diffusion equation we cannot superpose two different solutions of the system. Therefore, in order to apply the method of reflection we need to have certain assumptions. Let $u^{(1)}$ be a solution of the nonlinear reaction-diffusion equation in 1-D and $u^{(2)}$ be its reflection with respect to the boundary. Both u's satisfy the nonlinear equation

$$u_t = du_{xx} + \rho u(1 - u), \tag{6.26}$$

where d is the scalar diffusion coefficient. When we superpose the two solutions we get

$$\begin{aligned}
(u^{(1)} + u^{(2)})_t &= d(u^{(1)} + u^{(2)})_{xx} \\
&+ \rho(u^{(1)} + u^{(2)})(1 - u^{(1)} - u^{(2)}) \\
u_t^{(1)} + u_t^{(2)} &= du_{xx}^{(1)} + du_{xx}^{(2)} \\
&+ \rho u^{(1)}(1 - u^{(1)}) + \rho u^{(2)}(1 - u^{(2)}) - 2\rho u^{(1)}u^{(2)}.
\end{aligned} \tag{6.27, 6.28}$$

We see that the superposition of the two solutions do not satisfy the equation due to the nonlinearity. However, in this work we are interested in low values of u since
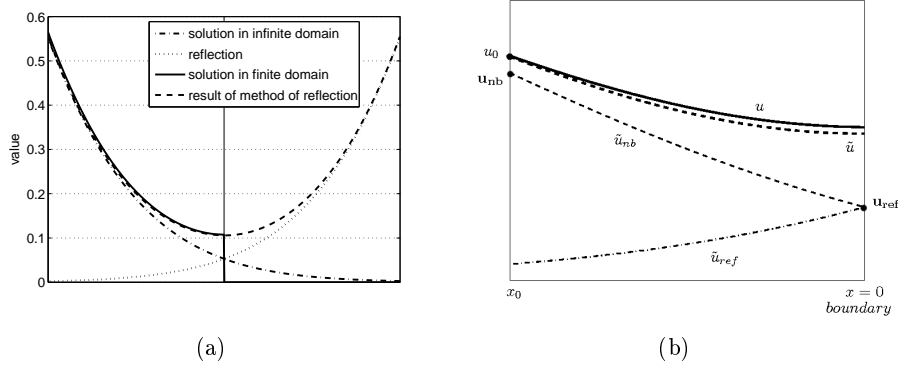
(a)   (b)

Figure 6.7: (a) For linear partial differential equations the solution under the Neumann boundary conditions can be constructed by removing the boundary and adding a reflected wave on the other side of the boundary. The figure demonstrates this for the 1-D reaction-diffusion equation under the boundary conditions. (b) Figure illustrates how we use the method of reflection for approximating the boundary effect in the extrapolation formulation. The actual density distribution u is shown in solid curve and the estimation $\tilde{u}$ in the dark dashed one. As suggested by the method of reflection, $\tilde{u}$ is formed by two parts: the no boundary approximation $\tilde{u}_{nb}$ and the $\tilde{u}_{ref}$. The boundary resides at $x = 0$ and the $u = u_0$ point resides at $\xi = 0$.

we try to extrapolate the tumor cell density distribution below some threshold u_0. Therefore, the values of $u^{(1)}$ and $u^{(2)}$ are low. Based on this, we assume that

$$\frac{(1 - u^{(1)})}{u^{(2)}} >> 1 \quad \text{and} \quad \frac{(1 - u^{(2)})}{u^{(1)}} >> 1. \tag{6.29}$$

Using this assumption we can say that

$$\rho(1 - u^{(1)})u^{(1)} >> \rho u^{(1)}u^{(2)} \quad \text{and} \quad \rho(1 - u^{(2)})u^{(2)} >> \rho u^{(1)}u^{(2)}. \tag{6.30}$$

Hence, we assume that the superposition of two solutions satisfy the nonlinear reaction-diffusion equation for low values of u.

In Section 6.2.1 we have seen that we can reconstruct the shape of traveling wave solutions of nonlinear reaction-diffusion equations by local approximations and integrating over them. This reconstruction was done in the infinite domain. In the finite domain, we can construct $\tilde{u}$ using the idea of superposing two different parts so that it takes into account the effect of the boundary conditions. Without loss of generality let us assume that we know the value of u at x_0 such that $u(x_0) = u_0$ (in the context of the tumor delineation the value x_0 is the location of the delineation and the value u_0 is the imaging threshold.), see Figure 6.7. In order to construct the shape of the solution of Equation 6.26 starting from x_0 including the effect of the boundary we superpose two approximations $\tilde{u}_{nb}$ and $\tilde{u}_{ref}$. Each of these

approximations have the integral form like the one given in Equation 6.20:

$$\tilde{u}_{nb}(x) = \int_0^x -\lambda(1 - \sqrt{\tilde{u}_{nb}})\tilde{u}_{nb}d\xi \quad \text{with} \quad \tilde{u}_{nb}(\xi = 0) = \mathbf{u_{nb}} \qquad (6.31)$$

$$\tilde{u}_{ref}(x) = \int_0^x -\lambda(1 - \sqrt{\tilde{u}_{ref}})\tilde{u}_{ref}d\widehat{\xi} \quad \text{with} \quad \tilde{u}_{ref}(\widehat{\xi} = 0) = \mathbf{u_{ref}}, \quad (6.32)$$

where $\widehat{\xi}$ is the moving frame traveling at the same speed but in the opposite direction as ξ. Moreover, the point $\xi = 0$ is the location of the tumor delineation while the point $\widehat{\xi} = 0$ is the boundary, see Figure 6.8. The approximation $\tilde{u}$ consists
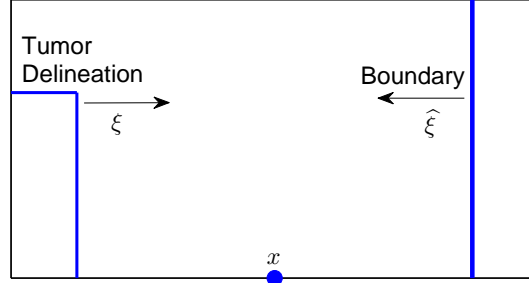

Figure 6.8: The two parts of the approximation $\tilde{u}$ have different coordinate systems as given in Equations 6.31 and 6.32. The two moving frames ξ and $\widehat{\xi}$ have opposite directions and different origins. The $\xi = 0$ corresponds to the tumor delineation while $\widehat{\xi}$ corresponds to the boundary.

of a part that is constructed by ignoring the boundary condition, $\tilde{u}_{nb}$, and the reflection of this part on the boundary, $\tilde{u}_{ref}$, as demonstrated in Figure 6.7(b). The reflection $\tilde{u}_{ref}$ decreases in the opposite direction of $\tilde{u}_{nb}$ in order to satisfy the no-flux boundary condition and this is represented by the relation between the variables $\widehat{\xi}$ and ξ such that $d\widehat{\xi}/d\xi = -1$. The initial conditions $\mathbf{u_{nb}}$ and $\mathbf{u_{ref}}$ are used to fit the approximation to the observation and also to the boundary condition. Under this setting, constructing the low density infiltration estimation $\tilde{u}$ corresponds to finding the values for the coefficients. Once the coefficients are found, at any location the superposition of these solutions gives us the final form of the solution of Equation 6.26 including the effect of the boundary,

$$\tilde{u}(x) = \tilde{u}_{nb}(x) + \tilde{u}_{ref}(x). \qquad (6.33)$$

There are two criteria which determine the coefficients $\mathbf{u_{nb}}$ and $\mathbf{u_{ref}}$. The first one is the no-flux boundary condition

$$\frac{d}{dx}\tilde{u}|_{x=0} = [\frac{d}{dx}\tilde{u}_{nb} + \frac{d}{dx}\tilde{u}_{ref}]_{x=0} = 0. \qquad (6.34)$$

It provides us the relation between the coefficients. Using the fact that the two parts are going in opposite directions ($d\widehat{\xi}/d\xi = -1$) we see that Equation 6.34 gives us

$$\frac{d}{dx}\tilde{u}|_{x=0} = \lambda(1 - \sqrt{\tilde{u}_{nb}})\tilde{u}_{nb}|_{x=0} - \lambda(1 - \sqrt{\mathbf{u_{ref}}})\mathbf{u_{ref}} = 0, \qquad (6.35)$$

where we used the fundamental theorem of calculus. This suggests that once we construct the $\tilde{u}_{nb}$ by ignoring the boundary, we can find the reflection part $\tilde{u}_{ref}$ based on the value of $\tilde{u}_{nb}$ on the boundary such that the no-flux boundary condition will be satisfied. However, this relation is a 4th order polynomial and solving such polynomials is costly especially if we consider that we will solve this equation for many different points on a 3D boundary. This will become clearer when we consider the higher dimension in the next section. In order to have a simpler form we make the approximation

$$\frac{(1 - \sqrt{\mathbf{u_{ref}}})\mathbf{u_{ref}}}{(1 - \sqrt{\tilde{u}_{nb}})\tilde{u}_{nb}|_{x=0}} \approx \frac{\mathbf{u_{ref}}}{\tilde{u}_{nb}|_{x=0}}, \tag{6.36}$$

which is very close for low values of u. As a result of this approximation we obtain a simpler relation to find $\mathbf{u_{ref}}$ value:

$$\mathbf{u_{ref}} = \tilde{u}_{nb}(x = 0). \tag{6.37}$$

The second criterion is the fidelity of the approximation to the observation. Since we observe the location of the $u = u_0$ point (iso-density contour), the approximation should be coherent with this observation. Using the ξ variable as in the previous section to represent the location of $u = u_0$ point, we can write this criterion as

$$\tilde{u}|_{\xi=0} = [\tilde{u}_{nb} + \tilde{u}_{ref}]_{\xi=0} = u_0. \tag{6.38}$$

This relation basically states that when we add the two parts of the approximation the location of the $\tilde{u} = u_0$ should match the $u = u_0$ point. While the boundary condition gives the relation between the coefficients, Equation 6.38 provides us the numerical values for them.

Algorithm 3 The iterative algorithm for finding the effect of Neumann boundary conditions on the low density infiltration.

    Initialize the extrapolation: $\mathbf{u_{nb}}^0 = u_0$
    repeat
        $\mathbf{u_{ref}}^i = \tilde{u}_{nb}^i|_{x=0}$ for $i \geq 1$
        construct $\tilde{u}_{ref}^i$
        $\mathbf{u_{nb}}^{i+1} = u_0 - \tilde{u}_{ref}^i|_{\xi=0}$ for $i \geq 1$
    until both criteria are satisfied with enough accuracy.

We use an iterative scheme to find the coefficients $\tilde{u}_{nb}$ and $\tilde{u}_{ref}$ that satisfies the two criteria explained above. The scheme starts from the approximation constructed for the infinite domain in Section 6.2.1 setting it as the initial $\tilde{u}_{nb}$. At each iteration we construct $\tilde{u}_{nb}$, determine $\mathbf{u_{ref}}$ using the boundary condition, construct $\tilde{u}_{ref}$ and update $\mathbf{u_{nb}}$ according to the fidelity criterion. The pseudocode for this scheme is given in Algorithm 3. This iterative process is demonstrated in Figure 6.9 where the approximation at the beginning of the iterations ($\tilde{u}^0$) and at the end of the 2nd iteration ($\tilde{u}^2 = \tilde{u}$) are shown.
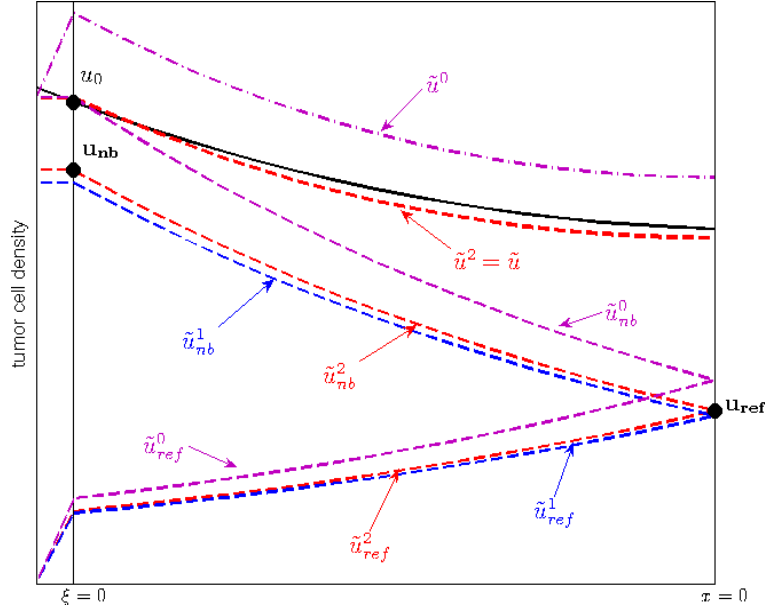
Figure 6.9: The figure illustrates the iterative process to find the coefficients $\mathbf{u_{nb}}$ and $\mathbf{u_{ref}}$. In order to approximate the actual profile (solid curve) $\tilde{u}^i_{nb}$ and $\tilde{u}^i_{ref}$ are constructed iteratively to satisfy the boundary condition given in Equation 6.34 and the fidelity criteria given in Equation 6.38.

Construction in higher dimensions

When applying the effect of the no-flux boundary condition on the low density extrapolation in 3-D (2-D) we use the same principles as we developed for the 1-D case. The boundary, which is a point in the 1-D case, becomes a surface (contour) $\partial\Omega$ in 3-D from which the tumor cells bounce back in the dynamic formulation of reaction-diffusion models. Hence, every point on the boundary will act as a reflector of tumor cells. In order to derive the appropriate relations for the low density infiltration estimation $\tilde{u}$ in 3D, let us assume that we have a homogeneous and anisotropic media characterized by the diffusion tensor D and we have a planar visible tumor front with the normal $\mathbf{n}$. $\tilde{u}$ is constructed again as the sum of two different parts as:

$$
\begin{aligned}
\tilde{u} &= \tilde{u}_{nb} + \tilde{u}_{ref}, \\
\tilde{u}_{nb}(\mathbf{x}) &= \int_0^x -\lambda_{nb}(1 - \sqrt{\tilde{u}_{nb}})\tilde{u}_{nb}d\xi \quad \text{with} \quad \tilde{u}_{nb}(0) = \mathbf{u_{nb}} \\
\tilde{u}_{ref}(\mathbf{x}) &= \int_0^x -\lambda_{ref}(1 - \sqrt{\tilde{u}_{ref}})\tilde{u}_{ref}d\widehat{\xi} \quad \text{with} \quad \tilde{u}_{ref}(0) = \mathbf{u_{ref}}
\end{aligned}
$$

$$\lambda_{nb} = \sqrt{\frac{\rho}{\mathbf{n}^T D \mathbf{n}}},$$

$$\lambda_{ref} = \sqrt{\frac{\rho}{\mathbf{n_\Omega}^T D \mathbf{n_\Omega}}},$$

$$\xi = \mathbf{n}^T \mathbf{x} - ct,$$

$$\widehat{\xi} = \mathbf{n_\Omega}^T \mathbf{x} - ct,$$

where $\mathbf{n}$ is the gradient direction of $\tilde{u}_{nb}$, $\mathbf{n_\Omega}$ is the normal to the boundary which by construction coincides with the gradient direction of $\tilde{u}_{ref}$ at the boundary and x is the distance of point $\mathbf{x}$ to the tumor delineation. Notice that due to the anisotropic diffusion tensor λ_{nb} and λ_{ref} differ. By convention we choose $\mathbf{n_\Omega}$ to be pointing towards the brain, i.e. $\mathbf{n}_\Omega^T \mathbf{n} < 0$. We construct $\tilde{u}_{nb}$ in the same manner as explained in Section 6.2.1. Once it is constructed, $\tilde{u}_{ref}$ is the only unknown in this setting and we set it so to satisfy the boundary condition which is given as:

$$\mathbf{n}_\Omega^T D \nabla u|_\Omega = 0, \tag{6.39}$$

stating that the component of the flux of tumor cells orthogonal to the boundary should be 0. The approximation $\tilde{u}$ should follow this condition as well.

To construct $\tilde{u}_{ref}$, we need to find the relation between $\tilde{u}_{nb}$ and $\tilde{u}_{ref}$ at each boundary point separately since every point acts as a cell reflector. At the point p on the boundary, in order to satisfy the boundary condition we should satisfy

$$\mathbf{n}_\Omega^T D(\nabla \tilde{u}_{nb} + \nabla \tilde{u}_{ref})|_p. \tag{6.40}$$

Placing the definitions of $\tilde{u}_{nb}$ and $\tilde{u}_{ref}$, for $\tilde{u}$ we obtain

$$\tilde{u} = \int_0^x -\lambda_{nb}(1 - \sqrt{\tilde{u}_{nb}})\tilde{u}_{nb}d\xi + \int_0^x -\lambda_{ref}(1 - \sqrt{\tilde{u}_{ref}})\tilde{u}_{ref}d\widehat{\xi}. \tag{6.41}$$

Using the fundamental theorem of calculus we can compute the gradient of $\tilde{u}$ at p

$$\nabla \tilde{u}|_p = -\lambda_{nb}(1 - \sqrt{\tilde{u}_{nb}})\tilde{u}_{nb}|_p \mathbf{n} - \lambda_{ref}(1 - \sqrt{\mathbf{u_{ref}}})\mathbf{u_{ref}}|_p \mathbf{n}_\Omega. \tag{6.42}$$

Forcing the boundary condition given in Equation 6.39 we obtain the relation we are looking for the points on the boundary

$$\begin{aligned} (1 &- \sqrt{\mathbf{u_{ref}(x)}})\mathbf{u_{ref}(x)} = \\ &- \frac{\mathbf{n}_\Omega^T D \mathbf{n}}{\sqrt{\mathbf{n}^T D \mathbf{n}}\sqrt{\mathbf{n}_\Omega^T D \mathbf{n}_\Omega}}(1 - \sqrt{\tilde{u}_{nb}(\mathbf{x})})\tilde{u}_{nb}(\mathbf{x}), \text{ for } \mathbf{x} \in \partial\Omega. \end{aligned} \tag{6.43}$$

Therefore, for each point on the boundary we can find $\mathbf{u_{ref}}$ by solving the 4th order polynomial given by the Equation above. As we have explained during the construction of the 1D solution this is costly therefore we apply the approximation we have introduced in Equation 6.36. In higher dimensions this approximation becomes

$$\frac{(1 - \sqrt{\mathbf{u_{ref}(x)}})\mathbf{u_{ref}(x)}}{(1 - \sqrt{\tilde{u}_{nb}(\mathbf{x})})\tilde{u}_{nb}(\mathbf{x})} \approx \frac{\mathbf{u_{ref}(x)}}{\tilde{u}_{nb}(\mathbf{x})}. \tag{6.44}$$

As a result of this approximation we transform Equation 6.43 into

$$\mathbf{u_{ref}}(\mathbf{x}) = -\frac{\mathbf{n}_\Omega^T D\mathbf{n}}{\sqrt{\mathbf{n}^T D\mathbf{n}}\sqrt{\mathbf{n}_\Omega^T D\mathbf{n}_\Omega}}\tilde{u}_{nb}(\mathbf{x}), \text{ for } \mathbf{x} \in \partial\Omega. \tag{6.45}$$

As done in the previous section, the construction of the approximation $\tilde{u}$ as explained above assumes homogeneous media and planar tumor front. However, these assumptions do not hold in the case of MR images of gliomas. To tackle this, we follow the same voxel based assumptions we made in Section 6.2.1 stating that the assumptions about the media and the shape of the tumor front holds true within a voxel. To repeat, we assume that within a single voxel, coefficients of the tumor growth model are constant and the tumor profile is not curved. Under
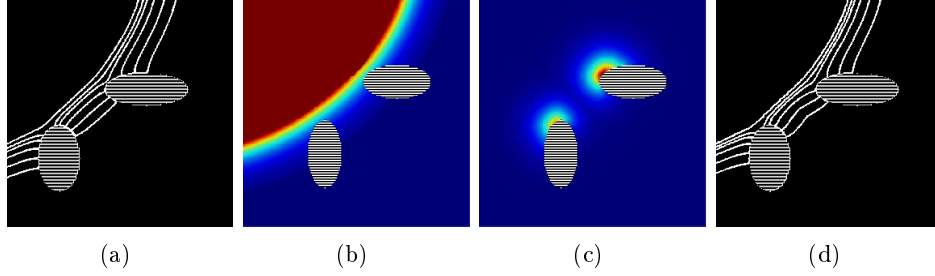

(a)   (b)   (c)   (d)

Figure 6.10: The 2-D example shown in the figures demonstrate the two parts of the estimation $\tilde{u}$ and the effect of including the boundary reflection. The striped regions are set to be the boundaries with the Neumann boundary condition. (a)The result of the reaction-diffusion equation for the low density region $0.002 \leq u \leq 0.08$ shows the actual iso-density contours. (b) The no boundary part of the low density region extrapolation $\tilde{u}_{nb}$. (c) The reflection part $\tilde{u}_{ref}$. (d) The iso-density contours of the superposition: Low density region estimation $\tilde{u}$.

these assumptions, we use the fact that $\tilde{u}_{nb}$ and $\tilde{u}_{ref}$ satisfy the anisotropic Eikonal equations

$$\frac{\sqrt{\nabla\tilde{u}_{nb} \cdot (D\nabla\tilde{u}_{nb})}}{\sqrt{\rho}\tilde{u}_{nb}(1 - \sqrt{\tilde{u}_{nb}})} = 1, \quad \tilde{u}_{nb}(\Gamma) = \mathbf{u_{nb}}(\Gamma), \tag{6.46}$$

$$\frac{\sqrt{\nabla\tilde{u}_{ref} \cdot (D\nabla\tilde{u}_{ref})}}{\sqrt{\rho}\tilde{u}_{ref}(1 - \sqrt{\tilde{u}_{ref}})} = 1, \quad \tilde{u}_{ref}(\partial\Omega) = \mathbf{u_{ref}}(\partial\Omega), \tag{6.47}$$

where $\mathbf{u_{nb}}$ is a function on the initial contour around the visible tumor just as $\mathbf{u_{ref}}$ is on the boundary. This allows us to apply the same construction method as we did in the previous section once the coefficients $\mathbf{u_{nb}}$ and $\mathbf{u_{ref}}$ are set.

As a result of the increase in dimension, the fidelity criterion is now defined over the visible part of the tumor, Γ, which represents the $u = u_0$ iso-density surface, and can be written as

$$\tilde{u}(\Gamma) = \tilde{u}_{nb}(\Gamma) + \tilde{u}_{ref}(\Gamma) = u_0. \tag{6.48}$$

Similarly, the iterative scheme can be carried over to the general higher dimensional case by defining the update scheme on the surfaces Γ and $\partial\Omega$. Figure 6.10, for a simple 2-D example, shows the low density infiltration regions computed by solving the reaction-diffusion equation and the two parts of the estimation $\tilde{u}$ along with itself (a,b,c and d respectively). We observe that the effect of the Neumann boundary condition is well captured by adapting the method of reflection in the low density infiltration extrapolation. The algorithm summarizing the overall method explained in this chapter is given in Algorithm 4.

Algorithm 4 The algorithm for extrapolating the low density infiltration of gliomas.

Inputs: Tumor delineation in the image (MR,CT,...), DT-MRI of the patient, White-gray matter segmentation, personalized growth parameters for the reaction-diffusion model (see Chapter 4)

- Construct the tumor diffusion tensors using the parameters d_w, d_g, the DT-MRI image and the white-gray matter segmentation.

- Initialize the extrapolation by setting $\tilde{u}$ to u_0 on the delineation.

repeat

-   Construct the extrapolation $\tilde{u}_{nb}$ ignoring the boundaries by solving Equation 6.46, see Section 6.2.1. This equation is solved using the anisotropic Fast marching method explained in Chapter 8.

-   Compute the reflection from the boundary by Equation 6.45 and compute $\tilde{u}_{ref}$ using Equation 6.47.

-   Check the fidelity criterion given in Equation 6.48.

-   Update the value of $\tilde{u}$ on the tumor delineation as explained in Algorithm 3.

until Fidelity criterion given in Equation 6.48 is satisfied with enough accuracy.

Extrapolating Glioma Invasion in MR images: Results

Contents

Context

In the previous chapter we have presented the extrapolation formulation for constructing the low density infiltration estimation of gliomas $\tilde{u}$ to offer a solution to the problem of limited tumor density visualization of medical images. We started from the reaction-diffusion growth models for gliomas and derived the proposed solution using their asymptotic behaviors. This chapter is devoted to the experiments and the analysis of the extrapolation tool. We first analyze the tool by evaluating its quality in extrapolation. Following that we devise synthetic irradiation experiments and show the potential benefits of the proposed tool in defining irradiation margins.

7.1 Experiments

In this chapter, we assess the quality of the extrapolation method and the constructed estimation $\tilde{u}$ using synthetic tumors simulated by the reaction-diffusion growth model given in Equations 6.3, 6.4, 6.5. For these synthetic cases, first we compare the actual tumor cell density distribution beyond the visible mass in the image with the estimation $\tilde{u}$ constructed by the proposed method. In the second part we propose a method to tailor irradiation margins based on the estimated low density infiltration. We compare these irradiation margins with the conventionally used constant one through geometric comparisons. These comparisons include the number of tumor cells **not** targeted and the volume of healthy tissue set to be irradiated.

In both of the experiments shown in this chapter, we perform our analysis on the synthetic dataset created in the Chapter 4. Here we briefly review the dataset, for more details please refer to Section 5. In order to create this dataset we used MR images taken from a healthy subject consisting of T1 weighted, T2 weighted

and diffusion tensor images (DTI) with the resolution of $1mm \times 1mm \times 2.6mm$. Using the reaction-diffusion model explained in Section 6.2 we simulated the growth of 180 different synthetic tumors in three different locations and with 60 different parameter sets. In this chapter, for clarity we show the results for 10 of these tumors with 5 different parameter sets and 2 different locations. The locations of the tumor seeds are one in the frontal lobe and the other one in the parietal lobe as shown in Figures 7.1. We have chosen these two locations with different tissue compositions to test the effect of tissue heterogeneity in our experiments. The difference between the tumors at the same location is obtained by using different growth parameters (diffusion coefficients and proliferation rates). These parameter sets used to grow the synthetic tumors using the reaction-diffusion model are given in the table in Figure 7.1 under the column "Real Parameters". As explained in the previous chapter each tumor was grown using the reaction-diffusion model. For each tumor the detection and the first image acquisition take place when the visible tumor reaches the size of 1.5cm in diameter. After the detection a synthetic image is created every 50 days using the image function Im given in Equation 6.1. These images are then used as the inputs to our extrapolation method to estimate their low density infiltration distribution.

The extrapolation methodology proposed in this chapter assumes that the tumor growth parameters for the reaction-diffusion model D and ρ are known. These parameters are not available clinically however, in the previous chapter we have shown that we can estimate these parameters from time series of images under certain conditions. Therefore, here instead of using the real parameters of the reaction-diffusion model we find it more appropriate to use the estimated ones. In the experiments presented here we use the parameters estimated in the previous chapter for extrapolating the tumor cell density distribution beyond the visible part for the synthetic tumors. The estimated parameters for different tumors are given in the table in Figure 7.1 under the column "Estimated Parameters". By using the estimated parameters we simulate a clinical situation where first we estimate the parameters using numerous images and then use the estimated parameters to extrapolate the infiltration of the glioma in an image.

The computation time to run the extrapolation method in the created images depends on different factors such as u_0 (which is in our case $u_0 = 0.4$), the final value up to which we will extrapolate, the parameters (D and ρ), the location of the tumor and the desired accuracy of the iterative method for including boundary conditions. As an example, in our simulations it took around 5 minutes to extrapolate the low density distribution of the tumor at the frontal lobe with median diffusion rate, starting from $u_0 = 0.4$ to $u = 0.00001$ with a very high accuracy using a 4Gb memory 2.26GHz computer.

7.2   Assessing the Estimation Quality

The proposed extrapolation method constructs an estimate for the tumor cell distribution of gliomas beyond their visible part in the image. This construction uses the visible part of the tumor and the anatomical information based on the reaction-

(a) Frontal Lobe (b) Parietal Lobe
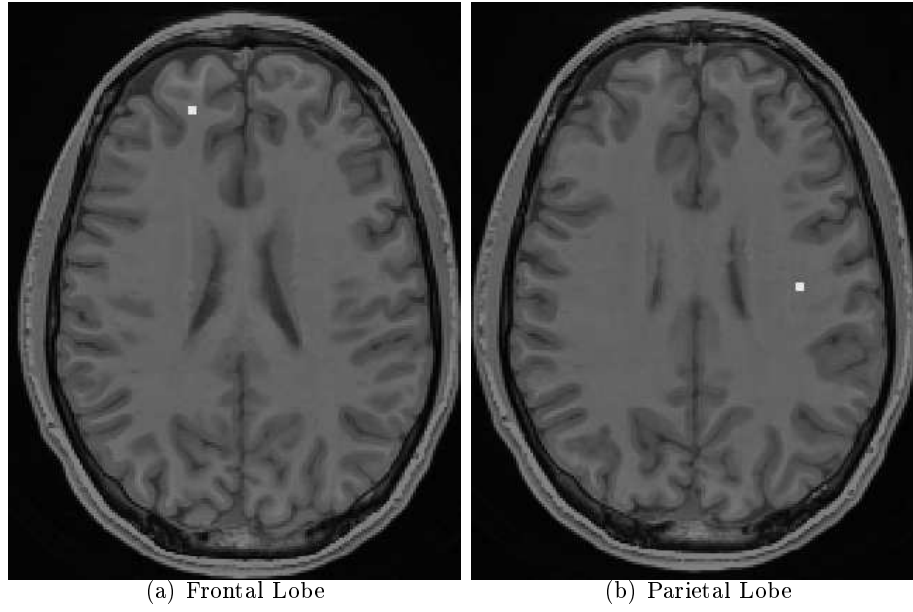
| name	Real Parameters			Estimated Parameters		
	d_w $\frac{mm^2}{day}$	d_g $\frac{mm^2}{day}$	$\rho\ \frac{1}{day}$	d_w	d_g	ρ
median	0.25	0.01	0.012	0.27	0.024	0.012
high $d_{w,g}/\rho$	0.5	0.025	0.009	0.53	0.066	0.009
low $d_{w,g}/\rho$	0.1	0.005	0.024	0.116	0.009	0.024
lower anisotropy	0.1	0.025	0.012	0.115	0.035	0.012
higher anisotropy	0.5	0.005	0.012	0.507	0.021	0.012

Figure 7.1: Figures (a),(b): Different initializations of the synthetic tumors are shown. Table: Different diffusion and proliferation rates used for the simulations. 10 different tumors are created with these 5 set of parameters in the locations given in Figures (a) and (b).

diffusion growth models. The first step we take in assessing the method is to compare the actual low density tumor cell distribution with the estimated one for synthetic tumors created using the reaction-diffusion model. Starting from the 10 synthetic tumors explained above, we extrapolate the corresponding tumors low density infiltration regions (tails) and compare the extrapolated part with the actual density distribution, see Figure 7.2.

In order to quantitatively compare the *spatial resemblance* of the actual density distribution of the synthetic tumors beyond their visible part and the density distribution extrapolated using the images we compute the distance between their corresponding iso-density contours. For the density value v and for the image taken
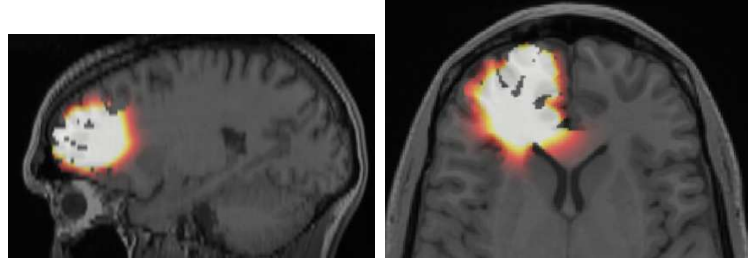
(a) Simulated tumor density distribution - Reaction-Diffusion Model
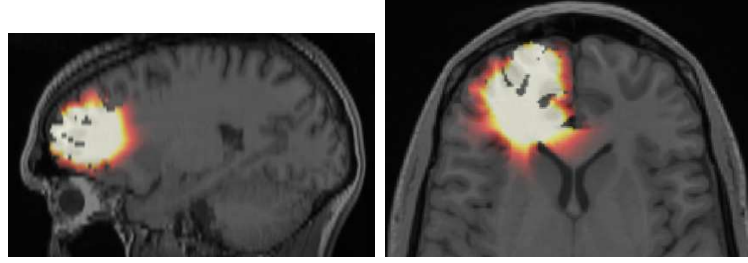
(b) Tumor density extrapolated from the visible boundary of the tumor $u_0 = 0.4$ - Reconstructed infiltration
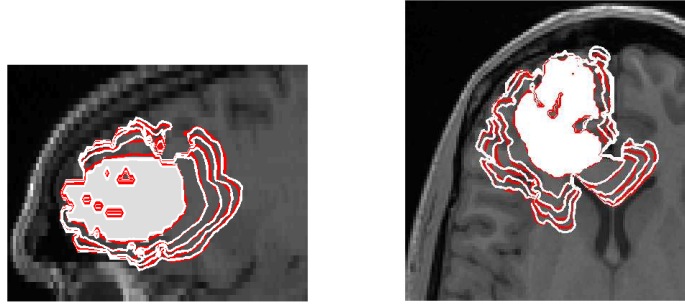
(c) Comparison of iso-density contours

Figure 7.2: Example of an extrapolated image for a synthetic tumor (the median tumor in the frontal lobe shown in Figure 7.1). (a) The image ($u_0 = 0.4$) created for a synthetic tumor is shown, where the white region is the visible part in the images. The low density infiltration, which is normally not visible in the image, is also shown in color from yellow (high density) to red (low density). (b) The extrapolated low density infiltration computed by our method starting from the visible part of the tumor (c) Several iso-density contours of the originally simulated tumor distribution (red solid) and the corresponding ones of the extrapolated distribution (white solid) are shown for comparison. We observe that the global resemblance between the distribution of the synthetic tumor and the extrapolated one is very high.

t days after the detection we define the error measure $\epsilon_v(t)$.

$$
\begin{aligned}
\epsilon_v(t) &= \frac{1}{2}[dist(\Gamma_1^v, \Gamma_2^v) + dist(\Gamma_2^v, \Gamma_1^v)] \qquad (7.1) \\
\Gamma_1^v &= \{x | u(x,t) = v\} \\
\Gamma_2^v &= \{x | \tilde{u}(x) = v\} \\
dist(A,B) &= \frac{1}{\sharp A} \sum_{a \in A} dist_{min}(a, B),
\end{aligned}
$$

where $dist_{min}(a, B)$ is the minimum Euclidean distance between point a and the set B, v is a density value for which the iso-density surfaces of u and $\tilde{u}$ are extracted and $\tilde{u}$ is extrapolated based on the image taken at time t. Using this the total resemblance error between two distributions at a given image taken t days after the detection is defined as:

$$\epsilon(t) = \frac{1}{\mathcal{V}} \sum_{v \in V} \epsilon_v(t), \tag{7.2}$$

where V is the set of density values spanning the low density region. We have 16 iso-density values in the set V with the minimum $v_{min} = 0.005$, which are logarithmically spaced to ensure that the corresponding iso-density contours will be equally spaced (due to the exponential drop of the front profile). This global error criterion $\epsilon(t)$ is the average over different values and provides a global spatial resemblance measure.

In Figures 7.3(a) and (b) we plot $\epsilon(t)$ for different time instances showing the resemblance between estimated and the actual tumor cell density distributions. To better understand the quality of the extrapolation method for different parameters, we plot the error measure for tumors with different diffusion and proliferation rates and for tumors at different locations (one at a region with heterogeneous tissue type and the other at a region with homogeneous tissue type). In Figures 7.4(a) and (b) we show $\epsilon_v(t)$ at $t = 200$ *days* after the detection for different v values to show the change of the error measure with respect to the iso-density contour value.

Observing Figures 7.3 and 7.4 we notice that the difference between the two profiles remains within the range of $[0, ..., 1.5]$ mm, which tells us that the extrapolated distribution remains within 1 to 2 voxel distance from the actual one (voxel size is $1 \times 1 \times 2.6$ mm^3). Analyzing the change of this difference with respect to several parameters, we can state the followings about the quality of the extrapolation method in approximating the low density parts of a reaction-diffusion process:

- The average distance between the two distributions remains less than 1.0 mm for all cases. The worst case error is reached at day 300 however, the difference is not significant.

- *When the ratio between diffusion of tumor cells and the proliferation rate (d/ρ) is low, the discrepancy between the extrapolated distribution and the real one is lower.* When this ratio is higher the error seems to be higher. The reason for this is that as the dispersion of tumor cells is faster the tumor cell density distribution covers a larger space. Extrapolating a larger space brings higher error because as we go further away from the tumor delineation we accumulate errors. Therefore, the difference between the two distributions rises. Moreover, we estimate the tumor cell distribution created by a reaction-diffusion process with a convection one. As the process is dominated by diffusion the effect of the curvature on the profile increases and raises the discrepancy.

- *When the anisotropy coefficient d_w/d_g is lower the extrapolation is closer to the actual distribution.* The reason for this is that as the convection process estimates well the spherical growth. When there is anisotropy, the growth diverges from spherical growth and the dynamics of diffusion becomes more
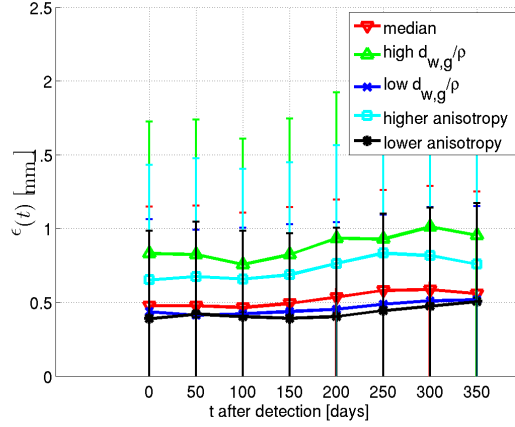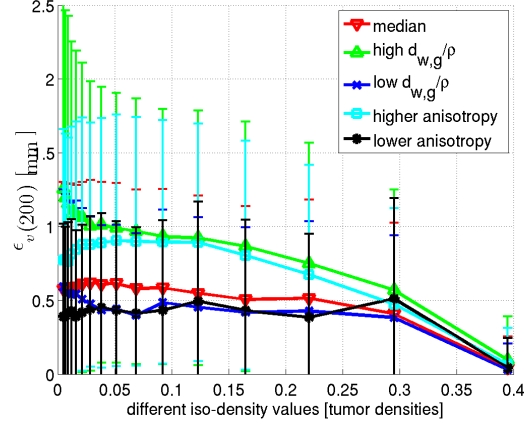
(a) homogeneous tissue region
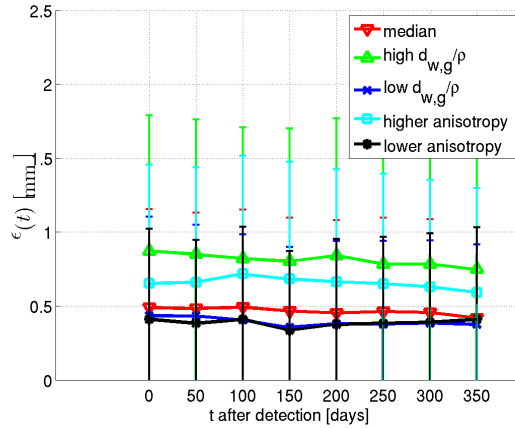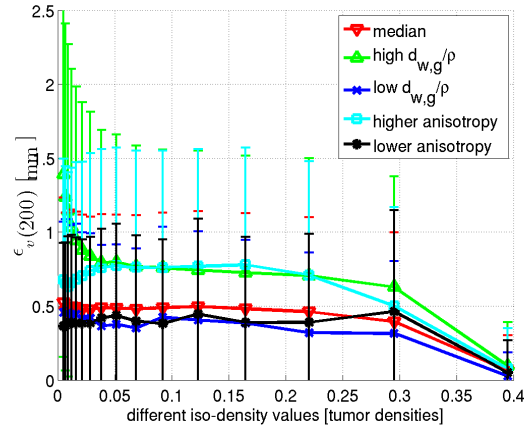

(b) heterogeneous tissue region

Figure 7.3: Figures demonstrate the global difference between the actual and the estimated tumor cell density distributions beyond the visible mass of the tumor at different time instances. Figures (a)-(b): The global resemblance metric $\epsilon(t)$ and its change in time for 10 different tumors with different diffusion and proliferation rates and at 2 different locations are demonstrated. The mean global difference between two distributions remain within 1 voxel, smaller than 1.0 mm for all cases. (Red: high $d_{w,g}/\rho$, Blue: low $d_{w,g}/\rho$, Black: median, Green: lower anisotropy, Cyan: higher anisotropy.)

important. Therefore, the error we make by estimating diffusion by convection becomes more apparent.

- $\epsilon_v(t)$ *increases as v decreases suggesting that the difference between the extrapolated and the actual distribution increases as we move away from the visible part of the tumor.* This is due to our construction of the extrapolation as an integral solution which causes an accumulation of errors. However, the mean

(a) homogeneous tissue region

(b) heterogeneous tissue region

Figure 7.4: The differences between the corresponding iso-density contours of the actual and the estimated low density infiltration regions for different density values for the image taken 200 days after detection are shown. Figures (a)-(b) For the 10 tumors, $\epsilon_v(200)$ is plotted for different iso-density contour values v. The values show that the error of approximation at different iso-density values remain within a 1 to 2 voxels, smaller than $1.5mm$ in all cases. (Red: high $d_{w,g}/\rho$, Blue: low $d_{w,g}/\rho$, Black: median, Green: lower anisotropy, Cyan: higher anisotropy.)

error in this case remains below 1.5 mm for all cases, which corresponds to 1.5 voxels.

- Although we see some difference between the $\epsilon(t)$ and $\epsilon_v(t)$ plots for the tumors placed in different locations of the brain, it is not significant to draw a conclusion about the effect of the tissue composition on our formulation.

7.3   Comparing Irradiation Margins

Radiotherapy has an important role in treating invasive brain tumors as a spatial treatment. The target irradiation region is constructed based on the tumor geometry visible in medical images. It contains the visible tumor plus a constant margin around the delineation to deal with the low cell density infiltration of the tumor not visible in images. This constant margin approach does not take into account the growth tendencies of the tumor, particularly the differential motility of tumor cells in the white and the gray matters.

The method to extrapolate the tumor cell density distribution beyond the visible part of gliomas proposed in this work gives us the opportunity to tailor the irradiation region based on the growth dynamics captured by the reaction-diffusion models. In order to demonstrate this, in this section we construct *variable* irradiation margins based on the extrapolated density distributions. Then, we geometrically compare the potential efficacy of such margins with the conventionally used constant margins in the case of synthetic tumors simulated by reaction-diffusion models explained in 6.2. In the construction of the variable margin, we use the same quantity of irradiation as the constant margin (same total volume to be irradiated) but reshape it according to the estimation of the low density infiltration.

Since for the synthetic tumors, the cell density at every location is known, we carry out a quantitative comparison. We do this by testing the *spatial accuracies* of both of these approaches via two different clinically critical measures:

- R: number of tumor cells not targeted

- Vol: volume of healthy tissue targeted by the irradiation margin.

In Chapters 4 and 6 we have shown the reaction-diffusion model in its normalized form. In order to compute the R value we need to return to the dimensional form by including the maximum number of tumor cells a voxel of brain can handle. Consistent with the values given in [Tracqui 1995] in this part we use that a voxel of $1 \times 1 \times 2.6$ mm^3 can hold a maximum of 9.1×10^4 tumor cells. Therefore the values given in this analysis are found and should be considered with respect to this value.

We construct the constant margin irradiation region M_c by taking the $2cm$ margin around the visible part of the tumor and removing the skull and the ventricles from it as shown in Figure 7.5(b). The construction of the variable margin irradiation region M_v is done in two parts. First we construct the low density infiltration estimate starting from the visible part of the tumor, creating M_v^1, and then we include a constant error margin around it based on the error values we found in Section 7.2 creating M_v^2. The variable irradiation margin M_v is the union of these two regions, see Figure 7.5(c). In order to ensure that the amounts of irradiation (assumed to be given by the volume) in M_c and M_v are the same, we tailor the different parts of M_v as

$$
\begin{aligned}
M_v^1 &= \{x | \tilde{u}(x,t) > \delta\} \\
M_v^2 &= \{x | dist_{M_v^1}(x) < \epsilon_d\}
\end{aligned}
$$
$$
\text{choose } \delta \text{ such that } Vol(M_v^1 \cup M_v^2) = Vol(M_v) = Vol(M_c). \qquad (7.3)
$$

where $dist_{M_v^1}$ is the distance transform in the brain from the set M_v^1, ϵ_d is the error margin we would like to include in our irradiation region and δ is the dependent parameter. We determine δ so that the volume constraint given in Equation 7.3 is satisfied. Based on the error measures we found in the Section 7.2 we set $\epsilon_d = 4mm$ so that the error margin would be large enough to take into account the $\epsilon(t)$ $\forall t$ and $\epsilon_v(t)$ $\forall v$.

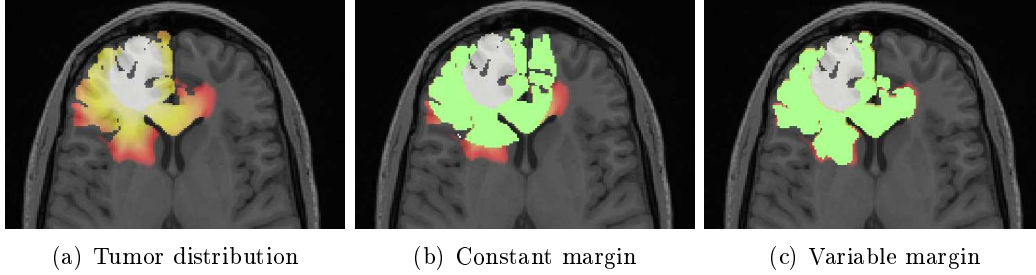(a) Tumor distribution   (b) Constant margin   (c) Variable margin

Figure 7.5: The proposed variable irradiation region construction takes into account the growth dynamics of the tumor. Figure shows the two irradiation margin construction approaches and the synthetic tumor cell distribution they aim to target. Figure (a) shows the low density cancerous cell distribution of the synthetic tumor. The white region corresponds to the visible part (visible in the image) while the colored region is the infiltration non visible in the image. Figures (b) and (c) show constant and variable irradiation regions overlaid on the tumor distribution respectively. Transparent green regions represent the areas set to be irradiated. For the synthetic tumor the variable margin better covers the extent of the infiltration therefore might provide a better targeting.

As in the previous section we carry our analysis for the 10 different tumors consisting 5 different growth parameter sets at 2 different locations and at images taken at different time instances. The comparison between the constant and the variable irradiation margins are given in Figures 7.6-7.10, where R and Vol graphs are plotted. Analyzing the results given in Figures 7.6-7.10 we notice that including the tumor growth dynamics in tailoring the irradiation margin greatly improves the spatial targeting of the therapy in the case of synthetically grown tumors. Observing these figures we see that for all the cases we have experimented with, the R and Vol curves for the variable irradiation margin remains well below the curves for the constant margin, with a great difference in most cases. For example 350 days after the detection of the tumor the difference in number of tumor cells targeted between the two approaches can go up to 6×10^8 $Cells$. On the other hand the difference in volume of healthy tissue targeted between the constant and variable margin approaches goes up to 13 cm^3. These values suggest that assuming tumor growth tendencies are well captured by reaction-diffusion models, the variable irradiation margin is more efficient in targeting tumor cells and irradiating less healthy brain tissue. Moreover, we can state the followings after observing the graphs:

- Looking at the R graphs we notice that the difference between the constant
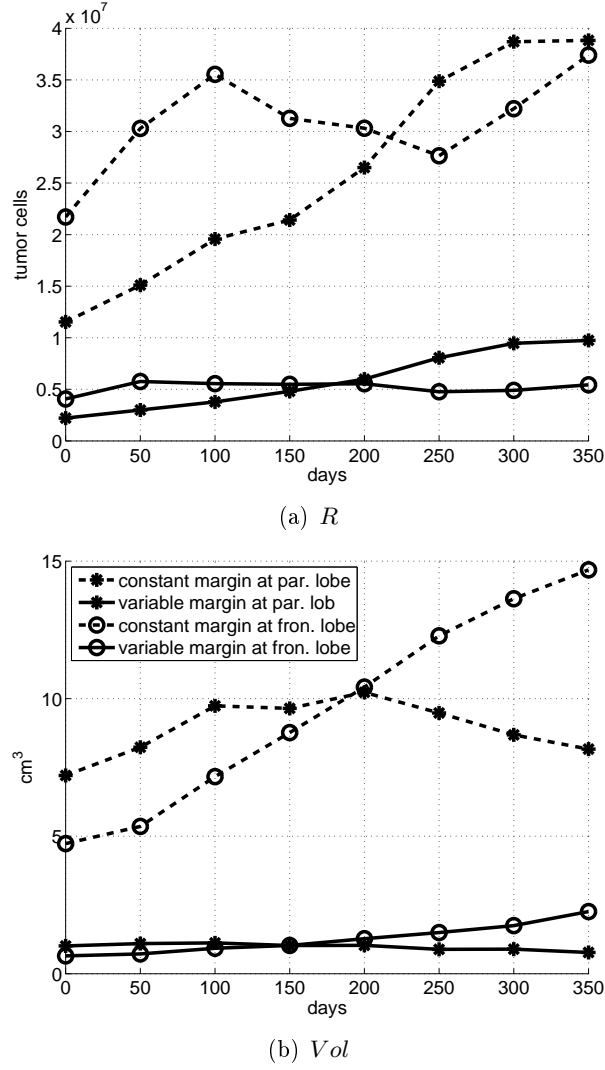
(a) R

(b) Vol

Figure 7.6: R and Vol vs. time plots for the synthetic tumor: median (see the table in Figure 7.1). Graphs show the difference between the constant and variable region irradiation in the case of the synthetic tumor. R represents the number of tumor cells **not** targeted by the irradiation. Vol represents the volume of healthy (tumor free) tissue targeted. Dashed lines are the plots obtained with the constant margin while the solid ones are the ones obtained with the variable margin. Plots obtained for tumors with the same parameters but at different locations (par=parietal lobe, fron=frontal lobe, see Figure 7.1) are plotted on the same graph. The variable irradiation margin seems to target more tumor cells (difference goes up to 3.5×10^7 cells) and less healthy tissue (difference goes up to $13 \ cm^3$).

and the variable margins in targeting tumor cells increases as time passes. For example in the average diffusion rate case for the tumor at the parietal lobe, the difference between targeted tumor cells rises from 1×10^7 to 3×10^7 from
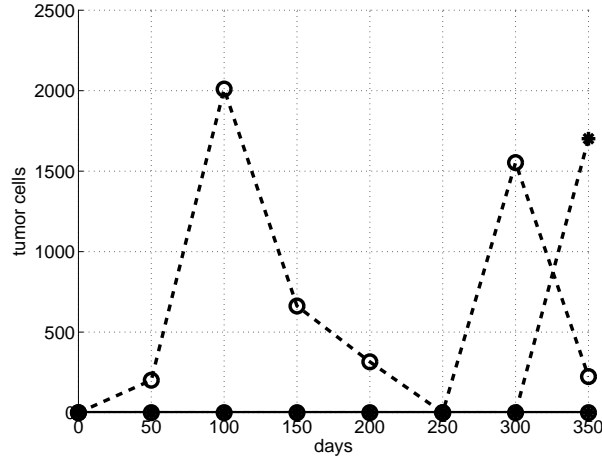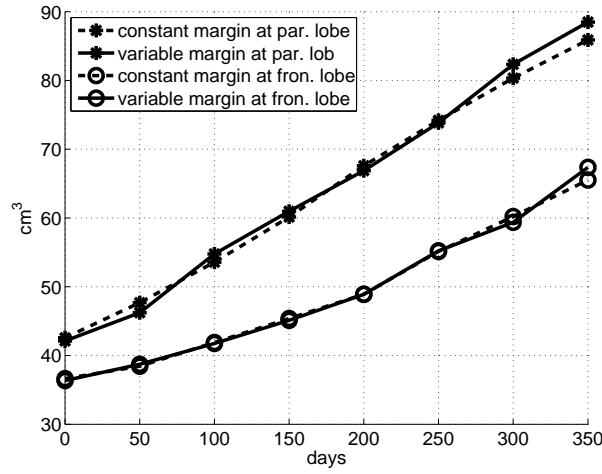
(a) R for $u_0 = 0.4$

(b) Vol for $u_0 = 0.4$

Figure 7.7: R and Vol vs. time plots for the synthetic tumor: low $d_{w,g}/\rho$ (proliferation dominated growth). Dashed lines are the plots obtained with the constant margin while the solid ones are the ones obtained with the variable margin. Values obtained at two different locations are plotted on the same graph. We see that for slowly diffusing tumors the difference between the variable and constant margin is very low.

the image taken at day 0 to the one taken at day 350. This is related to the fact that tumor cells infiltrate more as time passes yielding a more anisotropic distribution in the tissue, and the variable margin takes this into account.

- Comparing Figures 7.6, 7.7 and 7.8, we observe that both schemes are more successful in targeting tumor cells when the diffusion is less and the proliferation is higher (the growth is more proliferation dominated). This is due to the fact that with higher diffusion tumor cells infiltrate further away in the
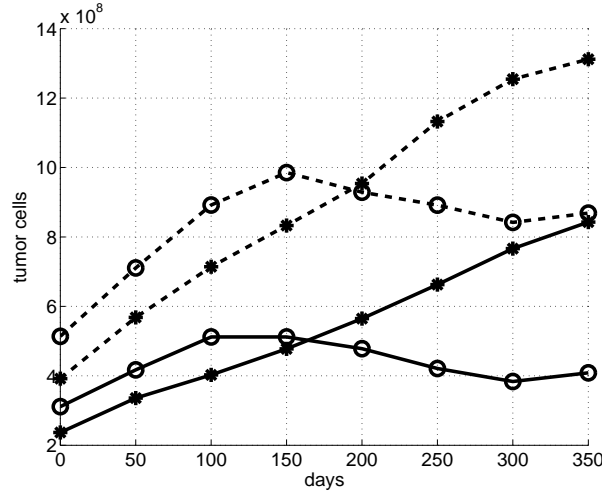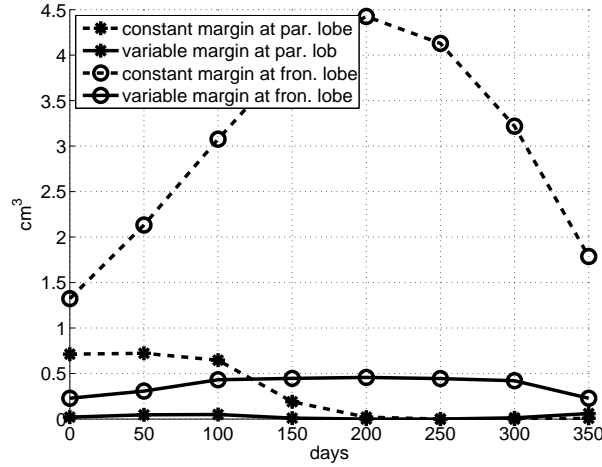
(a) R for $u_0 = 0.4$

(b) Vol for $u_0 = 0.4$

Figure 7.8: R and Vol vs. time plots for the synthetic tumor: high $d_{w,g}/\rho$ (diffusion dominated growth). Dashed lines are the plots obtained with the constant margin while the solid ones are the ones obtained with the variable margin. Values obtained at two different locations are plotted on the same graph. Although the curves of R look close their numerical difference goes up to 6×10^8 tumor cells.

brain parenchyma creating a need for a larger irradiation margin to achieve the same success rate. We also note that the difference between the two schemes is nearly none for the tumor which does not diffuse much. However, as the tumor becomes more diffusive we observe that the difference between the two schemes, both in terms of tumor cells not targeted and healthy tissue irradiated, increases.

- Comparing Figures 7.6, 7.9 and 7.10, we see that when the anisotropy is higher
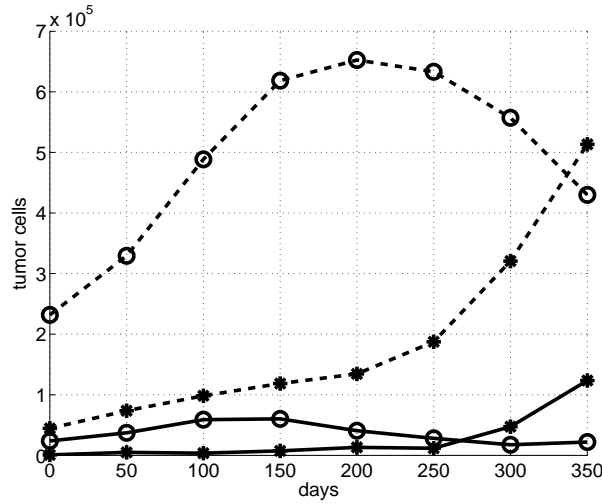
(a) R for $u_0 = 0.4$

(b) Vol for $u_0 = 0.4$

Figure 7.9: R and Vol vs. time plots for the synthetic tumor: lower anisotropy. Dashed lines are the plots obtained with the constant margin while the solid ones are the ones obtained with the variable margin. Values obtained at two different locations are plotted on the same graph.

the difference in number of tumor cells not targeted between the two schemes is much higher. Also the difference in the volume of healthy tissue irradiated is greater in the higher anisotropy case. This is expected since as the anisotropy is lower the tumor grows "more" spherically and the difference between the variable and the constant margin decreases.

- Observing Vol plots we notice that as the diffusion rate increases and when the underlying media becomes more heterogeneous (white-gray heterogeneity) the variable margin approach becomes more efficient in distinguishing healthy
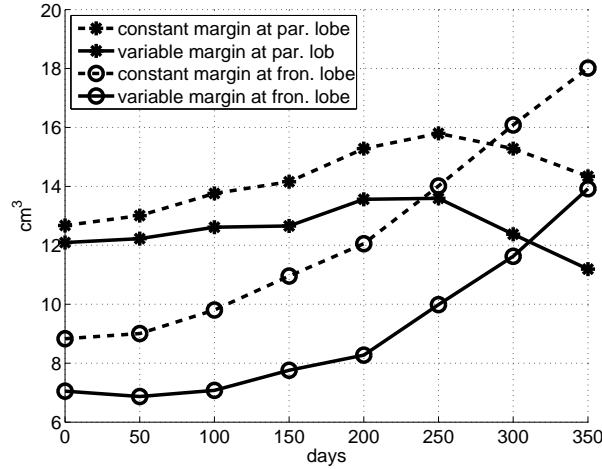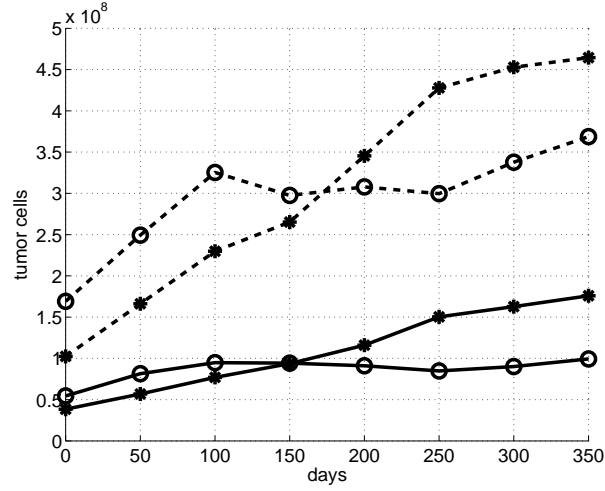
(a) R for $u_0 = 0.4$
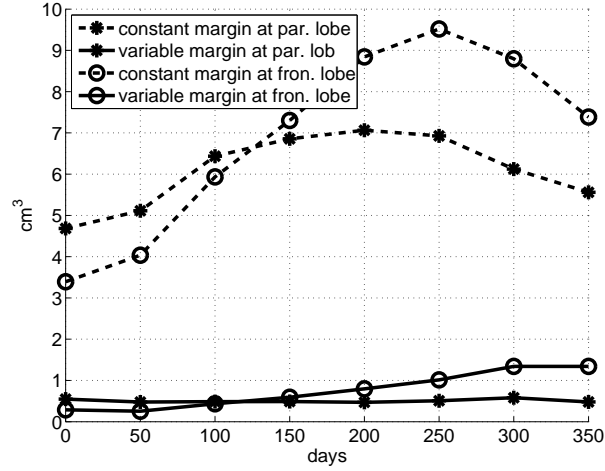
(b) Vol for $u_0 = 0.4$

Figure 7.10: R and Vol vs. time plots for the synthetic tumor: higher anisotropy. Dashed lines are the plots obtained with the constant margin while the solid ones are the ones obtained with the variable margin. Values obtained at two different locations are plotted on the same graph.

and infiltrated tissue. This is also related to the fact that the variable margin approach takes into account the anisotropic nature of the tumor growth.

7.4   Conclusion

In this chapter, we have addressed the problem of limited tumor visualization of medical images through mathematical tumor growth modeling. Especially for invasive gliomas, although images can show the mass part of the tumor they are not able to visualize the low density infiltration which causes a serious problem in treating

this pathology. We proposed a novel formulation which integrates macroscopic tumor growth models with medical images to extrapolate the low density infiltration regions of gliomas starting from the visible part of the tumor. In deriving the proposed formulation, we have started from the well known reaction-diffusion models assuming that the growth dynamics of gliomas are well captured by this type of modeling. We then used asymptotic approximations of reaction-diffusion models to formulate the proposed solution to the mentioned problem of predicting the extents of the tumor infiltration. The resulting formulation, in a sense, complements the imaging process and provides a larger view of the extent of the tumor infiltration. The proposed extrapolation method can also be applied to other applications which are modeled by partial differential equations which bear traveling wave solutions (e.g. wound healing [Maini 2004], cardiac modeling [Franzone 1990]).

One of the most important assumptions we have made in this work was that the tumor growth dynamics are well captured by the reaction-diffusion type models as proposed in different works such as [Swanson 2002b, Jbabdi 2005, Clatz 2005]. These models cover the general features of tumor growth such as macroscopic heterogeneity and anisotropy of tumor growth and provide a good match with clinical cases [Swanson 2008b]. Reaction-diffusion models have few parameters which can be directly related to the information available in the medical images. Therefore, the models can be adapted to specific patient cases. Although reaction-diffusion models do not include microscopic spatio-temporal factors affecting the growth process, this problem can be overcome as more image modalities become available in the clinical setting. One can imagine that when high resolution metabolical images become available, which would allow us to visualize different integrins and enzymes for each patient, then the proposed formulation can be adapted such that it takes into account different spatio-temporal effects yielding a more realistic prediction of the extent of tumor infiltration.

In Chapter 7, we performed two types of experiments evaluating the proposed extrapolation method. First, we showed that the tumor cell density distribution extrapolated using the proposed method remains within the vicinity of 1-2 voxels of the actual distribution of the tumor beyond its visible mass. This demonstrates that the extrapolation formulation is successful in reconstructing the solution of the reaction-diffusion model at a given time instance from sparse observations like the image. This approximation can naturally be improved by including the effect of tumor fronts curvature and convergence characteristics of the reaction-diffusion equation the expense of increasing complexity and loosing generality.

In the second part of Chapter 7 we have shown the significance of using the proposed extrapolation scheme for radiotherapy. We constructed variable irradiation regions, which take into account the possible infiltration extents of gliomas, and compared them to the constant margins used conventionally in clinical practice. The geometrical comparisons presented demonstrates that the proposed method has the potential to target more tumor cells while harming less healthy brain tissue. This suggests the possible higher efficiency we can obtain in radiation therapy by using irradiation margins taking into account the growth dynamics. Besides the static geometrical comparisons, one can also compare the dynamic time course of radiotherapy under the two different schemes. However, for this purpose the dose

delivery mechanisms and the response of tumor cells to the radiation should also be modeled. Considering the discrete nature of tumor response to radiotherapy (cell cycles, varying mitotic potential of tumor cells and phase durations) using a discrete model for these dynamics might be more appropriate. There have been several works on discrete models and tumor response to radiotherapy using such models, [Drasdo 2005, Stamatakos 2006b]. Using a combination of the continuum approach given in this work and a discrete model as explained in the cited works one can simulate the radiotherapy process under the two different schemes and compare their outcomes. However, the modeling of tumor response to therapy and therefore this comparison are outside the scope of this work.

In all the experiments shown in this chapter we tried to stay in the limits of the clinical practice. Namely, for the synthetic images we created, we did not assume that we knew the parameters of the growth model. We personalized the general growth model to fit these images through estimating the parameters of the model (Chapter 4) and then using these parameters to perform the extrapolation. In this sense, we tried to simulate realistic clinical conditions. On the other hand there still remains a big issue regarding the parameter estimation in the context of radiotherapy. Most of the time the radiotherapy starts as soon as the tumor is detected, specially for the high grade gliomas. Therefore, in order to have a more realistic tool we also need to find a way to estimate the parameters of the growth model from a single image. This problem is not tackled int his thesis however, it is one of our ongoing research topics.

The results and experiments we presented in this work are all synthetic cases. In order to understand the real benefits of the formulation proposed in this work, validations with real patient cases and clinical validation should be performed. Although we have not performed them, we envision two types of validations to be done. The first one is the validation of the proposed extent of the tumor infiltration. Through microscopic investigations of post-mortem brain cross-sections or animal models we can determine the real tumor cell distribution in the brain tissue *ex-vivo*. Moreover, newly developing techniques for *in-vivo* microscopy can be used to obtain tumor cell distribution for the patients [Vercauteren 2008]. The comparison of this distribution with the extrapolated one would let us understand how close we can get to the real infiltration margin using the proposed method. After the *in-vivo* validation, clinical validations should also be performed to understand whether adapting the irradiation margins of the radiotherapy to the extrapolated infiltration extent of tumor is beneficial or not. Such an adaptation may suggest critical structures to be irradiated while this may turn out to be harmful for the patient.

In this chapter we have shown how mathematical growth models can be applied in the therapy process. Our focus was given to radiotherapy but chemotherapy can also benefit from the mathematical models and simulations obtained from them. New therapy agents proposed in the literature [Batchelor 2007, Ricard 2007] can be tested extensively using the mathematical simulations while, the usage of already existing drugs can be optimized based on virtual experiments [Stamatakos 2006a, Swanson 2002a].

Anisotropic Fast Marching

Contents

Context

The importance of a specific type of partial differential equation the "anisotropic Eikonal equation" has become evident in Chapters 4 and 6. In this chapter we propose and briefly analyze a numerical method to solve such equations fast and accurately. Such a method gives us the basic tool to solve the problems mentioned in the previous chapters.

8.1 Introduction

In the attempt to bridge the gap between the reaction-diffusion type growth models to medical images we have encountered static Hamilton-Jacobi equations and in particular anisotropic Eikonal equations frequently in the previous chapters. We have seen that the reaction-diffusion type growth models mathematically describe the evolution of tumor cell density distributions. However, the images can only visualize "delineations" of tumors, which are assumed to be iso-density surfaces of the tumor density distribution. Both in the case of formulating the growth speed of this delineation and in extrapolating the tumor cell distribution beyond the visible part in the image we ended up with a static Hamilton-Jacobi equation of the form

$$F\sqrt{\nabla T' D \nabla T} = 1 \tag{8.1}$$
$$T(\Gamma) = g(x),$$

where T is an implicit function (which we refer to as "time" in this chapter), D is a tensor (positive definite matrix) , F is a speed term, Γ is a surface where the Dirichlet type boundary conditions for T is defined as $g(x)$. In the previous chapters we have seen that F is usually a spatially varying function which might depend on

T and its derivatives. In this chapter we focus our attention on the case where F is a spatially varying function that does not depend on T nor its derivatives. In this case Equation 8.1 takes the form of an *anisotropic Eikonal equation.* Although we focus on this specific type of equation, this does not constrain us from applying the methodology explained here to more general cases. As we have seen in Chapter 4 through an appropriate iterative scheme we can solve for more general F using the scheme explained here.

The anisotropic Eikonal equations are not inherent to tumor growth modeling. There are many other applications where these equations arise, e.g., cardiac electrophysiology, wound healing, geology. Therefore, numerical solvers for these equations are needed in many different domains as the one we are interested in.

There have been many different ways proposed to solve equations with the form of Equation 8.1 or in general convex, static Hamilton-Jacobi equations. These ways can be coarsely classified into four: algorithms using single-pass methods [Sethian 2003], sweeping methods [Qian 2006], iterative methods [Kao 2005] and embedding methods [Osher 1993]. Single-pass methods start from points where time (T) values are already known and follow the *characteristic direction* of the PDE to compute T at other points. This approach is based on the fact that in equations such as Eqn. 8.1, the value of T at a point is only determined by a subset of its neighboring points, which lie along the characteristic direction [Kevorkian 2000]. In the isotropic case, where $D = d\mathbf{I}$ is an isotropic tensor, these methods are very efficient because they follow the gradient direction, which coincides with the characteristic direction [Sethian 1999]. In other words, they only use immediate neighbors of a point with lower values of T to compute the new arrival time at that point using an upwind scheme. These concepts are explained in detail in Section 8.2. In the anisotropic case, the characteristic direction does not necessarily coincide with the gradient direction and the same idea used for isotropic case yields false results. In order to deal with this, Sethian and Vladimirsky enlarged the neighborhood around a point used to compute the new arrival time such that the characteristic direction remains within the neighborhood [Sethian 2003]. But size of the enlarged neighborhood increases with increasing anisotropy of D. Unfortunately, this results in large number of points used to calculate new values and a high computational load in case of high anisotropies.

Sweeping methods use the same idea of characteristics as the single-pass methods however, they do not start from the known points. Instead they sweep the domain in many different directions and update the values at each voxel at each sweeping, [Qian 2006, Kao 2005]. By using many different directions they make sure that for each voxel at least one sweeping direction matches the characteristic direction of the PDE. The sweeping continues until the computed T map converges. These methods do not have a problem with anisotropy. However, depending on the spatial variation of D and the amount of anisotropy, these methods might need a high number of sweepings to converge, and therefore, high computation times. Moreover, they need an ordering of the underlying mesh to sweep the domain, which might not be trivial to obtain for general meshes.

Iterative methods start from an initial distribution of T and iterate using upwind, monotone, and consistent discretization until T satisfies the Equa-

tion 8.1, [Rouy 1992]. They use minimization techniques at each iteration to find the T at the next iteration. As it is the case for the sweeping methods, iterative methods might take a long time to converge in the case of spatially varying and/or highly anisotropic D.

The embedding methods do not solve the anisotropic Eikonal equation directly. They transform the static Equation 8.1 into a dynamic Hamilton-Jacobi equation [Osher 1993]. This transformation consists of embedding the iso-time surfaces of T as zero level-sets of another implicit function and transforming the gradient of T as follows

$$v(x,t) = 0 \quad \text{for} \quad \{x|T(x) = t\} \tag{8.2}$$

$$\frac{v_x}{v_t} = T_x \ , \ \frac{v_y}{v_t} = T_y \ , \ \frac{v_z}{v_t} = T_z. \tag{8.3}$$

where the v is a time varying implicit function and the subscripts denote partial derivatives. As a result of this transformation Equation 8.1 becomes

$$v_t - F\sqrt{\nabla T' D \nabla T} = 0, \tag{8.4}$$

which is a dynamic equation. This equation uses the idea of level-sets as proposed in [Sethian 1999]. Based on this it profits from subvoxel accuracy and many different numerical methods proposed to solve it [Jiang 2000, Bryson 2003, Sethian 1999]. On the other hand, initializing the implicit function v from a given surface and solving it can be computationally costly.

In this chapter, we propose an efficient and accurate algorithm to solve the anisotropic Eikonal equation given in Equation 8.1. Our algorithm is a single-pass method that is based on the well known "Fast Marching" methods [Sethian 1999]. Contrary to the single-pass method proposed in [Sethian 2003], through including "recursive correcting" we manage not to increase the neighborhood that is used to compute the value at a given point. We detail our algorithm in Section 8.2. In Section 8.3, we compare our algorithm to one of the state-of-the-art sweeping methods [Qian 2006]. Moreover, we provide some analysis on the effect of the anisotropy on the performance our algorithm.

8.2   Method

In this section first we review some of the basic concepts about Hamilton-Jacobi equations such as "characteristic directions" and "group velocity" necessary to explain our method. Following these concepts we review the well known Fast Marching method and see why it fails in the case of anisotropic equations. We then detail the proposed algorithm.

8.2.1   Basic Concepts

In order to understand the basic concepts for first order Hamilton-Jacobi equations let us start by a simple equation

$$Fu_x + u_t = 0 \tag{8.5}$$

$$u(x,0) = f(x), \tag{8.6}$$

where subscripts denote partial derivatives, F is a scalar constant and $f(x)$ is the initial condition. The solution for this equation is given by

$$u(x,t) = u(x - Ft) = f(x - Ft). \qquad (8.7)$$

In this solution we notice that the value of u remains constant along the vector $\mathbf{V} = F\mathbf{i} + \mathbf{j}$, where i is the unit vector in x and j is the unit vector in the t direction. This vector is called the *characteristic vector* of the PDE given in Equation 8.5 (and its direction is called the *characteristic direction*). The lines that are parallel to this vector are called *characteristic lines* [Strauss 1992]. In Figure 8.1 we show
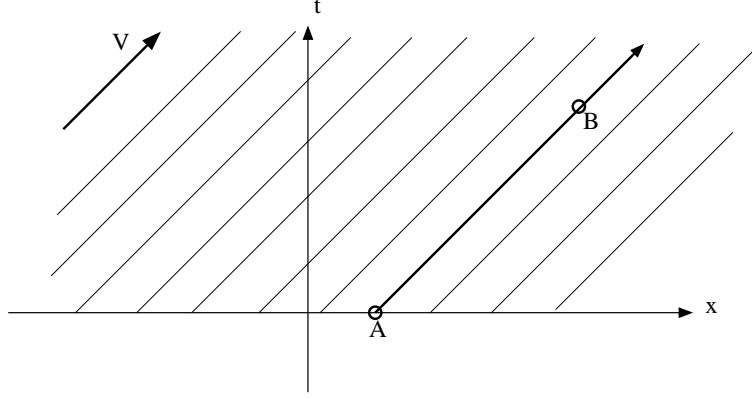

Figure 8.1: Figure shows the characteristic lines for an example PDE in the form of the Equation 8.5. Values of u along these lines are constant. As a result $u(B)$ is only defined by $u(A)$.

an example demonstrating characteristic lines in the (x,t) coordinate system. Each line represents a characteristic line and by definition the value of u is constant along each line. As a result, if we pick a point B in this coordinate system, the value of u at this point only depends on the value of u at A and to none of the other points. In other words the *domain of dependence* of B is point A and the line connecting these two points. On the other hand, the value of u at A is carried along the half line $\overrightarrow{AB}$. Along this line all the points will have the same value of A. In other words the *domain of influence* of A is the line $\overrightarrow{AB}$.

For more general first order Hamilton-Jacobi equations the characteristic lines and the relations of the domain of dependence and the domain of influence do not have to be this simple. Domain of dependence of a point may contain a region and a point may influence a region as shown in Figure 8.2. The numerical schemes that are in the categories of sweeping methods and the single-pass methods use the domain of dependence and influence in their formulation. The basic idea is to compute the value of u at the point B by using other points which are in the domain of dependence of B. Another way to formulate this is to state that the characteristic direction of the PDE at B remains within the neighborhood which is used to compute the value of u at B.
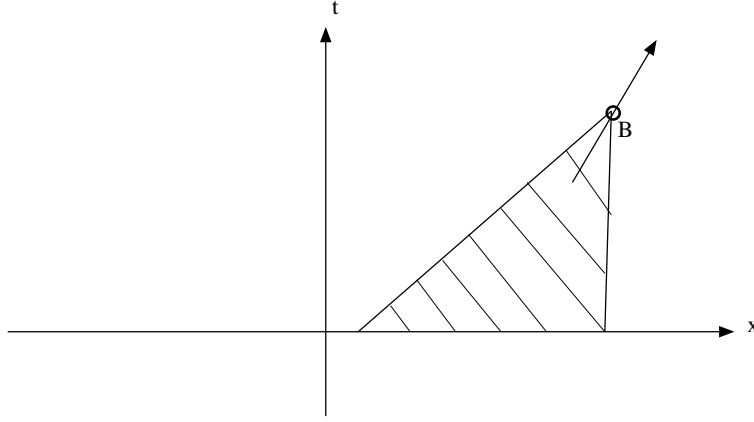
Figure 8.2: Figure shows a more general domain of dependence. The value of u at B is determined by the shaded region. The important point is that the characteristic vector at B shown as an arrow remains within the domain of dependence.

For general first order static Hamilton-Jacobi equations in the form

$$H(x, \nabla T) = 0 \tag{8.8}$$

the characteristic vector is given by the gradient of H with respect to ∇T. In the case of the anisotropic Eikonal equation this characteristic vector is given as

$$\mathbf{V} = \frac{FD\nabla T}{\sqrt{\nabla T' D \nabla T}}. \tag{8.9}$$

As we have explained the direction of this vector is called the characteristic direction. On the other hand, this vector is also called the *group velocity* $\mathbf{V}_g$ a term borrowed from geometrical optics. In explaining the proposed numerical method we will use these two terms frequently.

8.2.2 Fast Marching Methods

The Fast Marching Method (FMM) is an efficient single-pass algorithm for solving the isotropic version of the Eikonal equation:

$$F|\nabla T| = 1 \tag{8.10}$$
$$T(\Gamma) = T_0, \tag{8.11}$$

where the second equation is the Dirichlet type boundary condition [Sethian 1999] and T is the implicit function. For the rest of this chapter we will refer to T as the arrival time function where the value at each point represents the time a virtual front passes over it. The FMM algorithm starts from the surface Γ and constructs the solution T by following the characteristic directions of the equation. It constructs a thin layer around the region for which T values are known, computes the T values in this layer, adds the new points in the known region and marches the thin layer

to sweep the domain. The key ingredient is the choice of the new points which will
be added to the known region. Through the correct choice the FMM follows the
characteristic directions of the PDE. It constructs the T function in an increasing
(decreasing) order starting from the small (high) values proceeding to higher (lower)
ones.

There are two parts of the FMM algorithm. The computation of the T values
using the immediate neighborhood of a point and the overall algorithm. At a point
p the computation of T only uses the neighbors of p whose values are already known.
The discretization at p which takes into account the characteristic directions for the
Equation 8.10 in 2D is given as

$$\left[\begin{array}{l} \max(d_p^{-x}T,0)^2 + \min(-d_p^{+x}T,0)^2 \\ + \max(d_p^{-y}T,0)^2 + \min(-d_p^{+y}T,0)^2 \end{array} \right]^{1/2} = \frac{1}{F_p}, \tag{8.12}$$

where d_p is the discrete derivative operator in the direction of its superscript, i.e.
$d_p^{-x} = (T_p - T_p^{-x})/dx$ with dx as the spacing in the x direction. From this equation
we see that there are two points neighboring p used to compute T_p, let us call them
q_1 and q_2. Equation 8.12 has a quadratic form and its solution can be found easily.
In all cases the roots of the quadratic equation must be real however, there are
two of them. The FMM chooses the minimum of these solutions which satisfies
$T_p \geq max(T_{q_1}, T_{q_2})$.

In order to briefly explain the overall algorithm let us examine a 2D setting.
Assume that there is a point for which the T value is known, the red point in
Figure 8.3(a). The first step is to set a tag for this point as $KNOWN$. Following
this, FMM computes the values of the points adjacent to the known one and sets
their tags as $TRIAL$, shown in green in Figure 8.3(b). The next step is to choose
the $TRIAL$ point with the minimum T value, change its tag to $KNOWN$ and
compute T values for its adjacent points setting their tag as $TRIAL$. Moreover,
the T values at the points that had already the tag $TRIAL$ are updated using
the new $KNOWN$ point, see Figure 8.3(c). The algorithm continues like this, as
shown in Figure 8.3(d), until all the points in the domain have the tag $KNOWN$.
 In Algorithm 5 we summarize the FMM algorithm. In the algorithm we refer the
computation of T at a point by the $UPDATE$ routine, for which the details are
given in Equation 8.12.

The computation of T combined with the overall algorithm creates a single-pass
numerical scheme that which follows the *gradient direction* of T. Due to the fact that
the gradient direction is indeed the characteristic direction for the isotropic Eikonal
equations the FMM algorithm follows the characteristics. In doing so it uses the
correct domain of dependence for each point constructing the correct solution in a
single pass.

The anisotropic Eikonal equation, given as Equation 8.1, poses extra difficulties
for the FMM algorithm. The characteristic direction for the anisotropic equation
does not have to coincide with the gradient direction of T. We see in Equation 8.9
that the characteristic direction of T depends on the tensor D. Therefore, following
the gradient directions the algorithm uses incorrect domain of dependence and yields
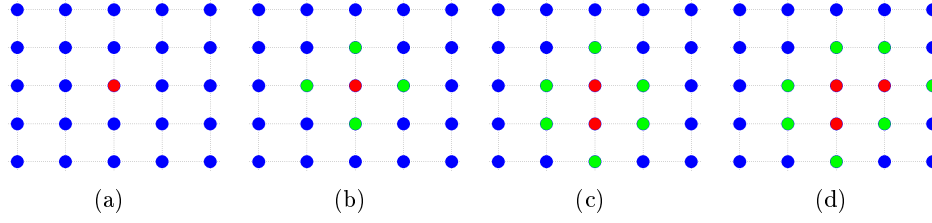false results as shown in Figure 8.4.

Figure 8.3: The steps of the FMM algorithm. (a) Algorithm starts by the known point in red and the unknown ones in blue. (b) It computes the T values at its adjacent points setting their tag as $TRIAL$ in green. (c) Following this it chooses the $TRIAL$ point with the minimum T value and change its tag to $KNOWN$. Using this value it updates the T values at all the $TRIAL$ points and the neighbors of the newly $KNOWN$ point. (d) The algorithm continues in this fashion until all the points in the domain are tagged as $KNOWN$.

Algorithm 5 Fast Marching Method.

  Initialization
  for all $X \in KNOWN$ (red points) **do**
    for all $Y_i \in \mathcal{N}(X)$ and $Y_i \in FAR$ (blue points) **do**
      compute $T(Y_i) \leftarrow \text{UPDATE}(Y_i, X)$
      remove Y_i from FAR and add Y_i to $TRIAL$ (green)
    end for
  end for
  Main Loop
  while $TRIAL$ not empty **do**
    $X \leftarrow \text{argmin}_{X \in TRIAL} \, TRIAL$
    remove X from $TRIAL$ and add X to $KNOWN$
    for all $Y_i \in \mathcal{N}(X)$ and $Y_i \in TRIAL \cup FAR$ **do**
      compute $\overline{T}(Y_i) \leftarrow \text{UPDATE}(Y_i, X)$
      if $Y_i \in TRIAL$ and $\overline{T}(Y_i) < T(Y_i)$ **then**
        $T(Y_i) \leftarrow \overline{T}(Y_i)$
      else if $Y_i \in FAR$ **then**
        $T(Y_i) \leftarrow \overline{T}(Y_i)$
        remove Y_i from FAR and add Y_i to $TRIAL$
      end if
    end for
  end while

8.2.3 Recursive Anisotropic Fast Marching

The recursive anisotropic fast marching, proposed in this chapter, is based on the single-pass idea and it uses immediate neighborhood to compute arrival times. It is based on the principles of the FMM and modifies this algorithm such that the effect of the anisotropic tensor D is taken into account. As a novel step, on top of the FMM algorithm, it adds a recursive correction scheme and uses a more general
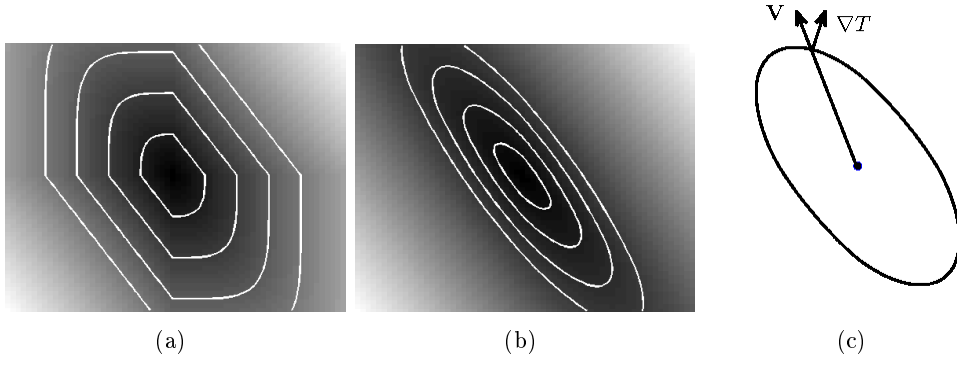
(a)   (b)   (c)

Figure 8.4: Solutions of $F\sqrt{\nabla T' D \nabla T} = 1, T(\text{center}) = 0$ with a constant anisotropic D. The solution of the system obtained using the FMM (left) and the solution solved by anisotropic methods (right). We see that the FMM solution is not correct due to the problem of following the gradient directions and not the characteristic directions. On the schema on the left we show the characteristic direction $\mathbf{V}$ and the gradient direction ∇T. We see that the two directions do not coincide.

formulation to compute the T values at each point. This algorithm works efficiently under general meshes, high anisotropies and highly varying D fields. Moreover, it can be applied to more general forms of static, convex Hamilton-Jacobi equations, which is beyond the scope of this work. In this work we focus on the equation

$$F\sqrt{\nabla T' D \nabla T} = 1 \quad T(\Gamma) = T_0, \tag{8.13}$$

where Γ is a surface on which the T values are known and equal to T_0.

Algorithm

The overall algorithm is similar to the original fast marching method. The main differences are the recursive correction scheme and the computation of T values. The initialization steps for initializing the method are the same. First, we go over points whose value are already known and add them to a list called $KNOWN$. Following this we compute the traveling times for points neighboring the points in the $KNOWN$ list and whose values are not computed yet (such points are kept in the FAR list). We compute the trial T values for these points using only the known points and add them to the $TRIAL$ list while removing them from the FAR list, see Algorithm 6. By neighborhood $\mathcal{N}(X)$ we mean all points directly connected to the point X in some preferred connectivity sense (e.g. 4-8 in 2D and 6-18-26 in 3D Cartesian grid). As explained in the previous section, the FMM algorithm follows the same operations throughout its main loop. (The $TRIAL$ point with the minimum value of T, Y, is removed from the $TRIAL$ list, added to the $KNOWN$ list, trial values of unknown neighbors of Y are computed, if they are in the FAR list they are added to the $TRIAL$ list and removed from the FAR one, and if they are already in the $TRIAL$ list their values are updated.)

Algorithm 6 Anisotropic Fast Marching: Initialization

  for all $X \in KNOWN$ **do**
    for all $Y_i \in \mathcal{N}(X)$ and $Y_i \in FAR$ **do**
      compute $T(Y_i) \leftarrow \text{UPDATE}(Y_i, X)$
      remove Y_i from FAR and add Y_i to $TRIAL$
    end for
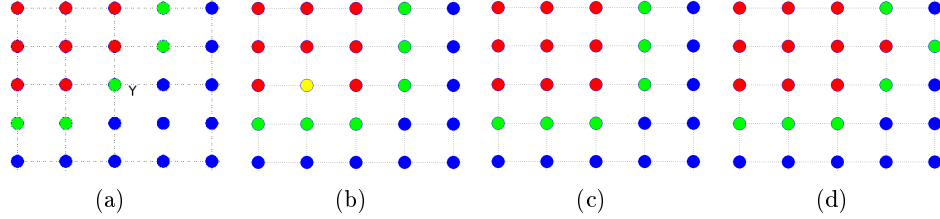 **end for**

(a)   (b)   (c)   (d)

Figure 8.5: The Recursive Correction: (a) Among the $TRIAL$ points the one with the minimum T value is chosen, Y. (b) Beside computing the values for the unknown and trial neighbors of Y we also update the T values of its known neighbors. In the case a lower T value for any of these known neighbors is found it is moved into the $CHANGED$ list as it becomes yellow in the figure. (c) When the main loop starts again it starts from this $CHANGED$ point and updates its neighbors. (d) When the $CHANGED$ list is empty the algorithm continues as the FMM.

In order to take into account the anisotropy in the equation, we insert the recursive correction in the main loop of the FMM. In the main loop we choose the point in the $TRIAL$ list with the minimum value of T, call the point Y, and move it to the $KNOWN$ list, as shown in Figure 8.5(a). At this point, besides computing the trial values of unknown neighbors of Y, we also recompute its known neighbors' values. The reason for this is that when values of these points were computed Y was not used since it was not known. Hence, the characteristic direction may not have been contained in the known neighborhood at the time, which was used to compute their T values. If we obtain a lower value of T during this recomputation we update the value and add the point to the $CHANGED$ list, which holds known points whose values have been changed. In Figure 8.5 a known neighbor of Y is updated and it is added in the $CHANGED$ list as it becomes yellow. This correction is based on the fact that the lowest T value for a point is obtained when the characteristic direction is contained in the neighborhood used in its T values computation [Qian 2006, Sethian 2003]. Every time the main loop restarts it checks if the $CHANGED$ list is empty, if this is not the case then instead of taking a point from the $TRIAL$ list it takes from the $CHANGED$ list. In other words the main loop tries to empty the $CHANGED$ list first. In the example in Figure 8.5(b) the algorithm computes the values around the yellow point and then moves it to the $KNOWN$ list as it becomes red once again, see Figure 8.5(c). If there are no more points in the $CHANGED$ list, in other words no more yellow points, then the

algorithm continues as the normal FMM as seen in Figure 8.5(d). The pseudo code for this algorithm gives a clear summary of the recursive correction in Algorithm 7.

Algorithm 7 Anisotropic Fast Marching: Main Loop with Recursive Correction

---
while $TRIAL$ or $CHANGED$ lists are not empty **do**
  if $CHANGED$ list is not empty **then**
    $X \leftarrow \operatorname{argmin}_{X \in CHANGED} CHANGED$
    remove X from $CHANGED$
  else
    $X \leftarrow \operatorname{argmin}_{X \in TRIAL} TRIAL$
    remove X from $TRIAL$ and add X to $KNOWN$
  end if
  for all $X_i \in \mathcal{N}(X)$ and $X_i \in KNOWN$ **do**
    compute $\overline{T}(X_i) \leftarrow \text{UPDATE}(X_i, X)$
    if $\overline{T}(X_i) < T(X_i)$ **then**
      $T(X_i) \leftarrow \overline{T}(X_i)$
      add X_i to $CHANGED$ list
    end if
  end for
  for all $Y_i \in \mathcal{N}(X)$ and $Y_i \in TRIAL \cup FAR$ **do**
    compute $\overline{T}(Y_i) \leftarrow \text{UPDATE}(Y_i, X)$
    if $Y_i \in TRIAL$ and $\overline{T}(Y_i) < T(Y_i)$ **then**
      $T(Y_i) \leftarrow \overline{T}(Y_i)$
    else if $Y_i \in FAR$ **then**
      $T(Y_i) \leftarrow \overline{T}(Y_i)$
      remove Y_i from FAR and add Y_i to $TRIAL$
    end if
  end for
end while

Local Solver

Up to now we have not detailed the computation of $T(X)$ value using $\mathcal{N}(X)$, namely the $UPDATE$ routine. For the FMM algorithm this routine was simply solving a quadratic equation. In the anisotropic case it is a bit more complicated. We have defined $\mathcal{N}(X)$ as the set of immediate neighbors of X and naturally there exists a set of elements corresponding to this neighborhood, set of triangles ($\triangle_X$) in 2D or set of tetrahedras (TET_X) in 3D. In Figure 8.6 for a 2D example we demonstrate the $\mathcal{N}(X)$ and the $\triangle_X$. The $T(X)$ value both in 2D and in 3D is calculated inside every element using linear interpolation between nodes and solving a minimization problem. We can write this minimization problem using the principles borrowed from geometrical optics. Based on the properties of the anisotropic Eikonal equation we know that there exists a single ray passing from the point X that coincides with the characteristic direction of the PDE and determines the value of T at X. For
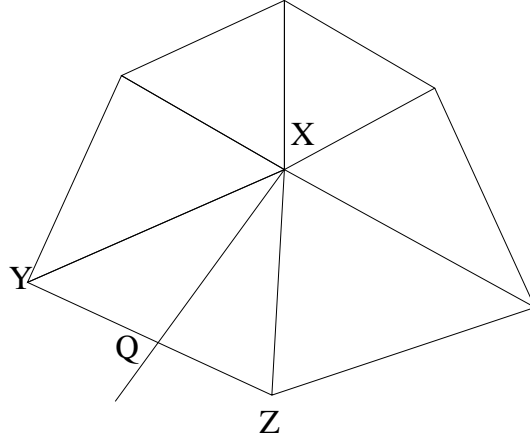
Figure 8.6: For the point X the figure shows the $\mathcal{N}(X)$ and also the $\triangle_X$ corresponding to the neighborhood.

the example shown in Figure 8.6, assume that this ray remains within the triangle $\widehat{XYZ}$, it passes through the point Q and its direction from X is given with the vector $\mathbf{v} = \overrightarrow{XQ}$. Based on the characteristic vector, as defined in Equation 8.9, we can write the relation between the gradient of T and $\mathbf{v}$ as

$$\nabla T = \kappa D^{-1}\mathbf{v}, \tag{8.14}$$

where κ is a scalar constant which ensures that ∇T satisfies the anisotropic Eikonal equation

$$\nabla T' D \nabla T = \kappa^2 (D^{-1}\mathbf{v})' D (D^{-1}\mathbf{v}) = \frac{1}{F^2} \tag{8.15}$$

$$\kappa = \frac{1}{[(D^{-1}\mathbf{v})' D (D^{-1}\mathbf{v})]^{1/2} F} = \frac{1}{[\mathbf{v}' D^{-1}\mathbf{v}]^{1/2} F}. \tag{8.16}$$

From this relationship the group velocity (as given in Equation 8.9) at the point X can be written as

$$\mathbf{v_g} = \frac{F\mathbf{v}}{[\mathbf{v}' D^{-1}\mathbf{v}]^{1/2}}. \tag{8.17}$$

Assuming that the T value at the point Q is known we can apply linear interpolation and find the value of T at X using the group velocity

$$T(X) = T(Q) + \frac{|\overrightarrow{XQ}|}{|\mathbf{v_g}|}, \tag{8.18}$$

where the second part on the right hand side is just distance over speed [Qian 2001]. As a result, once we are given a triangle such as the one $\widehat{XYZ}$ it suffices to find the point Q to find the right value of T at X. Since we know that the correct point Q provides us the lowest possible value of T for X we can formulate the problem

of finding Q as a minimization assuming linearity. The respective minimization problems for 1D, 2D and 3D are given as

$$
\begin{aligned}
f_{1D}(X,Y) &= T(Y) + \frac{[\mathbf{v}_{1D}^t D^{-1} \mathbf{v}_{1D}]^{1/2}}{F} && (8.19)\\
f_{2D}(X,Y,Z) &= \min_{p \in [0,1]} \{T(Y)p + T(Z)(1-p) && (8.20)\\
&\quad + \frac{[\mathbf{v}_{2D}(p)^t D^{-1} \mathbf{v}_{2D}(p)]^{1/2}}{F}\}\\
f_{3D}(X,Y,Z,W) &= \min_{p,q \in [0,1] \times [0,1]} \{[T(Y)p + T(Z)(1-p)]q && (8.21)\\
&\quad + T(W)(1-q) + \frac{[\mathbf{v}_{3D}(p,q)^t D^{-1} \mathbf{v}_{3D}(p,q)]^{1/2}}{F}\}
\end{aligned}
$$

where

- $\mathbf{v}_{1D} = \overrightarrow{YX}$,

- $\mathbf{v}_{2D}(p) = \overrightarrow{YX}p + \overrightarrow{ZX}(1-p)$ and

- $\mathbf{v}_{3D}(p,q) = [\overrightarrow{YX}p + \overrightarrow{ZX}(1-p)]q + \overrightarrow{WX}(1-q)$.

Algorithm 8 Computation of $\overline{T}(X_i) = UPDATE(X_i, X)$

IN 2D
$\overline{T}(X_i) \leftarrow \infty$
for all $\triangle(XX_iY) \in \triangle_{X_i}^X = \{\triangle(XX_iY)|Y \in \mathcal{N}(X_i)\}$ **do**
  if $Y \in KNOWN$ **then**
    $\overline{T}(X_i) \leftarrow \min(\overline{T}(X_i), f_{2D}(X, X_i, Y))$
  else
    $\overline{T}(X_i) \leftarrow \min(\overline{T}(X_i), f_{1D}(X, X_i))$
  end if
end for
IN 3D
$\overline{T}(X_i) \leftarrow \infty$
for all $TET(XX_iYZ) \in TET_{X_i}^X = \{TET(XX_iYZ)|Y,Z \in \mathcal{N}(X_i)\}$ **do**
  if $Y,Z \in KNOWN$ **then**
    $\overline{T}(X_i) \leftarrow \min(\overline{T}(X_i), f_{3D}(X, X_i, Y, Z))$
  else if $Y \in KNOWN$ **then**
    $\overline{T}(X_i) \leftarrow \min(\overline{T}(X_i), f_{2D}(X, X_i, Y))$
  else if $Z \in KNOWN$ **then**
    $\overline{T}(X_i) \leftarrow \min(\overline{T}(X_i), f_{2D}(X, X_i, Z))$
  else
    $\overline{T}(X_i) \leftarrow \min(\overline{T}(X_i), f_{1D}(X, X_i))$
  end if
end for

As in the original fast marching algorithm we only use known points in $\mathcal{N}(X)$ to compute the value T at X. For a given element either triangular or tetrahedral not

all the nodes have to be in the $KNOWN$ list. In such cases we only use the known nodes and compute $T(X)$ using the respective element. As an example, in the case of a tetrahedral element we use Equation 8.21 when all nodes of the tetrahedra are known, Equation 8.20 when 2 nodes are known and Equation 8.19 when only 1 node is known, see Algorithm 8. The minimization of Equation 8.20 has an analytical solution however, the one in Equation 8.21 is not trivial. Instead of solving it with a minimization algorithm, which would increase the computational load, we use the quadratic equation in $T(X)$ obtained by discretizing equation $F\sqrt{\nabla T^t D \nabla T} = 1$ on the nodes of the tetrahedral element. We check if this computed value of $T(X)$ satisfies the causality condition, which is that the characteristic direction should lie inside the element used. Practically this is just computing ∇T using the new computed $T(X)$ on the element and checking if $D\nabla T$ vector resides within the tetrahedra. If this is the case, the minimum lies inside the tetrahedra and it is approximated with the computed $T(X)$. If this is not the case we search the minimum on the triangular sides of the tetrahedra using f_{2D}. This method was proposed by Qian *et al.* [Qian 2006] and it speeds up the overall algorithm greatly. For more details on this please refer to [Qian 2006].

8.3   Experiments

In our experiments we have performed two different type of tests. The first type of tests were intended to demonstrate the recursive anisotropic fast marching can work on different geometries in reasonable computational times. We have tested the proposed algorithm by solving $F\sqrt{\nabla T^t D \nabla T} = 1$ in 2D, 3D Cartesian grid and on surfaces using triangulation where F is taken to be 1. These results are shown in Figures 8.7 and 8.8. Computation times for these results can be found in Table 8.1, where we also compare our algorithm with the sweeping algorithm proposed in [Qian 2006], for which we used our own implementation done in the best possible way. Comparison is only done for cases in 2D Cartesian grid based on the examples provided in the mentioned reference. The sweeping method has been iterated until convergence, where the maximum number of iterations was 12 in the variable D case. In the recursive anisotropic fast marching algorithm the size of the $CHANGED$ list did not exceed 3 for these cases. The following computational times were obtained with Matlab7.1 for 2D cases and C++ for 3D cases on a 2.4GHz Intel Pentium machine with 1Gb of RAM. Cases given in Table 8.1 correspond to images shown in Figures 8.7 and 8.8. The proposed algorithm is fast and visually accurate even in the case of very high and variable anisotropy. Moreover, applying the explained method to general meshes bears no difficulty. In our experiments with triangular meshes on 2D and on surfaces, the algorithm was apparently much faster.

The second tests we have performed aims to understand the effect of the strength of anisotropy on the computation time. In our experiments we have observed that as the strength of anisotropy increases the computation time also increased. In order to test this we performed 2D experiments using spatially homogeneous tensors with

Case (D is anisotropic in all cases)	Sweeping Method [Qian 2006] (seconds)	Anisotropic Fast Marching (seconds)
2D: constant D, 64×64 grid	24.43	16.15
2D: constant D, 128×128 grid: Fig. 8.7(a)	91.06	63.39
2D: spirally varying D, 64×64 grid: Fig. 8.7(c)	80.6076	13.56
2D: spirally varying D, 128×128 grid	319.34	49.48
3D: constant D, $64 \times 64 \times 18$ grid: Fig. 8.8(g)		26
3D: helix D, $64 \times 64 \times 64$ grid: Fig. 8.8(h)		65
3D: constant D, 13000 nodes mesh: Fig. 8.8(e)		2

Table 8.1: Computation times

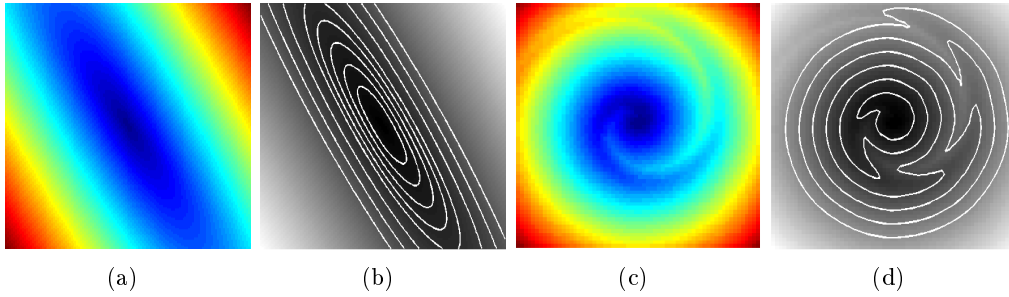(a)   (b)   (c)   (d)

Figure 8.7: a) 2D Cartesian grid, high anisotropy in 120° increasing distance from blue to red, b) iso-contours of a, c) 2D Cartesian grid, D is highly anisotropic inside a spiral following it, isotropic in other regions, d) iso-contours of c.

different anisotropies. We have constructed different tensors as

$$D = V \Lambda V' \tag{8.22}$$

$$V = \begin{bmatrix} 0.6 & -0.8 \\ 0.8 & 0.6 \end{bmatrix} \tag{8.23}$$

$$\Lambda = \begin{bmatrix} \lambda_1 & 0 \\ 0 & \lambda_2 \end{bmatrix}, \tag{8.24}$$

where λ_1 and λ_2 are the first and the second eigenvalues respectively. The strength of the anisotropy of D depends on the ratio between these two eigenvectors. Using different ratios we have constructed the solution of

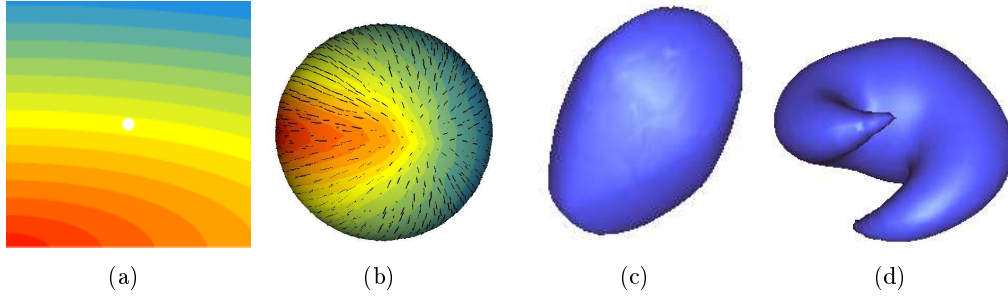$$F\sqrt{\nabla T' D \nabla T} = 1 \quad T(0) = 0. \tag{8.25}$$

Figure 8.8: a) 2D triangular mesh with 13000 nodes anisotropy in x direction, colors represent iso-contours, b) 2D triangular mesh on a surface D is anisotropic and principle eigenvector is shown in black lines, colors represent iso-contours, c) 3D Cartesian grid, anisotropic D d) 3D Cartesian grid, D is highly anisotropic inside a helix following it, isotropic in other regions.

The computation time for this process depends on the ration λ_1/λ_2. In Figure 8.9 we plot the computation time as a function this ratio along with some of the results found with different ratios. We observe from Figure 8.9(a) that as the anisotropy strength increases the computation time increases as well. Moreover, the rate of increase is almost linear.

8.4 Conclusions

The static Hamilton-Jacobi equations and in particular the anisotropic Eikonal equations are frequently encountered in biological modeling. We have seen in the previous chapters the importance of such equations for bridging the gap between clinical images and the mathematical tumor growth models. Besides tumor growth models, such equations arise in cardiac electrophysiology, geophysics, fluid dynamics and computer vision. Therefore, having an efficient, accurate and a fast numerical solver for such equations is crucial.

In this chapter, we proposed the *recursive anisotropic fast marching* algorithm for solving anisotropic Eikonal equations numerically. The algorithm is based on the well known Fast Marching Methods and in that sense it enjoys the many advantages of the single-pass methods. We have shown that the algorithm is successful in handling high anisotropies, which are often encountered in biological modeling, and general meshes. Moreover, we have compared it with one of the state-of-the-art methods to show its relative performance. We have seen that the proposed algorithm is faster than the mentioned method. We have also shown that the computation of the proposed algorithm depends highly on the strength of the anisotropy of the tensor D. The experiments have shown that the computation times was almost linearly related to the strength of the anisotropy.

In the previous chapters we have seen the usage of the anisotropic fast marching method in the context of tumor growth modeling. Having a fast solver gave us the opportunity to solve the parameter estimation problem in clinically reasonable time
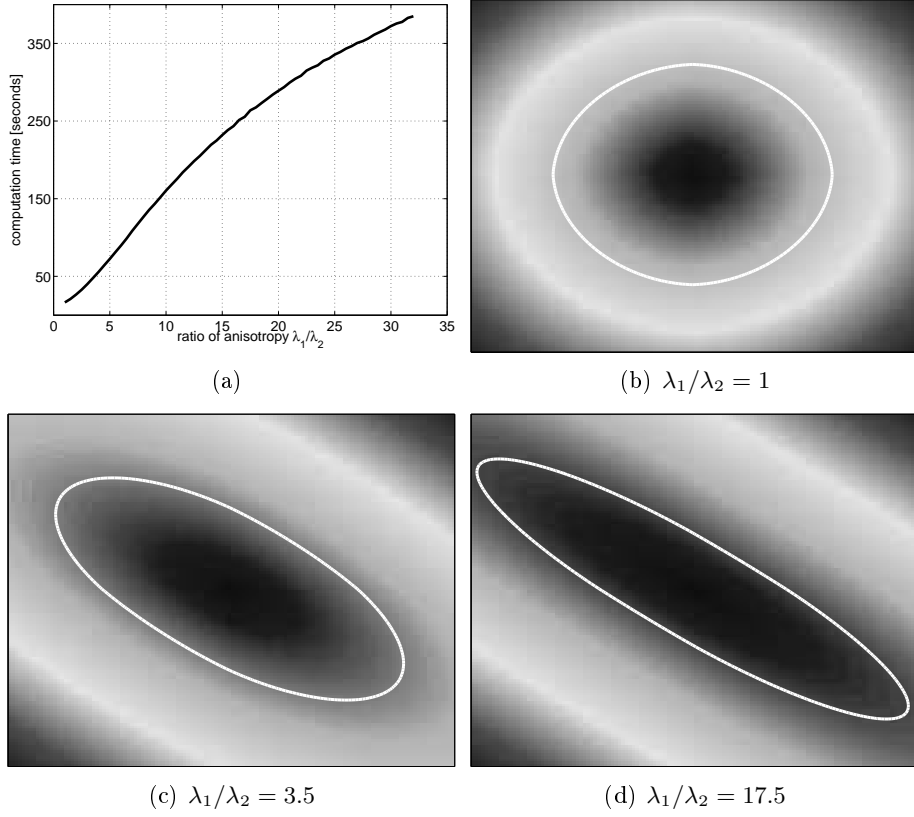
(a)

(b) $\lambda_1/\lambda_2 = 1$

(c) $\lambda_1/\lambda_2 = 3.5$

(d) $\lambda_1/\lambda_2 = 17.5$

Figure 8.9: (a) The computation time increases almost linearly with the strength of anisotropy of the tensor D. The figure show the plot of the computation time as a function of the ratio λ_1/λ_2 of D. (b)-(d) We show the results of the Equation 8.25 with different D's having different anisotropy strengths.

spans. Moreover, considering the high anisotropy and the high non-homogeneity of the diffusion tensors we have encountered, the anisotropic fast marching method proved itself to be very useful.

The anisotropic fast marching method explained here is a general tool and can be used for the different applications mentioned. Moreover, the algorithm can also be used for solving general static, convex Hamilton-Jacobi equations encountered in computer vision and material science. In this work we have focused on the algorithmic details. The future work should concentrate on the convergence characteristics of the algorithm and the worst case complexity in order to have a better understanding of the proposed method. Among different points to be tackled in a theoretical manner are the accuracy, robustness and convergence analysis of the method.

Conclusions and Perspectives

Contents

9.1 Conclusions

The main focus of the thesis presented here was on linking the mathematical tumor growth models and medical images. We have built our research on *reaction-diffusion* based tumor growth models which are shown to be suitable for modeling the macroscopic dynamics of tumor growth as visible in medical images. Previous works have successfully integrated the anatomical and diffusion information in their mathematical description of tumor growth. This integration was either based on the use of atlases or single patient images and aimed to include different tissue classes and/or white matter fiber structure in the growth formulation. In this sense, these *generic* models have adapted the anatomical information for modeling the growth and invasion of brain gliomas. In this thesis, we have studied the integration in the other sense, adapting the growth models to specific patient cases. Therefore, we have taken a step towards *patient specific* tumor growth models.

9.1.1 Parameter Estimation

As a first step in adapting the reaction-diffusion based tumor growth models to patient images, in Chapter 4 we have proposed a formulation for estimating the parameters of the growth model based on time series of medical images. We have seen that the generic growth model contains two different parameters, the diffusion tensor of tumor cells D and the proliferation rate ρ. Moreover, the construction of the diffusion tensor may contain several parameters, which in our case was 2, the diffusion rate in the white matter d_w and in the gray matter d_g. Estimating

parameters in this context means finding the numerical values of these parameters so that the evolution of the tumor described by the model best fits the evolution observed in the medical images.

One of the main problems for parameter estimation is the inconsistency between the information observable in the medical images and the information needed by the reaction-diffusion model. The reaction-diffusion models describe the temporal evolution of tumor cell density distributions throughout the brain. Therefore, for simulating the growth of the tumor these models need the knowledge of the spatial distribution of tumor cell density. Conventionally used medical images on the other hand, do not provide this information. They rather visualize enhanced regions where it is assumed that the tumor cell density is higher than a certain threshold. This enhanced region is named either as *visible tumor boundary* or *tumor delineation*. In order to solve this inconsistency we have proposed to use a front evolution formulation. This formulation describes the evolution of the tumor delineation based on the growth dynamics of reaction-diffusion models. These kind of formulations have already been proposed in the literature for different applications. In this thesis we have built on these existing works and improved them to take into account the second order effects such as time convergence and better handling of the effect of curvature.

Once we had a formulation for the growth of the tumor consistent with the images we formulated the parameter estimation as an optimization problem. The optimum parameters yielded us the best fit between the evolution of the tumor delineation observed in the images and the one described by the front evolution. We have performed thorough theoretical analysis of this method using synthetically grown tumors and encountered its drawbacks. Most importantly we have seen the coupling between the parameters of the tumor growth model and shown that these parameters cannot be identified separately in the presented context. On the other hand, we have seen that several identities such as the *growth speed of the tumor* can be identified uniquely from medical images. Following these theoretical studies we have applied the proposed method to some real cases and shown promising preliminary results. These real cases have demonstrated the potential usage of the parameter estimation method and the prediction power of personalized reaction-diffusion models.

To the best of our knowledge, in this thesis we have presented one of the first parameter estimation methodologies using medical images in the context of tumor growth models. In this sense, it is one of the first scientific contributions on *personalizing tumor growth models*. The theoretical analysis and preliminary results on real cases also constitute new scientific contributions not yet published elsewhere. During the course of this thesis we have presented our work regarding the parameter estimation and the front evolution of tumor delineation in different international conferences [Konukoglu 2007a] and [Konukoglu 2007b]. Moreover, we have submitted a journal article covering a larger part of the analysis and techniques shown in this thesis [Konukoglu ttedb].

9.1.2 Extrapolating Invasion Margins

Following the parameter estimation problem, in Chapter 6 we have focused on the potential benefits the tumor growth models can offer to the treatment of brain gliomas, particularly to radiotherapy. The treatment of brain gliomas are difficult and pose extra problems for radiotherapy due to their diffusive nature. The medical images play a very important role and guide the therapy process however, they are not able to visualize the whole extent of the infiltration of the tumor. In order to tackle this problem conventional radiotherapy applies irradiation not only to the visible part of the tumor but also to a healthy looking region around the tumor. This region is constructed by taking a constant margin around the tumor assuming the invisible infiltration remains in this part. This approach does not take into account the fact that tumor cells diffuse faster in the white matter. As a result they may underestimate the invasion of the white matter and not target the whole infiltration. On the other hand, for the gray matter, the constant irradiation margin approach may overestimate the infiltration and target healthy cortex causing unnecessary damage.

The tumor growth models, once personalized, can offer solutions to the visualization problem encountered in the case of diffusive tumors, particularly gliomas. In Chapter 6 we have proposed such a solution. The proposed formulation extrapolates the tumor cell density distribution beyond the part visible in the image, starting from the delineation of the tumor. This formulation was derived from the reaction-diffusion growth models through asymptotic approximations. As a result, the extrapolated density distribution takes into account the differential motility of tumor cells and the spiky nature of its growth. Using simulations on synthetically grown tumors we have shown the theoretical success of the proposed algorithm in extrapolating the infiltration not visible in the images. Following this, we have proposed a way to construct irradiation margins that take into account the infiltration of gliomas. Again, using synthetically grown tumors we have shown the potential benefits of using the proposed method in contouring irradiation margins. Our experiments have shown that by taking into account the infiltration dynamics of gliomas one may target more tumor cells and harm less healthy tissue using the same amount of irradiation.

Although earlier research by others has addressed the question of constructing the irradiation margins automatically, in the best of our knowledge, the work presented in this thesis is one of the first methods to address this question by including tumor growth models. Moreover, it is also one of the first attempts to use tumor growth models in therapy planning assuming clinical constraints, such as being able to use expert delineations. Combined with the parameter estimation methodology, we believe that the methods proposed in this thesis have the potential to be used in the clinical conditions. We have presented our work on extrapolating the infiltration extent of gliomas in different conferences and workshops [Konukoglu 2006]. The details of the final algorithm and the final experimental results have also been submitted as a journal paper [Konukoglu tteda].

9.1.3   Anisotropic Fast Marching

In the last part of this thesis, we have focused on a more algorithmic and fundamental problem. During our analysis of the reaction-diffusion models we have seen that *anisotropic Eikonal equations* play an important role. Both for estimating parameters and extrapolating the not detected infiltration of gliomas we have encountered this type equations in our methods. In Chapter 8 we have proposed a novel numerical method to solve anisotropic Eikonal equations in a fast and accurate manner. The advantages of this method are that it is a fast method, it can handle high anisotropies and it can easily be implemented on general meshes. In our experiments, for demonstrating its speed, we have compared the proposed algorithm with a state of the art method in terms of computation times. The proposed algorithm proved itself to be faster in the cases we have examined. This novel numerical method have been used throughout this thesis and thus it proved its use in the context of tumor growth modeling. Moreover, it can also be applied to different applications such as cardiac electrophsiological modeling, wound healing, geophysics,... We have presented the proposed numerical method in international conferences in the context of tumor growth modeling [Konukoglu 2007a]. We have also used the proposed method for simulating the evolution of potential fronts in the context of electrophysiological modeling of the heart [Sermesant 2007].

9.1.4   Other Contributions

Besides the technical contributions explained above we have also contributed in review and state of the art articles focusing on the use of mathematical tumor growth models and their potential importance in clinical cancer research [Clatz 2006, Angelini 2007, Mandonnet 2008]. As a new field, we have written a state of the art review chapter on tumor growth models in oncological image analysis which will appear in next edition of the Handbook of Medical Imaging [Konukoglu 2008a]. The details of this work are also presented in the Chapter 3 of this thesis.

This thesis is aimed to be a coherent combination of our works on modeling brain gliomas and linking these models to medical images. As a side topic we have also worked on monitoring the growth of very slowly growing tumors. In the case of tumors where the growth is extremely slow and the follow-up takes years the methods explained in this thesis might not be suitable. However, such tumors are not very uncommon both in the case of children, pilocytic astrocytomas, and adults, meningiomas. Change detection is a critical task in the diagnosis of these pathologies. In [Konukoglu 2008b], we have described an approach that semi-automatically performs this task using longitudinal medical images. Our focus was on meningiomas, which experts often find difficult to monitor as the tumor evolution can be obscured by image artifacts such as intensity differences or pose changes. We have tested the proposed method on synthetic data with known tumor growth as well as ten clinical data sets. We have shown that the results of our approach highly correlate with expert findings but seem to be less impacted by inter- and intra-rater variability.

9.2 Perspectives

9.2.1 Technical Improvements

This thesis focused on reaction-diffusion type tumor growth models with a particular interest in anisotropic models proposed recently. In terms of the methods presented here there are still lots of improvements and analysis that can be and should be made. In the first phase model for the evolution of the tumor delineation should be studied and formulated better. Especially the effect of curvature should be better handled. On the other hand, we have not analyzed the anisotropic fast marching method theoretically enough. Therefore, a convergence analysis and worst-case complexity should be studied.

In terms of the parameter estimation methodology presented, we have not taken into account the mass effect of the tumor which is especially observable for the high grade gliomas. This effect should be included in the method for a complete parameter estimation. The way the mass effect is taken into account in the existing literature is through coupling the tumor cell density distributions with the local pressure exerted on the brain tissue. This poses a difficulty for the front evolution formulation we have used in the method proposed. The attempt for taking into account the mass effect should overcome this problem and link the evolution of the tumor delineation with the deformation applied to the brain tissue. One way for this would be to combine the extrapolation method with the parameter estimation and create the tumor cell distribution for each parameter set during the estimation process. Using this one can integrate the mass effect in the parameter estimation method.

For the extrapolation of invasion margins and constructing variable irradiation regions one should think of integrating a model for radiotherapy in the proposed methodology. Although constructing irradiation margins consistent with the tumor infiltration is a good first step, one should include the effect of therapy and the response of the tumor to the therapy to simulate the real benefits of using variable irradiation margins. For this purpose only macroscopic models would not be enough because the stochastic nature of the response to therapy would not be captured. Instead a hybrid model combining the microscopic and macroscopic models can be used.

Our main concentration in this thesis, as we said, was on linking the medical images and reaction-diffusion type growth models. However, there are many different improvements one can think of in the reaction-diffusion models. The first set of these are structural changes in the model. The reaction-diffusion formalism can be extended using advection and convection processes which would better explain the migratory behavior of tumor cells especially on the white matter. Moreover, subdiving the tumor into different compartments such as the necrotic core, bulky part of the tumor and the infiltrative part might be a better and more accurate modeling strategy. Following this one would apply different model equations to each compartment and couple them to create the link between the evolution of each part. Such a partitioning can also be used for the brain tissue describing different behavior of the tumor in different parts of the brain. In this context one can also

study different construction methods for the tumor cell diffusion tensor using water diffusion tensor. We have seen two examples in this thesis however, more general construction methods can be used.

The models studied here were deterministic models and therefore, they were not able to take into account the stochastic nature of tumor growth. The natural extension to these models would be to include the stochastic behavior. One way to realize this would be to propose hybrid models which would have a microscopic part and a macroscopic part. The general evolution would be captured by the macroscopic part while the stochastic nature would be present through the microscopic part. One other way would be to use stochastic partial differential equations and model the evolution of probabilities of growth rather than having a deterministic evolution. In this context one should also study the link between micro and macro models. The effect of microscopic dynamics on the macroscopic parameters are not well explained for the tumor growth models. There are a few works which aimed to build this link however, this field is still untraveled.

One other natural extension to the type of growth models presented in this thesis is the modeling of therapy. There are two major reasons for this. The first one is that the clinical cases always have the effect of therapy on them. Therefore, in order to correctly apply tumor growth models to the patient cases one should take into account the therapy administered. The second reason is inherent in the aim of the cancer research. In trying to find a cure for the cancer, mathematical models can serve as the initial "playgrounds" for the new therapy techniques where extensive tests can be simulated. Correct and accurate modeling of the therapy process and the response of the tumor to the therapy becomes a crucial for this purpose.

In the models we have studied anatomical and diffusion MR images were used to formulate the growth of tumor. As new techniques become available and more accessible one should think of integrating more imaging modalities in the mathematical descriptions. PET, MRSI, perfusion images and others can help improve the accuracy of the models.

9.2.2   Application to Clinical Images

During the course of this thesis we have realized the difficulty of obtaining patient database where the proposed methodologies can be tested. In conventional clinical setting only anatomical MR images are acquired and most of the time they do not have a high resolution. On the other hand, in the models we have seen the importance of high resolution images and the diffusion information in accurately describing the growth process. Therefore, most of the patient images acquired at the moment are not suitable for testing and validating the reaction-diffusion type growth models and the methodologies presented in this thesis. Here we would like to take the opportunity and describe the ideal patient database that could be used for evaluating the methods presented in this thesis and the tumor growth models. The anatomical images play a very important role in the modeling process as they provide the geometry and location of the tumor and the brain structures. Moreover, they provide the white matter gray matter segmentation which is crucial for modeling the differential motility of tumor cells. The differential motility is not only

modeled by this segmentation though, one needs to have high resolution accurate information about the fiber structures of the brain as well. The diffusion tensor images provide this information. On the other hand, the tumor growth models describe the evolution of the tumor. This evolution can only be observed from time series of images. As a result, we see that the ideal dataset consists of high resolution anatomical and diffusion images taken regularly from the same patient using the same protocols and the same imaging devices. We were lucky enough to find 2 such cases in this thesis and show preliminary results.

The ideal dataset explained above might not be available for all the patients. High resolution anatomical and/or diffusion images might be missing for different cases. In order to be able to apply the presented methodologies and tumor growth models in the generic clinical situations one needs to overcome these problems. Registration techniques proposed for anatomical and diffusion images is a very good candidate for solving these problems. One can imagine to fill the place of the missing image by registering an atlas to the patient space and continuing with the analysis. However, the effect of using registration algorithms on the simulations should be studied. And moreover, atlas images will not carry the patient specific diffusion information as present in different tumor regions. Therefore, effect of this should also be analyzed.

9.2.3 Validation

The *in-vivo* validation and evaluation of the methods presented here and in more general of the tumor growth models is a big challenge. In this thesis and in most of the previously proposed works "indirect" validation of the methods and models have been performed. Measures such as, the resemblance of simulated and real data, the mass effect of the tumor and deformation in the brain tissue and survival rates have been widely used. Although these measures provide promising hints they are not quantitatively validating the behavior of tumor cells and in this sense they are not "direct" validations.

In the case of *in-vitro* experiments, direct validation can be achieved easier and have been performed in different works. Through microscopic analysis the tumor cell density on the petri-dish can be compared with the density distribution simulated by the model which would serve as a validation both for the model itself and the extrapolation method presented in this thesis. Using similar analysis the parameters of the tumor cells in the petri-dish can be identified and these would be used to validate the parameter estimation method. This sounds plausible however, in petri-dish experiments the tumor is grown outside the body, *in-vitro*. The dynamics of the tumor growth inside the body and on a petri may have differences and therefore, although the *in-vitro* experiments provides valuable information they do not reflect the behavior of the tumor *in-vivo*.

The *in-vivo* evolution of the tumor can be observed through medical images and biopsies. As a first step these sources of information can be used for a preliminary validation. Such a work bears certain difficulties like creating a large database of brain gliomas, having regular follow-ups and spatially linking the biopsies to the images. For a thorough validation on the other hand, we have seen that the information

available in the medical images are limited and the biopsy is a very local technique that does not provide a global information about the tumor. Using these sources we cannot obtain information regarding the tumor cell density distributions and microscopic dynamics, which are crucial in validating the methods and the growth models in general. For this purpose whole brain autopsies and animal models can be useful. Microscopic analysis of several cross-sections of the post-mortem brain, the animal model or a tumor resected as a whole can provide us the information we seek about the tumor cell density distribution. Moreover, these analysis can be combined with high resolution MR images to give us the opportunity to understand what we observe in the medical images.

9.2.4 Future

The tumor growth modeling in the context of medical images is an emerging field. Several preliminary works have been proposed that showed the potential of such models and also pointed out the big challenges. As data acquisition techniques and our understanding of the tumor biology improve these models will become more realistic and accurate. Simulations will become a common ingredient in the therapy development and testing as we see today for the other fields.

On the other hand, with the enhancing generic models, there will also be big advancements in the personalization of these models. In the end we would be able to obtain *patient-specific* models which would be used in the clinical setting both for the diagnosis and treatment planning of the tumor. Based on the current state of the patient the doctors will be able to simulate the possible outcomes under the effects of different therapies and choose the right treatment for each patient.

Hamilton-Jacobi Equations: A Brief Review

Hamilton-Jacobi (HJ) equations are first order nonlinear partial differential equations with the general form

$$\frac{\partial \Phi(\mathbf{x}, t)}{\partial t} + H(\mathbf{x}, \Phi, \nabla\Phi, t) = 0, \quad \mathbf{x} \in \mathbb{R}^n, \tag{A.1}$$

where H is called the Hamiltonian, Φ is called the Hamilton's principal function and ∇ is the gradient operator. These equations play an important role in calculus of variations as they can be linked to optimization problems through certain transformations on the function Φ and its derivatives [Brunt 2004, Giaquinta 1996]. Therefore, they are important for a large field of applications such as computer vision, image processing, optimal control theory, geometric optics and geophysics. Equation A.1 has a time dependence and describes the temporal change of the function Φ therefore, it is a *dynamic* Hamilton-Jacobi equation. When the equation does not have a time dependence then we have the *static* Hamilton-Jacobi equation which has the general form

$$H(\mathbf{x}, T, \nabla T) = 1, \quad \mathbf{x} \in \mathbb{R}^n. \tag{A.2}$$

This equation as its dynamic counter part can also be nonlinear due to the form of the H function. Osher in [Osher 1993] have linked the dynamic and the static equations by showing that static HJ equations can be transformed into dynamic ones through embedding the T function into an implicit function. We also used this link in Chapter 4. The HJ equations are by definition first order. However, in the literature certain equations involving second order derivatives are referred to as second order Hamilton-Jacobi equations i.e. *the curvature flow*, [Sethian 1999]. The HJ equations are very general and in this thesis we are mostly interested in a specific form of this general class, namely the *Eikonal* equation.

The Eikonal equation is a static HJ equation whose general form is

$$F(\mathbf{x})|\nabla T| = 1, \quad \mathbf{x} \in \Omega \tag{A.3}$$

where $F(\mathbf{x})$ is called the *speed function* and $|\cdot|$ denotes the norm of a vector. This equation simply describes the spatial gradient relationship of the function T under the effect of the speed function F. Equation A.3 together with a Dirichlet type boundary condition of the form

$$T|_{\partial\Omega} = 0, \tag{A.4}$$

creates the *boundary value problem* (BVP), where $\partial\Omega$ is the boundaries of the computation domain. Physically, the solution T of this problem at any point $\mathbf{p}$ represents the shortest time needed to travel from $\partial\Omega$ to $\mathbf{p}$. Therefore, T is usually referred to as the *traveling time function*. The iso-value surfaces of this function provides us *iso-time* (or *isochrones*) surfaces. Each iso-time surface is a combination of points equidistant from the boundary $\partial\Omega$, see Figure A.1. The type of Eikonal equation
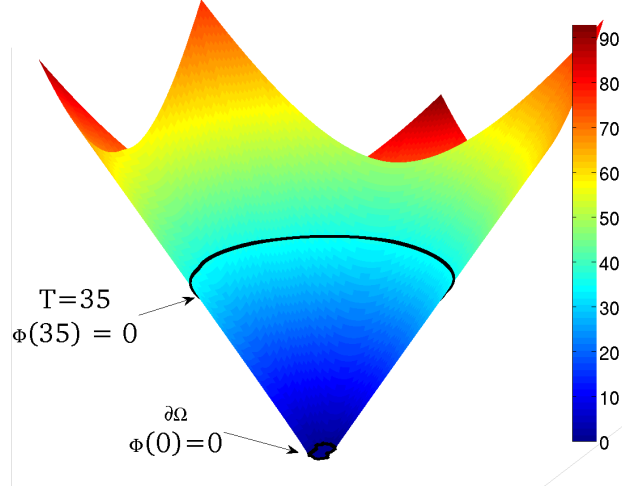

Figure A.1: The traveling time function T shown in color using the boundary condition given in Equation A.4. The iso-time contours/surfaces are ensemble of points equidistant from the boundary $\partial\Omega$. The Eikonal equation is also linked to a level-set equation through embedding the iso-time surfaces as zero level-sets of another implicit function Φ. As a result the evolution of the zero level-set of Φ corresponds to the T function.

we have majorly dealt with in this thesis is defined with respect to a tensor (3x3 positive definite matrix) and therefore has a slightly different form:

$$F(\mathbf{x})\sqrt{\nabla T' D \nabla T} = 1, \quad \mathbf{x} \in \Omega, \tag{A.5}$$

where D is a tensor. Although this equation is different than Equation 4.3 its physical meaning is the same under the assumption of an anisotropic speed map implicitly governed by the tensor D and it is also a static HJ equation.

The static HJ equation given in A.3 can be linked to a dynamic one by following the embedding and the transformation proposed by Osher in [Osher 1993]. If we construct an implicit function Φ through the embedding

$$\Phi(\mathbf{x}, t) = 0 \iff T(\mathbf{x}) = t \tag{A.6}$$

and use the transformation

$$\frac{\partial T}{\partial x_i} = \frac{\Phi_{x_i}}{\Phi_t} \ i \in [1, n] \in \mathbb{N} \tag{A.7}$$

we obtain the type of dynamic HJ equation which is also referred to as a *level-set* equation.

$$\frac{\partial \Phi}{\partial t} = F(\mathbf{x})|\nabla \Phi|. \tag{A.8}$$

This equation describes the temporal evolution of the zero level-set of Φ through the evolution of the whole implicit function. During the embedding, at a given time t the only constraint on Φ is around the $T = t$ iso-time surface. Therefore, for the construction of the rest of the Φ there is a freedom, which is most of the time used in favor of a *signed distance function $SDF()$*. The SDF is the distance map of a closed surface (curve) (such as the boundary $\partial \Omega$) which has negative/positive values inside the surface and positive/negative values outside it. The surface itself becomes the zero level-set of this function as its distance from itself is zero. Assuming such a construction for the Φ, the boundary condition given in Equation A.4 becomes an initial condition

$$\Phi(\mathbf{x}, 0) = SDF(\partial \Omega) \tag{A.9}$$

and Equation A.8 combined with this one creates an *initial value problem* (IVP). As the function Φ evolves in time its zero level-set changes its location and the evolution of this zero level-set in time corresponds to the T function, see Figure A.1.

We have presented the level-set equation in relation to what we have mainly used in the thesis, namely the Eikonal equations. However, level-set functions and methods are in fact much more general. The general form of level-set equations includes additional terms on its right hand side

$$\frac{\partial \Phi}{\partial t} = F(\mathbf{x})|\nabla \Phi| + V(\mathbf{x}) \cdot \nabla \Phi + G(\mathbf{x})\kappa, \tag{A.10}$$

where V is an external vector field, G is a scalar function and κ is the mean curvature. As it was the case for Equation A.8 this equation also describes the motion of its zero level-set. The effect of the three components on the right hand side are

- The first component $F(\mathbf{x})|\nabla \Phi|$ provides the motion of the zero level-set in the normal direction. This term is called the propagation or convection term.

- The second component $V(\mathbf{x}) \cdot \nabla \Phi$ provides the drifting motion of the zero level-set under the effect of the external vector field V. This term is called the advection term.

- The third term $G(\mathbf{x})\kappa$ is the curvature flow, which has a smoothing effect on the zero level-set. This term is called the curvature term.

One important thing to note here is that the mean curvature κ is a term that includes second order derivatives. As we have explained, HJ equations are first order by definition however, in the literature equations such as (A.10) are also referred to as second order HJ equations. Further details on the level-set equations and methods can be found in [Sethian 1999].

Unconstrained Optimization by Quadratic Approximation [Powell 2002]

The multidimensional minimization problems are very common in many diverse fields. In Chapter 4 we have formulated such a problem in the context of parameter estimation for reaction-diffusion type tumor growth models. In this appendix we briefly explain the optimization algorithm we have used to solve that minimization problem. The algorithm is proposed by Powell in [Powell 2002] and for further details on the algorithm please refer to this reference and the other accompanying ones [Moré 1983, Powell 2001, Powell 2003].

The optimization algorithm we have used in this thesis does not use the derivatives of the objective function instead it builds quadratic approximations to it and uses the 1st and the 2nd derivatives of these approximations. Therefore, for the problems where the derivatives of the objective function are not available it is preferable. Moreover, because the algorithm constructs quadratic approximations using interpolation, it is more robust to noise than the other algorithms computing explicit derivatives. Before going into details of the algorithm we first explain briefly "trust region methods" and the "trust region problem", which will be used.

Trust region problem is an optimization problem whose solution is bounded in a region such as

$$\min\{\psi(w) : ||w|| \leq \Delta\}, \qquad (\text{B}.1)$$

where ψ is the function to minimize, w is the solution we seek and Δ is the trust region radius. We see that this problem searches for the solution under a magnitude constraint, Δ. We readily notice that the size of Δ gives us the coarseness of the algorithm. Meaning that, if Δ is large we are at a coarser resolution while if Δ we are more focused on finer search. Trust region methods are a general class of optimization algorithms which requires the solution of a trust region problem between each iteration of the overall algorithm.

As we have noted the optimization algorithm in [Powell 2002], instead of the derivatives of the objective function F, uses the derivatives of the quadratic model

$$Q(\mathbf{x}) = c_Q + g'_Q(\mathbf{x} - \mathbf{x_b}) + \frac{1}{2}(\mathbf{x} - \mathbf{x_b})'G_Q(\mathbf{x} - \mathbf{x_b}) \ \ \mathbf{x} \in \mathbb{R}^n, \qquad (\text{B}.2)$$

which is an approximation of F around the point x_b. This model, in which g_q is a vector and G_Q is a symmetric matrix, is constructed by interpolation to values of

the objective function. Since this system has $m = 1/2(n+1)(n+2)$ dimensions we need to use m points to construct the model. So the interpolation satisfies

$$Q(\mathbf{x_i}) = F(\mathbf{x_i}), \quad i = 1, ..., m. \tag{B.3}$$

The points $\mathbf{x_i}$, "the interpolating points", are found automatically in the algorithm [Powell 2002]. The other ingredient used in the minimization algorithm is the Lagrange functions of the interpolation problem. There exists as many Lagrange functions as the dimension of the problem and these functions are defined as quadratic polynomials that satisfy

$$
\begin{align}
l_j(\mathbf{x_i}) &= \delta_{ij}, \quad i = 1, ..., m, \tag{B.4} \\
l_j(\mathbf{x}) &= c_j + g_j'(\mathbf{x} - \mathbf{x_b}) + \frac{1}{2}(\mathbf{x} - \mathbf{x_b})'G_j(\mathbf{x} - \mathbf{x_b}), \quad \mathbf{x} \in \mathbb{R}, , \tag{B.5} \\
Q(\mathbf{x}) &= \sum_{j=1}^{m} F(\mathbf{x_j})l_j(\mathbf{x}), \tag{B.6}
\end{align}
$$

where δ_{ij} is the Kronecker delta and l_j denotes the jth Lagrange function with the coefficients c_j, g_j and G_j.

The overall optimization algorithm is mainly concerned with constructing a good quadratic approximation Q to F within a region and minimizing Q in that given region. As the algorithm iterates this region moves towards the minimum (maximum) of F and for each region a new Q is constructed. Therefore we see that there 2 different questions: "How do we construct Q and then move it?" and "How do we find the minimum of Q in a region?".

We start the algorithm with 4 inputs, the objective function F, the initial optimum guess x_b, initial trust region radius ρ_{beg} and the final trust region radius ρ_{end} (with $\rho_{beg} > \rho_{end}$). The first step is to construct the interpolation function Q for which the details can be found in [Powell 2002]. As we have noted the trust region radius determines the coarseness of our search, we start our search for the minimum at the coarser resolution $\rho = \rho_{beg}$ by solving the trust region problem

$$\min(Q(\mathbf{x_k} + \mathbf{d})) \text{ such that } ||\mathbf{d}|| \le \Delta, \quad \Delta \ge \rho, \tag{B.7}$$

where x_k is the point among the interpolating points which has the minimum F value and Δ is another trust region radius which is added to increase the efficiency of the algorithm, [Powell 2002]. At this point there are two outcomes, the first one is that we find a d value which satisfies $F(\mathbf{x_k} + \mathbf{d}) < F(\mathbf{x_k})$. This means we found a new minimum, therefore we move a "suitable" point interpolating point $\mathbf{x_i}$ to $\mathbf{x_k} + \mathbf{d}$, reconstruct Q, l_j's and solve Equation B.7. The second one is that we do not find such a d. In this case we first ask the question whether Q is a good approximation for F. If the distance between one or more of interpolating points $\mathbf{x_i}$ and the minimum point $\mathbf{x_k}$ is greater than $||\mathbf{x_i} - \mathbf{x_k}|| > 2\rho$ we move this point closer to $\mathbf{x_k}$, reconstruct Q, l_j's and solve Equation B.7. In order to find the new location of $\mathbf{x_i}$ we solve another trust region problem given as

$$\max(l_i(\mathbf{x_k} + d)) \text{ such that } ||\mathbf{d}|| \le \rho. \tag{B.8}$$

This problem provides us a new location $\mathbf{x_i} = \mathbf{x_k} + \mathbf{d}$ such that the nonsingularity of Q constructed using this new point will be assured, [Powell 2001]. On the other hand, if we cannot find a point far away from $\mathbf{x_k}$ we trust the quality of our approximation Q and decide that we are in the basin of attraction and we need to go into finer details. We reduce the trust region radius ρ and construct a finer quadratic approximation Q and Lagrange functions l_j's. After this point the algorithm continues as before. The stopping criteria is given by ρ where once $\rho < \rho_{end}$ we stop. The overall algorithm is also summarized briefly in Figure B.1. For a more detailed description please refer to [Powell 2002].

The number of times the value of the objective function is computed for different points remains low in this algorithm. As the initialization we call the objective function m times. Later on for each iteration we only call it once and then reconstruct the quadratic approximation and Lagrange functions through updating the interpolating points, see [Powell 2002]. Therefore, in the case where computation of the objective function F takes time, this algorithm becomes a good choice.
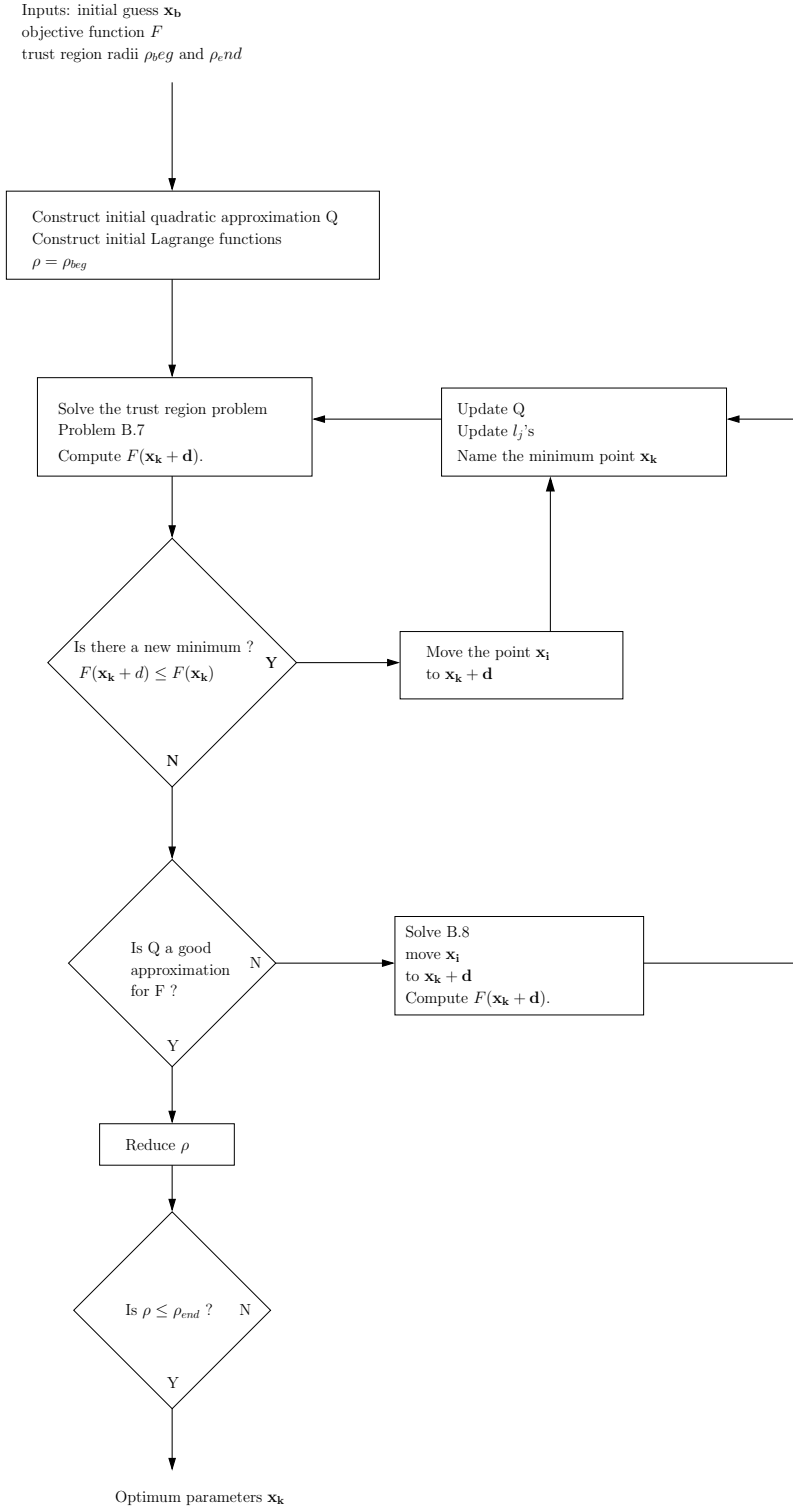
Inputs: initial guess $\mathbf{x_b}$
objective function F
trust region radii $\rho_b eg$ and $\rho_e nd$

Construct initial quadratic approximation Q
Construct initial Lagrange functions
$\rho = \rho_{beg}$

Solve the trust region problem
Problem B.7
Compute $F(\mathbf{x_k} + \mathbf{d})$.

Update Q
Update l_j's
Name the minimum point $\mathbf{x_k}$

Is there a new minimum ?
$F(\mathbf{x_k} + d) \leq F(\mathbf{x_k})$

Y

N

Move the point $\mathbf{x_i}$
to $\mathbf{x_k} + \mathbf{d}$

Is Q a good
approximation
for F ?

N

Solve B.8
move $\mathbf{x_i}$
to $\mathbf{x_k} + \mathbf{d}$
Compute $F(\mathbf{x_k} + \mathbf{d})$.

Y

Reduce ρ

Is $\rho \leq \rho_{end}$?   N

Y

Optimum parameters $\mathbf{x_k}$

Figure B.1: The overall optimization algorithm used in Chapter 4 proposed in [Powell 2002]

Preliminary Results of the Parameter Estimation Methodology with Real Cases: Extra Images

In this appendix we provide additional images for the results presented in Section 5.2. In that section we have presented the preliminary results of the parameter estimation methodology on the real cases both for fitting the observed evolution and also for predicting the further evolution of the tumor. Each page in this appendix is devoted to different axial slices of an MR image taken at the same time instance.

In Section C.1 we provide the additional images for the results given in Section 5.2.1. We start from the first images (Figures C.1 and C.5) and show 15 axial slices of those image including the manual delineations (in white). After that we provide the following images in the time series including both the manual delineations (in white) and the evolution of the tumor delineation obtained with the estimated parameters (in black).

In Section C.2 we provide the additional images for the results given in Section 5.2.2. We start from the last image (Figures C.9 and C.11) that was used in the estimation of the parameters and show 15 axial slices of those image including the manual delineations (in white). After that we provide the final image showing the final state of the tumor both the with manual delineation (in white) and the predicted evolution of the tumor delineation (in black).

C.1 Fitting the Observed Evolution: Additional Images

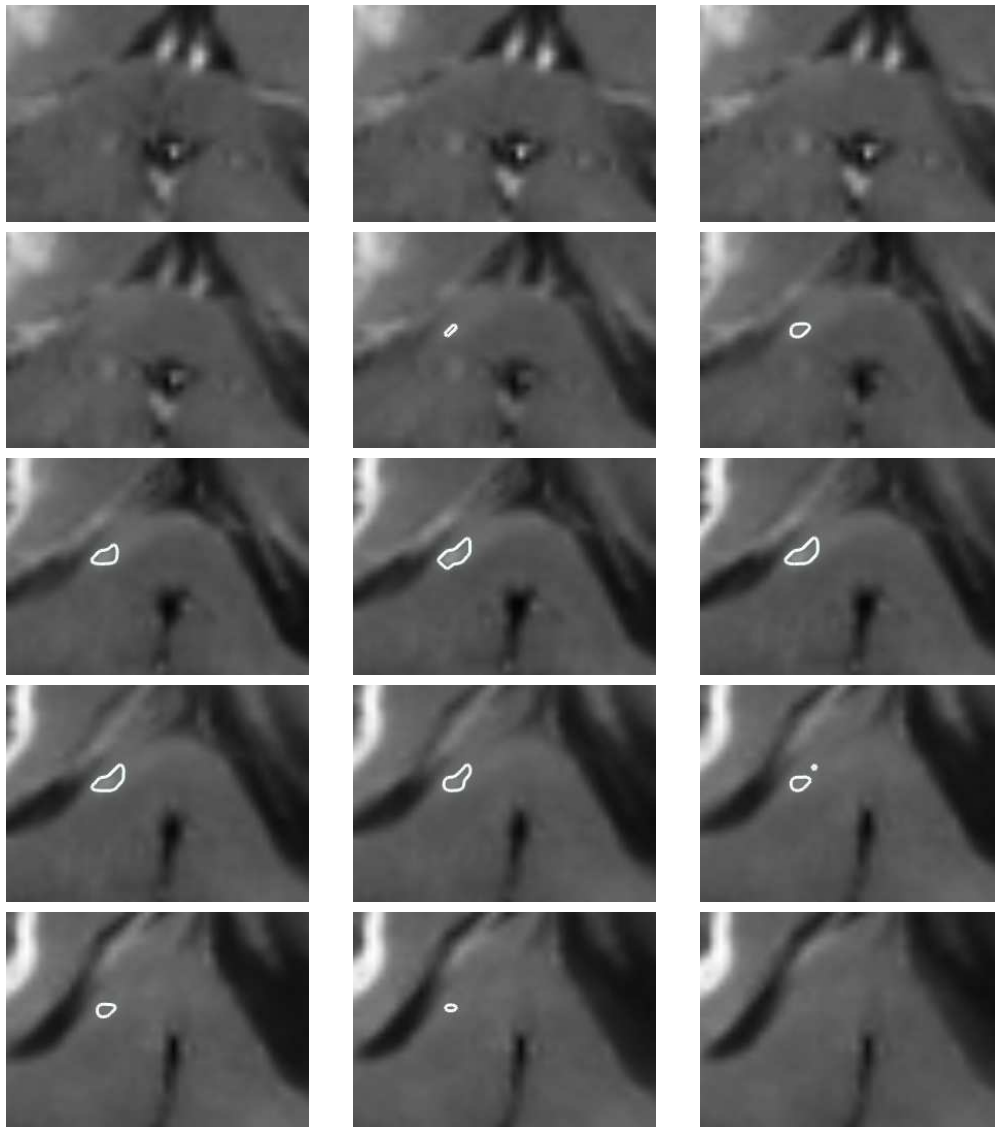## C.2 Predicting the Further Evolution: Additional Images

Figure C.1: The MR image taken at the first time point for the first patient. White contour denotes the manual delineations.
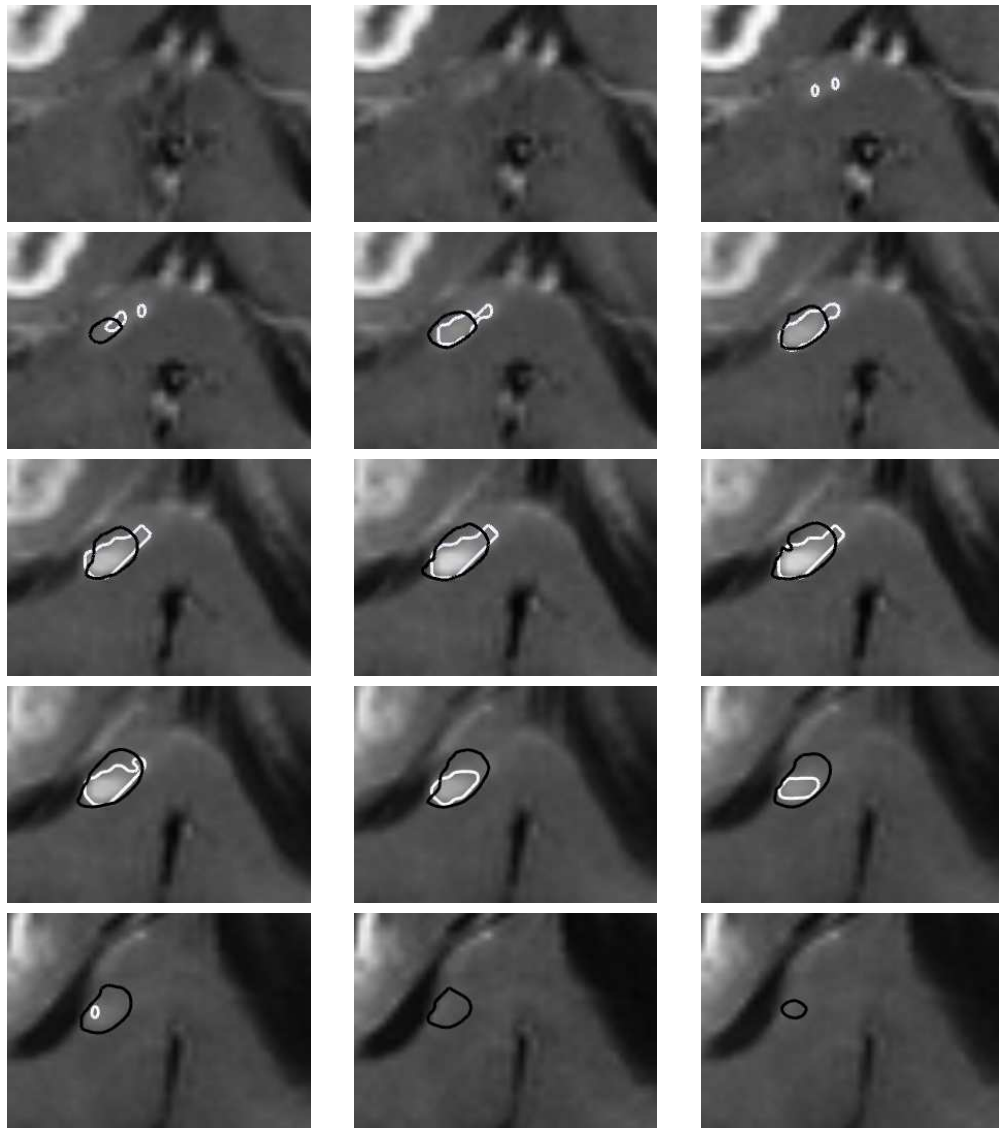
Figure C.2: The MR image taken at the second time point for the first patient. The white contour denotes the manual delineations and the black contour is the estimated evolution of the tumor delineation.
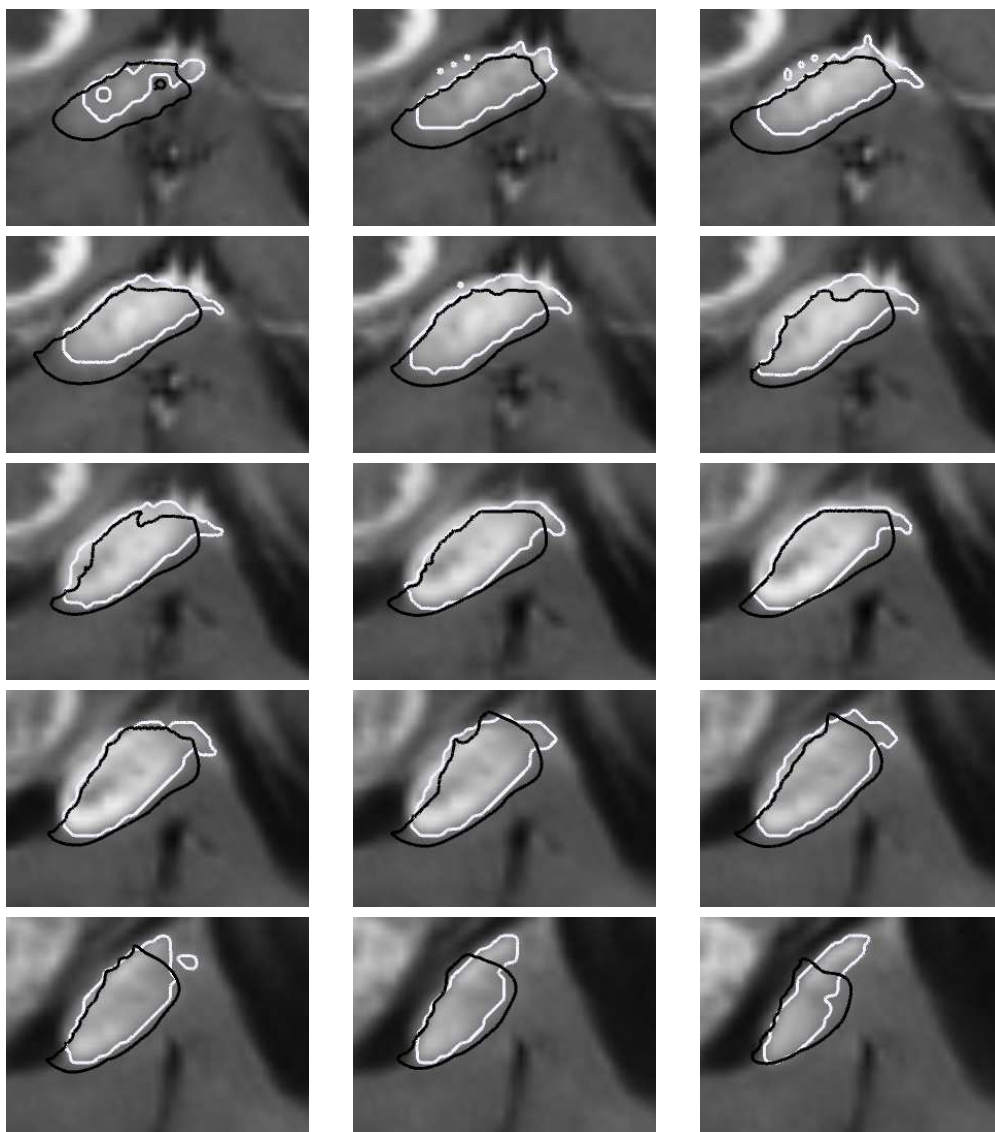
Figure C.3: The MR image taken at the third time point for the first patient. The white contour denotes the manual delineations and the black contour is the estimated evolution of the tumor delineation.
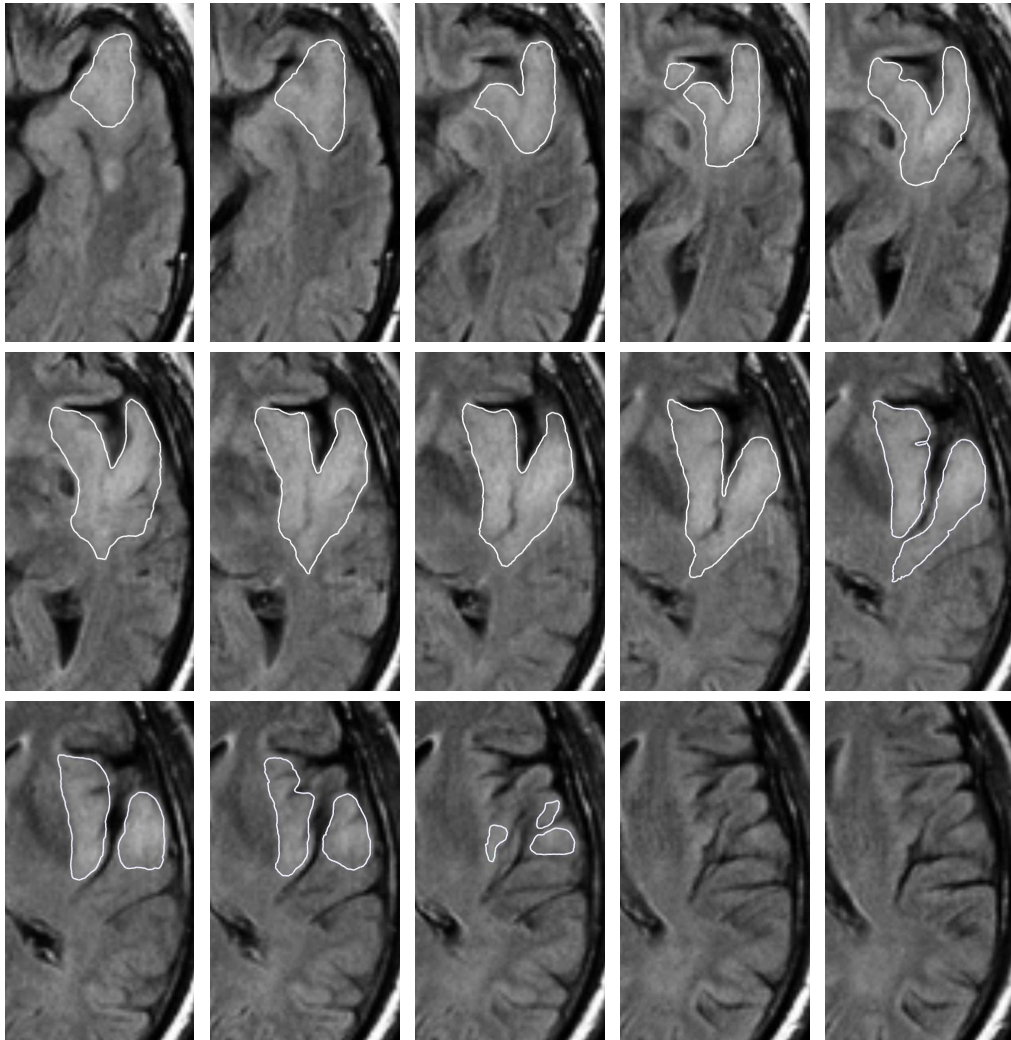
Figure C.4: The MR image taken at the first time point for the second patient. White contour denotes the manual delineations.
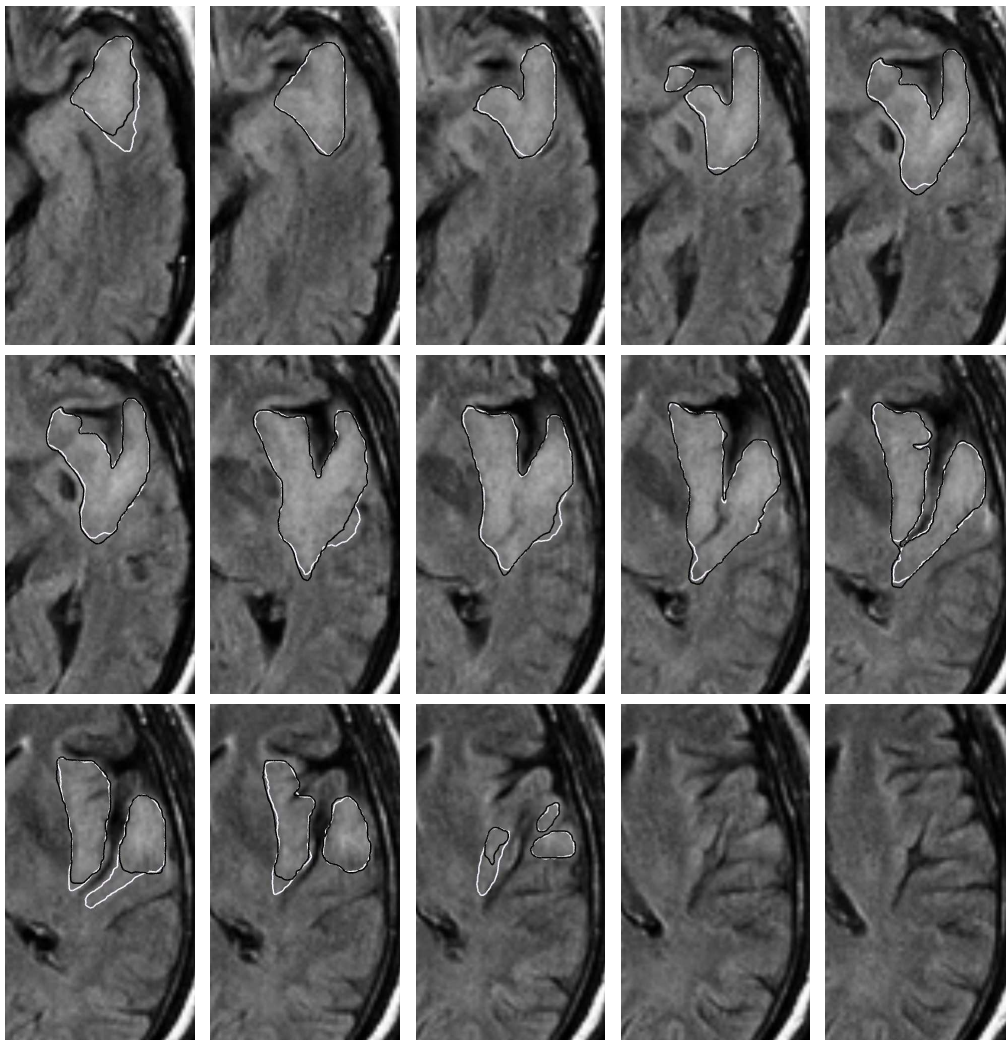
Figure C.5: The MR image taken at the second time point for the second patient. The white contour denotes the manual delineations and the black contour is the estimated evolution of the tumor delineation.
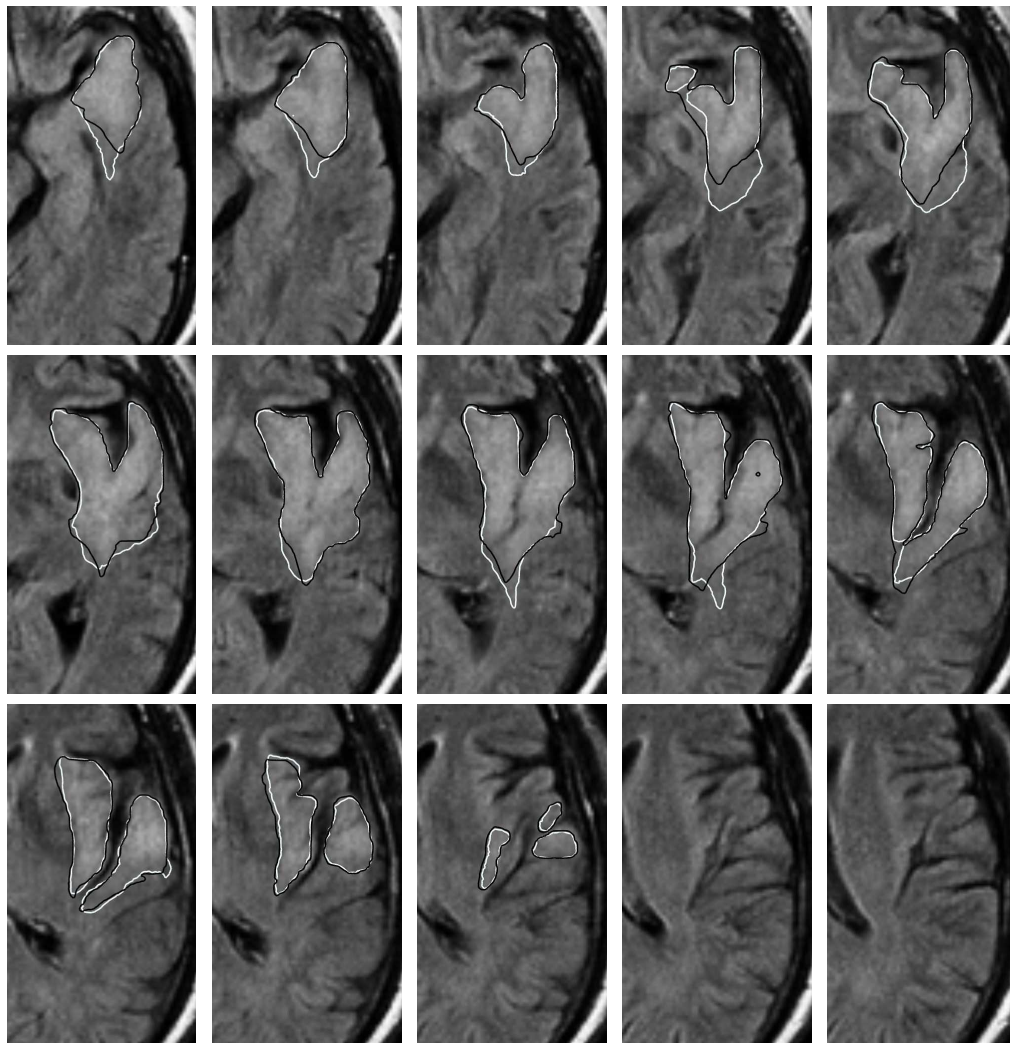
Figure C.6: The MR image taken at the third time point for the second patient. The white contour denotes the manual delineations and the black contour is the estimated evolution of the tumor delineation.

Figure C.7: The MR image taken at the fourth time point for the second patient. The white contour denotes the manual delineations and the black contour is the estimated evolution of the tumor delineation.
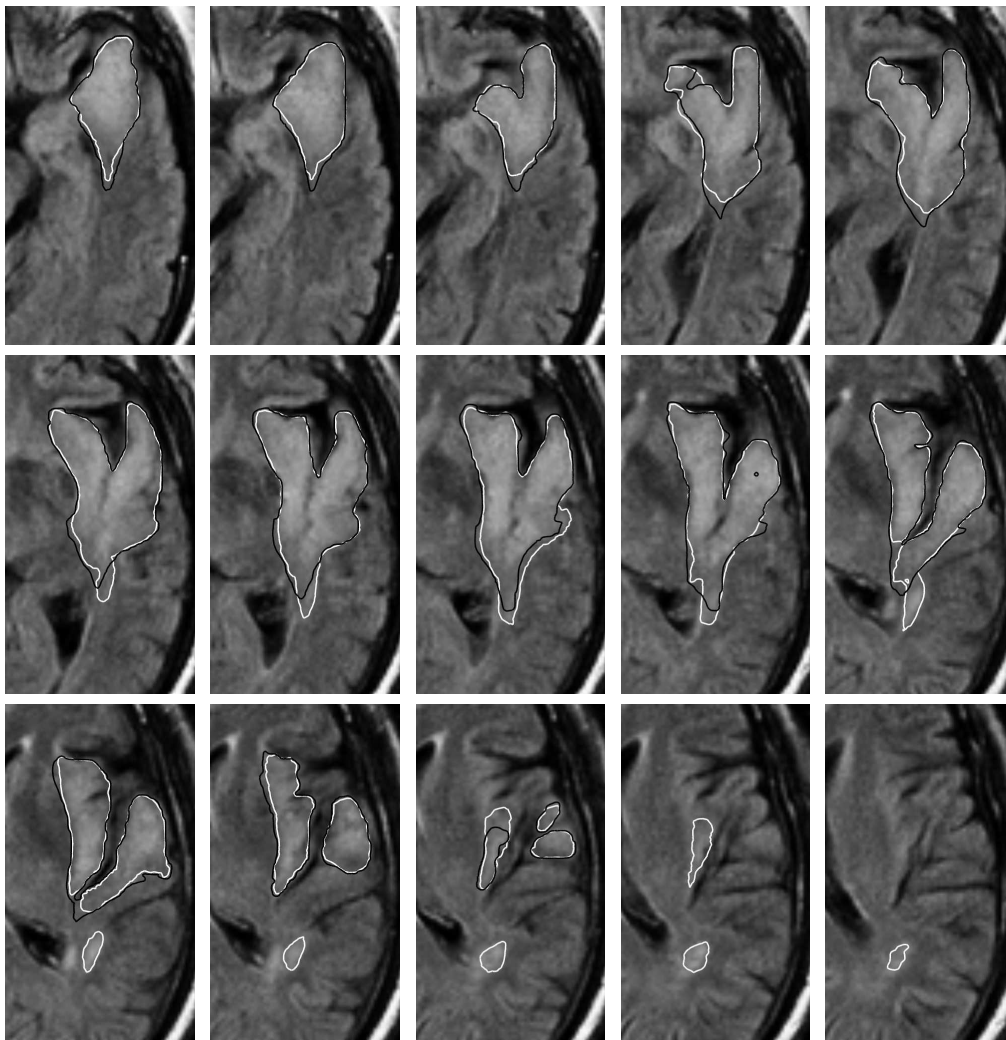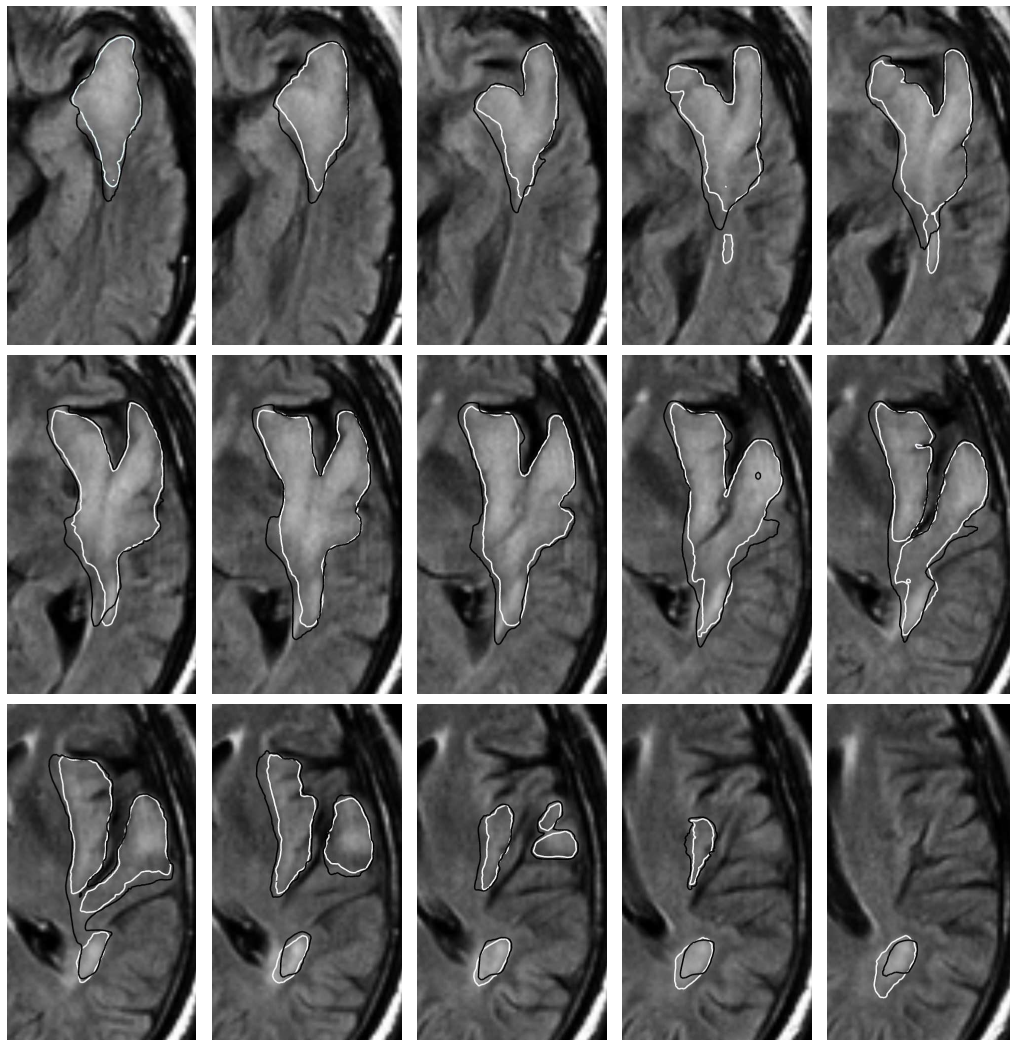
Figure C.8: The MR image taken at the fifth time point for the second patient. The white contour denotes the manual delineations and the black contour is the estimated evolution of the tumor delineation.
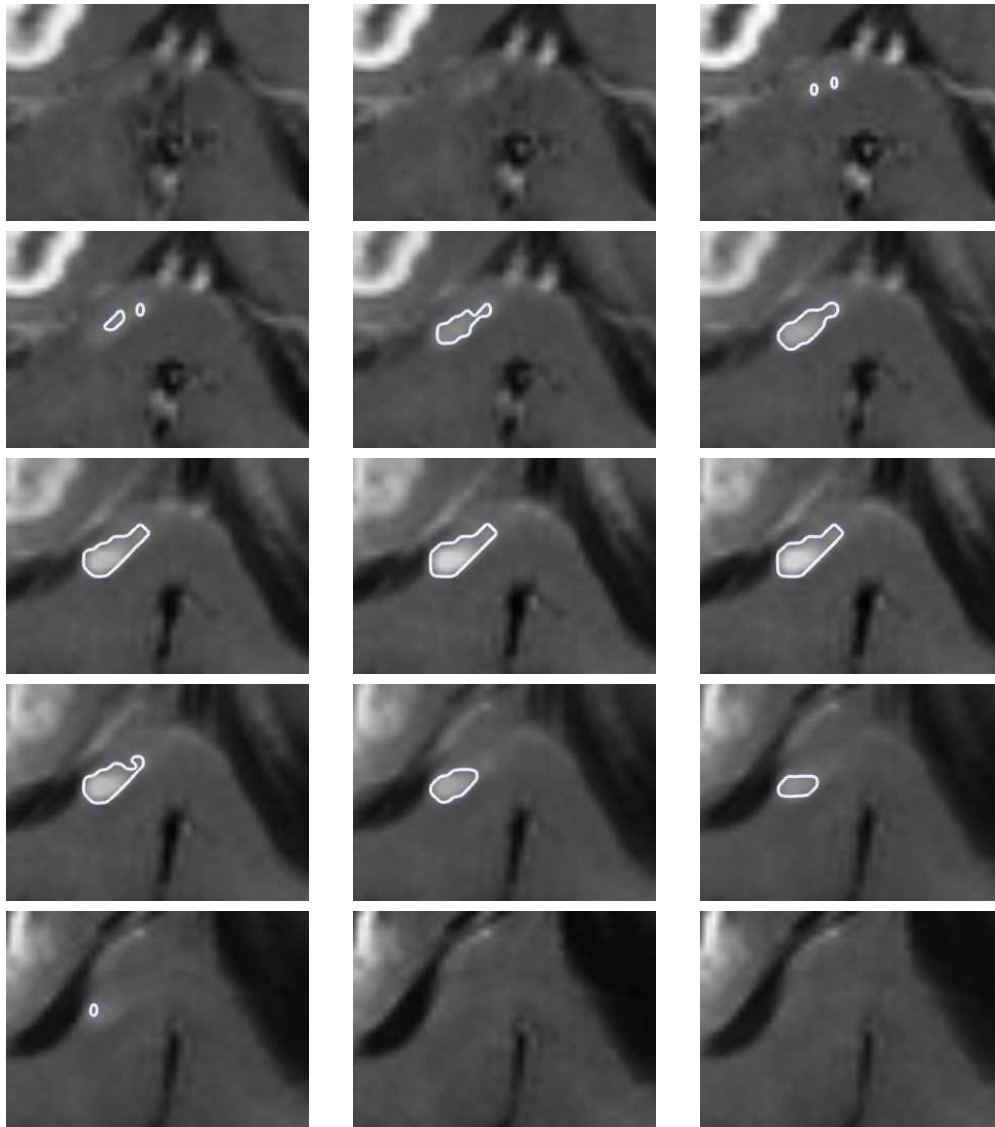
Figure C.9: The last image that was used in estimating the parameters of the reaction-diffusion growth model for the first patient.

Figure C.10: The final image showing the final state of the tumor along with the tumor delineation predicted by the model (in black) and segmented by the expert (in white).

Figure C.11: The last image that was used in estimating the parameters of the reaction-diffusion growth model for the second patient.
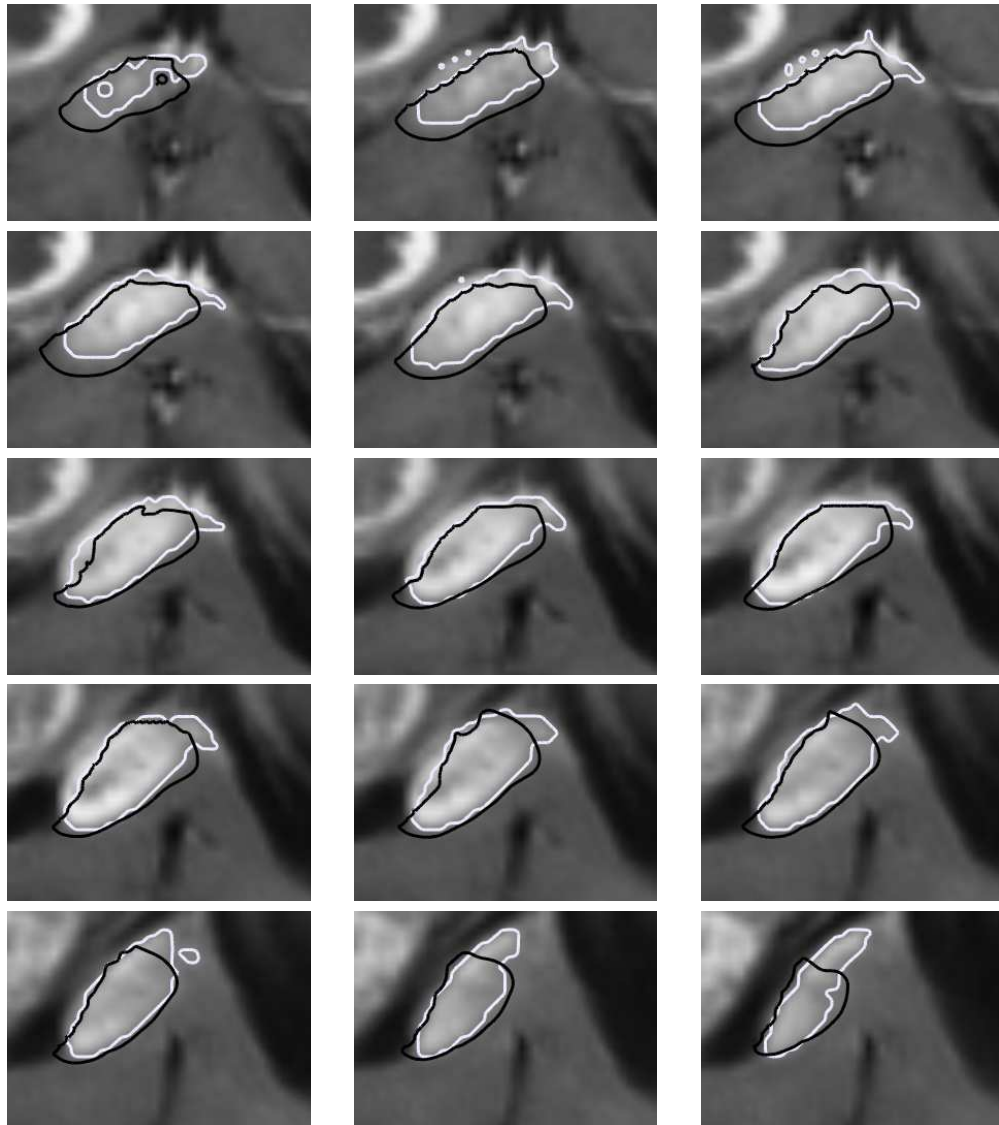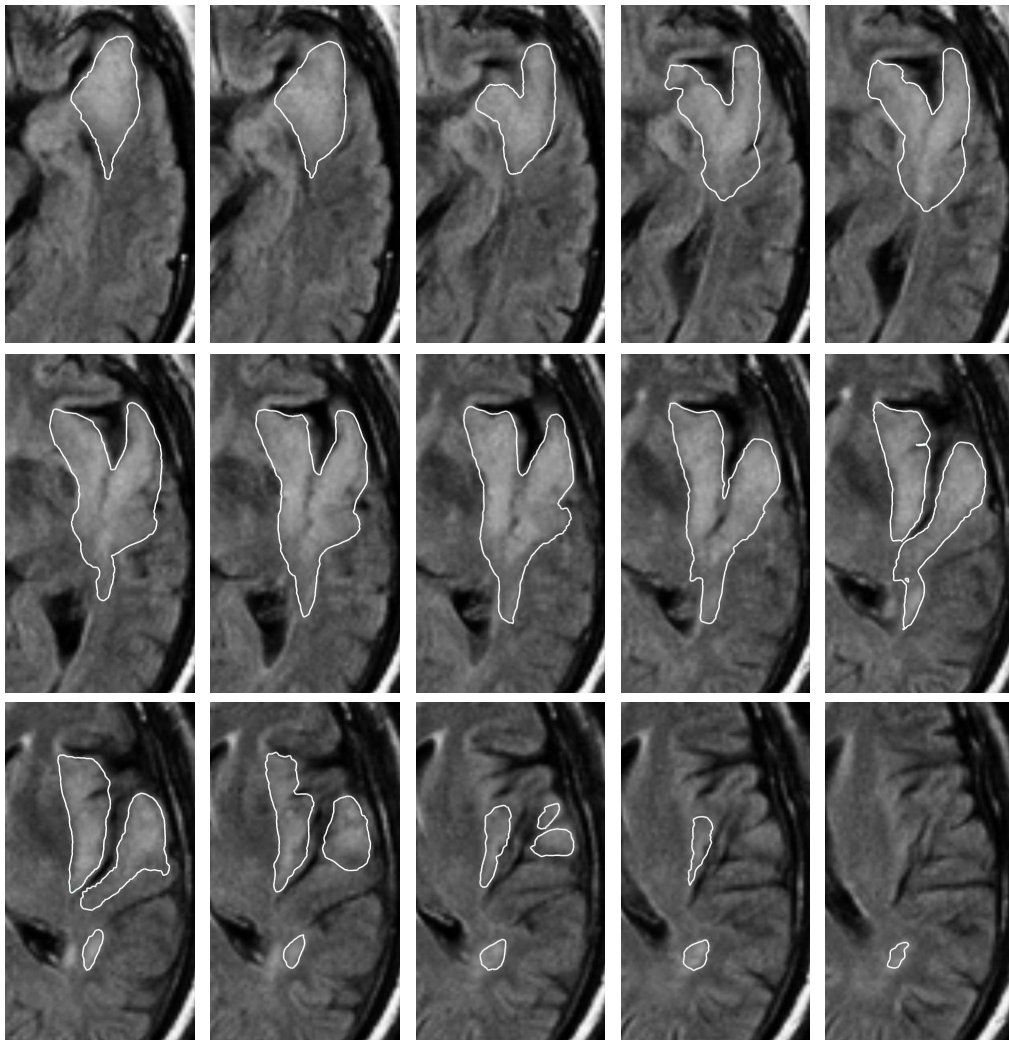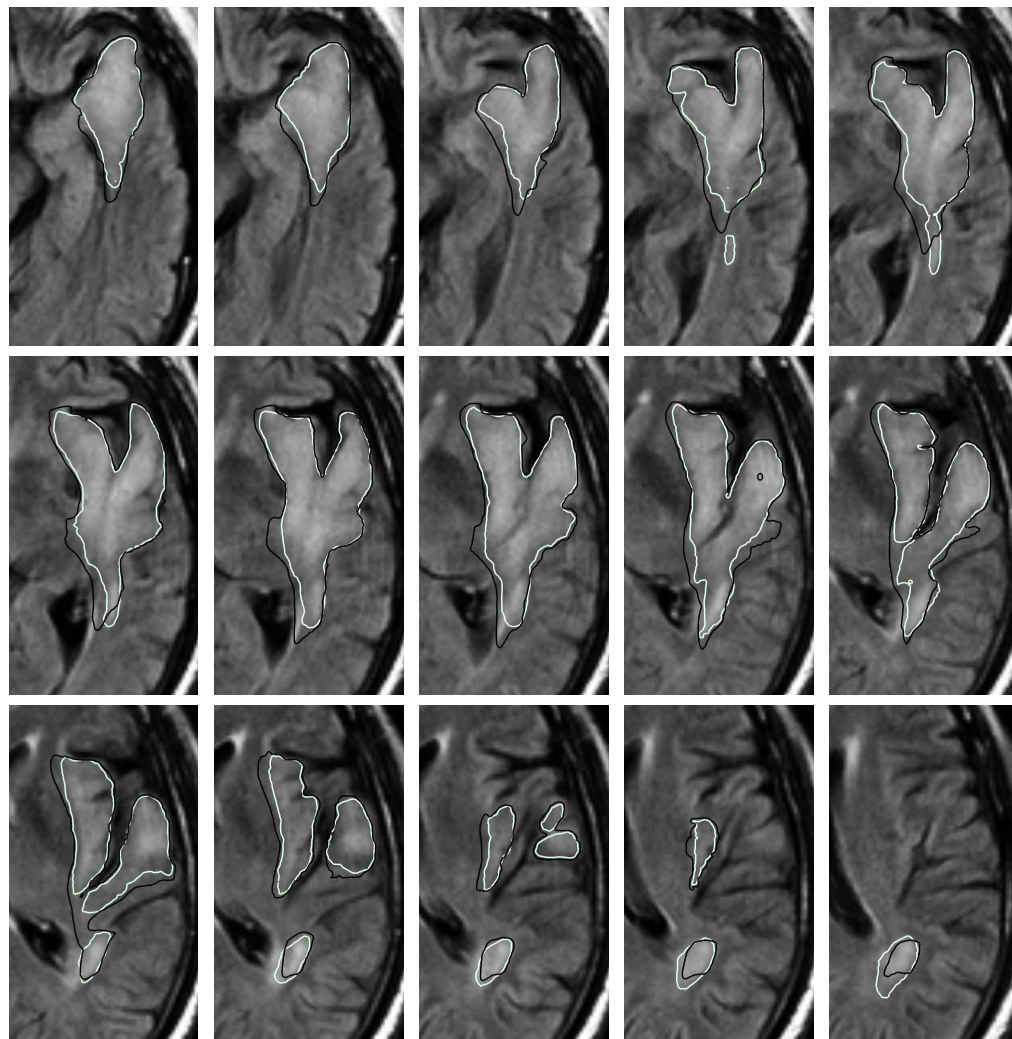
Figure C.12: The final image showing the final state of the tumor along with the tumor delineation predicted by the model (in black) and segmented by the expert (in white).

Abbreviations and Acronyms

BVP   Boundary Value Problem, 151

CA   Cellular Automata, 27
CSF   Cerebrospinal Fluid, 11
CT   Computed Tomography, 10
CTV   Clinical Target Volume, 91

DT   Diffusion Tensor, 11
DT-MRI   Diffusion Tensor MRI, 11
DWI   Diffusion Weighted Images, 11

EC   Endothelial Cell, 24
ECM   Extracellular Matrix, 17
EGFR   Epidermal Growth Factor Receptors, 28

FA   Fractional Anisotropy, 15
FM   Fast Marching, 102
FMM   Fast Marching Method, 131
fMRI   functional Magnetic Resonance Imaging, 11

GBM   glioblastoma multiforme, 9
Gd   Gadolinium, 11
GIF   Growth Inhibiting Factor, 21

HJ   Hamilton-Jacobi, 151

IVP   Initial Value Problem, 153

MD   Mean Diffusivity, 15
MR   Magnetic Resonance, 10
MRI   Magnetic Resonance Imaging, 10
MRS   Magnetic Resonance Spectroscopy, 11

NMR   nuclear magnetic resonance, 10

ODE   Ordinary Differential Equation, 48

PCA   Principal Component Analysis, 40
PDE   Partial Differential Equation, 31
PET   Positron Emission Tomography, 10

RD   Reaction-Diffusion, 2
RF   Radio Frequency, 11

SDF   Signed Distance Function, 153

TAF   Tumor Angiogenesis Factor, 24
TDT   Tumor Diffusion Tensor, 32
TE   Echo Time, 11
TMZ   Temozolomide, 37
TR   Repetition Time, 11

VEGF   Vascular Endothelial Growth Factor, 24

WHO   World Health Organization, 8

Bibliography

[ABTA 2008a] American Brain Tumor Association ABTA. *Facts and Statistics, 2008*, 2008.

[ABTA 2008b] American Brain Tumor Association ABTA. *Types of Brain and Spinal Cord Tumors*, 2008.

[Alarcón 2004] T. Alarcón, H.M. Byrne et P.K. Maini. *Towards whole-organ modeling of tumour growth*. Prog. Biophys. Mol. Biol., vol. 85, 2004.

[Alexander 2001] D. C. Alexander, C. Pierpaoli, P. J. Basser et J. C. Gee. *Spatial transformations of diffusion tensor magnetic resonance images*. IEEE Trans Med Imaging, vol. 20, pages 1131–1139, Nov 2001.

[Anderson 1998] A.R.A. Anderson et M.A.J. Chaplain. *A mathematical model for capillary network formation in the absence of endothelial cell proliferation*. Appl. Math. Lett., vol. 11, 1998.

[Anderson 2000] A.R.A. Anderson, M.A.J. Chaplain, C. Garcia-Reimbert et C.A. Vargas. *A gradient driven mathematical model of antiangiogenesis*. Math. Comput. Modeling, vol. 32, 2000.

[Angelini 2007] Elsa Angelini, Olivier Clatz, Emmanuel Mandonnet, Ender Konukoglu, Laurent Capelle et Hugues Duffau. *Glioma Dynamics and Computational Models: A Review of Segmentation, Registration, and In Silico Growth Algorithms and their Clinical Applications*. Current Medical Imaging Reviews„ vol. 3, pages 262–176, 2007.

[Araujo 2004] R.P. Araujo et D.L.S. McElwain. *A history of the study of solid tumour growth: the contribution of mathematical modelling*. Bulleting of Mathematical Biology, vol. 66, 2004.

[Aronson 1978] D.G. Aronson et H.F. Weinberger. *Multidimensional Nonlinear Diffusion Arising in Population Genetics*. Advances in Mathematics, vol. 30, 1978.

[Athale 2005] C. Athale, Y. Mansury et T.S. Deisboeck. *Simulating the impact of a molecular 'decision-process' on cellular phenotype and multicellular patterns in brain tumors*. J. Theor. Biol., vol. 233, pages 469–481, Apr 2005.

[Athale 2006] C.A. Athale et T.S. Deisboeck. *The effects of EGF-receptor density on multiscale tumor growth patterns*. J. Theor. Biol., vol. 238, pages 771–779, Feb 2006.

[Batchelor 2007] T.T. Batchelor, A.G. Sorenson, E. di Tomaso, W.-T. Zhang, D.G. Duda, K.S. Cohen, K.R. Kozak, D.P. Cahill, P.-J. Chen, M. Zhu, M. Ancukiewicz, M.M. Mrugala, S. Plotkin, J. Drappatz, D.N. Louis, P. Ivy, D.T.

Scadden, T. Benner, J.S. Loeffler, P.Y. Wen et R.K. Jain. *AZD2171, a Pan-VEGF Receptor Tyrosine Kinase Inhibitor, Normalizes Tumor Vasculature and Alleviates Edema in Glioblastoma Patients.* Cancer Cell, vol. 11, pages 83–95, 2007.

[Bertuzzi 2003] A. Bertuzzi, A. Fasano et A. Gandolfi. *Cell kinetics in tumour cords studied by a model with variable cell cycle length.* In Second M.I.T. Conf. Comp. Fluid and Solid Mech., 2003.

[Breward 2002] C.J.W. Breward, H.M. Byrne et C.E. Lewis. *The role of cell-cell interactions in a two-phase model for avascular tumour growth.* J. Math. Biology, vol. 45, 2002.

[Breward 2004] C.J.W. Breward, H.M. Byrne et C.E. Lewis. *A multiphase model describing vascular tumour growth.* Bull. Math. Biol., vol. 01, 2004.

[Brunt 2004] Bruce Van Brunt. The calculus of variations. Springer, first édition, 2004.

[Bryson 2003] S. Bryson et D. Levy. *Central Schemes for Multidimensional Hamilton-Jacobi Equations.* SIAM J. Sci. Comput., vol. 25, 2003.

[Burger 1988] P.C. Burger, E.R. Heinz, T. Shibata et P. Kleihues. *Topographic anatomy and CT correlations in the untreated glioblastoma multiforme.* J. Neurosurg., vol. 68, pages 698–704, May 1988.

[Burton 1966] A.C. Burton. *Rate of growth of solid tumors as a problem of diffusion.* Growth, vol. 30, 1966.

[Byrne 1995] H.M. Byrne et M.A.J. Chaplain. *Growth of nonnecrotic tumours in the presence and absence of inhibitors.* Math. Biosci., vol. 130, 1995.

[Byrne 1996] H.M. Byrne et M.A.J. Chaplain. *Explicit solutions of a simplified model fo capillary sprout growth during tumor angiogenesis.* Appl. Math. Lett., vol. 9, 1996.

[Byrne 2003] H. Byrne et L. Preziosi. *Modelling solid tumour growth using the theory of mixtures.* Math Med Biol, vol. 20, pages 341–366, Dec 2003.

[Byrne 2006] H.M. Byrne, M.R. Owen, T. Alarcon, J. Murphy et P.K. Maini. *Modelling the response of vascular tumours to chemotherapy: a multiscale approach.* Mathematical Models and Methods in Applied Sciences, vol. 16, no. 7S, pages 1219–1241, 2006.

[Chaplain 1998] M.A.J. Chaplain et M.E. Orme. Mathematical modeling of tumor-induced angiogenesis, chapter Vascular morphogenesis: *In vivo, in vitro, in mente.* Boston:Birkhauser, 1998.

[Chaplain 2000] M.A.J. Chaplain. *Mathematical modelling of angiogenesis.* J. Neuro-Oncology, vol. 50, 2000.

[Clatz 2005] O. Clatz, M. Sermesant, P.Y. Bondiau, H. Delingette, S.K. Warfield, G. Malandain et N. Ayache. *Realistic simulation of the 3D growth of brain tumors in MR images coupling diffusion with biomechanical deformation.* IEEE T.M.I., vol. 24, no. 10, 2005.

[Clatz 2006] Olivier Clatz, Emmanuel Mandonnet, Stéphane Chanalet, Christine Lebrun, Ender Konukoglu, Hervé Delingette, Nicholas Ayache et Pierre-Yves Bondiau. *Modèles Biomathématiques de Croissance Des Gliomes : Recherche en Informatique et Perspectives en Neuro-oncologie.* Neurologies, vol. 9, no. 93, pages 665–667, 2006.

[Cristini 2003] V. Cristini, J. Lowengrub et Q. Nie. *Nonlinear simulation of tumor growth.* J. Math. Biol, vol. 46, 2003.

[Cruywagen 1995] G.C. Cruywagen, D.e. Woodward, P. Tracqui, G.T. Bartoo, J.D. Murray et E.C. Alvord. *The modelling of diffusive tumours.* J. Biol. Systems, vol. 3, 1995.

[Cuadra 2004] M.B. Cuadra, C. Pollo, A. Bardera, O. Cuisenaire, J.-G. Villemure et J.-P. Thiran. *Atlas-based segmentation of pathological MR brain images using a model of lesion growth.* IEEE Tran. Med. Imag., vol. 23, 2004.

[Deakin 1975] A.S. Deakin. *Model for the growth of a solid in vitro tumor.* Growth, vol. 39, 1975.

[DeAngelis 2001] L.M. DeAngelis. *Brain tumors.* N. Engl. J. Med., vol. 344, pages 114–123, Jan 2001.

[Demuth 2004] T. Demuth et M.E. Berens. *Molecular mechanisms of glioma cell migration and invasion.* J. Neurooncol., vol. 70, pages 217–228, Nov 2004.

[Devos 2005] A. Devos, A.W. Simonetti, M. van der Graaf, L. Lukas, J.A. Suykens, L. Vanhamme, L.M. Buydens, A. Heerschap et S. Van Huffel. *The use of multivariate MR imaging intensities versus metabolic data from MR spectroscopic imaging for brain tumour classification.* J. Magn. Reson., vol. 173, pages 218–228, Apr 2005.

[Drasdo 2005] D. Drasdo et S. Höhme. *A single-cell-based model of tumor growth in vitro: monolayers and spheroids.* Phys. Biol., vol. 2, pages 133–147, 2005.

[Fiveash 2003] J.B. Fiveash et S.A. Spencer. *Role of radiation therapy and radiosurgery in glioblastoma multiforme.* Cancer J, vol. 9, pages 222–229, 2003.

[Franzone 1990] P.C. Franzone, L. Guerri et S. Rodiva. *Wavefront propagation in an activation model of the anisotropic cardiac tissue: asymptotic analysis and numerical simulations.* J. Math. Biol., vol. 28, pages 121–176, 1990.

[Frieboes 2007] H.B. Frieboes, J.S. Lowengrub, S. Wise, X. Zheng, P. Macklin, E.L. Bearer et V. Cristini. *Computer simulation of glioma growth and morphology.* NeuroImage, vol. 37, pages S59–S70, 2007.

[Gardner 2003] S.N. Gardner et M. Fernandes. *New tools for cancer chemotherapy: computational assistance for tailoring treatments.* Mol. Cancer Ther., vol. 2, pages 1079–1084, Oct 2003.

[Garg 2008] I. Garg et M.I. Miga. *Preliminary investigation of the inhibitory effects of mechanical stress in tumor growth.* In Proceedings of SPIE. SPIE, 2008.

[Gatenby 1996] R.A. Gatenby et E.T. Gawlinski. *A reaction-diffusion model of cancer invasion.* Cancer Res., vol. 56, 1996.

[Giaquinta 1996] Mariano Giaquinta et Stefan Hildebrandt. Calculus of variations II: the Hamiltonian formalism. Springer, first édition, 1996.

[Giese 1996] A. Giese, L. Kluwe, B. Laube, H. Meissner, M.E. Berens et M. Westphal. *Migration of human glioma cells on myelin.* Neurosurgery, vol. 38, pages 755–764, Apr 1996.

[Greenspan 1972] H.P. Greenspan. *Models for the growth of a solid tumor by diffusion.* Stud. Appl. Math., vol. 52, 1972.

[Habbal 2005] A. Habbal. *A topology Nash game for tumoral antiangiogenesis.* Biomed. Appl., vol. 29, 2005.

[Hillen 2006] T. Hillen. *M5 mesoscopic and macroscopic models for mesenchymal motion.* J Math Biol, vol. 53, pages 585–616, Oct 2006.

[Hogea 2006] C.S. Hogea, F. Abraham, G. Biros et C. Davatzikos. *A framework for soft tissue simulations with applications to modeling brain tumor mass-effect in 3D images.* In Workshop on Computational Biomechanics for Medicine. MICCAI, 2006.

[Hogea 2007] C. Hogea, C. Davatzikos et G. Biros. *Modeling Glioma Growth and Mass Effect in 3D MR Images of the Brain.* In Lec. Notes Comp. Sci. 4791, pages 642–650. Medical Image Computing and Computer-Assisted Intervention MICCAI 2007, 2007.

[Holmes 2000] M.J. Holmes et B.D. Sleeman. *A mathematical model of tumour angiogenesis incorporating cellular traction and viscoelastic effects.* J. Theor. Biol., vol. 202, 2000.

[Jbabdi 2005] S. Jbabdi, E. Mandonnet, H. Duffau, L. Capelle, K.R. Swanson, M. Pélégrini-Issac, R. Guillevin et H. Benali. *Simulation of anisotropic growth of low-grade gliomas using diffusion tensor imaging.* Magnetic Reson. in Med., vol. 54, 2005.

[Jiang 2000] G.-S. Jiang et D. Peng. *Weighted ENO Schemes for Hamilton-Jacobi Equations.* SIAM J. Sci. Comput., vol. 21, no. 6, pages 2126–2143, 2000.

[Johnson 1989] P.C. Johnson, S.J. Hunt et B.P. Drayer. *Human cerebral gliomas: correlation of postmortem MR imaging and neuropathologic findings.* Radiology, vol. 170, pages 211–217, Jan 1989.

[Kantor 2001] G. Kantor, H. Loiseau, A. Vital et J.J. Mazeron. *Descriptions of GTV and CTV for radiation therapy of adult glioma.* Cancer Radiother., vol. 5, no. 5, pages 571–580, 2001.

[Kao 2005] C. Kao, S. Osher et Y. Tsai. *Fast sweeping methods for static hamilton-jacobi equations.* SIAM J. Numer. Anal., vol. 42, 2005.

[Kaspari 1997] N. Kaspari, B. Michaelis et G. Gademann. *Using an artificial neural network to define the planning target volume in radiotherapy.* Journal of Medical Systems, vol. 21, pages 389–401, 1997.

[Kato 2008] T. Kato, J. Shinoda, N. Oka, K. Miwa, N. Nakayama, H. Yano, T. Maruyama, Y. Muragaki et T. Iwama. *Analysis of 11C-methionine Uptake in Low-Grade Gliomas and Correlation with Proliferative Activity.* AJNR Am J Neuroradiol, Aug 2008.

[Keener 1998] J. Keener et J. Sneyd. Mathematical physiology. Springer, 1998.

[Kevorkian 2000] J. Kevorkian. Partial differential equations: Analytical solution techniques. Springer, 2000.

[Konukoglu 2006] E. Konukoglu, O. Clatz, P.Y. Bondiau, H. Delingette et N. Ayache. *Extrapolating tumor invasion margins for physiologically determined radiotherapy regions.* Med Image Comput Comput Assist Interv Int Conf Med Image Comput Comput Assist Interv, vol. 9, pages 338–346, 2006.

[Konukoglu 2007a] E. Konukoglu, O. Clatz, P.Y. Bondiau, M. Sermesant, H. Delingette et N. Ayache. *Towards an identification of tumor growth parameters from time series of images.* In Lec. Notes Comp. Sci. 4791, pages 549–556. Medical Image Computing and Computer-Assisted Intervention âĂŞ MICCAI 2007, 2007.

[Konukoglu 2007b] E. Konukoglu, M. Sermesant, O. Clatz, J-M. Peyrat, H. Delingette et N. Ayache. *A Recursive Anisotropic Fast Marching Approach to Reaction Diffusion Equation: Application to Tumor Growth Modeling.* In LNCS Proceedings of the 20th IPMI, 2007.

[Konukoglu 2008a] E. Konukoglu, X. Pennec, O. Clatz et N. Ayache. *Tumor growth modeling in oncological image analysis.* In Isaac Bankman, editor, Handbook in Medical Image Analysis, chapter 18. Elsevier, 2008.

[Konukoglu 2008b] E. Konukoglu, W.M. Wells, S. Novellas, N. Ayache, R. Kikinis, Black P M et K.M. Pohl. *Monitoring Slowly Evolving Tumors.* In In Proceedings of the IEEE Internation Symposium on Biomedical Imaging: From Nano to Macro (ISBI'08), Paris, France, May 2008.

[Konukoglu tteda] E. Konukoglu, O. Clatz, P.-Y. Bondiau, H. Delingette et N. Ayache. *Extrapolating glioma invasion margin in brain magnetic resonance images: suggesting new irradiation margins.* Med. Im. Ana., vol. –, pages –, submitted.

[Konukoglu ttedb] E. Konukoglu, O. Clatz, B. Menze, E. Mandonnet, H. Delingette et N. Ayache. *Tumor growth parameter identification for reaction-diffusion models using time series of images*. IEEE TMI, vol. –, pages –, submitted.

[Kracht 2004] L.W. Kracht, H. Miletic, S. Busch, A.H. Jacobs, J. Voges, M. Hoevels, J.C. Klein, K. Herholz et W.D. Heiss. *Delineation of brain tumor extent with [11C]L-methionine positron emission tomography: local comparison with stereotactic histopathology*. Clin. Cancer Res., vol. 10, pages 7163–7170, Nov 2004.

[Kyriacou 1999] S.K. Kyriacou, C. Davatzikos, S.J. Zinreich et R.N. Bryan. *Nonlinear elastic registration of brian images with tumor pathology using a biomechanical model*. IEEE TMI, vol. 18, 1999.

[Landman 2001] K.A. Landman et C.P. Please. *Tumour dynamics and necrosis: surface tension and stability*. IMA J. Math. Appl. Med. Biology, vol. 18, 2001.

[Levine 2000] H.A. Levine, B.D. Sleeman et M. Nilsen-Hamilton. *A mathematical model for the roles of pericytes and macrophages in angiogenesis. I. the role of protease inhibitors in preventing angiogenesis*. Math. Biosci., vol. 168, 2000.

[Liang 2000] Z.-P. Liang et P.C. Lauterbur. Principles of magnetic resonance imaging. Wiley Interscience, 2000.

[Liotta 1974] L.A. Liotta, G.M.Saidel et J.Kleinerman. *Diffusion model of tumor vascularization and growth*. Bull. Math. Biology, vol. 34, 1974.

[Lloyd 2007] B.A. Lloyd, D. Szczerba et G. Székely. *A coupled finite element model of tumor growth annd vascularization*. In Lec. Notes Comp. Sci. 4792. MICCAI, 2007.

[Lloyd 2008] B. A. Lloyd, D. Szczerba, M. Rudin et G. SzÃľkely. *A computational framework for modelling solid tumour growth*. Philos Transact A Math Phys Eng Sci, vol. 366, pages 3301–3318, Sep 2008.

[Lu 2003] S. Lu, D. Ahn, G. Johnson et S. Cha. *Peritumoral diffusion tensor imaging of high-grade gliomas and metastatic brain tumors*. AJNR Am J Neuroradiol, vol. 24, pages 937–941, May 2003.

[Lu 2004] S. Lu, D. Ahn, G. Johnson, M. Law, D. Zagzag et R.I. Grossman. *Diffusion-tensor MR imaging of intracranial neoplasia and associated peritumoral edema: introduction of the tumor infiltration index*. Radiology, vol. 232, pages 221–228, Jul 2004.

[Maggelakis 1990] S.A. Maggelakis et J.A. Adam. *Mathematical model of prevascular growth of a spherical carnicoma*. Math. Comput. Modelling, vol. 13, 1990.

[Mahajan 2005] A. Mahajan, I.E. McCutcheon, D. Suki, E.L. Chang, S.J. Hassenbusch, J.S. Weinberg, A. Shiu, M.H. Maor et S.Y. Woo. *Case-control study of stereotactic radiosurgery for recurrent glioblastoma multiforme*. J. Neurosurg., vol. 103, pages 210–217, Aug 2005.

[Maini 2004] P.K. Maini, D.L.S. McElwain et D.I. Leavesley. *Traveling wave model to interpret a wound-healing cell migration assay for human peritoneal mesothelial cells*. Tissue Eng., vol. 10, 2004.

[Mandonnet 2008] E. Mandonnet, J. Pallud, O. Clatz, L. Taillandier, E. Konukoglu, H. Duffau et L. Capelle. *Computational modeling of the WHO grade II glioma dynamics: principles and applications to management paradigm*. Neurosurg Rev, vol. 31, pages 263–269, Jul 2008.

[Mantzaris 2004] N.V. Mantzaris, S. Webb et H.G. Othmer. *Mathematical modeling of tumor-induced angiogenesis*. Journal of Mathematical Biology, vol. 49, 2004.

[Mayneord 1932] W.V. Mayneord. *On a low of growth of Jensen's rat sarcoma*. Am. J. Cancer, vol. 16, 1932.

[McCorquodale 2001] P. McCorquodale, P. Colella et H. Johansen. *A cartesian grid embedded boundary method for the heat equation in irregular domains*. J. Comp. Phys., vol. 173, no. 2, 2001.

[McElwain 1978] D.L.S. McElwain et L.E. Morris. *Apoptosis as a volume loss mechanism in mathematical models of solid tumor growth*. Math. Biosci, vol. 39, 1978.

[McElwain 1993] D.L.S. McElwain et G.J. Pettet. *Cell migration in multicell spheroids: swimming against the tide*. Bull. Math. Biology, vol. 55, 1993.

[Miwa 2004] K. Miwa, J. Shinoda, H. Yano, A. Okumura, T. Iwama, T. Nakashima et N. Sakai. *Discrepancy between lesion distributions on methionine PET and MR images in patients with glioblastoma multiforme: insight from a PET and MR fusion image study*. J. Neurol. Neurosurg. Psychiatr., vol. 75, pages 1457–1462, Oct 2004.

[Mohamed 2005] A. Mohamed et C. Davatzikos. *Finite element modeling of brain tumor mass-effect from 3D medical images*. In Lec. Notes Comp. Sci 3749. MICCAI, 2005.

[Mohamed 2006] A. Mohamed, E.I. Zacharaki, D. Shen et C. Davatzikos. *Deformable registration of brain tumor images via a statistical model of tumor-induced deformation*. Med. Im. Anal., vol. 10, 2006.

[Moré 1983] J.J. Moré et D.C. Sorensen. *Computing a trust region*. SIAM J. Sci. Comput., vol. 4, no. 3, pages 553–572, 1983.

[Murray 2002] J. Murray. Mathematical biology. Springer-Verlag, 2002.

[Nandi 2008] S. Nandi, I.V. Ulasov, M.A. Tyler, A.Q. Sugihara, L. Molinero, Y. Han, Z.B. Zhu et M.S. Lesniak. *Low-dose radiation enhances survivin-mediated virotherapy against malignant glioma stem cells.* Cancer Res., vol. 68, pages 5778–5784, Jul 2008.

[Ogawa 1993] T. Ogawa, F. Shishido, I. Kanno, A. Inugami, H. Fujita, M. Murakami, E. Shimosegawa, H. Ito, J. Hatazawa et T. Okudera. *Cerebral glioma: evaluation with methionine PET.* Radiology, vol. 186, pages 45–53, Jan 1993.

[Orme 1996a] M.E. Orme et M.A.J. Chaplain. *A mathematical model of the first steps of tumour-related angiogenesis: Capillary sprout formation and secondary branching.* IMA J. Math. Appld. Med. Biol., vol. 13, 1996.

[Orme 1996b] M.E. Orme et M.A.J.Chaplain. *A mathematical model of vascular tumor growth and invasion.* Mathematical Computational Modelling, vol. 23, 1996.

[Osher 1993] S. Osher. *A level set formulation for the solution of the Dirichlet problem for Hamilton-Jacobi equations.* SIAM J. Math. Anal., vol. 24, no. 5, 1993.

[Patel 2001] A.A. Patel, E.T. Gawlinkski, S.K. Lemieux et R.A. Gatenby. *A cellular automaton model of early tumor growth and invasion: the effects of native tissue vascularity and increased anaerobic tumor metabolism.* J. Theor. Biol., vol. 213, 2001.

[Perumpanani 1999] A.J. Perumpanani et J. Norbury. *Numerical interactions of random and directed motility during cancer invasion.* Math. Comput. Modelling, vol. 30, 1999.

[Petrovskii 2001] S. Petrovskii et N. Shigesada. *Some exact solutions of a generalized Fisher equation related to the problem of biological invasion.* Math. Biosc., vol. 172, pages 73–94, 2001.

[Pettet 2001] G.J. Pettet, C.P. Please, M.J. Tindall et D.L.S. McElwain. *The migration of cells in multicell tumor spheroids.* Bull. Math. Biology, vol. 63, 2001.

[Plank 2004] M.J. Plank et B.D. Sleeman. *Lattice and non-lattice models of tumour angiogenesis.* Bull. Math. Biol., vol. 66, pages 1785–1819, Nov 2004.

[Please 1999] C.P. Please, G.J. Pettet et D.L.S. McElwain. *Avascular tumour dynamics and necrosis.* Math. Models Methods Appl. Sci., vol. 9, 1999.

[Powell 2001] M.J.D. Powell. *On the Lagrange functions of quadratic models that are defined by interpolation.* Optimization Methods and Software, vol. 16, pages 289–309, 2001.

[Powell 2002] M.J.D. Powell. *UOBYQA: unconstrained optimization by quadratic approximation.* Math. Program. Ser. B, vol. 92, 2002.

[Powell 2003] M.J.D. Powell. *On trust region methods for unconstrained minimization without derivatives.* Math. Program. Ser. B, vol. 97, pages 605–623, 2003.

[Prastawa 2005] M. Prastawa, E. Bullitt et G. Gerig. *Synthetic ground truth for validation of brain tumor MRI segmentation.* In Lec. Notes Comp. Sci. 3749. MICCAI, 2005.

[Prastawa 2008] M. Prastawa, E. Bullitt et G. Gerig. *Simulation of brain tumors in MR images for evaluation of segmentation efficacy.* Med Image Anal, Dec 2008.

[Price 2003] S.J. Price, N.G. Burnet, T. Donovan, H.A. Green, A. Peña, N.M. Antoun, J.D. Pickard, T.A. Carpenter et J.H. Gillard. *Diffusion tensor imaging of brain tumours at 3T: a potential tool for assessing white matter tract invasion?* Clin Radiol, vol. 58, pages 455–462, Jun 2003.

[Price 2007] S.J. Price. *The role of advanced MR imaging in understanding brain tumour pathology.* Br J Neurosurg, vol. 21, pages 562–575, Dec 2007.

[Qian 2001] J. Qian et W.W. Symes. *Paraxial eikonal solvers for anisotropic quasi-p travel times.* J. Comp. Physics, vol. 173, pages 256–278, 2001.

[Qian 2006] J. Qian, Y. Zhang et H. Zhao. *A fast sweeping method for static convex hamilton-jacobi equations.* UCLA Comp. and App. Math. Reports, vol. 06-37, 2006.

[Rexilius 2004] J. Rexilius, H.K. Hahn, M. Schlüter, S. Kohle, H. Bourquain, J. Böttcher et H.-O. Peitgen. *A framework for the generation of realistic brain tumor phantoms and applications.* In Lec. Notes Comp. Sci. 3217. MICCAI, 2004.

[Ricard 2007] D. Ricard, G. Kaloshi, A. Amiel-Benouaich, J. Lejeune, Y. Marie, E. Mandonnet, M. Kujas, K. Mokhtari, S. Taillibert, F. Laigle-Donadey, A.F. Carpentier, A. Omuro, L. Capelle, H. Duffau, P. Cornu, R. Guillevin, M. Sanson, K. Hoang-Xuan et J.Y. Delattre. *Dynamic history of low-grade gliomas before and after temozolomide treatment.* Ann. Neurol., vol. 61, pages 484–490, May 2007.

[Roberts 2005] T.P. Roberts, F. Liu, A. Kassner, S. Mori et A. Guha. *Fiber density index correlates with reduced fractional anisotropy in white matter of patients with glioblastoma.* AJNR Am J Neuroradiol, vol. 26, pages 2183–2186, Oct 2005.

[Rodrigo 2003] M. Rodrigo. *Evolution of bounding functions for the solution of the KPP-Fisher equation in bounded domains.* Studies in App. Math., vol. 110, pages 49–61, 2003.

[Rouy 1992] E. Rouy et A. Tourin. *A viscosity solutions approach to shape-from-shading.* SIAM J. Num. Anal., vol. 29, no. 3, pages 867–884, 1992.

[Saidel 1976] G.M. Saidel, L.A. Liotta et J. Kleinerman. *System dynamics of a metastatic process form an implanted tumor.* J. Theor. Biology, vol. 56, 1976.

[Sanga 2007] S. Sanga, H.B. Frieboes, X. Zheng, R. Gatenby, E.L. Bearer et V. Cristini. *Predictive oncology: A review of multidisciplinary, multiscale in silico modeling linking phenotype, morphology and growth.* NeuroImage, vol. 37, pages S120–S134, 2007.

[Seither 1995] R.B. Seither, B. Jose, K.J. Paris, R.D. Lindberg et W.J. Spanos. *Results of irradiation in patients with high-grade gliomas evaluated by magnetic resonance imaging.* Am. J. Clin. Oncol., vol. 18, pages 297–299, 1995.

[Sermesant 2007] M. Sermesant, E. Konukoglu, H. Delingette, Y. Coudiere, P. Chinchaptanam, K.S. Rhode, R. Ra zavi et N. Ayache. *An anisotropic multifront fast marching method for real-time simulation of cardiac electrophysiology.* In Proceedings of Functional Imaging and Modeling of the Heart 2007 (FIMH'07), volume 4466 of *LNCS*, pages 160–169, 7-9 June 2007.

[Sethian 1999] J.A. Sethian. Level set methods and fast marching methods: Evolving interfaces in computational geometry, fluid mechanics, computer vision, and materials science. Cambridge University Press, 1999.

[Sethian 2003] J. Sethian et A. Vladimirsky. *Ordered upwind methods for static hamilton-jacobi equations: theory and algorithms.* SIAM J. Numer. Anal., vol. 41, 2003.

[Shen 2002] D. Shen et C. Davatzikos. *HAMMER: Hierarchical attribute matching mechanism for elastic registration.* IEEE Tran. Med. Imag., vol. 21, 2002.

[Sinha 2002] S. Sinha, M.E. Bastin, I.R. Whittle et J.M. Wardlaw. *Diffusion tensor MR imaging of high-grade cerebral gliomas.* AJNR Am J Neuroradiol, vol. 23, pages 520–527, Apr 2002.

[Stamatakos 2006a] G.S. Stamatakos, V.P. Antipas et N.K. Uzunoglu. *A Spatiotemporal, Patient Individualized Simulation Model of Solid Tumor Response to Chemotherapy in Vivo: The Paradigm of Glioblastoma Multiforme Treated by Temozolomide.* IEEE Tran. Bio. Med. Eng., 2006.

[Stamatakos 2006b] G.S. Stamatakos, V.P. Antipas, N.K. Uzunoglu et R.G. Dale. *A four-dimensional compute simulation model of the in-vivo response to radiotherapy of glioblastoma multiforme: studies on the effect of clonogenic cell density.* Brit. J. Rad., 2006.

[Stein 2007] A.M. Stein, T. Demuth, D. Mobley, M. Berens et L.M. Sander. *A mathematical model of glioblastoma tumor spheroid invasion in a three-dimensional in vitro experiment.* Biophys. J., vol. 92, pages 356–365, Jan 2007.

[Stevens 2000] A. Stevens. *The derivation of chemotaxis equations as limit dynamics of moderately interacting stochastic many-particle systems.* SIAM J. Appl. Math., vol. 61, no. 1, pages 183–212, 2000.

[Stokes 1991] C.L. Stokes et D.A. Lauffenburger. *Analysis of the roles of microvessel endothelial cell random motility and chemotaxis in angiogenesis.* J. Theor. Biol., vol. 152, 1991.

[Strauss 1992] W.A. Strauss. Partial differential equations: An introduction. Wiley and Sons, New York, 1992.

[Swanson 2000] K.R. Swanson, E.C. Alvord et J.D. Murray. *A quantitative model for differential motility of gliomas in grey and white matter.* Cell Prolif., vol. 33, 2000.

[Swanson 2002a] K.R. Swanson, E.C. Alvord et J.D. Murray. *Quantifying efficacy of chemotherapy of brain tumors with homogeneous and heteregeneous drug delivery.* Acta Biotheoretica, vol. 50, 2002.

[Swanson 2002b] K.R. Swanson, E.C. Alvord et J.D. Murray. *Virtual brain tumours (gliomas) enhance the reality of medical imaging and highlight inadequacies of current therapy.* British Journal of Cancer, vol. 86, 2002.

[Swanson 2004] K.R. Swanson, E.C. Alvord et J.D. Murray. *Dynamics of a model for brain tumors reveals a small window for therapeutic intervention.* Discrete and Continous Dynamical Systems-Series B, vol. 4, no. 1, pages 289–295, 2004.

[Swanson 2008a] K.R. Swanson. *Quantifying glioma cell growth and invasion in vitro.* Math. Comp. Model., vol. 47, pages 638–648, 2008.

[Swanson 2008b] K.R. Swanson, R.C. Rostomily et E.C. Alvord. *A mathematical modelling tool for predicting survival of individual patients following resection of glioblastoma: a proof of principle.* British Journal of Cancer, vol. 98, pages 113–119, 2008.

[Tabatai 2005] M. Tabatai, D.K. Williams et Z. Bursac. *Hyperbolastic growth models: theory and application.* Theor. Biol. Med. Modelling, vol. 2:14, 2005.

[Taylor 1996] M.E. Taylor. Partial differential equations 1: Basic theory. Springer, 1996.

[Thirion 1998] J.-P. Thirion. *Image matching as a diffusion process: An analogy with Maxwell's demons.* Med. Im. Anal., vol. 2, 1998.

[Thomlinson 1955] R.H. Thomlinson et L.H. Gray. *The histological structure of some human lung cancers and the possible implications for radiotherapy.* Br. J. Cancer, vol. 9, 1955.

[Tong 2000] S. Tong et F. Yuan. *Numerical simulations of angiogenesis in the cornea.* Microvasc. Res., 2000.

[Tovi 1993] M. Tovi. *MR imaging in cerebral gliomas analysis of tumour tissue components.* Acta Radiol Suppl, vol. 384, pages 1–24, 1993.

[Tovi 1994] M. Tovi, M. Hartman, A. Lilja et A. Ericsson. *MR imaging in cerebral gliomas. Tissue component analysis in correlation with histopathology of whole-brain specimens.* Acta Radiol, vol. 35, pages 495–505, Sep 1994.

[Tracqui 1995] P. Tracqui, G. Cruywagen, D. Woodward, G. Bartoo, J. Murray et E. Alvord. *A mathematical model of glioma growth: the effect of chemotherapy on spatio-temporal growth.* Cell Proliferation, vol. 28, no. 1, 1995.

[U. Ebert 2000] W.v. Saarloos U. Ebert. *Front propagation into unstable states: universal algebraic convergence towards uniformly translating pulled fronts.* Physica D: Nonlinear Phenomena, vol. 146, 2000.

[Vercauteren 2008] Tom Vercauteren. *Image Registration and Mosaicing for Dynamic In Vivo Fibered Confocal Microscopy.* Phd thesis, École Nationale Supérieure des Mines de Paris, January 2008.

[Wasserman 1996] R. Wasserman et R. Acharya. *A patient-specific in-vivo tumor model.* Math. Biosci., vol. 136, 1996.

[Westbrook 1998] C. Westbrook et C. Kaut. Mri in practice. Blackwell Science, second édition, 1998.

[Wette 1974a] R. Wette, I.N. Katz et E.Y. Rodin. *Stochastic processes for solid tumor kinetics i. Surface-regulated growth.* Math. Biosci, vol. 19, 1974.

[Wette 1974b] R. Wette, I.N. Katz et E.Y. Rodin. *Stochastic processes for solid tumor kinetics ii. Diffusion-regulated growth.* Math. Biosci, vol. 21, 1974.

[Wilson 1999] C.B. Wilson et M.S. Berger. The gliomas. W.B. Saunders Company, 1999.

[Zacharaki 2006] E.I. Zacharaki, D. Shen, A. Mohamed et C. Davatzikos. *Registration of brain images with tumors: Towards the construction of statistical atlases for therapy planning.* In Proceedings of 3rd IEEE International Symposium on Biomedical Imaging. ISBI, 2006.

[Zhang 2007] L. Zhang, C.A. Athale et T.S. Deisboeck. *Development of a three-dimensional multiscale agent-based tumor model: simulating gene-protein interaction profiles, cell phenotypes and multicellular patterns in brain cancer.* J. Theor. Biol., vol. 244, pages 96–107, Jan 2007.

[Zheng 2005] X. Zheng, S.M. Wise et V. Cristini. *Nonlinear simulation of tumor necrosis, neo-vascularization and tissue invasion via an adaptive finite-element/level-set method.* Bull. Math. Biol., vol. 67, 2005.

[Zizzari 2004] A. Zizzari, B. Michaelis et G. Gademann. *Simulation and Modeling of Brain Tumors in Computer-Assisted Radiotherapy.* In Proc. IASTED Conf. Applied Simulation and Modelling, 2004.